A Phantom for the Study of Positional Brain Shift

Matthew Richard Potts

A thesis submitted for the degree of
Doctor of Philosophy

Supervisors
Prof. S. L. Evans
Prof. D. Marshall

2020

Abstract

Positional brain shift (PBS) is the term given to the displacement of the brain which occurs upon surgical reorientation of the head and presents as one of the many sources of targeting error in high precision neurosurgery. Due to the impracticality of imaging humans in non-standard positions, however, there is currently insufficient information for surgeons to utilize in order to mitigate against PBS in surgical planning.

To better characterise PBS, a novel synthetic model (phantom) of the brain-skull system was developed, comprising hydrogel brain (inc. imaging beads) with water filled ventricle cavity, elastomer dural septa, water filled subarachnoid space, and plastic skull. This phantom was validated by simulating the supine to prone PBS event and mechanically tuning the phantom's hydrogel brain such that the general magnitude of shift (measured through CT imaging) matched that reported in human MRI studies.

Using this phantom, brain shift characterisation was performed for a discrete representation of the continuous spectrum of possible positional transitions in neurosurgery. Here, brain shift was measured across eight positional transitions at 44 locations within the brain.

Eight novel PBS maps were produced as a result of this study, with mean brain shift ranging between 0.39 and 0.94 mm and the standard deviation of shift within each PBS map ranging between 0.12 and 0.44 mm. The greatest shift was found upon transition from the supine to elevated right decubitus position, with a shift of 2 mm being measured in the left parietal lobe. Importantly, it was found that, a) clinically significant brain shift took place across all transitions and, b) clinically significant variability took place between the brain shift patterns of individual transitions at the local level. Together these findings further highlight the need for the consideration of PBS in surgical planning and strongly suggest that versatile parametric software are likely needed to account for the variable shifting of neurosurgical targets.

The developed phantom has allowed for novel insights into an event otherwise difficult to study in humans. With further developments, it is believed that the phantom can be used to study other similarly problematic events, such as trauma.

I dedicate this to my parents, my brothers,
my family, my friends and my dogs.

Acknowledgements

I would like to first express my thanks to Professor Sam Evans and Professor Dave Marshall for their excellent supervision of my project. Their support and guidance throughout were instrumental to the successful completion of the project and for that I am very grateful. I would also like to extend my thanks to my fellow brain shift researchers, Nicholas Bennion and Stefano Zappalá, whom I worked alongside during the project. Their assistance and friendship throughout was invaluable and helped me retain most of my marbles.

In a similar vein, I would also like to thank the various academic and technical support staff of the School of Engineering, who collectively made my time at Cardiff University a pleasant one. Of the basement labs, I would specifically like to thank Richard Thomas, Ian King, Garry Shipley, Amanda Kitching and Harry Lane, who were of great help and who tirelessly put up with my terrible ignorance towards the names of basic tools and equipment (often having to resort to charades instead). Of the manufacturing labs, I would specifically like to thank James Spenceley, Franck Lacan and Justin Merridew for all the parts they built for me and who's combined 3D printing experience saved a considerable amount of time and expense throughout the project.

Similarly, I must also thank those at the Cardiff University Brain Research Imaging Centre (CUBRIC). Specifically, I would like to thank Peter Hobden and Allison Cooper for their help in MR scanning and Professor Derek Jones for his advice and guidance during the project. I would also very much like to thank Gill Gaywood at Velindre Cancer Centre for her help in CT scanning the phantom during its development. The phantom's development would undoubtedly had to have been cut short if it weren't for her help and I especially appreciated her willingness to scan during her own lunch break. Rhodri Smith at the Wales Research and Diagnostic Positron Emission Tomography Imaging Centre (PETIC) is also deserving of thanks for his help in the final CT scanning of the phantom at University Hospital Wales.

I must also thank Rob Harrison, Dr. Stephen Anderson and Renishaw plc, along with the Engineering and Physical Sciences Research Council (ESPRC), for their financial support and industrial guidance.

Of my friends which I have not yet mentioned, I would also like to thank Joe Redfern, Jon Poor, Sig Hill, Hayley Wyatt, Aled Owen, Dan Love, Andrew Jones, Tom Holmes, Nico Rey de Castro and Danny Rodgers for their personal support throughout.

Lastly, I would like to thank my family, for it was they who ultimately enabled the completion of this work. I need to express my gratitude towards my mum and dad for both their personal and financial support, and I must also thank Ollie, Jon, Chris, Lucy and Skyla for their endless encouragement in, what they liked to call, "Matt's jelly brains research".

CONTENTS

FIGURES

TABLES

INDEX

Common Abbreviations:

ABC – *Arachnoid Barrier Cell*

CAD – *Computer Aided Design*

CBM – *Composite Brain Mould*

CT – *Computed Tomography*

CSF *– Cerebrospinal Fluid*

DBC – *Dural Border Cell*

Di H_20 – *Deionised Water*

DS – *Dural Septa*

IF – *Initial Formulation*

LSH – *Lower Skull Half*

MR – *Magnetic Resonance*

MRI – *Magnetic Resonance Imaging*

MRE – *Magnetic Resonance Elastography*

PAC *– Pia-Arachnoid Complex*

PBS – *Positional Brain Shift*

PMBS – *Pneumocephalus Mediated Brain Shift*

PHY – *Phytagel*

PVA – *Polyvinyl Alcohol*

SAS – *Subarachnoid Space*

S→eS *– Supine to Elevated Supine*

S→U *– Supine to Upright*

S→eP – *Supine to Elevated Prone*

S→P *– Supine to Prone*

S→RD *– Supine to Right Decubitus*

S→eRD *– Supine to Elevated Right Decubitus*

S→eLD *– Supine to Elevated Left Decubitus*

S→LD *– Supine to Elevated Left Decubitus*

SF – *Sugar Formulation*

USH *– Upper Skull Half*

Standard Deviation: Unless otherwise specified, standard deviation is indicated by the use of the plus or minus symbol (±). A mean of 15 and a corresponding standard deviation of 5, for example, is presented as 15 ± 5.

1 Introduction

1.1 Project Outline

The human brain is a complex organ housed within an equally complex system of supportive structures. When pathology manifests, surgery is sometimes the best option. However, due to the encased nature of the brain, a particularly sophisticated means of carrying out the surgery is often required.

Stereotactic neurosurgery is a minimally invasive procedure wherein a rigid frame is attached to the patient's head and used to accurately deliver instruments through trajectories planned prior to the surgery with medical images of the patient. Stereotactic radiotherapy is another form of stereotaxy which again uses a frame to restrict the head, however, in this case the trajectories are used to deliver precise doses of radiation non-invasively. These procedures often present with a very low margin for spatial error, and for some, this margin can be as small as 1 mm [1].

Planning for these surgeries is traditionally done using preoperative scans taken with the head in the supine position, however, in the operating theatre, the patients head is often positioned differently with the brain loaded in a different anatomical direction by gravity (see Section 3.3, p38). Given that the brain is known to shift within the cranial cavity in the direction of gravity, this presents as a problem, as the surgical target no longer lies along the pre-planned surgical trajectory (see Section 3.5, p45). Because surgical targets cannot be reliably located with typically available intraoperative imaging systems (i.e. computerised tomography X-ray imaging - CT), the trajectory cannot be updated, leading to targeting error and, as a consequence, sub-optimal clinical outcomes.

Gravitational shifting of the brain within the surgically unopened cranial cavity is known as positional brain shift (PBS) and forms one of the many sources of targeting error in stereotactic neurosurgery (see Section 3.4, p42). If all these sources were fully understood, however, a correctional software could be developed for preoperative planning. This would present as a far cheaper, safer and less time-costly alternative to the intraoperative methods of trajectory correction: microelectrode recording (MER) and iMRI-guidance [2]. Because PBS occurs high up in the surgical workflow and precedes other brain shift events that occur upon the opening of the skull and manipulation of the brain, it presents as an important event to characterise. Due to impracticalities of imaging humans in non-standard positions, however, little is known about positional transitions other than supine to prone (S→P) (see Section 3.5, p45). The precise manner in which the brain shifts of course depends on the position to which it transitions. Therefore, it is important to investigate transitions to all head positions utilised in stereotactic procedures.

The main purpose of this project was to a) develop a means of investigating PBS beyond S→P, through the development of a synthetic model (phantom) of the brain-skull system, and b) produce a novel comprehensive PBS dataset covering a broader representative range of the spectrum of possible positional transitions in neurosurgery.

Connected to this project are two complementary PhD projects. One of these aims to develop techniques to further quantify S→P brain shift in humans using magnetic resonance imaging (MRI) (*in vivo*), while the other aims to recreate brain shift computationally with the finite element (FE) method (*in silico)*. A phantom, therefore, forms a half-way point between these two, combining elements of reality (e.g. real materials under load) and the artificial (e.g. use of tissue simulants). An important benefit of this multi-route approach is the ability to cross-validate models and cross-validate measurements produced through different methods.

Each of the three investigatory routes (Figure 1.1) naturally has its own particular set of limitations. While studying the problem directly, the *in vivo* route is limited by the difficulty of imaging humans in non-supine positions and the limited spatial resolution and known geometrical distortion associated with MRI scanners (see Section 3.1, p33). The phantom route, while unbound by ethical constraints, is limited by the difficulty of reproducing the morphologically complex material system of the head with contemporary fabrication methods and available material surrogates. The *in silico* route, although unburdened by practical constraints, is instead limited by the difficulty of modelling such a complex mechanical system with mathematics.

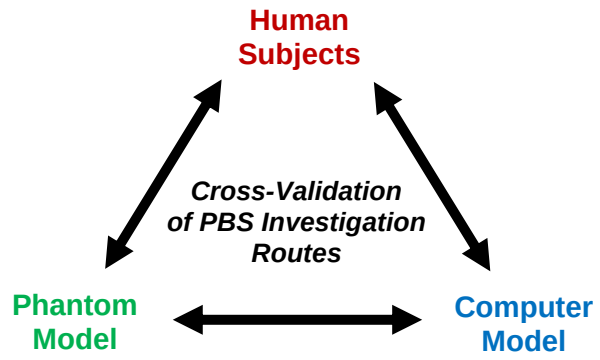

Figure 1.1: The three complementary PBS investigation routes.

If all three investigatory routes produce similar brain shift maps for transitions measurable by all three (e.g. S→P), then it can be said with a degree of confidence that a true PBS measurement has been made. Furthermore, it can also be said that that the phantom and *in silico* models have been somewhat validated. At this point, the models can then be used with confidence to provide displacement fields for transitions otherwise difficult to produce through measurement with humans. It is these displacement fields that would go towards the necessary information for the development of a correctional software for PBS in high precision neurosurgery.

In terms of this self-contained project, however, the aims were to:

1) *Develop a geometrically and mechanically realistic (biofidelic), imageable phantom of the brain-skull system that is capable of simulating the positional brain shift event.*

2) *Develop an apparatus for the orientation of the phantom in MRI/CT environments.*

3) *Generate brain shift data for a representative range of the spectrum of possible positional transitions in neurosurgery.*

4) *Compare and contrast brain shift data captured by the phantom to that produced in the literature and the emerging data being produced by the in vivo and in silico routes.*

This project was undertaken in partnership with Renishaw plc, a leading developer of stereotactic robots, software and surgical implements. It is anticipated, therefore, that the outputs of this project will go towards future developments.

1.2 Thesis Outline

Included in this section is a brief outline of the thesis.

Chapters 1-4 together form the introduction and literature review for the thesis. Chapter 1 contains an outline of the project, an overview of the thesis structure and a statement of the novel contributions contained within it. Chapter 2 contains an overview of the anatomy and tissue properties of the brain-skull system. Chapter 3 contains an overview of stereotactic neurosurgery and the role of positional brain shift in targeting error. Chapter 4 contains an analysis of brain-skull phantoms in the literature.

Chapters 5-8 contain the design and developmental work for the phantom. Chapter 5 contains an account of the process employed in designing the phantom. Chapter 6 contains an account of the process employed in constructing the phantom. Chapter 7 contains an account of the improvements made to the initial phantom design. Chapter 8 contains an account of the process employed in tuning the phantom to match literature accounts of positional brain shift.

Chapter 9 contains the study performed with the phantom, in which a novel comprehensive PBS dataset was generated for a discrete representation of the spectrum of possible positional transitions in neurosurgery.

Chapter 10 contains a conclusion of all the work and findings presented in the thesis and a discussion of further developments and investigations that could be undertaken with phantom.

1.3 Novelty Statement

This thesis details the design, validation and use of an entirely novel brain-skull phantom for the generation of a novel comprehensive PBS dataset. No similar phantom can be found in the literature (see Chapter 4) and the data produced by the study towards the end of the thesis represents the largest body of positional brain shift data currently available (see Section 3.5, p45).

Delineated further, the novel contributions within this thesis include:

- A composite brain mould for the moulding of the complete human brain in an established mechanical brain stimulant with realistic internal (ventricles) and external geometry (fissures). A novel use of coconut oil was also found as an investment-type sacrificial mould structure in cryo-hydrogel moulding.

  (This is presented in Chapters 5 and 6)

- A hydrogel formula and production workflow for the attainment of realistic mechanical properties in brains moulded with the composite brain mould.

  (This is presented in Chapters 5, 6 and 7)

- An MR and CT imaging compatible 3D printed skull model, with mechanically realistic attachable dural septa.

  (This is presented in Chapters 5, 6 and 7)

- A workflow for the assembly of a MR and CT imaging compatible brain-skull phantom, comprising hydrogel brain with ventricles and glass bead markers, water flooded subarachnoid space/ventricles, elastomer dural septa and rigid plastic skull.

  (This is presented in Chapters 5, 6 and 7)

- A multi-axis cradle for the orientation of the phantom within MR and CT imaging machines.

  (This is presented in Chapter 8)

- MR and CT imaging protocols for the imaging of the phantom and the brain shift which occurs within it.

  (This is presented in Chapters 7 and 8)

- The validation of the brain-skull phantom with respect to literature accounts of brain shift and data emerging from concurrent *in vivo* and *in silico* projects, underway at Cardiff University at the time of writing.

  (This is presented in Chapters 8 and 9)

- The production of positional brain shift data for a discrete representation of the continuous spectrum of possible positional transitions in neurosurgery.

  (This is presented in Chapter 9)

- An analysis of observed brain shift patterns and their validity with respect to the simplifications made in the phantom.

  (This is presented in Chapter 9)

This work was presented at the 16th International Symposium on Computer Methods in Biomechanics and Biomedical Engineering in 2019, under the title of “Imaging of positional brain shift in a deformable phantom”.

At the time of writing, the work is unpublished, however, two journal papers are in preparation:

- The first will focus on the phantom and its fabrication and validation methods. This is provisionally titled as “Utilization of the freeze-thaw hydrogel formation process for the fabrication of a positional brain shift phantom” and will be published in a journal such as Materials & Design.

- The second will focus on the study performed with the phantom and the novel comprehensive PBS dataset that was obtained. This is provisionally titled as “The multi-position characterisation of positional brain shift with a biofidelic head phantom” and will be published in a journal such as World Neurosurgery.

2 THE BRAIN-SKULL SYSTEM

The purpose of this chapter is to give the reader an overview of the anatomy and tissue properties of the brain-skull system relevant to understanding stereotactic neurosurgery and the building of a biofidelic model. Particular focus is given to features of the brain, meninges and skull that significantly influence the mobility of the brain within the cranial cavity and thus its capacity to shift under gravity.

2.1 Anatomy of the Brain

The human brain presents as a soft, delicate and geometrically complex organ. Although primarily thought of as a functional mass of interconnected neurons, a large majority (approximately 90%) of the brain's mass is in fact formed from cells (glia) and structures (e.g. ventricles) that serve to protect, nourish and enhance the functioning of the neural network [3].

The brain is formed from three interconnected but distinct parts: the cerebrum, cerebellum and brain stem (Figure 2.1). Embedded within the cerebrum and brain stem is a system of interconnected fluid filled ventricles that produce, contain and circulate cerebrospinal fluid (CSF). Together, the cerebrum, cerebellum and brain stem sit housed within the cranial cavity, held in place and supported by the spinal cord, cranial meninges and CSF [4].

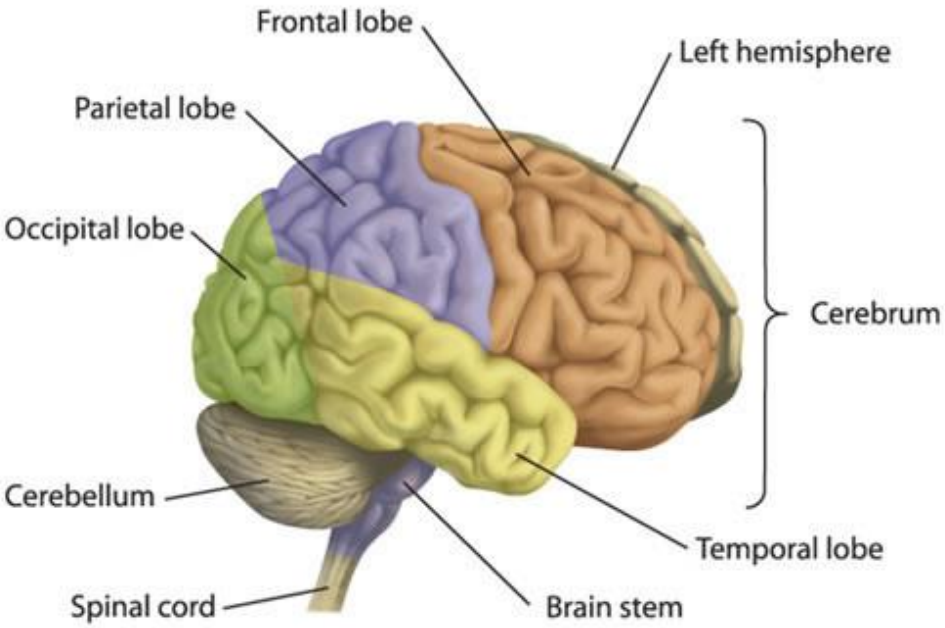

Figure 2.1: The human brain. Reproduced from Reference 5.

2.1.1 The Cerebrum

Comprised of the left and right cerebral hemispheres (connected by central structures), the cerebrum sits on top of the brain stem forming 85% of the brain's approximate 1.4 kg mass [6]. The bulk of the cerebrum, also known as the cerebral parenchyma, is primarily composed of four structures: white matter, grey matter, supporting vasculature and ventricles [4].

The white matter forms approximately 60% of the cerebral parenchyma and serves primarily to transmit information between the different regions of grey matter in the brain [7]. Within this tissue, far-reaching myelinated (fat enveloped) neurons bundle together into nerves and project their processes (axons) in an orientated fashion to and from different parts of the brain.

The grey matter forms approximately 40% of the cerebral parenchyma and is primarily formed of the closely associated and interconnected cell bodies of neurons [7]. Unlike the white matter, which serves to transmit information, the grey matter integrates and processes information to effectuate certain tasks (e.g. the processing of sensory information from the skin).

As illustrated in Figure 2.2, a great majority of the cerebral grey matter lies external to the white matter. Some grey matter nuclei, however, such as the subthalamic nuclei, exist as islands within the white matter. Collectively, these grey matter nuclei are known as the basal ganglia and are often the target of deep brain surgeries [8].

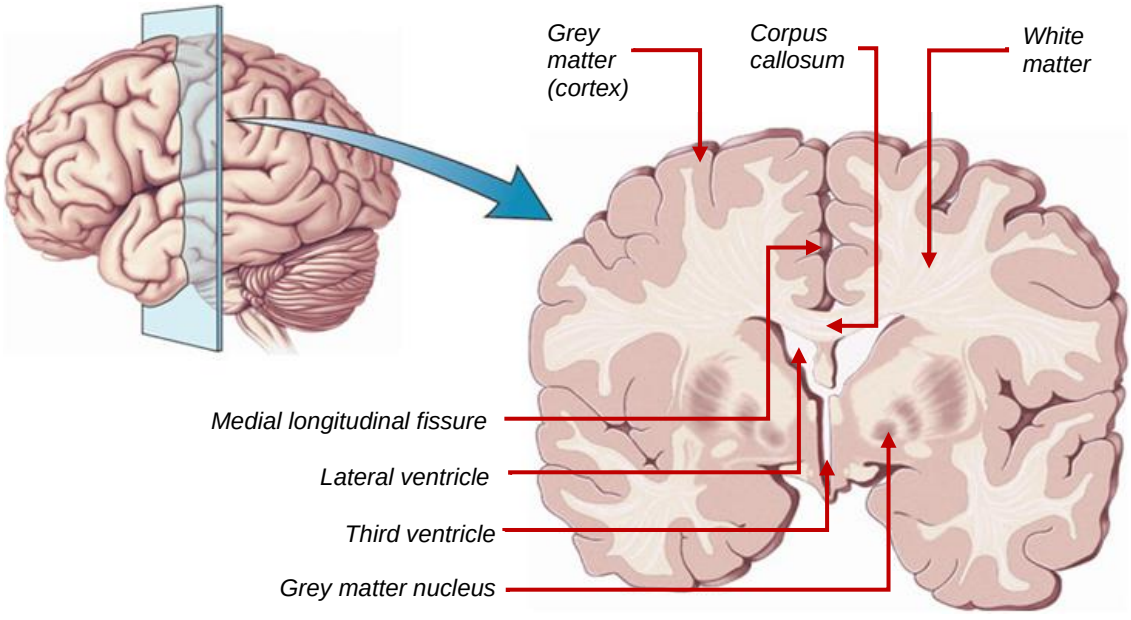

Figure 2.2: Coronal cross-section of the cerebrum. Adapted from Reference 9.

To maximise the volume of grey matter in the cerebrum, the external grey matter layer of the cerebrum (the cortex) forms an irregular pattern of folds [10]. These folds are known as gyri and produce corresponding grooves (sulci) that often harbour blood vessels navigating the surface of the brain [4].

An extension of the gyri are deep fissures that run along certain parts of the cerebrum. Unlike the gyri, however, the fissures are much more orientated, existing as longitudinal trenches that projections of the meninges (dural septa) use to anchor the brain within the cranial cavity. The largest and most prominent of these fissures is the medial longitudinal fissure, which extends all the way down from the surface of the cerebrum to the top of the corpus callosum, partitioning the cerebrum into the left and right cerebral hemispheres (see in Figure 2.2, p7) [4].

2.1.2 The Brain Stem

Comprised of the midbrain, pons and medulla, the brain stem forms the inferior most region of the brain (Figures 2.3-2.5, p9-10), and feeding inferiorly into the spinal cord, the brain stem acts to unite the constituent parts of the brain and anchor them towards the base of the cranium [4].

Similar to the cerebrum, the bulk of the brain stem is formed from grey matter, white matter, supporting vasculature and ventricles.

While white matter tracts in the cerebrum take on various orientations to interconnect its hemispherical structure, a majority of the white matter tracts in the brain stem run in a superior-inferior fashion [11].

2.1.3 The Cerebellum

The cerebellum presents as a small pear-shaped structure that sits underneath the occipital lobe of the cerebrum, attached to the posterior aspect of the brain stem (Figure 2.5, p10). Like the cerebrum, the cerebellum is divided into two hemispheres, connected by a central longitudinal structure (the vermis). The hemispheres of the cerebellum, however, are further divided into ten smaller lobules by a series of fissures that run medio-laterally [12].

Similar to the cerebrum, the cerebellum also features sulci (Figure 2.6, p10). The cerebellar sulci, however, are considerably more ordered, running almost exclusively medio-laterally, parallel to the cerebellar fissures, creating a ribbed pattern along the surface [12].

Although no ventricles are present in the cerebellum, the bulk of the cerebellum is also formed of white matter, grey matter and supporting vasculature [4]. A cerebellar cross-section shows the distribution of cerebellar grey and white matter to be somewhat similar to that of the cerebral matter, with white lying beneath grey.

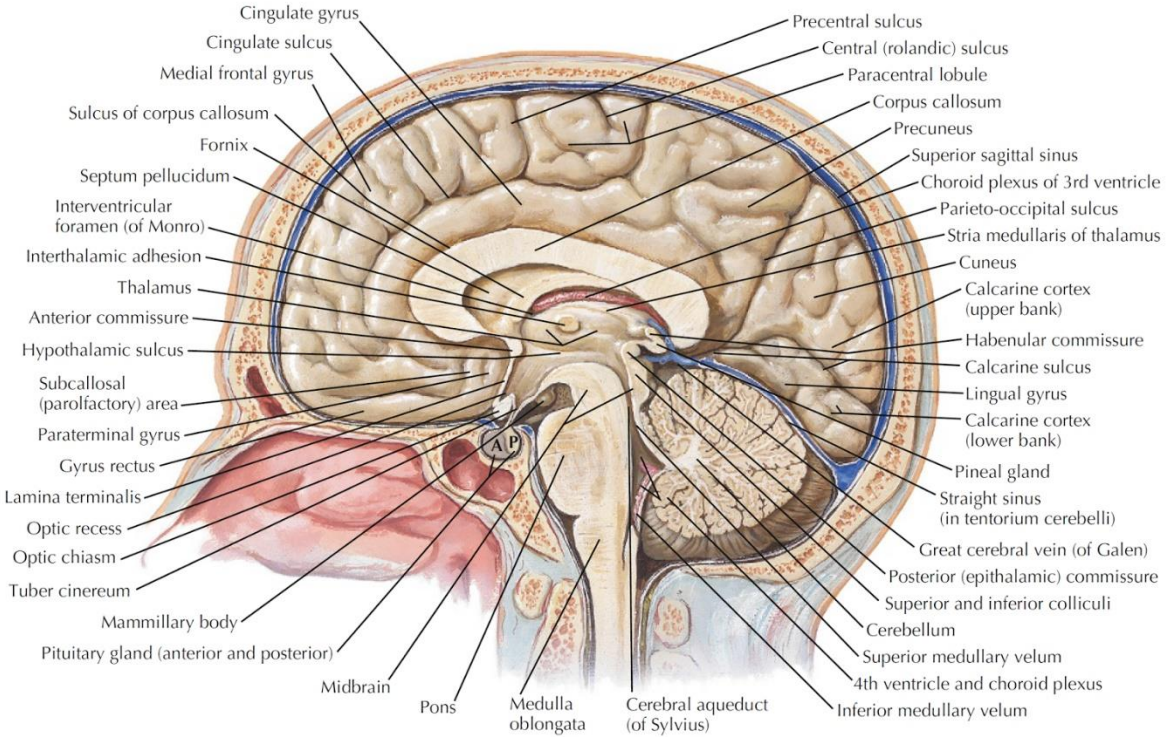

Figure 2.3: Sagittal cross-section of the head. Reproduced from Reference 13.

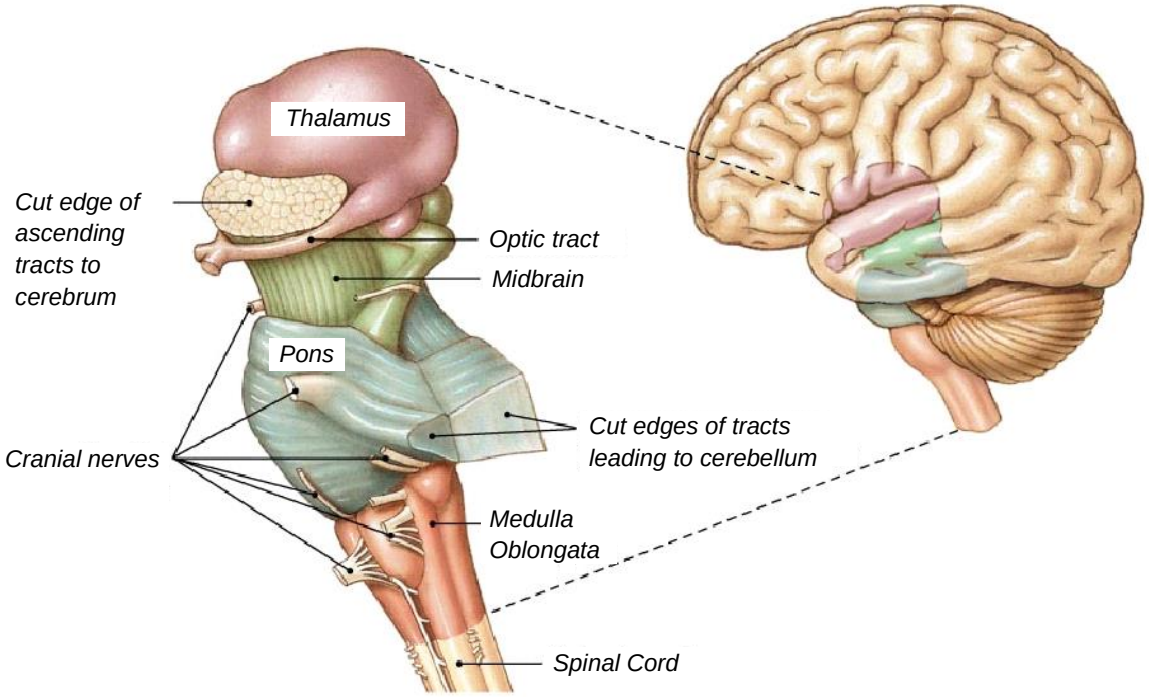

Figure 2.4: The brain stem. Adapted from Reference 14.

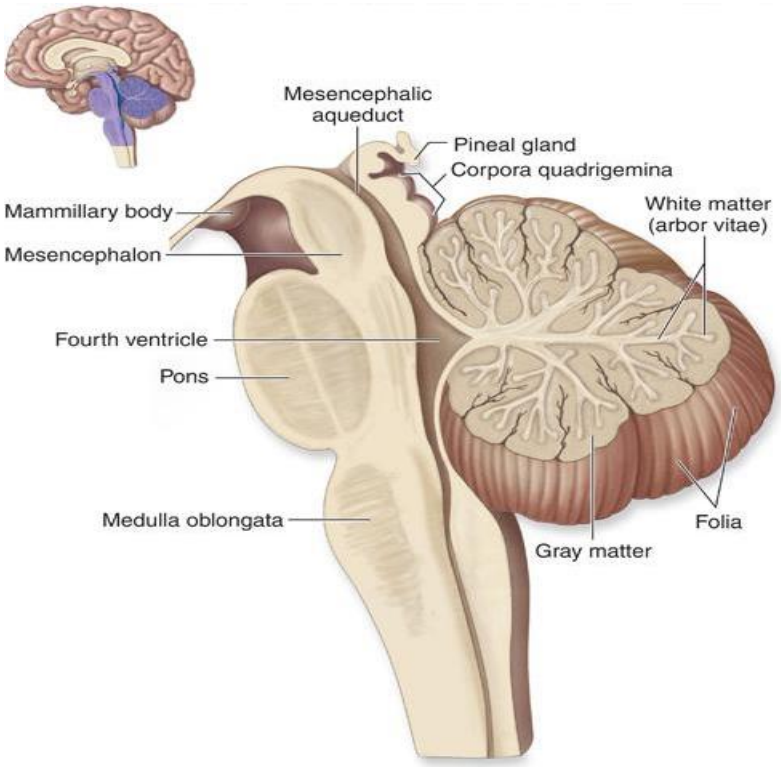

Figure 2.5: Sagittal cross-section of the brain stem and cerebellum. Reproduced from Reference 15.

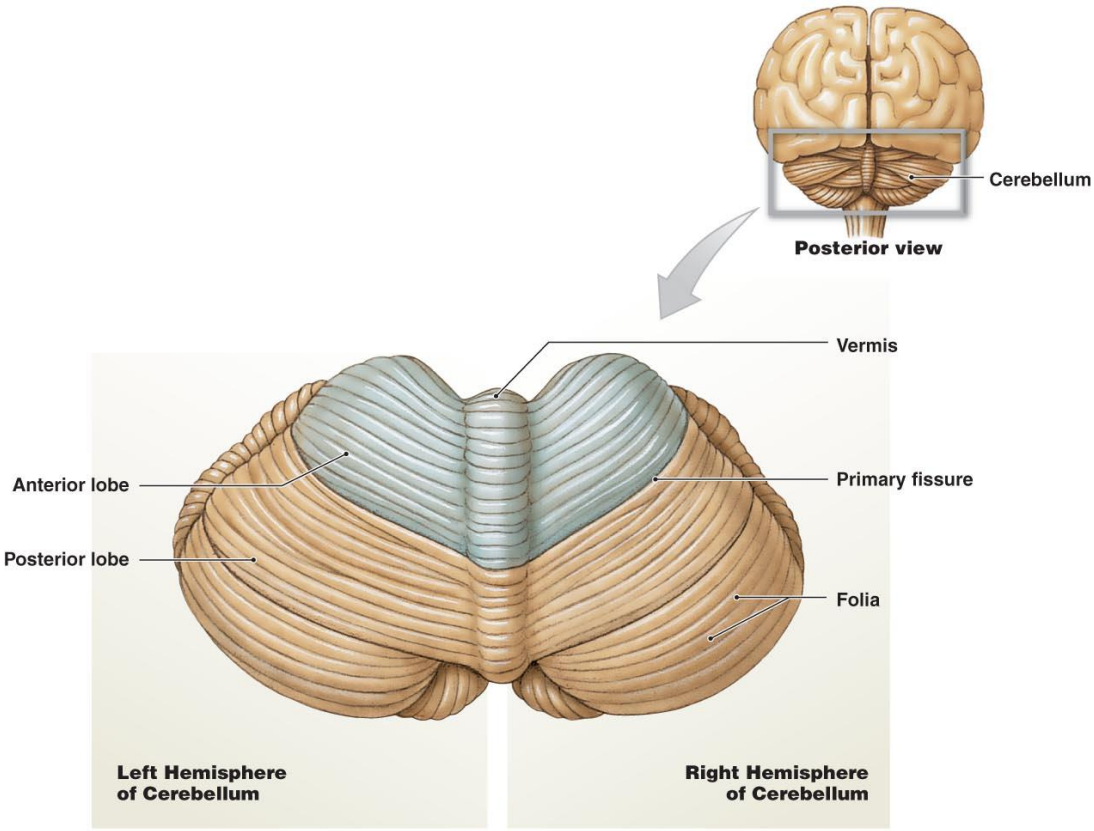

Figure 2.6: Posterior-superior view of the cerebellum. Reproduced from Reference 16.

2.1.4 The Ventricular System

The ventricular system of the brain consists of four inter-connected fluid filled spaces: the left and right lateral ventricles, the third ventricle and the fourth ventricle. While the lateral ventricles and third ventricle reside within the cerebrum, the fourth ventricle lies within the brain stem (see Figure 2.7).

Within the bounding tissues of each ventricle is a structure known as the choroid plexus which continuously produces a colourless fluid comprising water, proteins, sugars, ions and immune cells. This fluid is known as CSF and is produced at a rate of 0.2 - 0.7 ml per minute by the four ventricles of the ventricular system [17]. The choroid plexi then provide a pulsating motion that pulses the CSF through the ventricular system towards the fourth ventricle. At the fourth ventricle, the CSF exits into the cranial and spinal subarachnoid spaces (SASs) via the lateral and median apertures where it circulates towards the top of the brain and the base of the falx cerebri (see Section 2.2.6, p19), where small sections of the arachnoid mater (see Section 2.2.2, p14), known as arachnoid granulations, penetrate into the dura (see Section 2.2.1, p14) and the sinus harboured within. CSF is then passed into the dural sinus by the granulations, where it is absorbed into the major veins residing within [18].

The experiments conducted by Magendie, Luschka, Key and Retzius show that while the median aperture is freely communicating and capable of bi-directional flow, the lateral apertures appear to only support outward flow from the fourth ventricle into the SAS [19].

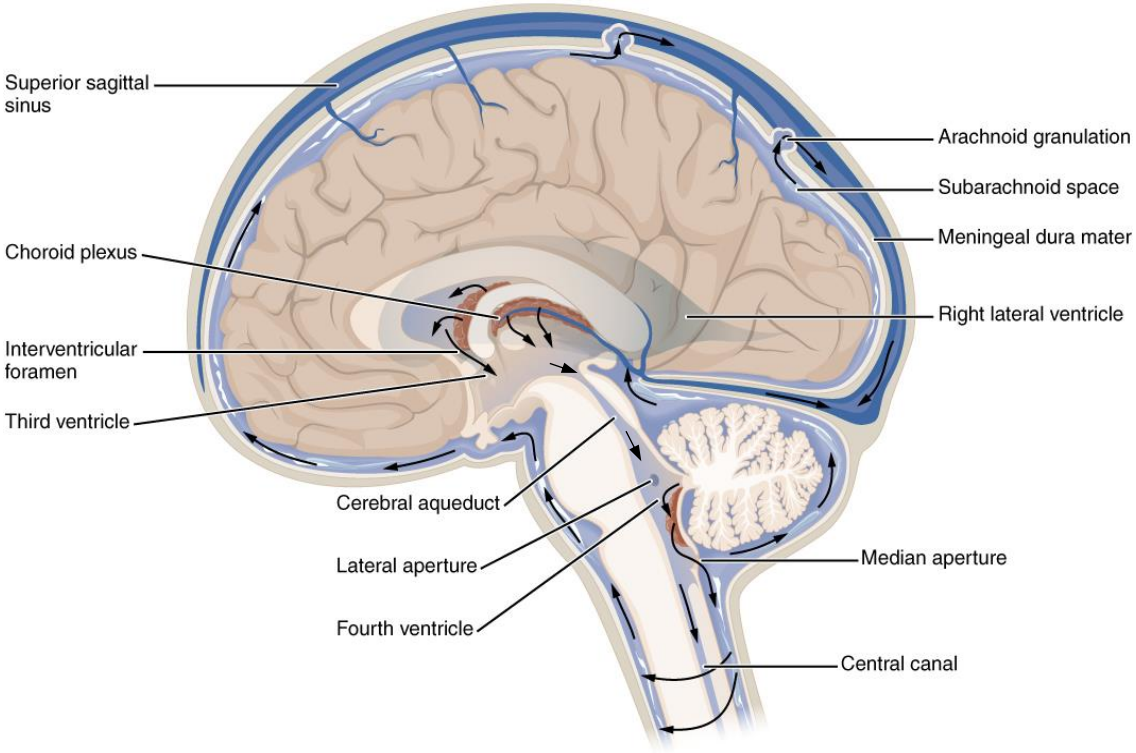

Figure 2.7: CSF flow and reabsorption routes. Reproduced from Reference 20.

Together, the four ventricles hold approximately 5 - 55 ml of fluid at any given time (see Figure 2.8), with an apparent increase in ventricular volume with age [21]. However, a large normal range exists and there is some ambiguity at which point the volume becomes pathological, as exhibited by the large spread of lateral ventricular volume displayed in Figure 2.9 and the overlap between “normal” patients and patients with atrophy (shrinkage of ventricles) or hydrocephalus (dilation of the ventricles) [22].

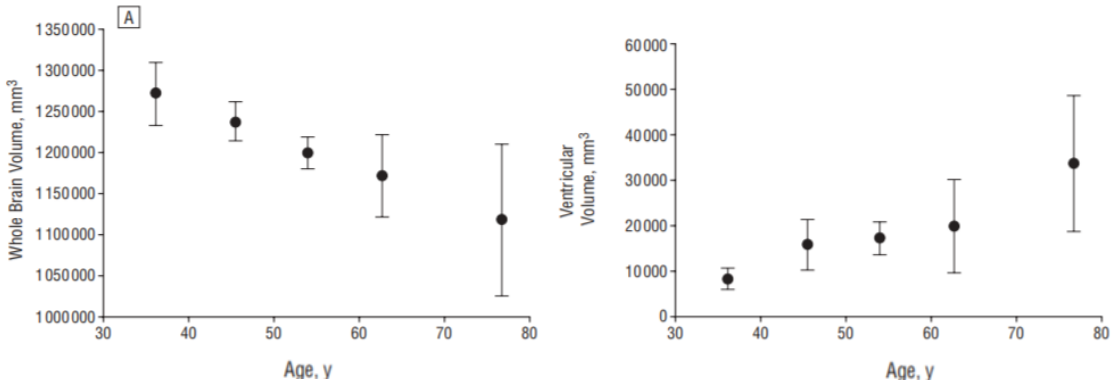

Figure 2.8: Total brain volume (left) and total ventricular volume (right) with age. Adapted from Scahill et al. [21].

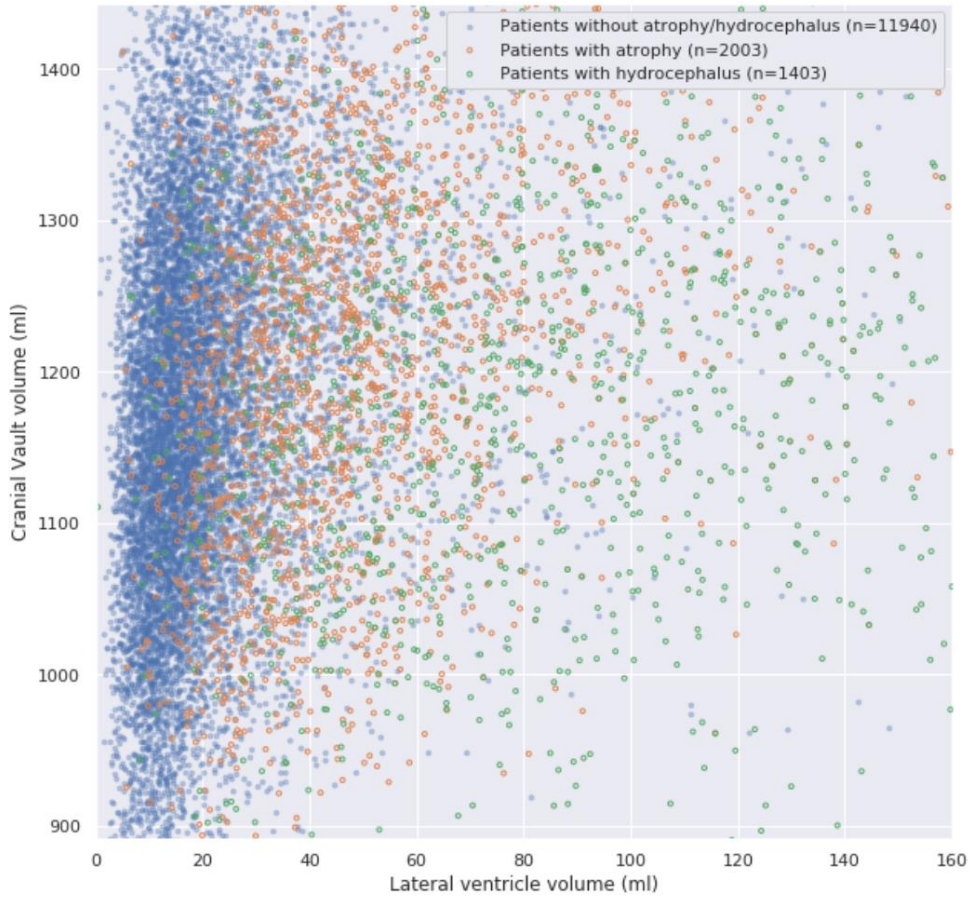

Figure 2.9: Lateral ventricle volume across normal patients and those with atrophy or hydrocephalus. Reproduced from Chilamkurthy et al. [22].

2.2 Anatomy of the Cranial Meninges

The cranial meninges are the three layers that envelop the brain. Collectively, the cranial meninges act to protect, anchor and nourish the brain within the cranial cavity [4].

The outermost layer of the cranial meninges, the dura mater, presents as a tough fibrous membrane, adherent to the inner surface of the skull, which tethers the deeper soft meningeal layers to the rigid skull and houses some of the larger blood vessels which branch off deep into the meninges and brain. In certain regions, the dura mater also provides highways (sinuses) for the major vessels that supply the brain and serves to anchor the brain via projections (septa) which extend into a number of fissures along the brain's surface [4].

Connecting the dura to the surface of the brain and comprising the remaining meningeal layers is the pia-arachnoid complex (PAC) (Figure 2.10). While the top layer of the PAC, the arachnoid mater, is contiguous with the dura and follows its contours, the bottom layer, the pia mater, lies at a short distance (approximately 0.5 – 2.5 mm) beneath the arachnoid and dura, closely adhered to the brain's convoluted surface, tethered to the arachnoid by a spider-like mesh of collagenous structures known as the arachnoid trabeculae [23].

Host to the trabeculae mesh and bounded by the arachnoid and pia is a fluid filled space known as the subarachnoid space (SAS). Filled with circulating CSF, the SAS plays an important role in both the physiological health and mechanical support of the brain [24].

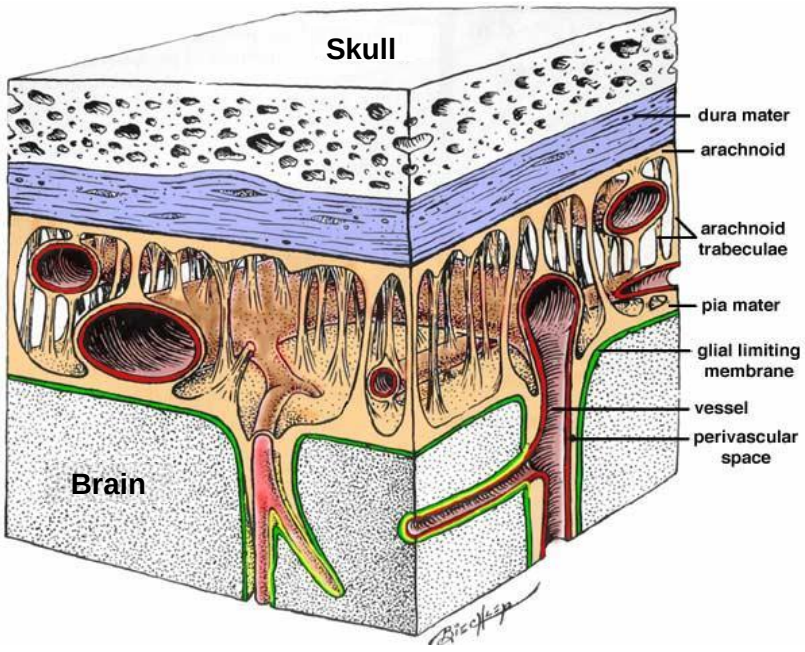

Figure 2.10: The cranial meninges. Adapted from Reference 25.

2.2.1 The Dura Mater

The dura mater comprises two layers: the periosteal layer and the meningeal layer (Figure 2.11, p15). The periosteal layer is adherent to the skull and follows its contours, with attachments being particularly strong along suture lines and at the base of the cranium [26]. The meningeal layer lies internal to the periosteal layer, remaining contiguous with it for the most part, except for in certain regions where the periosteal and meningeal dura separate to form cavities (sinuses) and septa [4].

Both layers of the dura are largely composed of fibroblasts embedded in an extensive extracellular collagen matrix. The periosteal dura, however, contains fewer fibroblasts and proportionally more collagen than the meningeal dura, in addition to blood vessels and nerves [26]. Together they form a layer approximately 0.4 - 1.4 mm thick [27,28].

At the base of the meningeal dura, where the dura connects with the arachnoid mater, lies a layer of cells different in composition to that of the rest of the dura. This layer is known as the dural border cell (DBC) layer and is composed of layered elongated fibroblasts, orientated parallel to the flat axis of the dura. Unlike the rest of the dura, extracellular collagen is lacking in the DBC layer and the irregular patterns of the processes of DBCs create extracellular spaces of inconsistent size. Furthermore, cells of the DBC layer also exhibit very few cell-cell junctions. For these reasons, the DBC layer presents as a structural weakness within the otherwise tough dura [26].

Although poorly understood, the DBC layer of the dura is conjectured to be the structural weakness that allows for formation of the subdural space under surgical or pathological conditions. Under abnormal loading of the meninges (e.g. upon CSF loss - see Section 3.4.4, p44), it is believed that a rupture occurs along the DBC layer creating a pathological space between the dura and the arachnoid layer [26].

2.2.2 The Arachnoid Mater

Unlike the dura, the arachnoid is thin (approximately 35 - 40 µm in spinal specimens [29]) and formed from just one functionally identifiable layer of cells, known as the arachnoid barrier cell (ABC) layer, and a basement membrane. The ABC layer, which forms a majority of the arachnoid mater, is composed almost entirely of tightly packed fibroblasts [30].

Although lacking an extensive extracellular collagen matrix like the dura, the presence of numerous tight junctions between ABCs make the arachnoid both tough and impermeable, allowing for the containment of CSF within the SAS.

In addition to the numerous junctions between ABCs, cell-cell junctions are also present between the ABCs and the DBCs, making the arachnoid and dura a material continuum [26].

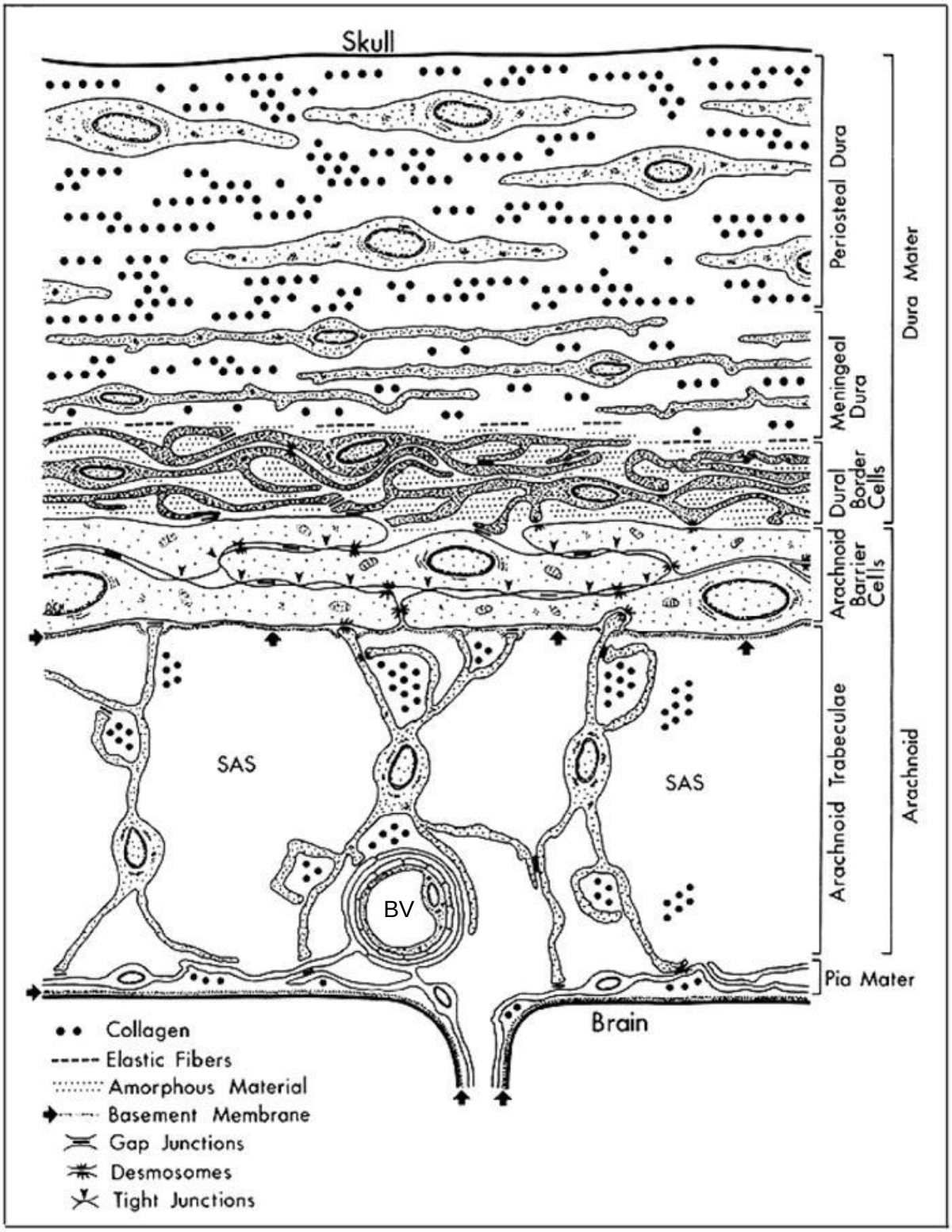

Figure 2.11: Artistic representation of the histology of the meningeal tissues. BV = blood vessel; see original key for others. Reproduced from Weller [30].

Internal to the ABCs lies a network of fibroblasts which traverse and occupy the SAS. These are known as the arachnoid trabeculae. The arachnoid trabeculae feature long and flattened irregular processes that attach to each other through cell-cell junctions which are reinforced by free collagen found adjacent or entwined within the processes of the trabeculae. By attaching via cell-cell junctions to the ABCs of the arachnoid at one end and the fibroblasts of the pia at the other, the arachnoid trabeculae act to tether the two membranes together.

Integrated with where the trabeculae attach to the ABCs lies the aforementioned basement membrane which also aids the containment of CSF within the SAS [26].

Although often depicted as simple string-like tethers within the simplified literature artwork (e.g. Figure 2.10, p13), studies of human and animal SAS have shown the trabeculae network to be much more complex [31,32,33]. Rather than neatly organised gap-bridging tethers, these studies show that, in a majority of cases, the arachnoid trabeculae associate with each other to form web-like meshes and coalesced sheets that span the space in a variety of configurations (Figure 2.12a-d, p17). These findings are consistent with the destructive theory behind the embryonic formation of the arachnoid trabeculae, wherein the arachnoid trabeculae are formed via the random removal of tissue from a solid SAS occupying ground substance, rather than through the organised generation of new structures in an empty space [35].

Further to the geometry of the arachnoid trabeculae, a study of pig's brains by Scott and Coats (2011) found the density of the trabecular mesh to vary greatly depending on location [33]. Through imaging the different regions of pig brain SASs with optical coherence tomography, Scott and Sadegh showed that while the volume fraction of the SAS (equivalent to the density of the trabecular mesh) averaged over the whole brain differed by just 5% between individual brains (average of 32%), averaged volume fractions in sub-regions within single brains differed by between 20 and 38%.

A significant part of the trabecular mesh is formed from the aforementioned bridging vessels. These vessels originate from the dura and traverse the SAS to penetrate into the brain. As shown in Figure 2.11, the bridging vessels are integrated with the trabecular mesh. This integration is achieved by the fibroblasts of the arachnoid and pia.

Figure 2.12e (p17) shows a freshly excised brain with the PAC present and Figure 2.12f shows a fixed brain with its PAC removed. Here it can be seen that, rather than being empty voids, the deep sulci spaces are in fact filled with the large bridging vessels. Given that the PAC vessels are integrated with the arachnoid trabeculae and that the trabeculae themselves attach to the gyral surfaces, neighbouring gyri can be considered as connected structures. This style of interconnection can also be seen in regions such as the sylvian fissures, which feature lobe to lobe and lobe to artery tethering (see Figure 2.12g-h).

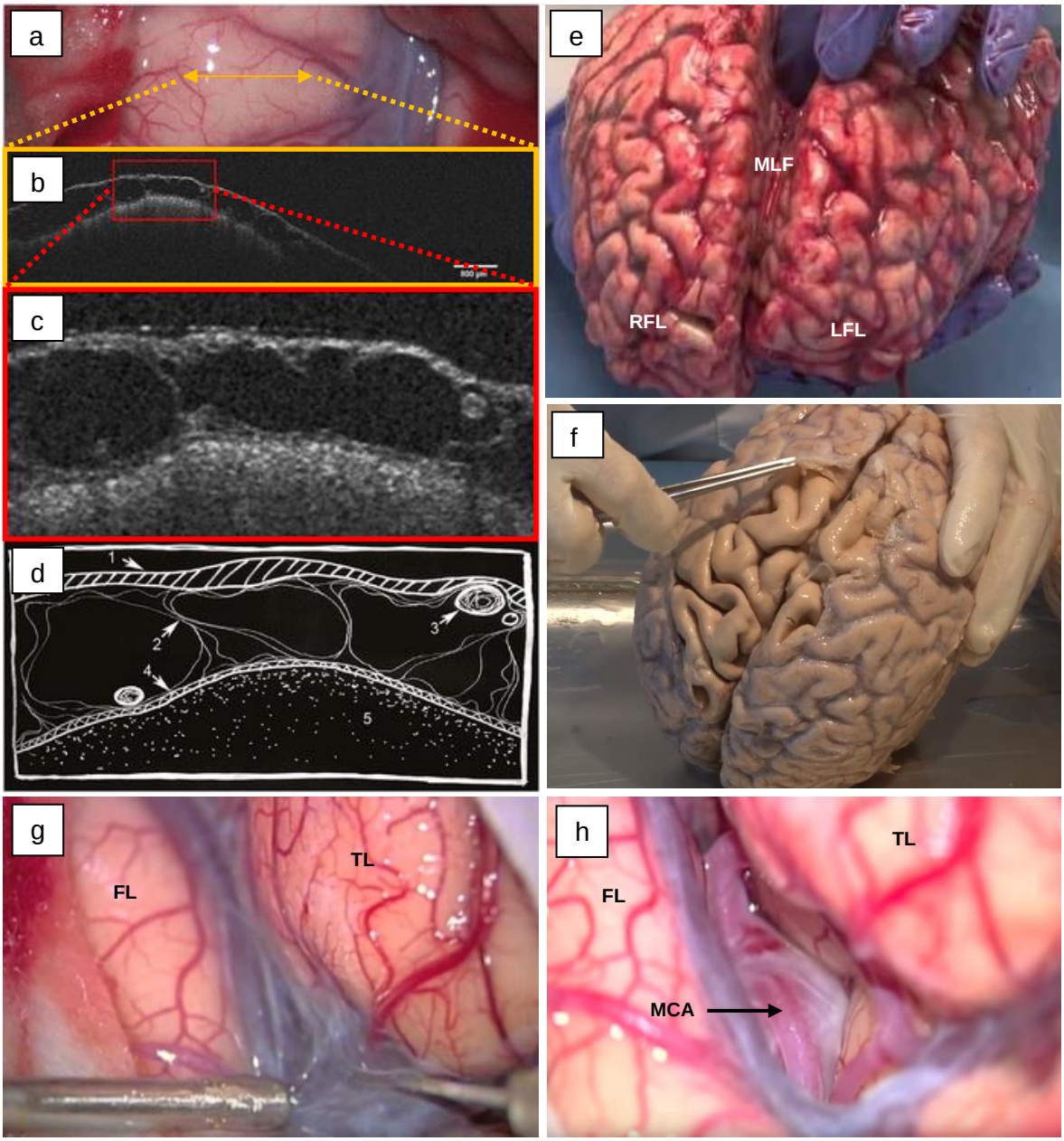

Figure 2.12: The human PAC. a) microscopic view of the brain's surface (dura removed) showing region of optical coherence tomography (OCT) scan shown in (b) (adapted from Hartmann et al. [34]); b) OCT image of the PAC at the region shown in (a), also showing region magnified in (c) (adapted from Hartmann et al. [34]); c) magnification of OCT image at region shown in (b) revealing distinct elements of the architecture of the PAC (adapted from Hartmann et al. [34]); d) artistic representation of (c) showing arachnoid barrier cell membrane (1), arachnoid trabeculae (2), blood vessel (3), pia (4) and brain parenchyma (5) (adapted from Hartmann et al. [34]); e) freshly excised human brain with labelled right frontal lobe (RFL), left frontal lobe (LFL) and medial longitudinal fissure (MLF), showing the occupation of the sulci by blood vessels and the arachnoid trabeculae mesh (adapted from Reference 36); f) fixed human brain with partially removed PAC (adapted from Reference 36); g) endoscopic view of the sylvian fissure (SF) showing extensive tethering between frontal lobe (FL) and temporal lobe (TL) (adapted from Reference 37); h) endoscopic view of sylvian fissure after surgical removal of the arachnoid trabeculae mesh, revealing the middle cerebral artery (MCA) (adapted from Reference 37).

2.2.3 The Pia Mater

Similar to the arachnoid mater, the pia mater is formed from just one functionally identifiable layer of cells and a basement membrane which is shared with the brain parenchyma. Dissimilar to the arachnoid, however, the fibroblasts of the pia characteristically have few organelles and feature few cell-cell junctions. Depending on location, pial fibroblasts may form a single layer, a number of layers or may even appear to be discontinuous with each other [26]. The pia mater measures to be approximately 8-15 μm thick [38].

Sandwiched between the pial fibroblasts and the surface tissues of the brain is a basement membrane which pial fibroblasts may attach directly. In other instances, a sub-pial space containing macrophages and collagen may intervene [26]. Pial fibroblasts attach directly to the arachnoid trabeculae through cell-cell junctions and thus, together form a material continuum with the other meningeal tissues [26,27].

2.2.4 The Subarachnoid Space

The SAS presents as fluid filled, meshed space between the arachnoid and pia. Although small in size, the SAS plays a crucial role in the functioning of the brain-skull system [4]. As described in Section 2.1.4, the SAS communicates with the ventricular system and is filled with circulating CSF. A by-product of this occupant fluid is a buoyancy force that significantly reduces the weight of the brain from an isolated weight of approximately 1.4 kg to a submerged weight of approximately 40 to 100 g (see Section 2.4.1, p23). Unopposed, this resultant weight would result in the full sinking of the brain towards the bottom of the cranial cavity, but due to the opposition by both the dural septa (see Section 2.2.6, p19) and the trabeculae mesh tethering the pia to the arachnoid and thus the brain to the skull, the brain remains more or less centred in the cranial cavity [4], albeit with a small degree of gravitational sagging (see Section 3.4.3, p43).

Due to gravitational sagging, the regional thickness of the SAS depends on the position the head is resting in. In the supine position, Frydrychowski et al. [23] measured the left and right frontal SASs (top of orientation) to have widths of 2.37 ± 1.10 and 2.40 ± 1.17 mm, respectively, and the left and right occipital SASs (bottom of orientation) to have widths of 0.44 ± 0.26 and 0.50 ± 0.35 mm, respectively. In the prone position, the authors found that the frontal lobe SAS width decreased on average by 0.62 ± 0.34 mm (~26%), a change consistent with the approximate 30% change observed by Rice et al. [39].

In addition to the trabeculae and CSF, the SAS also plays host to a network of vessels, known as bridging vessels, which use the space to navigate the brain and reach their penetration point along its surface. These vessels, which originate from the vascular network within the dura, pass through the SAS suspended within the trabeculae mesh, connected to the trabeculae by cell-cell junctions [32].

An extension of the SAS are the Virchow-Robin spaces. These spaces are found wherever branches of pial vessels penetrate into the brain parenchyma. Penetrating vessels merge with the brain parenchyma, shedding their external tunics and replacing them with a membrane formed from the processes of parenchymal astrocytes [40].

2.2.5 The Subarachnoid Cisterns

Due to the pia following the contours of the brain and the arachnoid following the contours of the skull, large spaces exist between the two layers wherever the brain geometry differs significantly to that of the skull. These enlarged spaces are known as the subarachnoid cisterns (see Figure 2.13, p20). The SAS is host to many cisterns, the largest of which being located towards the bottom of the brain, at the level of the brain stem [4].

2.2.6 The Dural Septa

In certain regions of the dura, the meningeal dura separates from the periosteal dura to form what are known as dural septa (see Figure 2.14, p20). In these regions, the meningeal dura peels away from the periosteal dura at two points either side of a central line, meeting at a distance beneath the periosteal dura to form a single layer of meningeal dura (septa) that projects inwards towards the centre of the cranial cavity. Together, the dural septa act to partition the cranial cavity, providing mechanical barriers between the different regions of the brain which prevent both linear and rotational intracranial movement [4].

Five septa belong to the dura: the falx cerebri, the left and right tentorium cerebelli, the falx cerebelli and the diaphragm sellae (Figure 2.15, p21) [4].

Separating the left and right cerebral and cerebellar hemispheres, respectively, the falx cerebri and falx cerebelli prevent rotation in the coronal plane and translation in the sagittal plane. Separating the left and right cerebral hemispheres from the left and right cerebellar hemispheres, respectively, the left and right tentorium cerebelli prevent rotation in the sagittal plane and translation in the coronal plane. The diaphragm sellae presents as a much lesser septum that exists primarily to secure the pituitary bulb [41].

2.2.7 The Dural Sinuses

At the base of each septum, where the two separating layers of meningeal dura have not yet converged beneath the periosteal dura, a cavity (sinus) is found. These longitudinal cavities present as highways within the tough dura for the major vessels, allowing greater volumes of blood to pass from the brain back to the heart, increasing overall brain perfusion capacity. Sinuses can also be found at other sites within the dura such as the internal ridge of the falx cerebri (inferior sagittal sinus) or the junction between the tentorium cerebelli and falx cerebri (straight sinus). Figure 2.16 (p21) illustrates the various dural sinuses that exist within the dura [4].

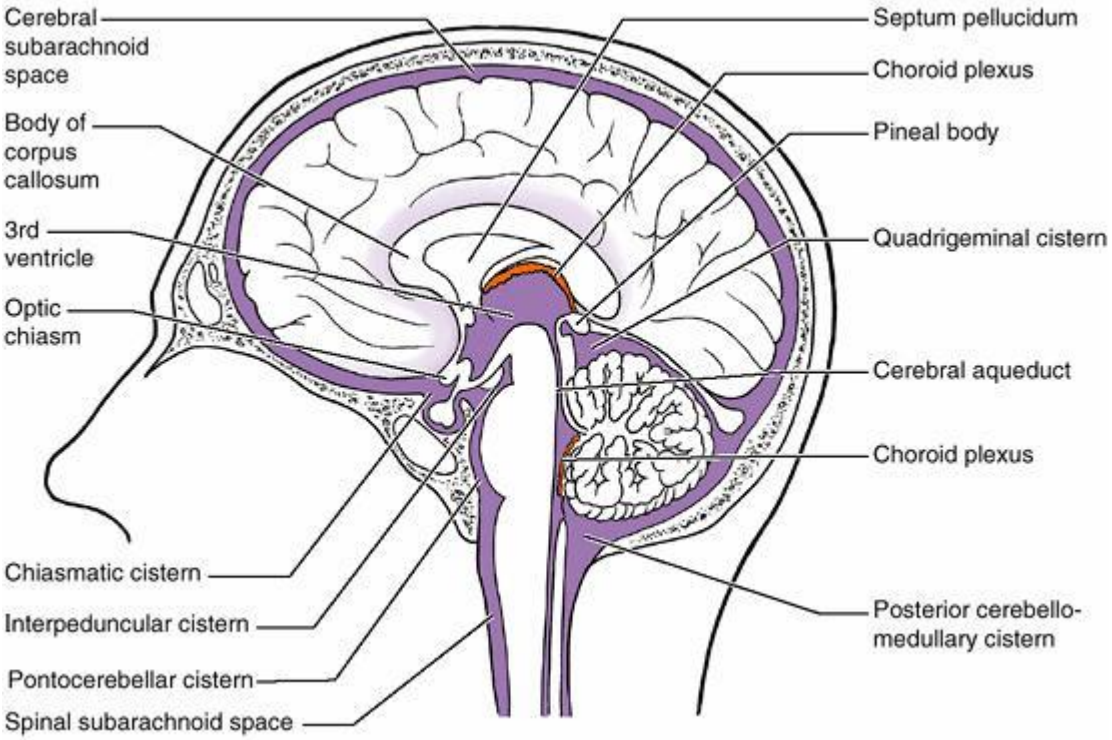

Figure 2.13: The subarachnoid cisterns. Adapted from Reference 43.

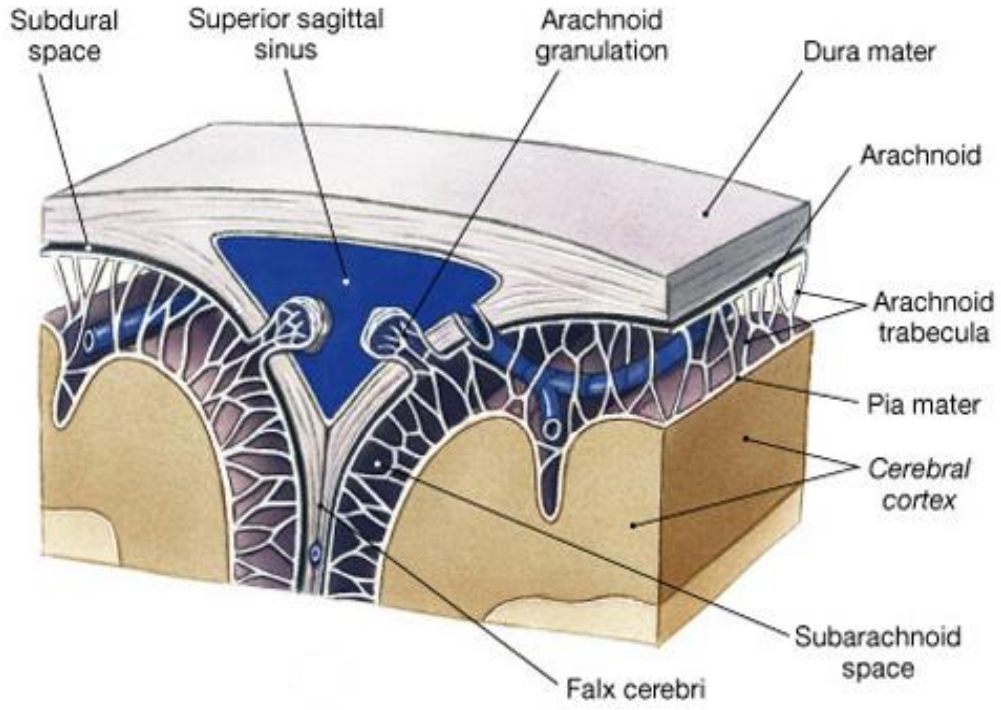

Figure 2.14: Architecture of the meninges at the location of the dural septa. Reproduced from Reference 44.

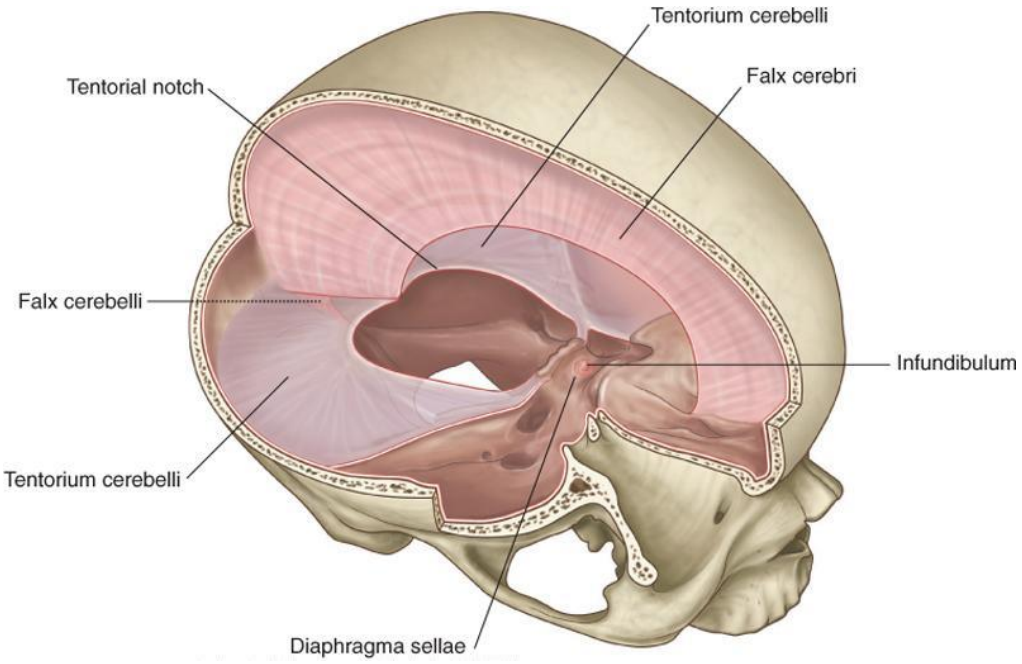

Figure 2.15: The dural septa. Reproduced from Reference 45.

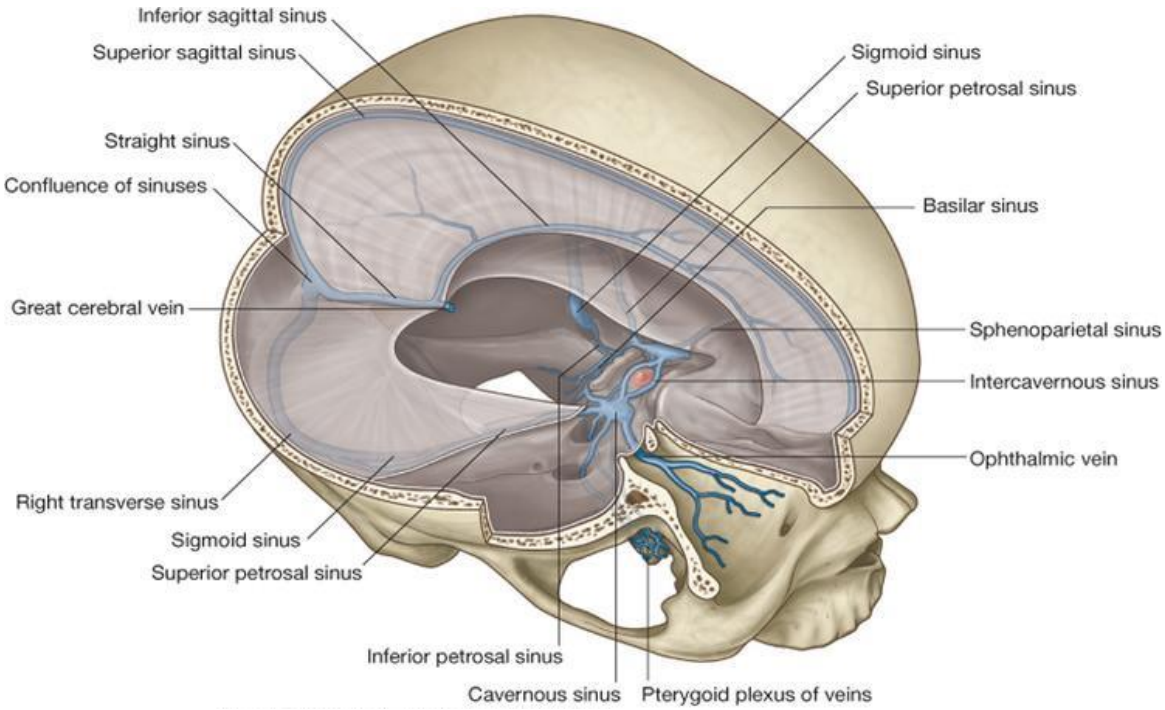

Figure 2.16: The dural sinuses. Adapted from Reference 46.

2.3 Anatomy of the Neurocranium

The human skull is formed from two parts: the facial skeleton, which forms the scaffolding of the face, and the neurocranium, which forms the hard, protective casing around the soft fragile brain. Comprising eight fused flat bones, the neurocranium acts to isolate the brain from potential harm and provide a shaping container for its deformable soft contents [4].

While the top half of the neurocranium presents as a smooth hemisphere, the bottom half of the neurocranium, the neurocranial base, presents as a complex structure with many ridges and foramen (holes) of varying size (Figure 2.17). The largest of the foramen, the foramen magnum, articulates with the atlas bone (C1) of the cervical spine, providing a gap in the neurocranium for the brain stem to exit into the spinal column, where it becomes the spinal cord [41].

Continuous with the meninges of the skull, the cranial meninges follow the brain stem into the spinal column where they become the spinal meninges. Similar to the architecture of the cranial meninges, the spinal meninges also act to tether the spinal cord to the bones of the spinal column and center the spinal cord within the spinal column. Consequently, the spinal column acts to constrain the inferior end of the brain stem [4].

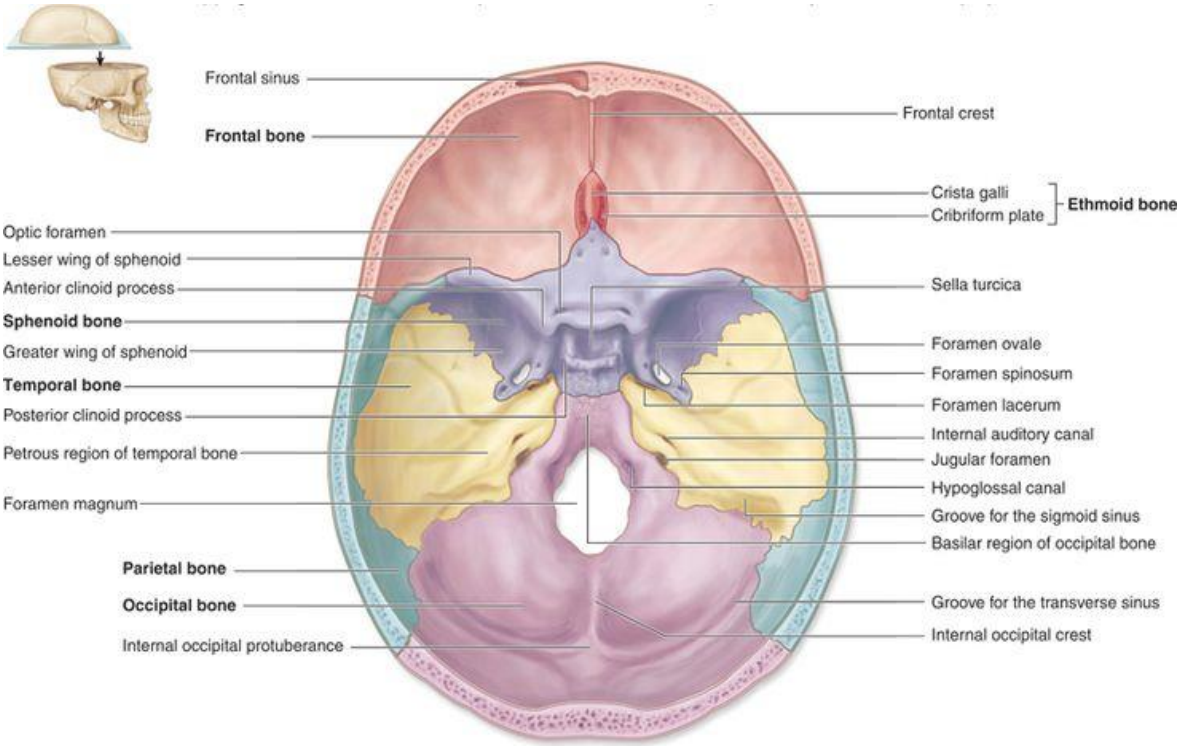

Figure 2.17: Anatomy of the neurocranial base. Reproduced from Reference 47.

2.4 Tissue Properties of the Brain-Skull System

The previous sections showed the brain-skull system to be formed from a variety of tissues and structures. With different composition and architecture, these naturally exhibit different mechanical properties. The following sections lay out our current knowledge of the mechanical properties of the brain-skull tissues.

2.4.1 Tissues of the Brain

Brain tissue is an incredibly complex, jelly-soft, composite material which varies regionally in composition and has a water fraction ranging between 0.75 and 0.95 [48]. Additionally, it exists under variable intracranial pressure, ranging between 7 and 15 mmHg when the body is laid horizontal and down to -15 mmHg when the body is standing [49]. Together, these features make brain tissue a difficult tissue to study.

Nonetheless, from five decades of study, the general properties of brain tissue have been reasonably well established. These are laid out in the literature reviews by Chatelin et al. [50], Bilston [51] and Budday et al. [52], which provide a review of all the mechanical tests that have been performed on human, monkey, pig (porcine), cow (bovine), rabbit and rat brain tissue over the years.

Brain tissue is primarily a non-linearly viscoelastic / poroelastic material which exhibits great strain-rate sensitivity and stiffens with increasing strain rate (see Figure 2.18) [52]. This bimodal elasticity is due to the high fluid content of the tissue and its complex permeability characteristics, which arise from the various micro and macro scale mechanisms the body has evolved to transport fluid throughout tissue. Fluid flow within the extracellular matrix, the capillaries and the larger vessels takes place across different time scales [52] and, therefore, when loaded at different rates a different mode of elasticity is adopted. At quasi-static loading rates, the tissue can be considered mostly poroelastic, whereas at higher rates it can be considered more viscoelastic [52].

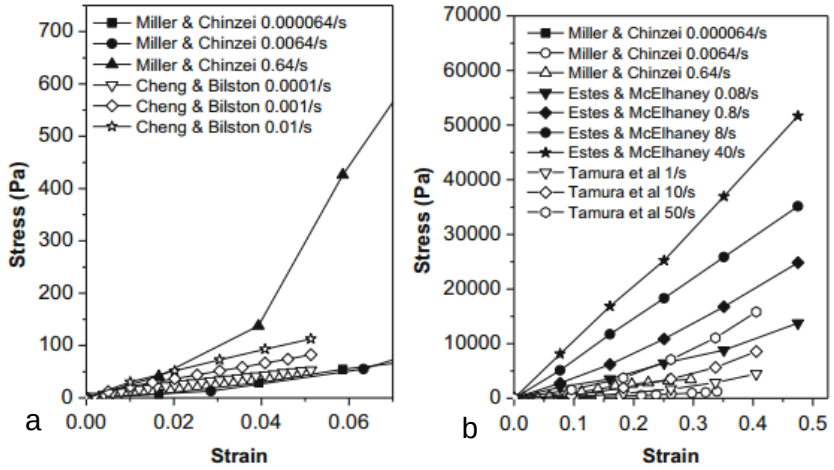

Figure 2.18: Compression loading response of brain tissue at slow to moderate (a) and slow to high (b) strain rates, measured across a number of studies. Reproduced from Bilston [51].

The relaxation behaviour of brain tissue under static load is very rapid and consistent with the tissues multi-scale porosity. As can be seen in Figure 2.19, a rapid decrease in resistance takes place when a compressive load is reached and then held. This decrease takes place exponentially, with a great majority of the relaxation taking place over the first few seconds, before levelling out over a time course of minutes. This profile of relaxation can be explained by initial fluid flow through the macro scale routes, followed by a combination of slower fluid flow through the micro scale routes and viscoelastic creep of the elastomer content of the tissue.

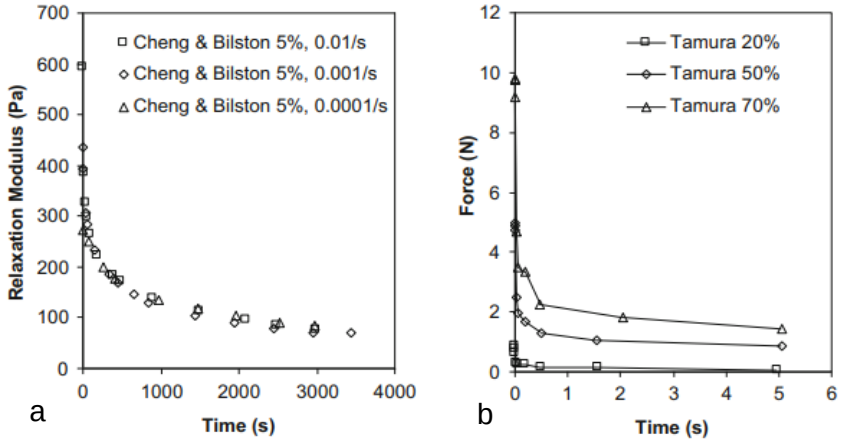

Figure 2.19: Relaxation of brain tissue when held at a compressive load. a) data produced by Cheng & Bilston at 5% strain at three loading rates; b) data produced by Tamura at 20, 50 and 70% strain. Reproduced from Bilston [51].

In terms of the general level of stiffness, elastic moduli of between 0.3 and 3.0 kPa [53,54,55,56] have been reported for brain tissue across a variety of indentation tests. These moduli are typically calculated using the stress/strain gradient at the pseudo-linear portion of the loading curve. As a point of reference, this level of stiffness is in the same ballpark as edible jelly, which is often considered a suitable surrogate for brain tissue under certain loading conditions [57,58].

Most of the available stiffness information, however, is reported as shear moduli garnered from rheometric, indentation and magnetic resonance elastography (MRE) tests, the latter being a technique in which vibration is applied simultaneously during an MRI scan and used to create a stiffness map from the imaged tissue response. Across these measurements, a wide range of values (see Figure 2.20, p25) have been reported, spanning multiple orders of magnitude. This large range, however, is well-known to be due to a combination of real variability in brain tissue and the lack of standardisation in its testing.

Species, age, sex, region measured, post-mortem time, method of tissue storage and method of testing, have all been demonstrated or hypothesized to influence the mechanical properties measured [50,51,52], and it is rare to see two studies with matching methods.

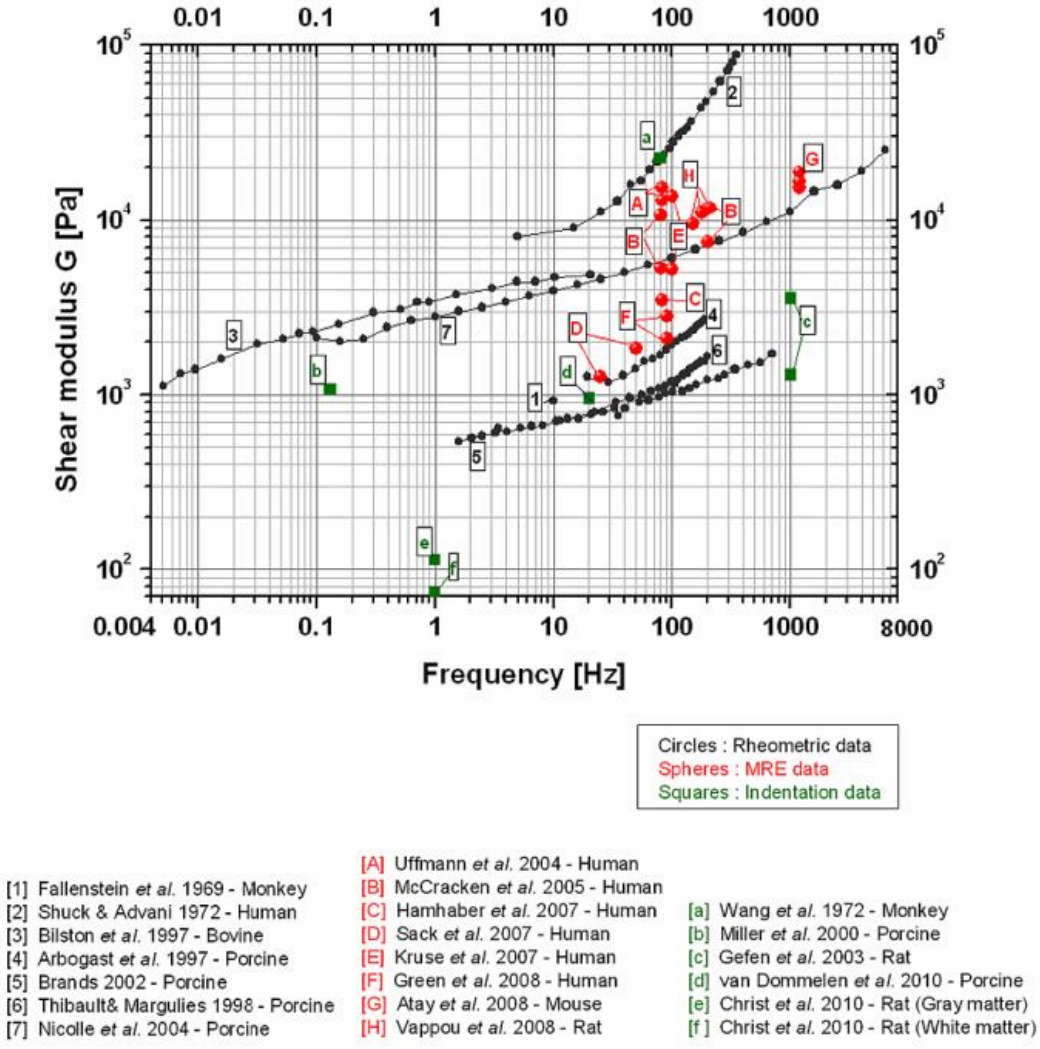

Figure 2.20: Shear moduli of brain tissue garnered from seven rheometric, eight MRE and six indentation measurements. Adapted from Chatelin et al. [50].

Because MRE can be done harmlessly on live humans it presents as a means of circumventing a number of the problems associated with testing *in vivo*, by opening the skull and indenting the surface of the brain, or *in vitro*, by harvesting and testing brain tissue from deceased brains. The technology is still in its infancy and has its own set of problems, however, the values garnered from it lie well in the middle of the range garnered from the rheometric and indentation tests, as seen in Figure 2.20. Yet, the values measured with MRE can still be seen to span orders of magnitude and so even with a technique that theoretically bypasses some of the methodological problems, the uncertainty is still not reduced to any significant degree.

In terms of the variation in stiffness throughout the brain, there is some evidence that white matter is stiffer than grey matter at high strain rates (higher than approximately 1 mm/s), but at lower strain rates, the difference is small, with some grey regions even being measured to be slightly stiffer than white matter (see Figure 2.21, p26 and Figure 2.22, p27) [52,59]. There also does not seem to be any notable anisotropy at the lower strains in either grey or white matter [52][59].

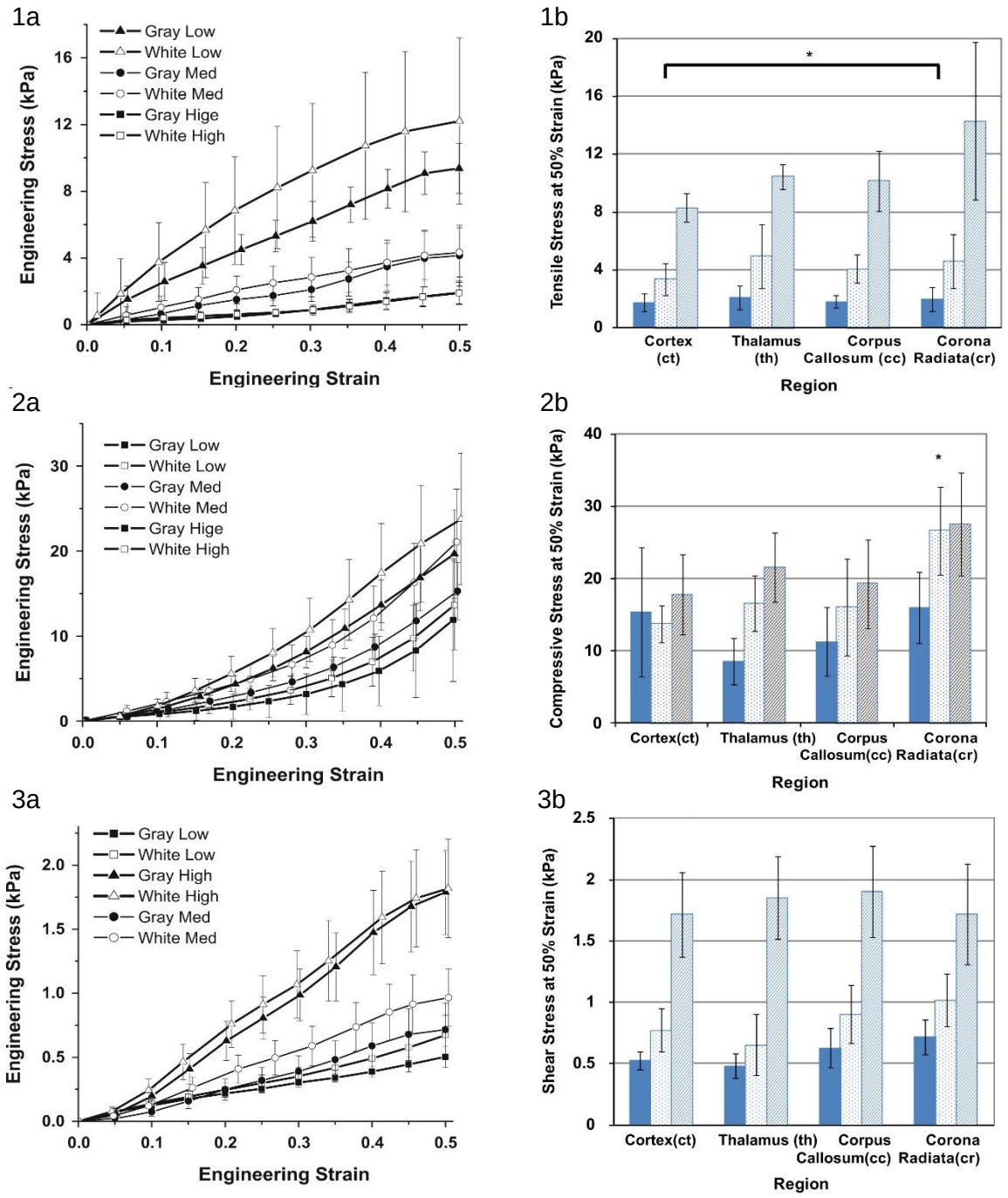

Figure 2.21: Regional differences in brain tissue stiffness measured by Jin et al. Left-hand graphs show the loading response of white and grey matter under tension (1a), compresion (2a) and shear (3a) at low (2.5 mm/s), medium (25 mm/s) and high (250 mm/s) strain rates. Right-hand graphs show the tensile (1b), compression (2b) and shear (3b) stress at 50% strain within two separate grey matter regions, the cortex and the thalamus, and two separate white matter regions, the corpus callosum and corona radiata. Graphs adapted from Jin et al. [59].

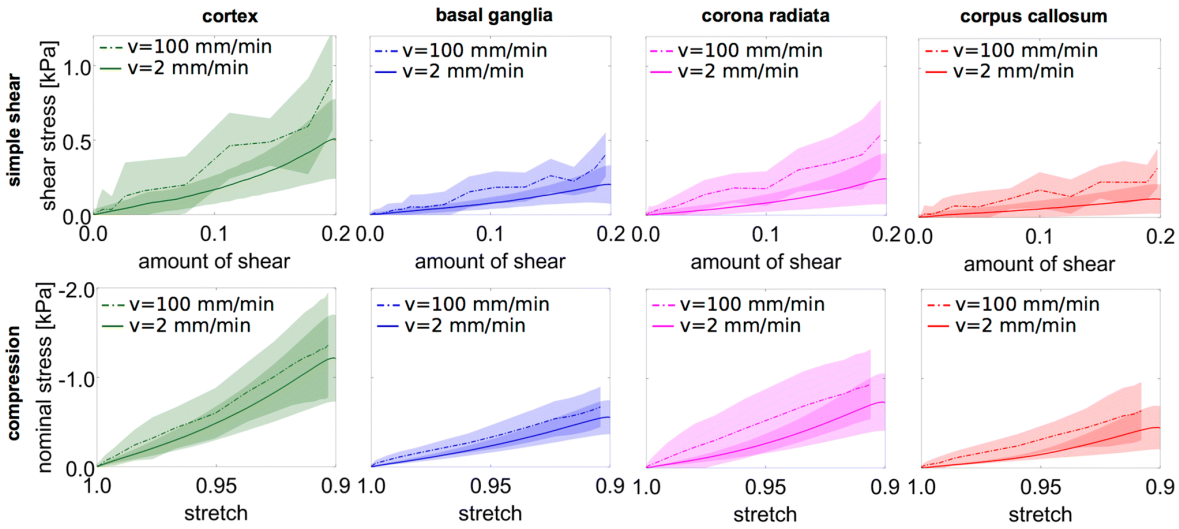

Figure 2.22: Regional differences in brain tissue stiffness measured by Budday et al. Graphs show the response of tissue from the cortex (grey matter), basal ganglia (grey matter), corona radiata (white matter) and corpus callosum (white matter) under simple shear (top row) and compression (bottom row), at loading rates of 2 and 100 mm/min. Reproduced from Budday et al. [52].

With the advent of MRE, greater measurements of stiffness between brain sectors has begun to emerge (e.g. frontal vs temporal lobe). The strain rate in MRE is high due to the vibrational nature of the loading and there are questions regarding its validity/reliability, however, MRE measurements show little variance in stiffness throughout the brain, with the exception of a softer cerebellum (Table 2.1) [60,61,62]. Given that a softer cerebellum has also been noted in *ex vivo* tests [63], one would perhaps expect the homogeneity observation to have a degree of validity.

Table 2.1: MRE measurements of individual sector brain stiffness from three studies. Measurements from [60] and [61] are for males and females, while measurements from [62] are reported separately.

Sector	**Mean Shear Storage Modulus (kPa)**			
	[60] M+F	**[61] M+F**	**[62] M**	**[62] F**
Cerebrum	2.44 ± 0.08	-	2.35 ± 019	2.33 ± 0.19
Frontal Lobes	2.53 ± 0.11	2.65 ± 0.15	2.25 ± 0.20	2.19 ± 0.21
Occipital Lobes	2.52 ± 0.12	2.65 ± 0.13	2.45 ± 0.19	2.43 ± 0.20
Parietal Lobes	2.35 ± 0.10	2.42 ± 0.10	2.11 ± 0.22	2.15 ± 0.19
Temporal Lobes	2.60 ± 0.11	2.69 ± 0.11	2.63 ± 0.17	2.59 ± 0.17
Deep GM/WM	2.73 ± 0.22	2.79 ± 0.25	2.27 ± 0.31	2.25 ± 0.26
Sensorimotor cortex	2.61 ± 0.19	2.82 ± 0.29	-	-
Cerebellum	2.09 ± 0.11	2.15 ± 0.11	1.78 ± 0.12	1.80 ± 0.14

Unlike the elastic properties of brain tissue, the mass/volume density has received little and sporadic attention. Only a handful of measurements have been made and the majority took place in the 19th and 20th century. Nonetheless, of the available data, a similarly wide range of values have been reported (Figure 2.23). Aside from the mean (± standard error) measurements of 1.081 ± 0.003 g/cm^3 for human brain and 1.100 ± 0.008 g/cm^3 for monkey brain by Barber et al. [64], most studies appear to measure brain tissue to have a density of around 1.030 to 1.050 g/cm^3 [65,66,67,68]. This is further supported by Degos et al. [69] which used CT scans to estimate the *in vivo* specific gravity of brain tissue in a study of traumatic brain injury. However, the study by Barber et al. represents the most comprehensive study of human brain tissue to date, measuring the density of 15 brain regions, using 412 samples from 55 brains aged between 17 and 84 years age at the point of death (average of 43 years).

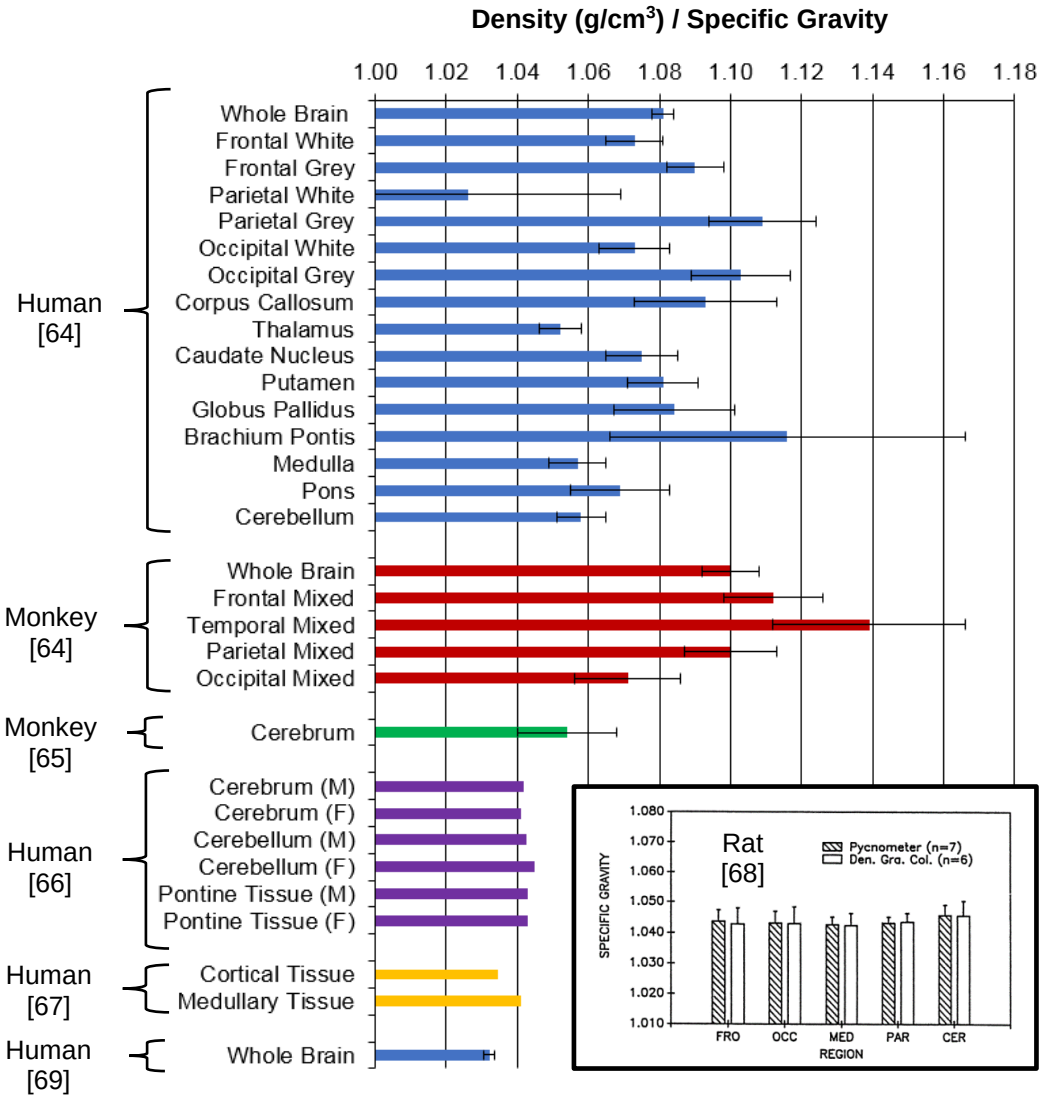

Figure 2.23: Density and specific gravity measurements of brain tissue from seven studies.

Barber et al. measured no significant differences between white and grey matter, hypothesising that the higher proportion of water content in grey matter (white: 60-75%; grey: 80-85%) is compensated by the conversely higher proportion of phospholipids in white. The authors also found no statistical significance between left and right sources of the same region (e.g. left and right occipital grey matter).

Since it is an integral part of the body of the brain, it is also important to remember the vasculature when considering its buoyancy. The vasculature predominately cradles the brains surface and, with the vessel walls having stiffness of approximately 200 to 600 kPa [70] and the lumen being pressurised, provides an added stiffness to the brain's body. However, in addition to the added stiffness, it may be that the vessels also increase the overall density of the brain. Barber et al. [64] measured the mean (±SE) cerebral artery wall density across 29 samples to be 1.378 (±0.095) g/cm^3 and, considering the approximate 1.060 g/cm^3 density of blood [71], the cerebrovasculature must have a density somewhere between 1.060 and 1.380 g/cm^3, which is somewhat higher than brain tissue. Using lumen and wall thickness measurements [72] for the arteries belonging to the Circle of Willis, for example, it is possible to roughly estimate (via area fraction) an effective density of between 1.250 and 1.300 g/cm^3 for these vessels. Measurements of the vasculature (vessel and blood) volume fraction of the brain are difficult to find, however, there are measurements of the volume fraction of blood (i.e. just the lumen) from nuclear imaging studies of radiolabelled red blood cells. This percentage is only measured to be about 4% [73] and the vessel walls would only likely add a few percent on top, so it is possible the vasculature is not overly influential in the brain's buoyancy.

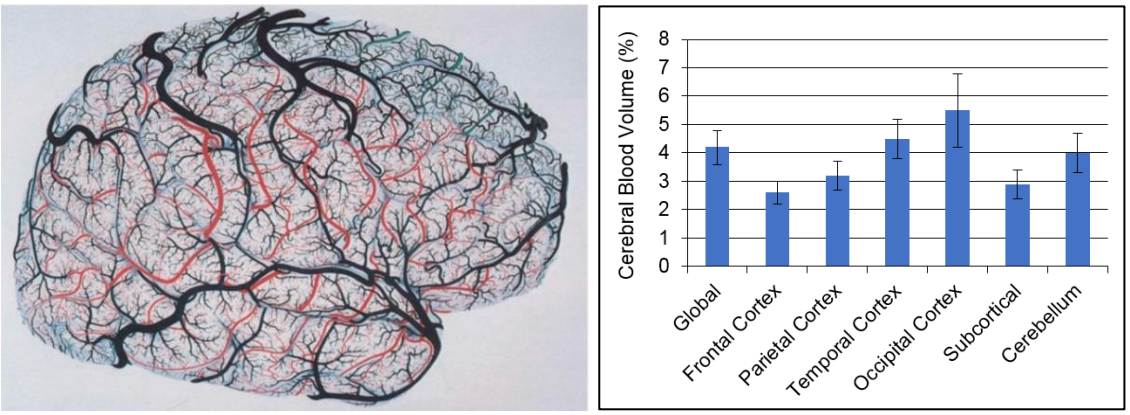

Figure 2.24: The vasculature of the cerebrum (left) (reproduced from Duvernoy et al. [74]) and percentage of brain volumes occupied by blood (right) (plotted data from Reinstrup et al. [73]).

The importance of the brain's density is of course its value relative to that of the fluid it is bathed in, the CSF. Measurements of CSF density appear to be much less variable with mean densities of 1.0007 ± 0.0002 , 1.0006 ± 0.0002 and 1.0005 ± 0.0002 g/cm^3 [75,76,77] being reported. With a CSF density of approximately 1.00 g/cm^3, the density differential between the brain and CSF is therefore approximately +0.03 to 0.08 g/cm^3. This gives a 1.4 L brain an effective weight of approximately 40 to 100 grams when submerged in CSF.

To summarize, the general properties of brain tissue can be considered well characterised, but the precise quantitative metrics one would ideally use to recreate the brain mechanically are not available. A general level of stiffness can be seen, but with published stiffness values spanning orders of magnitude. This is similarly the case for the question of the brain's density.

In recreating the brain, therefore, a viscoelastic/poroelastic simulant with similar strain rate sensitivity, similar relaxation characteristics and stiffness in the range of approximately 0.3 - 3.0 kPa should be sought. There is insufficient evidence to warrant the inclusion of anisotropy or regional differences and so a homogenous material should suffice. Paired with the CSF simulant, the density of the brain simulant should be such that a submerged weight in the range of 40 to 100 grams is achieved to create the same loading of the brain.

2.4.2 Tissues of the Pia-Arachnoid Complex

The cranial meninges consist of the dura, arachnoid and pia, however, in the biomechanical literature, the latter two are often referred to as one functional unit, the pia-arachnoid complex (PAC). This is because a large part of the mechanical function of the pia and arachnoid is in their relationship to each other through the arachnoid trabeculae and the cushioning/buoyancy effect of the CSF.

Most of the mechanical characterisation of the PAC has been done by Jin et al. [78,79,80,81] with bovine specimens. This group harvested sections of PAC from bovine brains and tested the PAC in traction and shear, which involved gluing the pia and arachnoid to separate blocks and pulling and shearing the blocks away from each other, respectively, and in tension, which involved clamping the pia and arachnoid together at opposite ends and pulling the specimen apart.

Figure 2.25: Harvested PAC. Reproduced from [80].

The authors performed these tests at loading rates of between 0.02 mm/s and 1.7 mm/s and yielded elastic moduli ranges of 61-148 kPa in traction, 11-22 kPa in shear and 6-40 MPa in tension, showing the PAC to stiffen with strain rate and to have pronounced anisotropy. In terms of regional differences, the authors found no significant differences in properties between frontal, parietal and occipital PAC specimens.

The anisotropy measured in the PAC is consistent with its architecture. The pia and arachnoid are collagenous membranes and so should present most stiff when stretched in plane (tension). With collagen reinforced arachnoid trabeculae tethering the pia and arachnoid together, the PAC should present next stiffest in traction. Lastly, with the ability of the arachnoid trabeculae to buckle, the PAC should present the least stiff in shear.

In another study of ovine (sheep) PAC, Natividad et al. [82] found the PAC to have a mean elastic modulus of 7.68 ±3.0 MPa when loaded in tension at a strain rate of 2 mm/s, which is comparable to the 6 MPa measured by Jin et al. at the lower strain rates. Furthermore, Fabris et al. [83] used atomic force microscopy indentation to measure the micro-regional compressional properties of the rat PAC, finding non-vascularised regions to have a mean elastic modulus of 1.32 ± 0.03 kPa, while vascularised regions were found to be twice as stiff at 2.79 ± 0.08 kPa.

Little information can be found regarding the properties of the arachnoid or pia alone, however, one study measured the tensile properties of the pia. Aimedieu et al. [84] reported a stiffness of 0.024 N/mm and 0.19 N/mm for the initial and elastic part of the loading curve, putting the elastic moduli in the order of MPa, assuming their specimens were approximately 15 μm thick (thickness was not reported).

2.4.3 Tissues of the Dura

Tensile tests of dura mater specimens have yielded elastic moduli in the MPa range. Zwirner et al. [27] measured an elastic modulus of 70 ± 44 MPa from 117 temporal dura specimens (Figure 2.26) (loading rate of 0.33 mm/s) harvested from cadavers aged 2-94 years, finding no statistical differences between dura from the left and right sides of the cranium or between males and females, but a declining stiffness with age.

Figure 2.26: Dural samples harvested by Zwirner et al. Reproduced from Zwirner et al. [27].

Aydin et al. [85] measured a similar elastic modulus of 77.86 ± 41.47 MPa from seven frontal dura specimens (loading rate of 0.17 mm/s), and similar moduli of 69.50 ± 1.28 and 61.50 ± 9.60 MPa were also measured by [86] and [87], respectively. A lower moduli range of 21.3 to 48 MPa, however, was reported by [88] using a loading rate of 0.83 mm/s.

No differentiation appears to have been made between the dural tissue lining the skull and that which makes up the dural septa. As a continuation of the skull adhered dura, however, it is not unreasonable to assume that the dural septa have similar properties.

2.4.4 Tissues of the Neurocranium

While the neurocranium does have similarly complex architecture and properties to the other tissues considered in this chapter, with an elastic modulus in the GPa range [89], it presents as a rigid container that does not deform when loaded by the weight of its intracranial contents. Therefore, in the context of this project the skull can be considered entirely rigid.

2.5 Chapter Summary

This chapter has included an overview of the anatomy and tissue properties of the brain-skull system.

Rather than “floating” in the cranial cavity as commonly believed, here it has been shown that the brain in fact sinks due to a marginally higher density than the cerebrospinal fluid it is bathed in. This sinking, however, is mitigated against by the tethering action of the arachnoid trabeculae and the claw-like dural septa which grip the brain along its fissures. Yet, despite these supportive features, the brain does still sag to a small degree in the direction of gravity.

Because the brain is typically shown exsanguinated (blood drained) or with the meninges removed, another common misconception is that the sulci and fissure spaces of the brain are empty. Here it has been shown that this is not the case and that these spaces are in fact occupied by large vessels which are tied to the flanking gyri by the trabeculae mesh.

In terms of mechanical properties, a wide range of values have been reported for the various tissues of the brain-skull system. Stiffness measures for the brain, for example, were found to range in orders of magnitude. However, like for most soft tissues, this range can be explained by a combination of real biological variability and the wide range of methods used to test the physiologically delicate tissue.

Given the uncertainty in mechanical properties, a deal of tuning will likely be required in order to build a phantom which can accurately recreate the positional brain shift event. Therefore, in developing a phantom, the use of a tuneable brain simulant will almost certainly be required.

Now that the system has been defined, the next chapter will take a look at stereotactic neurosurgery and the impact of positional brain shift on surgical accuracy.

3 POSITIONAL BRAIN SHIFT IN STEREOTACTIC NEUROSURGERY

The previous chapter included a description of the anatomy and tissue properties of the brain-skull system. This chapter contains an overview of targeting error in stereotactic neurosurgery and a discussion of the research concerning positional brain shift.

3.1 MR and CT Imaging

Magnetic resonance (MR) imaging (MRI) and computed tomography (CT) imaging are two of the most popular means of obtaining cross-sectional images of the brain for the study of its structure or the identification of pathology. Both imaging modalities are discussed frequently in this thesis and so a brief description of each is given here.

In MR imaging, the patient enters an MRI scanner which contains a powerful set of magnets and radiofrequency emitters/receivers. Part of the magnets' function is to set-up a powerful magnetic field that causes all the hydrogen atoms of the patient's water molecules to align their magnetic moments parallel to the magnetic field, either with or against it (Figure 3.1a-b). Rather than truly aligning, the atoms precess with respect to the magnetic field (Figure 3.1c), and are then detected by the MRI scanner by firing radiofrequency pulses at them (Figure 3.1d). This causes them to fall out of sync, somewhat like a collection of spinning tops being destabilised by a sudden crosswind. The magnetic field then eventually brings the atoms back into alignment, which in doing so, creates a number of signature radiofrequency signals that are read by the MRI scanner and converted into an image (Figure 3.1e) [90].

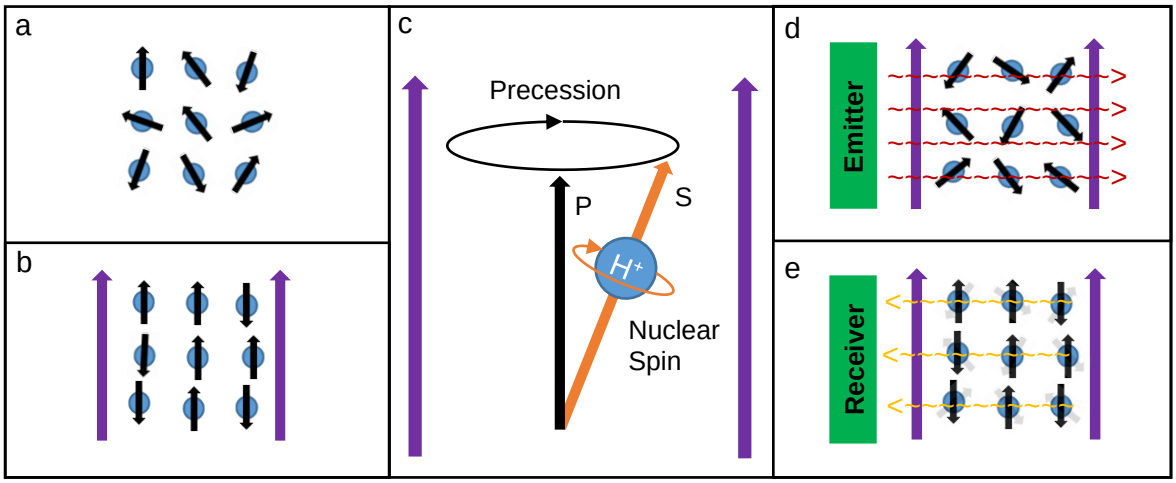

Figure 3.1: Principle of MRI. a) resting asynchrony of hydrogen magnetic moments in a cube of tissue; b) alignment of moments with or against magnetic field (purple arrow); c) illustration of nuclear precession (P = axis of precession; S = axis of nuclear spin) in magnetic field; d) destabilisation of aligned moments by emitted radiofrequency pulse; e) emission of radiofrequency signal from restabilising moments and detection by receiver.

Different signals are produced depending on the density and water content of the varying bodily tissues and so an anatomically detailed picture is often produced. The scanner obtains images in slices by creating a magnetic field gradient along the longitudinal axis of its bore. Then, because the radiofrequency energy required to disturb the precession of the atoms is proportional to the magnetic field strength [90], different slice volumes are selectively imaged by stepping the frequency of the radiofrequency pulse.

CT imaging, on the other hand, utilises X-ray to image the patient. Here, the patient enters a CT scanner which presents as a moveable bed with a doughnut shaped gantry at one end which the bed slides into when in operation. Inside the ring and located at opposite sides, with respect to the bore, is an X-ray emitter and an array of X-ray detectors (Figure 3.2). In operation, the ring is spun round, and when at the correct speed, the emitter begins to fire at intervals. During each emission, X-rays are fired through the patient and towards the detectors. Due to the differing densities of tissues, the X-rays experience regional resistance to penetration, which results in a silhouette image of the anatomy when the detectors measure what made it through the patient. By spinning and repeating this process through 360°, multiple silhouettes of the patient's anatomy are produced which can then be computed into a 3D image. The patient is also moved through the bore during scanning so as to obtain multiple volume slices of the patient [91].

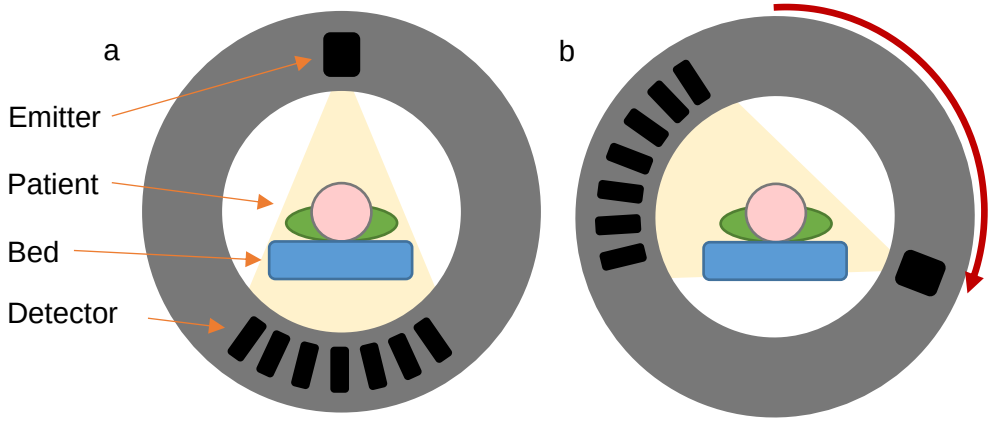

Figure 3.2: Image acquisition in CT imaging. a) CT scanner creating the first anatomical silhouette of the patient; b) gantry rotated around and creating another silhouette.

These brief descriptions give an overview of the two techniques, however, variants exist within each. Illustrated in Figure 3.4 (p35) are examples of the kinds of images that can be taken with MR and CT imaging. Broadly speaking, only a single kind of contrast picture can be taken with CT imaging. This is because, although certain parameters can be altered to subtly change the image, the process of X-ray emission-attenuation-detection is relatively fixed. With MR imaging, however, the utilisation of different radiofrequency pulse sequences can give rise to different signals being emitted back by the atoms and, therefore, different pictures of the anatomy. This is reflected in the four different types of MR scan presented in Figure 3.4.

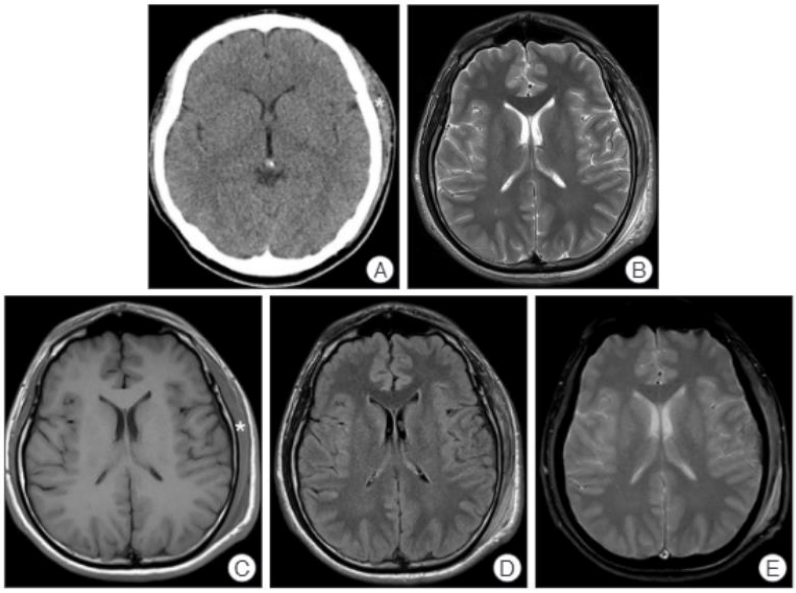

Figure 3.4: Axial CT and MR images of a patient with mild head injury. a) CT scan; b) T1 weighted MR scan; c) T2 weighted MR scan; d) T2 FLAIR MR scan; e) GRE MR scan. Adapted from Kim et al. [92].

In addition to the benefit of image variation, MRI also produces images with greater anatomical detail. However, MR images are well known to suffer from geometric distortion due to the assumptions made in image production [1,93,94]. The central erroneous assumption made by MRI scanners is that the magnetic field is homogenous, which is never true due to gradient nonlinearities produced by the magnets and the field distortion produced by the presence of the patient in the scanner. To mitigate against the resulting image distortion, distortion correction algorithms are used. However, these are imperfect and residual distortion after correction is a known problem in MR imaging (Figure 3.3) [1,93,94].

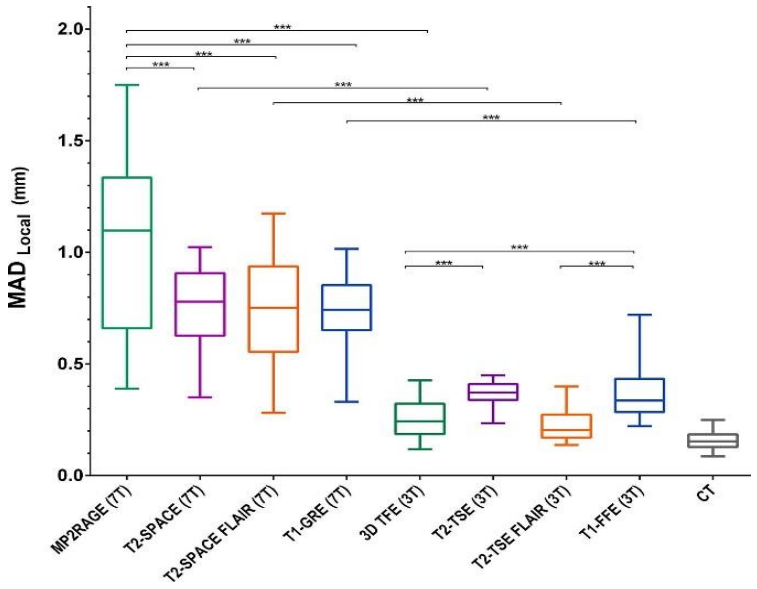

Figure 3.3: Residual geometric distortion after application of commercial distortion correction algorithms, showing variable distortion with individual scanning sequences and magnetic field strength (indicated by 7T or 3T). MAD local is a study specific measure of spatial distortion. Image distortion with CT imaging is also presented. Reproduced from Peerlings et al. [1].

Studies have shown that residual distortion varies with correction algorithm, magnetic field strength and imaging sequence [1,93,94] and it is therefore difficult to understand how much distortion is occurring in any particular image. Residual distortion presents as only a few mm of distortion in any particular image region and so for most applications it is acceptable. However, for applications such as stereotactic neurosurgical planning the distortion has the capacity to demolish the foundation of the technique.

CT imaging, on the other hand, is largely considered distortion free, at least spatially. This is not to say there is no geometric error in images produced by CT machines, rather that the fundamental method by which the images are taken are not based on a collection of large assumptions known to be false (e.g. homogenous magnetic field). The sources of geometrical error in CT are numerous, and together produce levels of distortion similar to the least distorting of the MR sequences (see Figure 3.3) [1], however, the distortion can be considered to be much more stable across different machines and scanning parameters.

Ultimately, each imaging technique has its pros and cons, and as a consequence, MR and CT are favoured for imaging different structures or pathologies (see next section).

3.2 Brain Pathology and Neurosurgery

Pathology presents within the brain in many different ways, however, one could group the pathological manifestations into two categories: those that are dominated by pathological tissue and those that are dominated by pathological function. Tumours, for example, are primarily a result of erroneous cellular function, but it is the huge growth of pathological tissue that is the dominant feature (Figure 3.5a). Epilepsy, on the other hand, is dominated by pathological function, with much more subtle pathology occurring in the tissue itself.

A number of conditions, however, do not fit neatly into these categories. Alzheimer's disease, for example, begins dominated by pathological function (e.g. memory loss), but as the disease progresses, the brain begins to atrophy and stiffen due to the aggregation of proteins, leading to an equal presentation of pathological function and pathological tissue.

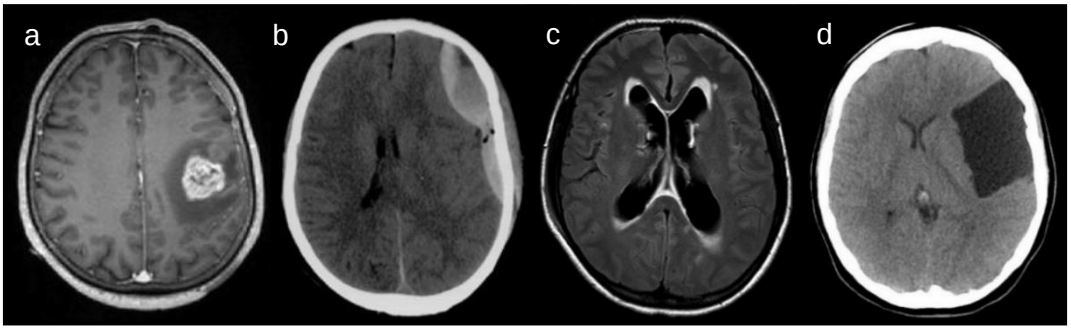

Figure 3.5: Four brain pathologies identified on MR and CT scans. a) tumour on MR scan; b) hematoma on CT scan; c) hydrocephalus on MR scan; d) cyst on CT scan. Images a, b, c and d are adapted from Blanchet et al. [95], Cauley et al. [96], Maugeri et al. [97] and Reference 98, respectively.

Generally, pathologies dominated by pathological tissue are identifiable through MR or CT imaging, either due to boundary changes (e.g. due to swelling or atrophy), changes to the density and/or water content of tissues, or both. Most tumours, for example, are very identifiable on MR/CT scans, due to their high density and clear boundaries, as displayed in Figure 3.5a. MR/CT images featuring hematoma (collection of haemorrhaged blood - Figure 3.5b), hydrocephalus (dilation of the ventricles due to excess fluid - Figure 3.5c) and a cyst (fluid filled cavity - Figure 3.5d) are also displayed as examples of visible pathology.

Often, the best course of action with pathology is to physically intervene. In these cases, surgery is indicated. Broadly speaking, there are three types of neurosurgery: endoscopic, craniotomy and stereotactic.

In endoscopic neurosurgery (Figure 3.6), a thin optical camera and a selection of surgical implements are passed into the cranial cavity through a small hole (burr hole) made into the skull. With video captured by the camera, the surgeon then directs the implements to operate on the patient. This type of surgery is most frequently used to treat fluid-based pathologies (e.g. cysts) and smaller tumours located in areas difficult to remove via craniotomy. Sometimes pathology is accessed by threading catheters up to the brain through blood vessel entry sites lower down in the body.

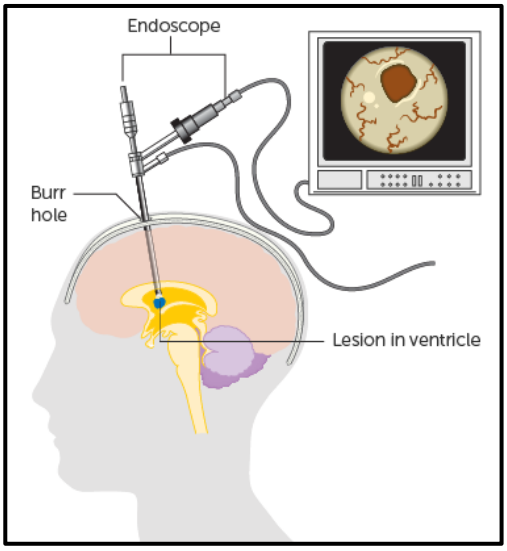

Figure 3.6: Endoscopic neurosurgery. Adapted from Reference 99.

In neurosurgical craniotomy (Figure 3.7), a segment of the skull is removed to provide a large area of brain access for the surgeon. After the patient has been operated on, the skull segment is put back in place. This type of surgery is often used to remove pathologies that would otherwise be difficult to remove through small access holes such as large tumours. Other pathologies treated with craniotomy neurosurgery include haemorrhages, abscesses and aneurysms. Neurosurgical craniotomy is considered the most invasive of the three types of neurosurgery.

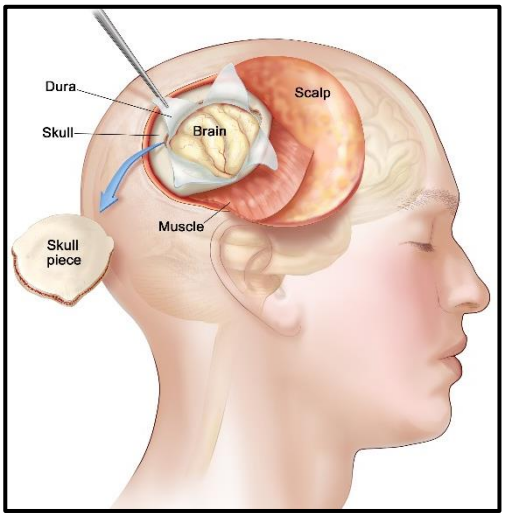

Figure 3.7: Neurosurgical craniotomy. Adapted from Reference 100.

Stereotactic neurosurgery is a type of minimally invasive surgery wherein a coordinate system is used to position and angle tool guides relative to entry points on the skull (Figure 3.8). These entry points lie along carefully planned surgical trajectories, commonly established prior to the surgery with MRI imaging, which ensure the correct delivery of surgical implements to surgical targets. This process allows the surgeon to operate with precision, despite the absence of intracranial vision [101]. Stereotactic neurosurgery is used to treat pathologies which require the utmost accuracy in physical intervention (see Section 3.3). Stereotactic radiotherapy employs a similar process to accurately deliver doses of radiation to specific tissue targets, non-invasively.

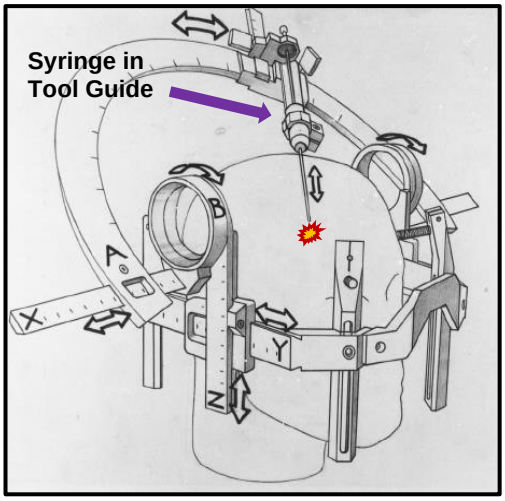

Figure 3.8: Stereotactic neurosurgery. Adapted from Dormont et al. [102].

3.3 Stereotactic Neurosurgery

Surgery of the brain is a delicate procedure which requires a particularly high degree of accuracy. This is due to the localisation of function within the brain, the low redundancy in neural tissue, and the general delicacy of brain tissue, both mechanically and biochemically.

Some surgeries of the brain, however, require a greater degree of accuracy than others. The procedure for the implantation of stimulatory electrodes to the subthalmic nucleus (STN), for example, requires the positioning of the active region of the electrode tip to within 2 mm of the target in order to provide optimal stimulation [99], while the requirement in a cyst drainage procedure is to generally puncture the cyst anywhere along its perimeter and drain out its fluid. Within these two examples there is not only a significant difference in the accepted error budget of the surgery, but also the size of the target involved. In the former example, the target involved is a sub-mm region of a nucleus of neurons not much larger than a grain of rice, while in the latter example, the cyst involved will be a number of centimetres in diameter.

When the highest accuracy is required, stereotactic neurosurgery will be performed. Common surgeries performed with stereotactic method include electrode lead implantation, catheter implantation, biopsy, ablation, resection and stereoelectroencephalography (SEEG - electrophysiological signal reading) [103].

The simplest example of modern stereotactic neurosurgery is mechanical frame stereotaxy. Within this procedure, preoperative MRI images of the patient are first acquired and used to plan an appropriate surgical trajectory towards the target, from an entry point on the

skull (Figure 3.9a-b). Then, in the operating theatre, a mechanical frame is rigidly attached to the skull, before CT scanning the patient and frame with an intraoperative mobile scanner (Figure 3.9c). The intraoperative scan, containing information of the relative position of the frame to the skull, is then registered to (aligned with) the preoperative scan, which contains information of the surgical trajectory relative to the skull (Figure 3.9d). Registering these two scans together then allows the surgeon to establish a spatial relationship between the frame's coordinate system and the pre-planned surgical trajectory (Figure 3.9e). Tool guides attached to the frame are then aligned with the surgical trajectory using the coordinate system (Figure 3.9f) and the surgery is performed [104].

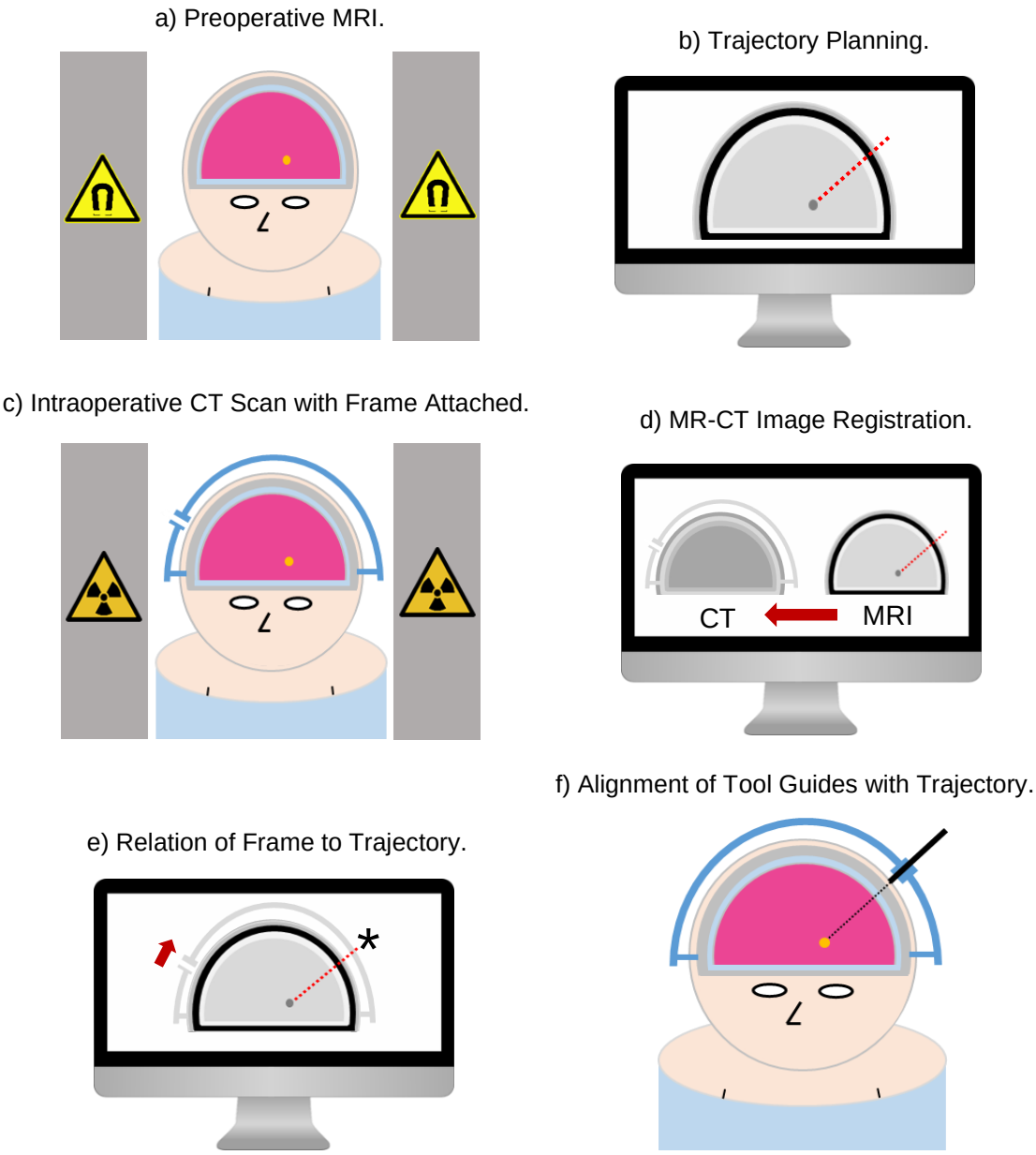

Figure 3.9: Simplified representation of the workflow employed in frame-based stereotaxy.

This example of stereotaxy is called frame-based stereotaxy. In contemporary stereotactic practice, however, there are considered to be three categories of stereotaxy: frame-based, frameless and image-guided.

Frame-based and frameless stereotaxy is performed in much the same way, except for the manner in which the head is restrained. In frame-based stereotaxy, a bulky metal frame is rigidly attached to the skull via pins, whereas in frameless stereotaxy, a custom, non-invasive face immobilisation mask is employed. Depending on the particular system used, the tool guides are either rigidly attached or separate from the structure which immobilizes the head [101].

A majority of the frame and frameless systems utilize manually operated ratchet and pinion mechanisms to position tool guides. However, an increasing number of modern systems are starting to employ robotics (Figure 3.10). These systems unsurprisingly deliver higher accuracy than purely mechanical systems due to reduced human involvement in the positioning and locking of tool guides [101,105].

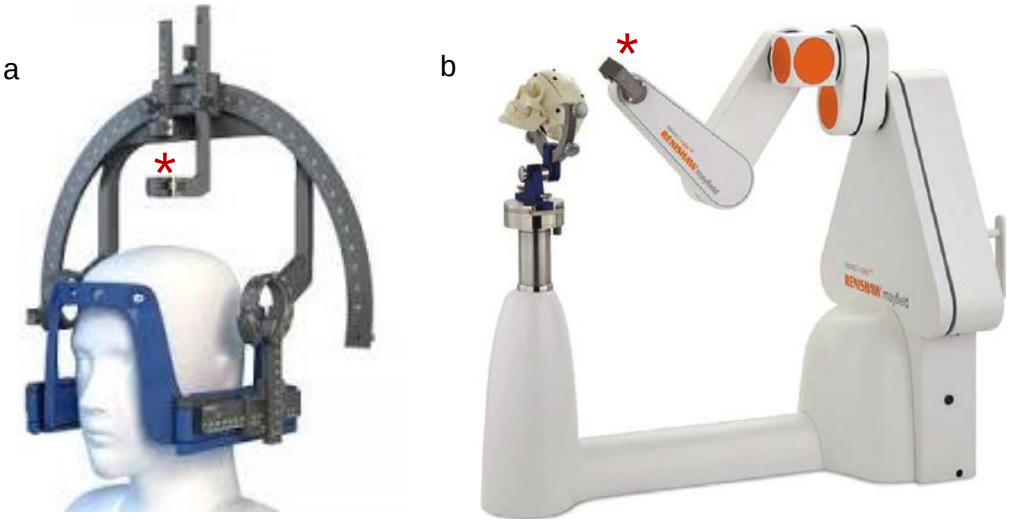

Figure 3.10: Mechanical and robotic frame based stereotactic systems. a) Leksell Vantage Stereotaxic System (Elekta, SE) (image reproduced from Reference 106); b) Neuromate Robotic System (Renishaw, UK) (image reproduced from Zanotto et al. [107]). Tool guides of each system are indicated by an asterix.

Image-guided stereotaxy utilizes advanced intraoperative imaging such as interventional MRI (iMRI) to further increase the accuracy of tool positioning through intraoperative verification of tool location. This form of stereotaxy requires state of the art technology, however, and is therefore rarely found in clinical practice. This is reflected in Figure 3.11, which shows the percentage of deep brain stimulation (DBS) electrode leads implanted by different stereotactic systems between 2001 and 2015 [101]. Here it can be seen that a majority of procedures are still being performed through the frame-based stereotactic method and with just one type of mechanical frame: the Leksell frame.

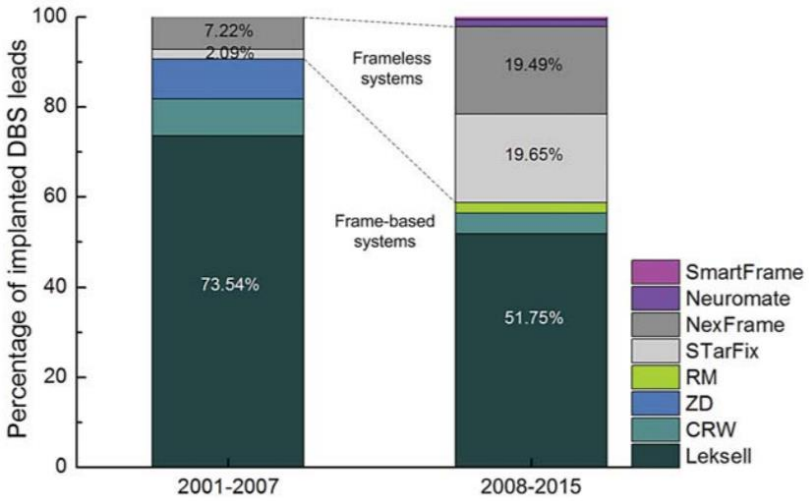

Figure 3.11: Percentage of deep brain stimulation (DBS) electrodes implanted by different stereotactic systems between 2001 and 2015. The Leksell, CRW (Cosman-Roberts-Wells), ZD (Zamorano-Dujovny), RM (Riechert-Mundinge) and the Neuromate systems are considered frame-based systems, whereas the StarFix and NexFrame systems are considered frameless systems. The SmartFrame is an iMRI guided stereotactic system. Reproduced from Li et al. [101]

A handful of comparative studies show that the robotic and iMRI-guided systems do indeed offer greater accuracy then the more basic frame-based and frameless mechanical systems. The Neuromate robot system, ROSA robot system and iMRI-guided SmartFrame, for example, were found to offer average lead implantation targeting errors of 0.86 ± 0.37 mm [105], 0.76, ± 0.37 mm [105] and 0.60 ± 0.50 mm [101], respectively, whilst average targeting errors for the conventional frame-based and frameless systems have generally been found to lie above 1mm (Figure 3.12).

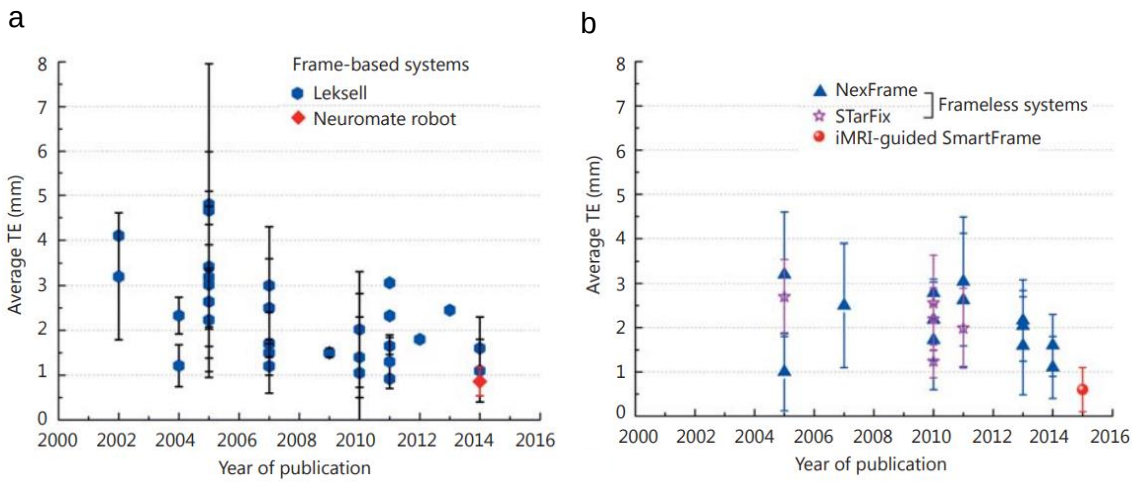

Figure 3.12: Comparison of targeting error (TE) of DBS electrode implantation between the Leksell and Neuromate systems (a) and the frameless and SmartFrame systems (b). Adapted from Li et al. [101].

The accuracy achieved with the iMRI-guided SmartFrame system is thought to be the highest achieved in DBS lead implantation surgery [101]. This is of course facilitated by the ability to visually verify the position of the electrode next to its target in the operating theatre.

An alternative to iMRI-guidance in electrode placement is microelectrode recording (MER) [2]. Here, a dual functioning electrode lead which can both stimulate and read electrophysiological signals is used in place of the purely stimulatory electrode lead. Use of this electrode lead then allows the surgeon to determine if the correct position has been achieved through analysis of read signal. MER only serves as a solution in electrode placement, however, and as discussed there are many other surgeries in stereotactic neurosurgery.

3.4 Targeting Error Sources

Both iMRI-guidance and MER guidance are certainly effective in the mitigation of targeting error as it arises intraoperatively, however, these corrections are not inconsequential. Intraoperative repositioning of electrode leads, for example, increases surgical duration and infection risk, and the burr-hole (skull opening) in iMRI-guided stereotaxy also has to be made larger (infection risk) to account for the changing surgical trajectory [104].

The sources of targeting error in stereotaxy are numerous. However, if all these sources were understood individually, one could theoretically either eliminate them from the surgical workflow altogether or account for them in the trajectory planning stage. This would allow for correct positioning on the first attempt and elimination of the risks associated with repositioning.

The following sections provide a brief summary of the targeting error sources in stereotactic neurosurgery. They are presented in the order they appear in the typical surgical workflow.

3.4.1 Geometric Distortion in MRI Imaging

Given that MR images are spatially distorted and that MR imaging is used to plan the spatially delicate surgery, an error is introduced at this stage in target localisation. Further error is then created when attempting to register the spatially distorted preoperative MR image to the relatively distortion free intraoperative CT images later on in the surgical workflow.

3.4.2 Image Registration Error

Image registration of 3D datasets produced through different imaging modalities is not a trivial task. MRI and CT scanners produce images with contrasting resolution (voxel size), image size (field of view) and intensity profile. Furthermore, the images are also subtly different due to MR distortion and so fundamentally cannot be perfectly aligned. In

combination, these contrasting features lead to errors in alignment of the preoperative and intraoperative patient images [108,109,110].

3.4.3 Patient Repositioning Mediated Brain Shift

The preoperative MRI scan is generally acquired with the patient in the supine position, with the brain sagging towards the occipital region of the cranial cavity (Figure 3.13a). During surgery, however, the patient's head is often positioned differently to the supine position, with the brain now sagging in a different anatomical direction. The consequence of this is that the target has drifted away from its location on the preoperative planning image and, therefore, no longer lies at the terminus of the planned surgical trajectory (Figure 3.13a-b).

This type of brain shift is known as positional brain shift (PBS) and is the focus of this project. A greater discussion of PBS is held in Section 3.5 (p45).

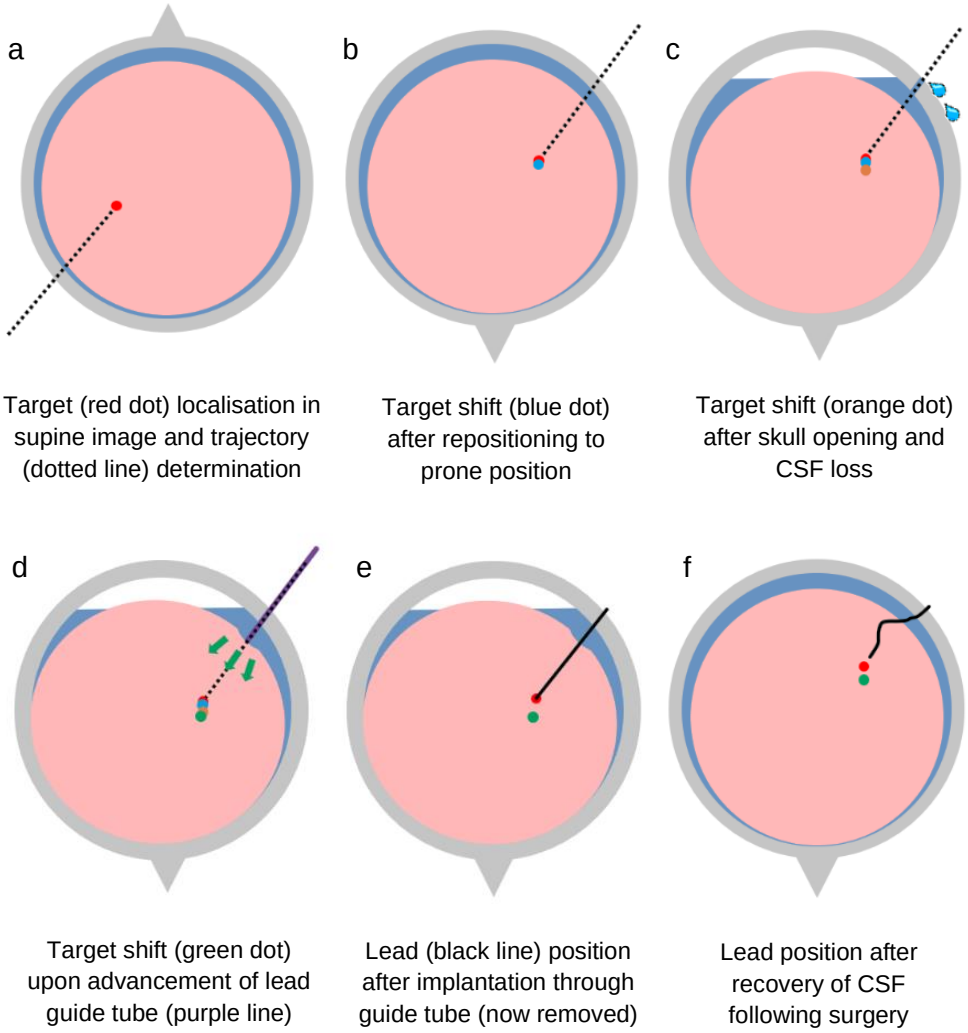

Figure 3.13: Brain shift events during DBS lead implantation surgery. Guide tube referred to in [d] is a rigid implement used to penetrate the brain and provide a channel for the delivery of the flexible and delicate electrode lead.

3.4.4 Pneumocephalus Mediated Brain Shift

When the skull and meningeal membranes are opened to access the brain a small portion of the CSF leaks out, which is concurrently replaced with extracranial air. This replacement of CSF with air is known as pneumocephalus and results in reduced buoyancy forces acting on the brain. The buoyancy forces combat against gravity and so their diminishment leads to further sagging of the brain in the direction of gravity, away from the surgical trajectory (Figure 3.13c) (Figure 3.14, p44) [111,112].

Large targeting errors can result from the loss of CSF if a large pneumocephalus develops. However, the extent of CSF loss can be significantly limited through the careful use of meningeal and cranial sealants when opening the head [113,114] and the appropriate positioning of the patient [111], where possible.

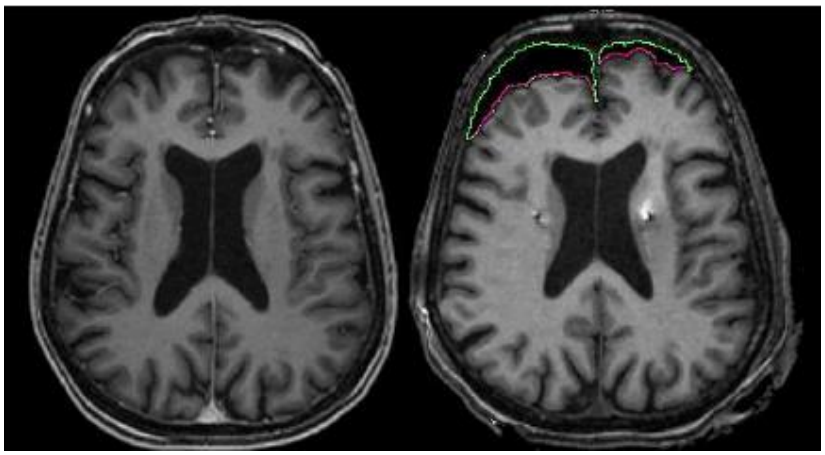

Figure 3.14: Pneumocephalus mediated brain shift. a) resting brain shape in supine position; b) brain shift upon CSF loss and introduction of air. Reproduced from Bilger et al. [115].

3.4.5 Surgical Implement Mediated Brain Shift

While soft, the brain offers a certain resistance to penetration that can cause more delicate surgical instruments to veer off course during insertion and advancement. This can occur either through instrument deflection or instrument bending and is particularly relevant in needle-based operations which utilise thin, flexible steering needles [116,117].

3.4.6 CSF Recovery Mediated Brain Shift

When the operation is complete and the patient is in the recovery stage, the homeostatic mechanisms of the head act to replace any lost CSF and expel the intracranial air. When this happens, the buoyancy forces return to what they were prior to the surgery and the extra brain sag introduced during surgery is eliminated. This can be problematic with electrode leads, for example, as they are implanted into the brain in its deformed state and anchored to the skull. Therefore, when the brain returns to its undeformed state, the lead deforms and the electrode tip retracts away from the target (Figure 3.15) [118,119].

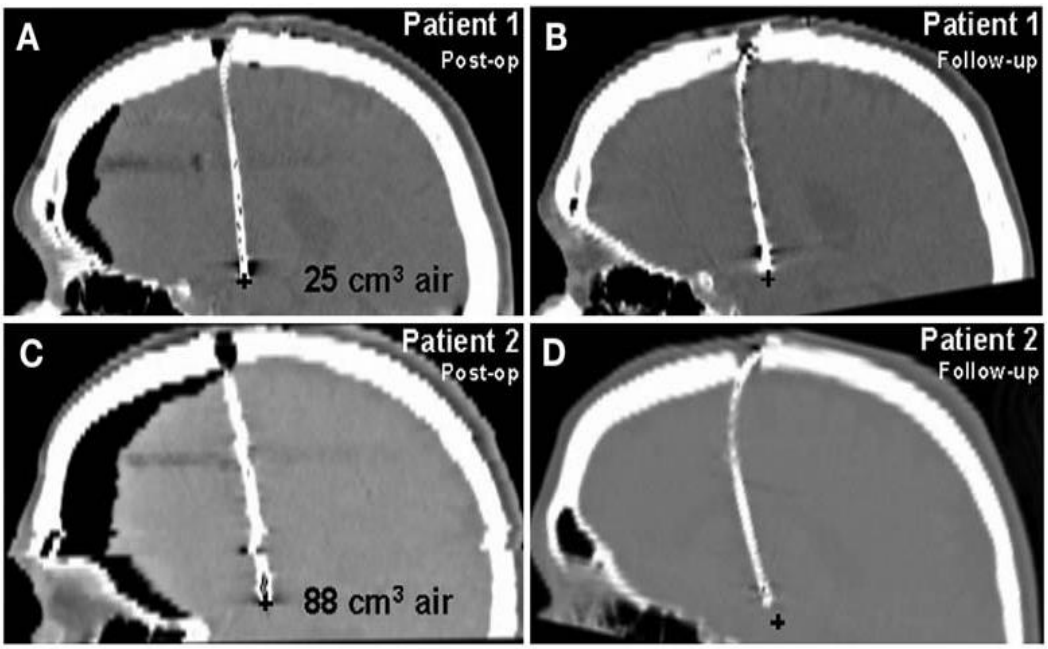

Figure 3.15: Lead bending and retraction away from target upon recovery of CSF. a) post-op scan of patient with 25 cm^3 of intracranial air (black); follow-up scan of patient with 25 cm^3 of intracranial air; c) post-op scan of patient with 88 cm^3 of intracranial air; d) follow-up scan of patient with 88 cm^3 of intracranial air. Adapted from van den Munckhof et al. [120].

3.5 Positional Brain Shift

Unlike other sources of targeting error, positional brain shift is a fundamentally unavoidable event in the traditional stereotactic workflow. If a surgery demands the patient's head be placed in a non-supine position, the brain will shift away from the planned trajectory. Given that it is difficult to scan patients in non-supine positions due to comfort issues, there is no available intervention for PBS and it is therefore an important event to characterise.

Little attention has been drawn to this event, however. Instead, much of the work has focussed on characterising some of the more dramatic brain shift events such as pneumocephalus mediated brain shift (PMBS).

Observational studies which correlate the volume of intracranial air gained during surgery and brain shift, however, do not account for PBS in their estimation of PMBS. Given that these studies are often used to determine the efficacy of pneumocephalus prevention methods, it is important to understand to what degree PBS is playing a part.

To date, only a handful of studies have studied PBS. A brief summary of each study is presented below:

- Thulin et al. [121] used encephalograms to study supine to upright PBS in 56 subjects awaiting surgery. Of the only two subjects lacking preoperative pneumocephalus, shifts in subcortical structures of 0.5-0.9 mm was observed.

- Hill et al. [122] used MRI to study supine to prone PBS in two subjects as part of a larger study of craniotomy brain shift. Although no values were quoted by the authors, observed cortical brain shift was stated to be less than 1 mm.
- Rice et al. [39] measured change in SAS width upon transition from the supine to prone position in three subjects using MRI. Transitioning from the supine to prone position was found to result in SAS width changes of up to 30% - corresponding to shifts of approximately 1 mm.
- Schnaudigel et al. [123] used MRI to study supine to prone PBS in 13 subjects. Transition from the supine to the prone position was found to result in posterior to anterior shifts of between 0.6 and 1.3 mm. PBS upon transition from left decubitus to the right decubitus position was also studied, with shifts of up to 1.8 mm being observed. Except for these values, a majority of the data in this paper is presented in vector graphic format (see Figure 3.16).

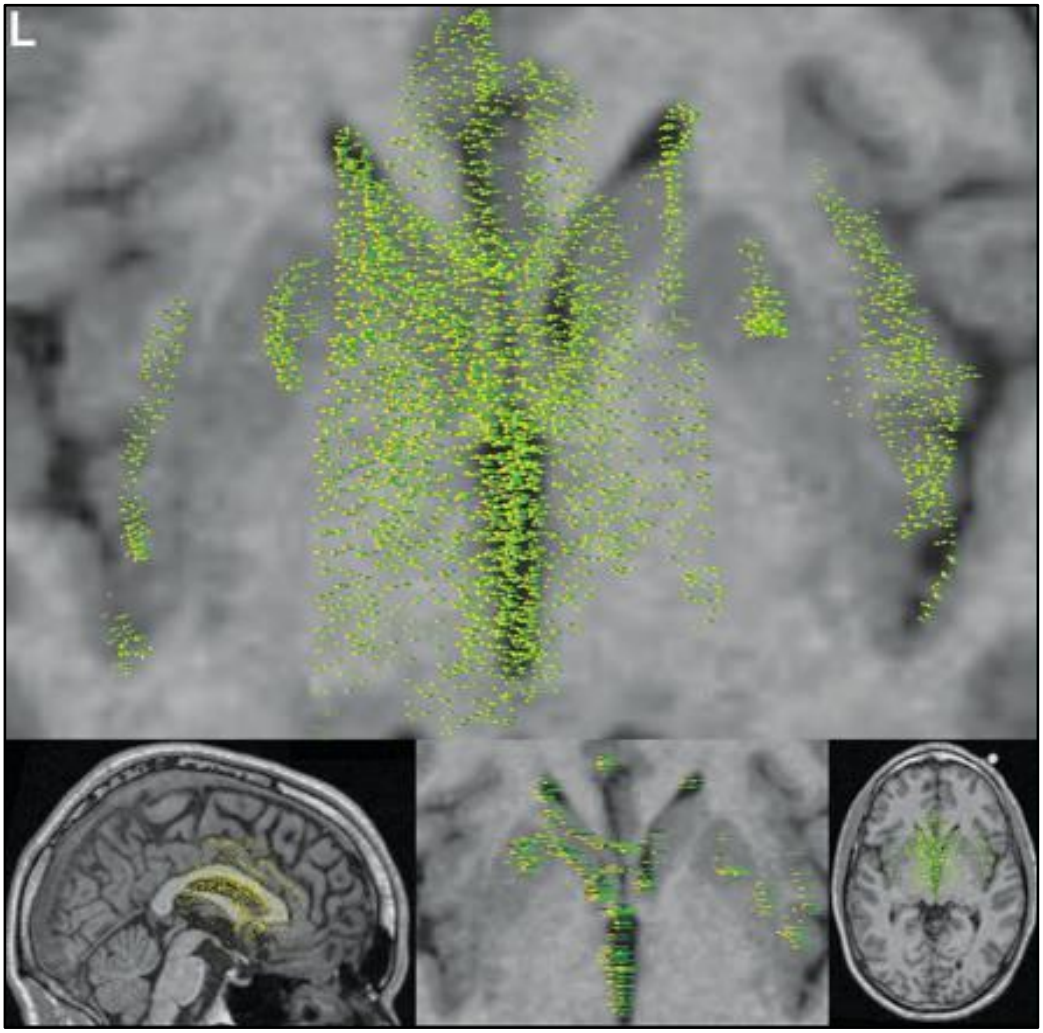

Figure 3.16: Vector graphic data presentation by Schnaudigel et al. [123].

- Monea et al. [124] used MRI to study supine to prone and left decubitus to right decubitus PBS in 30 subjects. These subjects were grouped into three age bands: < 20 years (band A), 25-40 years (band B), and > 60 years (band C). Brain shift normal to the surface was calculated at thousands of points on the cortical and ventricular surfaces, with outward shifts being considered positive and inward shifts being considered negative. A majority of the brain shift is reported as either values averaged across the whole brain area or in the format shown in Figure 3.17.

  Mean cortical and ventricular shifts upon transition from the supine to the prone position were found to be -0.25 ± 1.62 and 0.12 ± 0.87 mm for band A subjects, -0.47 ± 1.90 and 0.06 ± 0.63 mm for band B subjects and -0.16 ±1.19 and 0.23 ± 0.81 for band C subjects, respectively. Mean cortical and ventricular shifts upon transition from the left decubitus to the right decubitus position were found to be -0.66 ± 2.33 and 0.18 ± 1.08 mm for subjects in band A, -0.23 ± 1.35 and 0.18 ± 1.09 for subjects in band B and -0.05 ± 1.52 and 0.04 ± 1.18 mm for band C subjects, respectively.

  The authors did not find significant differences between age and gender. Although maximum shifts were reported to occur at the inferolateral aspects of the frontal and temporal lobes, regional values are not given.

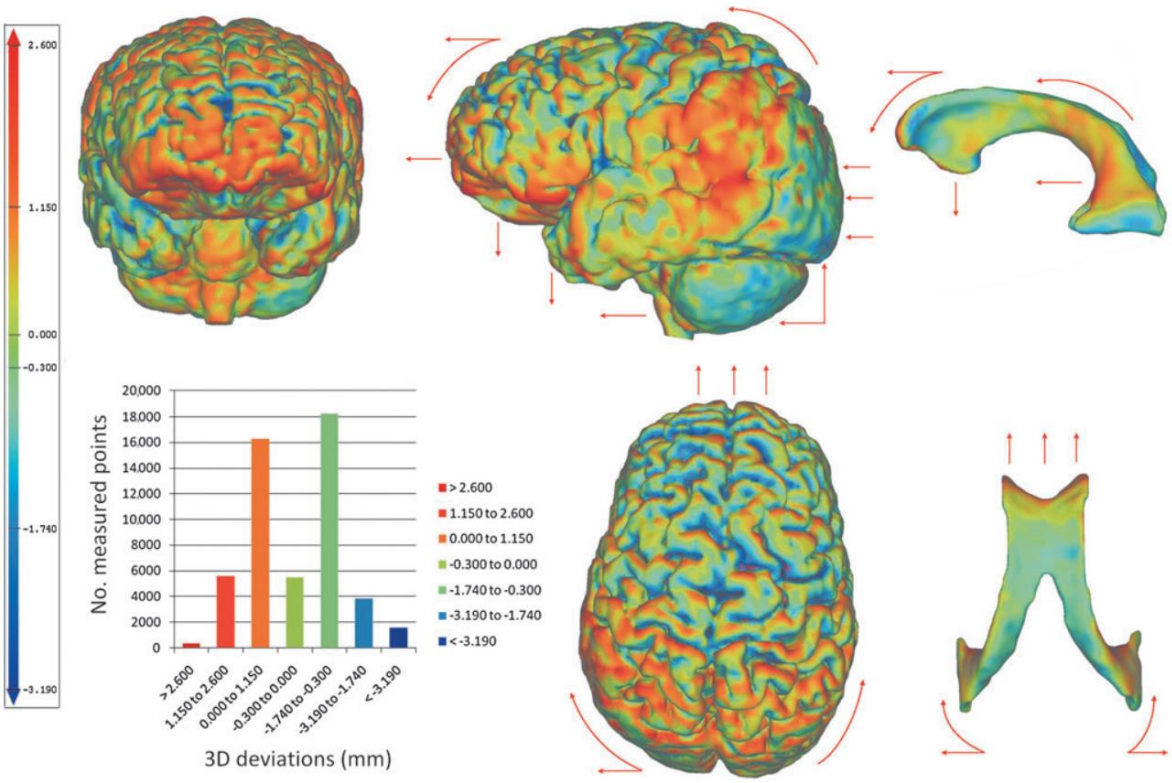

Figure 3.17: Supine to prone brain shift graphic presented by Monea et al. Reproduced from Monea et al. [124].

- Mikkonen and Laakso [125] used MRI to study supine to prone and supine to left decubitus PBS in five subjects. For each subject, the Spherical Demons algorithm was used to elastically register the brain surfaces of the prone and left decubitus images with the brain surface of the supine image, generating displacement vectors for each vertex defining the supine brain surface. Vertex displacement vectors were then averaged into one of 13 brain regions to obtain a mean regional displacement.

  Shift was found to be predominately forward and downward in transition from supine to prone and leftwards and downwards in transition from supine to left decubitus (see Figure 3.18). On average, the left and right hemispheres shifted by 0.7 ± 1.0 and 0.8 ± 1.1 mm, respectively, upon transition to the prone position and 0.9 ± 0.9 and 0.4 ± 0.8 mm, respectively, upon transition to the left decubitus position. Magnitude and direction of shift was found to vary between brain region, however, with regional average shifts ranging from between 0.2 and 1.6 mm.

  In transition to the prone position, the largest shift was observed in the parietal lobe of both the left and right hemispheres, while in transition to the left decubitus position the largest shifts were observed in the posterior region of the frontal lobe and the anterior region of the parietal lobe.

  Unlike other papers on PBS, the publication by Mikkonen and Laakso provides the reader with tabulated vector information on the regional displacement of the brain upon repositioning from the supine position.

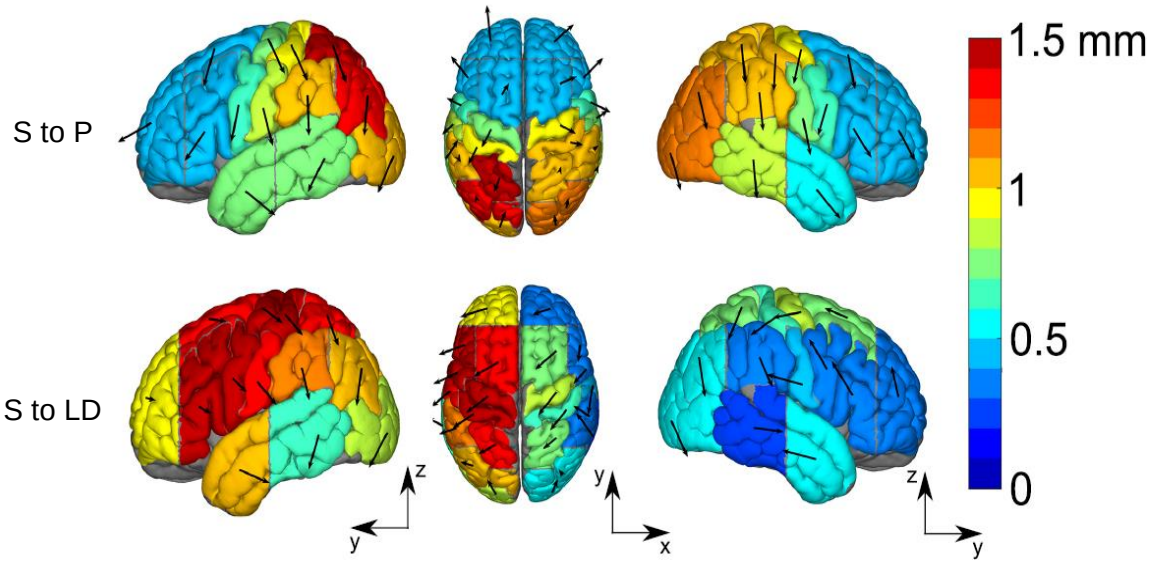

Figure 3.18: Graphical illustration of supine (S) to prone (P) and supine (S) to left decubitus (LD) PBS by Mikkonen and Laakso. Arrows show the direction of movement within the two dimensions of the sagittal and axial image planes, while the colour within each region represents the average magnitude of PBS in that region. Adapted from Mikkonen and Laakso [125].

- Ji et al. [126] used MRI to study the displacement and rotation of the brain stem and cerebellum with head flexion (up to 54 degrees elevated from supine) in five subjects. It was found that while the cerebellum rotated in the flexion direction, exceeding the skull rotation, the brain stem did not rotate. Instead the brain stem was found to shift towards the foramen magnum (see Section 2.3, p22) by between 0.8 and 1.6 mm (Figure 3.19).

- Ji and Margulies [127] used MRI to study displacement of the pons (see Section 2.1.2, p8) in 15 subjects with varying degrees of head flexion relative to the supine and prone positions. Similar to Ji et al., displacements of up to 2 mm towards the foramen magnum were observed.

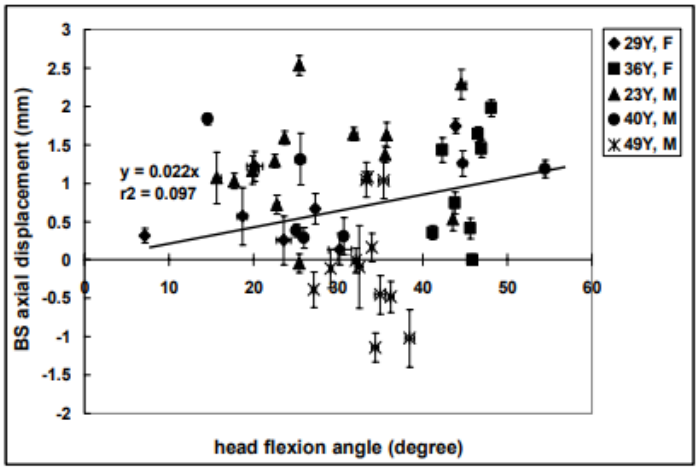

Figure 3.19: Brain stem displacement and head flexion angle. Reproduced from Ji et al. [126].

To the author's knowledge, these nine studies represent the only publications which contain displacement information of the brain as a consequence of positional change. Of the three major PBS studies [123,124,125], only the study by Mikkonen and Laakso appears to provide useable information for surgeons (component displacements tied to specific regions).

Given that the brain evidently shifts non-rigidly [123,124,125], the only useful information for surgeons are displacement fields which describe brain shift at each location within the brain for a given positional transition. Averaged shift information, therefore, has little value and the greater the size of the region the average is garnered from, the less useful the shift information becomes. The publication by Mikkonen and Laakso is the only publication which contains quantitative vector information approaching a displacement field. Their study, however, did not produce any information regarding brain shift beneath the brain's surface, which is considerably more important in the context of stereotactic neurosurgery.

Nonetheless, across the nine presented studies, there does seem to be an agreement towards the general magnitude of brain shift in PBS at around 1 ± 1 mm. However, only transitions (from supine) to upright, left decubitus and prone have been investigated.

3.6 Patient Positioning in Stereotactic Neurosurgery

Patient positioning in neurosurgery is not only dictated by the required surgical trajectory but also by other factors which typically fall under the remit of anaesthetic care [128,129]. Examples of these include airway access, avoidance of pressure sores, optimal cerebral venous drainage and homeostatic monitoring [128].

Common surgical positions in neurosurgery are the supine, lateral, sitting, prone, concorde and three-quarter prone positions (Figure 3.20). However, within these six main positions there are then a whole host of other variations [128]. Selection of position is done on a case by case basis through dialogue between surgeon and anaesthetist.

The most prevalent head positions in stereotactic neurosurgery appear to be the supine, elevated supine and upright positions, however, throughout the stereotactic neurosurgery literature, one can find evidence for use of almost any conceivable head position. It is, therefore, of importance to measure PBS upon transition to a similarly encompassing spectrum of head positions.

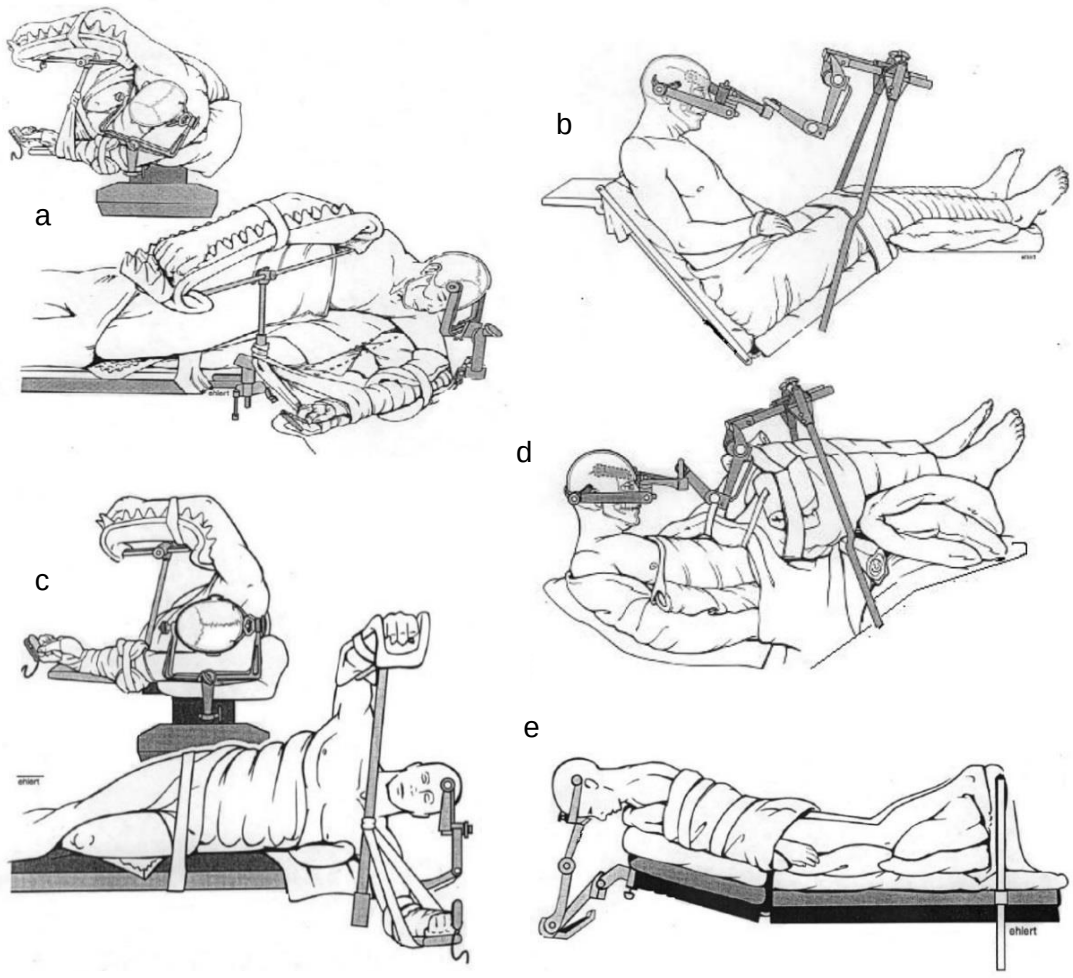

Figure 3.20: A selection of common non-supine patient positions utilised in neurosurgery. a) lateral-oblique positioning; b) classical sitting position; c) lateral position; d) semi-recumbent position; e) concorde position. Adapted from Rozet and Vavilala [128].

3.7 Chapter Summary

Stereotactic neurosurgery often requires exceptionally high accuracy. Although, this level of accuracy is largely achieved through the use of elaborate surgical workflows, a degree of targeting error persists.

The sources of targeting error are numerous, however, some have received much more attention than others. These sources (e.g. PMBS) generally provide a larger proportion of the total targeting error, or at least, have the capacity to.

However, while events like PMBS are potentially more impactful, they are often theoretically preventable (e.g. through the skilled use of meningeal sealants). PBS, on the other hand, is a fundamentally unavoidable event in the traditional stereotactic workflow. Given that studies have shown the brain to shift by around 0-2 mm upon repositioning from the supine position, and that for some surgeries the error margin is 1 mm, PBS presents as an equally important event to characterise. Few positional transitions have been investigated, however, and of those that have, the information produced for them is generally not sufficiently descriptive of the brain shift to be considered actionable by surgeons.

Current strategies to mitigate against targeting error involve the intraoperative repositioning of tools. This is a sub-optimal strategy for cost and patient risk reasons. However, if each source of targeting error were characterised, one could theoretically account for them in the trajectory planning stage and eliminate the potential need for intraoperative repositioning.

Now that both the brain-skull system and the PBS event are somewhat understood, the next chapter will examine the state of PBS phantoms in the literature.

4 EXISTING POSITIONAL BRAIN SHIFT PHANTOMS

The previous chapter detailed the problem of positional brain shift in stereotactic neurosurgery. This chapter contains an assessment of the existing brain shift/deformation phantoms in the literature.

4.1 Brain-Skull Phantoms

The human head is a complex system of materials that is difficult to recreate in its entirety with contemporary manufacturing technologies. For this reason, simplifications are invariably made when making a phantom. Given that the head cannot currently be fully reengineered, phantoms are often built to the minimum complexity required for a particular avenue of investigation. As no phantom studies have been used to study PBS, there is consequently no comparative phantom to be found in the literature.

The only phantom that could conceivably be repurposed to study PBS is that displayed in the works of Forte et al. [57,131] (Figure 4.1). This phantom comprises a hydrogel brain, plastic skull (with rudimentary integrated plastic falx) and water filled SAS (no tethering element). The remaining brain deformation/shift phantoms in the literature largely present as either isolated brain parts [132,133,134,135,136,137] or as brain simulant filled skulls [138,139] (see Figure 4.2, p53). An exception to this is the morphologically complex phantom by Bayer et al. [140], which comprises separate brain, with fluid inflatable ventricles/tumours and blood vessels, and skull, but with no fluid saturated SAS.

The key distinction between the phantom by Forte et al. [57] and the others is the pairing of a mechanically realistic brain (stiffness and density differential) with a geometrically realistic, fluid filled gap between the brain and skull. This pairing is essential in modelling PBS for two reasons: the first is that a gap is needed in order for shift to occur in the first place (rigidly or non-rigidly) and the second is that the shift is driven by the density differential between the brain and the fluid. Thus, without the gap the event cannot be reproduced.

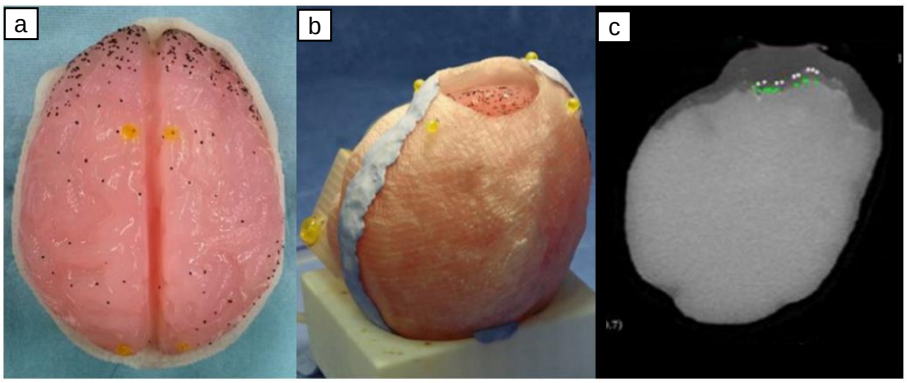

Figure 4.1: The SAS featuring phantom by Forte et al. a) top-down view of brain sitting in lower skull half; b) assembled phantom with skull segment removed (craniotomy); c) MRI scan of (b) showing brain sagging in fluid filled cranial cavity. Adapted from Forte et al. [57].

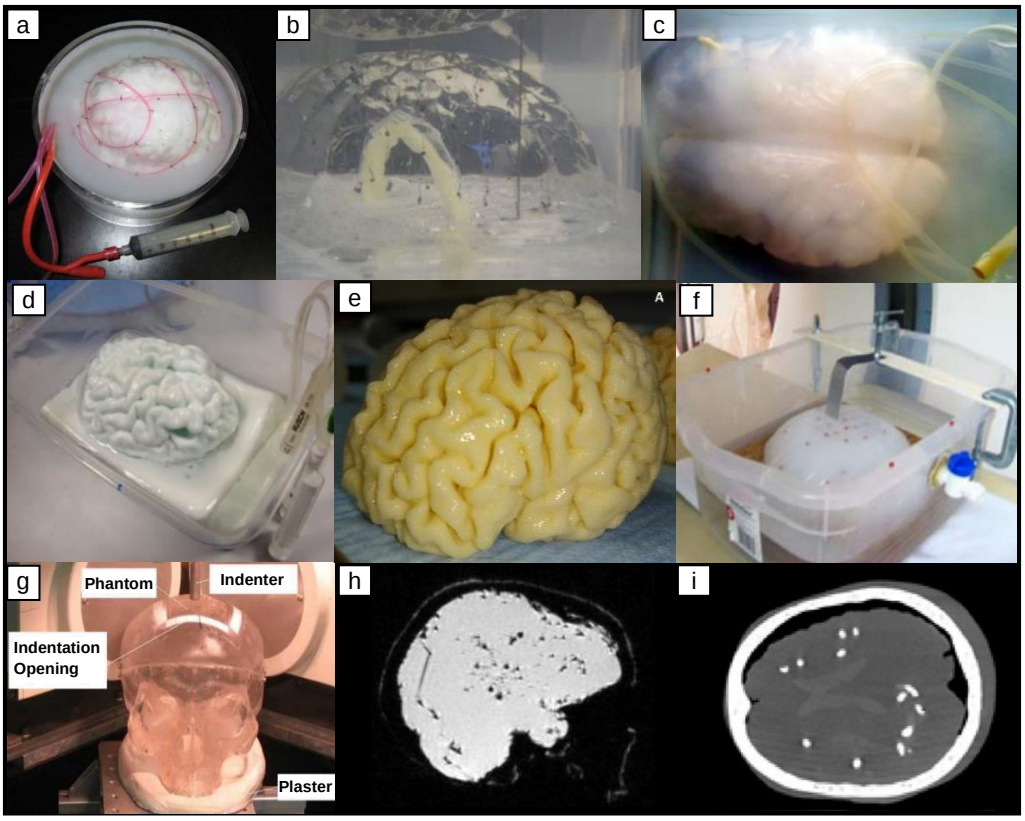

Figure 4.2: Representative sample of non-SAS-featuring phantoms in the literature. a) PVA hydrogel cerebrum with expandable ventricular cavity and embedded tubular vessels (adapted from Reinertsen and Collins [132]); b) silicone cerebrum with expandable ventricular cavity (adapted from Puzrin et al. [133]); c) PVA hydrogel cerebrum with expandable tumour-like volume (adapted from Mohammadi et al. [134]); d) PVA hydrogel left hemisphere featuring high topological definition (adapted from Chen et al. [135]); e) oil emulsion organogel cerebrum (made to 50% scale) (adapted from Lozoya [136]). f) rudimentary PVA hydrogel cerebrum (adapted from Chen et al. [137]); g) silicone filled skull being indented (adapted from Ma et al. [138]); h) MR image of gelatine hydrogel filled skull (adapted from DeLorenzo et al. [139]); i) MR image of phantom comprising polyurethane brain with inflatable ventricles/tumour and blood vessels and composite ceramic skull (internal black volume is air) (adapted from Bayer et al. [140]).

Including a SAS without introducing constraints elsewhere (e.g. brain material selection) is practically unavoidable. Therefore, it is unsurprising that a majority of groups do not include a SAS in their phantoms if not vital for their particular avenue of investigation.

The key difficulties in manufacturing a phantom with a fluid filled SAS are as follows:

1) Manufacturing a robust brain with realistic geometry, density and loading response.
2) Fabricating an openable skull with geometrically realistic cranial cavity.
3) Developing a method to transport the fragile brain into the skull without damaging it.
4) Replacing 100% of the intracranial air with fluid of appropriate density.
5) Securely sealing the skull such that no pneumocephalus occurs.

Forte et al. [57] overcame difficulties 1-3 in the fabrication of their phantom. However, as their investigation was in craniotomy-related brain shift, their phantom did not require a complete skull. They therefore did not need to seal the skull and could expel all intracranial air by simply overfilling the phantom.

The crucial development made by Forte et al. [57] with regards to overcoming difficulties 1-3 was in the brain material they developed. This material was a composite hydrogel (CH), comprising polyvinyl alcohol (PVA), phytagel (PHY) (a polysaccharide) and deionised water (Di H_2O), which importantly had similar loading response at slow to medium loading rates, reasonable density and similarly high strain to failure to brain tissue.

PVA and PHY are materials which form hydrogels when dissolved in hot water and then cooled down to their curing temperature range. PVA solutions form into hydrogels when they are frozen and subsequently thawed, whilst PHY solutions form into hydrogels when the hot solution is brought down to room temperature [57].

When PVA solution is frozen, the dissolved PVA polymer strands (Figure 4.3a) are forced together by expanding ice crystals (Figure 4.3b), such that when the system is thawed, and energy is put back in, hydrogen bonds are formed between the adjacent PVA strands (Figure 4.3c-d). With the ice returned to liquid water, the resulting system, when thawed, is a macro-porous hydrogel (Figure 4.3e) with high strength, relative to other hydrogels [141]. PHY, on the other hand, is a polymer of glucuronic acid, rhamnose and glucose and forms into a hydrogel when energy in the hot solution is lost and intermolecular bonds form between dissolved strands.

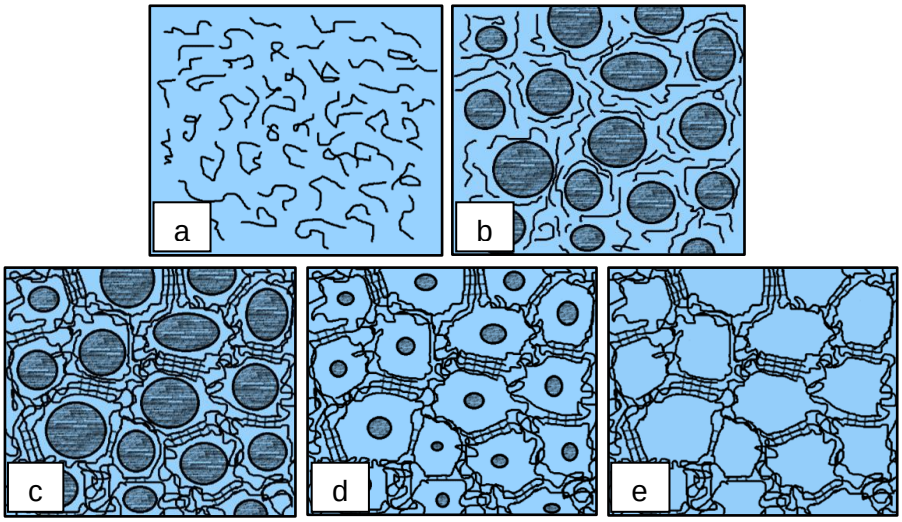

Figure 4.3: Freeze-thaw formation of PVA hydrogels. a) PVA polymer stands dissolved in water; b) ice crystals forcing PVA strands together; c) formation of hydrogen bonds between polymer strands as the system begins to thaw; d) continued thawing of ice crystals; e) formed hydrogel.

In searching for a suitable simulant for their phantom, Forte et al. [57] found the PVA hydrogel to have similar compressive stress to brain tissue at slow loading rates (0.00083 mm/s), but not at medium loading rates (0.083 mm/s), or with the correct rate dependent viscoelastic behaviour. On finding the phytagel hydrogel to be a suitably viscoelastic material, but offering a dissimilar stress response at medium or low loading rates, the authors created a composite of the two, finding the formulation *[3.00% PVA : 0.43% PHY : 96.57% Di H_20]* to produce properties most similar to that of brain tissue (see Figure 4.4, p55).

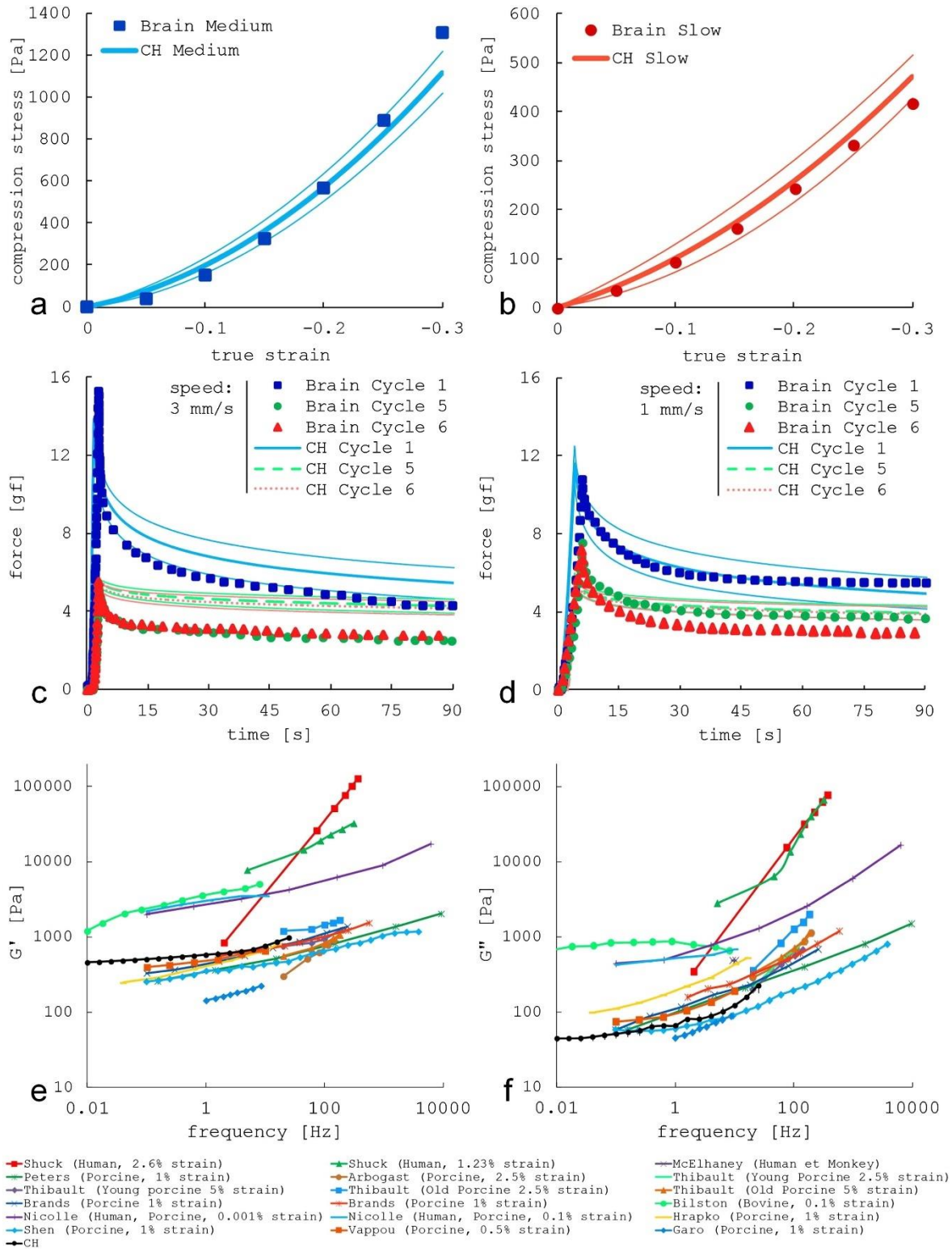

Figure 4.4: Loading response of the CH produced by Forte et al. A and B are unconfined compression tests of the CH and porcine brain tissue at 0.083 mm/s and 0.00083 mm/s, respectively. C and D are cyclic indentation-relaxation tests of the CH and porcine brain tissue at 3 mm/s and 1 mm/s, respectively. E and F are the storage and loss moduli, respectively, measured by sweep frequency analysis, with literature measurements of brain tissue also plotted. Reproduced from Forte et al. [57].

This formulation, presented as [6% PVA : 0.85% PHY] in [57], produced a gel with realistic loading response at medium and slow loading rates and realistic rate-dependent viscoelastic/poroelastic behaviour. The macroporous architecture of the CH can be seen to be consistent with its elastic behaviour (Figure 4.5).

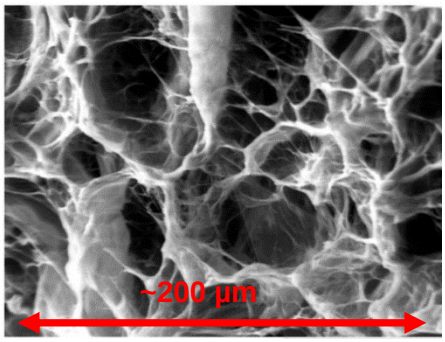

Figure 4.5: Scanning electron microscopy image of the CH material. Adapted from Forte et al. [57].

The density of the hydrogel was found to be a little low at 1.015 ± 0.013 g/cm^3 [131]. However, it nonetheless presents as one of the closest density matched simulants to brain tissue.

A similar loading response and density is important for modelling brain shift/deformation, however, a suitably high strain to failure is just as important given that the phantom must be able to survive assembly.

While strains higher than 0.3 are rarely reached in the skull confined brain under neurosurgical loading conditions, very high strains are quickly reached when the 1.4 kg brain is removed from its supported environment. This is seen whenever a brain is removed from the skull during post-mortem (see Figure 4.6b), where general handling and gravity then severely deform the brain's structure. Given that brains cast outside the skull need to be transported into the skull in order to construct a SAS featuring phantom, a suitably robust brain simulant is therefore required. This of course assumes a traditional assembly route.

As shown in Figure 4.6a, the strain to failure of the CH is very similar to that of brain tissue, which both begin to fail when stretched by a factor of approximately 2.5. Given a similar capacity to stretch as brain tissue, a brain cast in the CH material can therefore also withstand the deformations of extracranial handling.

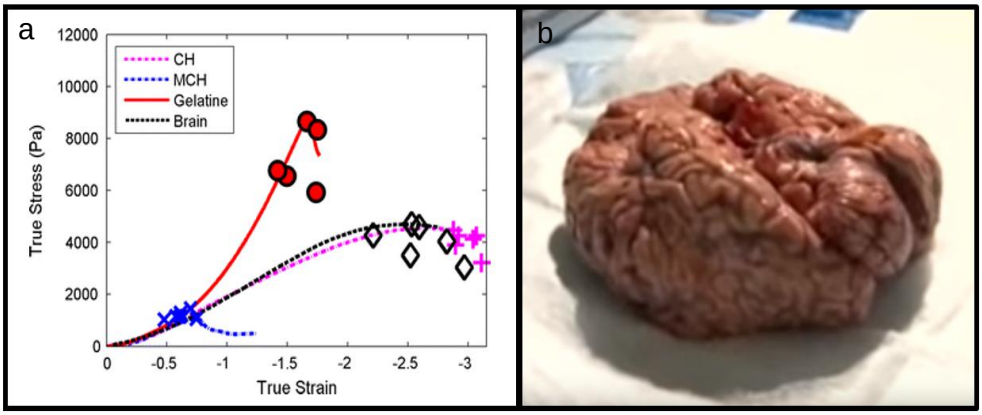

Figure 4.6: Compression to failure stress/strain responses (a) of composite hydrogel (CH), modified composite hydrogel (MCH), gelatine hydrogel (Gelatine) and brain tissue (Brain), and picture of freshly excised brain resting on table, heavily deformed under its own weight by gravity (b). Graphic from (a) is reproduced from Leibinger et al. [142]. Image of the human brain (b) is a still extracted from a YouTube video featuring an autopsy at the Banner Sun Health Research Institute [143].

One negative aspect of the CH, however, is that its material properties are heavily influenced by the thermal environment during thawing [144], and as such, it can be difficult to work with. Yet, this also provides a second means to tune the materials properties, the primary route being the adjustment of PVA, PHY and Di H_20 concentration.

4.2 Brain-Skull Tissue Simulants

4.2.1 Brain Tissue Simulants

The CH is but one of many identified brain tissue simulants. Other established brain simulants for brain shift/deformation include gelatine hydrogels, agarose hydrogels, phytagel hydrogels, hyaluronic acid hydrogels, PVA hydrogels, oil emulsion organogels, silicones, polyurethanes and various composites of the preceding materials where compatible. However, these all fall short in at least one of the three required properties for use in an SAS featuring phantom made through the traditional assembly route: loading response, density and strain to failure.

- As weak brittle materials, the gelatine, agarose, phytagel and hyaluronic hydrogels would unlikely survive the extracranial handling required in assembling a SAS featuring phantom. They also do not exhibit the same bimodal viscoelastic/ poroelastic behaviour as brain tissue [57].
- The PVA hydrogels have a high strain to failure and similar density to brain tissue, however, as pointed out by Forte et al. these materials do not quite match the elastic behaviour of brain tissue [57].
- Silicones such as 527 Sylgard will elastically undergo strains similar to the CH and usually much higher, however, they are often exceedingly sticky when mixed such that they have brain tissue level stiffness, making them difficult materials to handle in brain format. They are also not poroelastic [57] and have densities less than water, meaning that a fluid with even lower density would be required to fill the SAS when using a silicone brain. If a non-water fluid is then used, the phantom becomes difficult to image with MRI due to artifacts such as the chemical shift artifact.
- The polyurethanes suffer from the same set of problems as the silicones, but tend not to produce sticky surfaces that are difficult to handle.
- The oil emulsion organogels offer high strain to failure and similar loading response [136], but present with a problematic density. With a significant part of their composition being oils, the density of these materials is invariably less than that of water. Furthermore, the high oil content is likely to make the material incompatible with MRI based deformation / shift measurements (due to imaging artifacts).

The CH, therefore, presents as the most suitable established surrogate for brain tissue in an SAS featuring phantom, again assuming established assembly methods. Yet, if a method could be devised to cast the brain inside the skull while maintaining the SAS, more options would be freed up to act as the brain simulant. The fabrication of an assembly free phantom is explored in Section 5.2 (p64).

4.2.2 Meningeal and Cranial Simulants

To the author's knowledge, no phantoms have been produced which attempt to faithfully recreate the PAC, dura or dural septa. The phantom by forte et al. included a rudimentary version of the falx cerebri, however, this was just an extension of the plastic skull. Synthetic dural grafts have been developed, yet, they are not castable or 3D printable materials and would, therefore, be difficult to form into the complex shape of the dural septa.

In terms of skull recreation, most phantoms simply use a rigid 3D printable plastic, which is certainly sufficient in the context of creating a phantom for PBS.

4.3 Chapter Summary

The review of phantoms presented in this chapter reveals an absence of suitably complex phantoms for the study of PBS. The building of such a phantom, therefore, presents as a truly novel endeavour.

Due to its unique combination of properties, the CH material developed by Forte et al. was identified as the only suitable established brain simulant for use in an SAS featuring phantom, assuming established assembly methods.

Now that the system is understood, the event to be modelled is understood and a review of the phantom literature has been performed, the phantom design can begin. This is presented in the next chapter.

5 PHANTOM DESIGN

The previous chapter included a literature review of brain shift/deformation phantoms in the literature. Introduced by Figure 5.1, this chapter details the development of two model designs and contains the following novel work:

- An assessment of which tissues and features should be replicated in a PBS simulating phantom.
- The development of a tethered model design.
- The development of a secondary non-tethered model design.
- An analysis and comparison of each design's limitations.

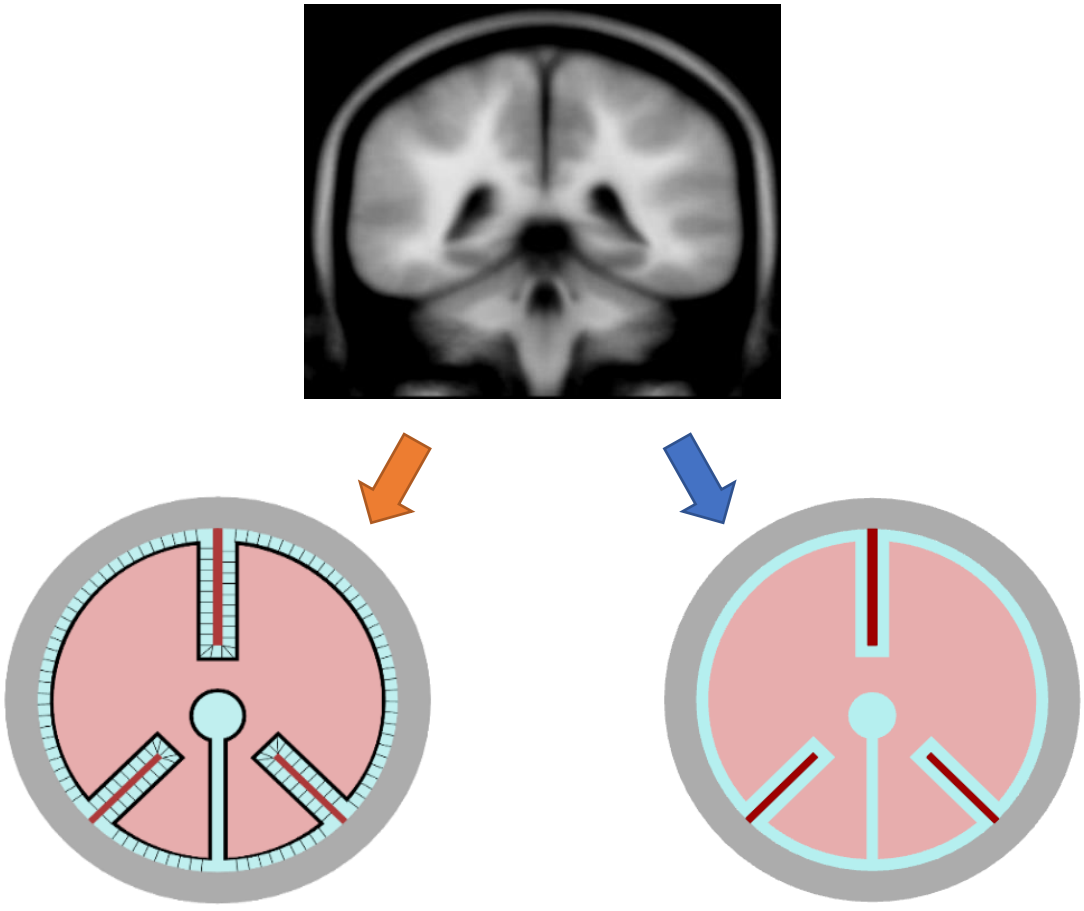

Figure 5.1: Chapter storyboard showing the development of two model designs. Images are reshown and discussed later in the chapter.

5.1 Identification of Important Mechanical Features

The brain-skull system is incredibly complex and impossible to recreate entirely with contemporary manufacturing technologies. Unlike our fabrication methods, which are largely additive or subtractive in nature, biological systems come with the ability to progressively differentiate and grow tissues *in situ*, which allows for the generation of complex material systems without assembly. Unfortunately, this means that some concessions need to be made in order to fabricate a model using current available methods.

Although many tissues make up the brain-skull system, not all need to be faithfully reproduced to build a realistic mechanical model. Whilst a mixture of cortical and cancellous bone, the skull, for example, can be reproduced with any sufficiently rigid material to replicate its function as an inflexible, shape-preserving container for the brain.

The purpose of this section is to best identify which tissues, structures and features are necessary in a phantom to reproduce the PBS event and where, if possible, concessions can be made.

5.1.1 Mechanical properties of the Brain

As identified in Section 2.4.1 (p23) there is insufficient evidence to warrant the inclusion of regional differences or anisotropy in a phantom for PBS simulation. It is therefore reasonable to use a single homogenous material to recreate the mechanical properties of the brain under gravitational loading. However, this material should ideally have the following properties:

1) Density within the 1.03 to 1.08 g/cm^3 range.
2) Stiffness within the 0.3 to 3.0 kPa range.
3) Realistic loading profile at medium and low strain rates.
4) Sufficient porosity to allow fluid egress on loading.

The first requirement, when paired with a CSF with density of 1.00 g/cm^3, ensures the correct loading of the brain under gravity, while the second, third and fourth ensure the correct loading response/deformation.

The fourth requirement, in particular, ensures that the brain can exchange fluid within its body and with the fluid in the subarachnoid/ventricular spaces. This is likely an important feature to recreate, as Schnaudigel et al. [123] observed PBS to take longer than 12 minutes to complete, suggesting that a longer timescale poroelastic deformation occurs as part of shift in PBS.

5.1.2 The External Geometry of the Brain

The external geometry of the brain is convoluted and difficult to reproduce with soft brain tissue surrogates. Although previous groups have managed to successfully mould the sulci of the brain for studies of the cerebrum alone [135,136], one can argue that it is more appropriate to reduce the depth of the sulci when approximating the mechanical operation of the closed brain-skull system. This is because in the biological brain the sulci spaces are occupied by vascular tissue which is tethered to the flanking gyri walls by the arachnoid trabeculae mesh (see Figure 2.12e, p17). Thus, in lieu of recreating the complex gyri-vessel-gyri tethering, it seems more appropriate to fill the sulci space with extra brain material rather than leaving them empty.

Similarly, the Sylvian fissures, which separate the frontal and parietal lobes from the temporal lobe on each side of the brain, harbour the middle cerebral artery, which is again tethered to the walls of the surrounding brain tissue by the arachnoid trabeculae (see Figure 2.12g-h, p17). Thus, within this region there is also tissue-vessel-tissue tethering, which could again be simplified by filling the fissure space with extra parenchymal material.

The medial longitudinal fissure and the transverse cerebral fissure exist as spaces for the falx cerebri and tentorium cerebelli, respectively, to occupy and cradle the brain. These are important mechanical features that are likely to be needed to recreate the correct mechanical response of the brain to gravitational loading.

5.1.3 The Internal Geometry of the Brain

If it is assumed that the communication between the ventricles and SAS is such that CSF can freely flow out of the ventricles into the SAS (see Section 2.1.4, p11), then the ventricles can be considered compressible. However, even if purely incompressible, the cavity would still allow redistribution of brain volume via shape deformation of the cavity. Therefore, it is likely to be important that these fluid filled spaces are reproduced to accurately simulate PBS.

5.1.4 The Pia-Arachnoid Complex

The PAC plays an important role in the mechanical operation of the brain, however, its geometry can be simplified without compromising its function in the context of gravitational loading.

Being only a few microns thick and contiguous with the dura mater, the substitution of the arachnoid mater for additional skull material is unlikely to influence the deformation of the brain. The pia mater and arachnoid trabeculae, however, act to tether the brain to the skull and thus restrict overall boundary motion of the brain within the cranial cavity. Thus, it is

likely to be important that the pia mater and arachnoid trabeculae are reproduced in some capacity in the model such that the tethering action is recreated.

A tractional stiffness in the range of 61-148 kPa should be achieved in the PAC recreation, alongside a shear stiffness in the range of 11-22 kPa (see Section 2.4.2, p30). Given the absence of data on the tensional stiffness of the pia alone, the lower end of the PAC's tensional stiffness range (6-40 MPa) could be assumed, erring on the side of underrepresenting the stiffness. Yet, given the difficulty of fabricating a precise 15 μm layer around the brain, it is likely that a thicker membrane will have to be used and, consequently, a lower material stiffness will be needed to maintain the correct flexibility of the layer.

The CSF present in the SAS acts to damp movements of the brain within the cranial cavity and provide a general buoyancy force that significantly reduces its otherwise deleterious weight from approximately 1.4 kg to 40-100 g (see Section 2.4.1, p23). Reproducing the CSF is undoubtedly important in the creation of a PBS simulating phantom and a CSF simulant with a density close to 1.00 g/cm^3 should be chosen to recreate the correct density differential.

5.1.5 The Dural Septa

While the dural septa present as important mechanical features for the restriction of brain movement in the cranial cavity, the remaining dural tissue exists as a thin (~1 mm) stiff sheet of material (approximately x5000 stiffer than brain tissue), adherent to the skull, which is unlikely to influence the deformation of the brain under gravitational loading. Thus, it is reasonable to suggest that this layer of the meninges could be reproduced as skull material for the sake of simplicity.

Given their prominence, stiffness and the manner in which they project into the brain (see Figure 2.15, p21), however, it is reasonable to suggest that the falx cerebri and tentorium cerebelli significantly influence the movement of the brain under gravitational loading and therefore should be reproduced in the phantom. The falx cerebelli and diaphragm sellae, however, present as considerably lesser structures, and so their reproduction is likely not to be necessary. A stiffness in the region of 70 MPa should be recreated in the dural septa (see 2.4.3, p31).

5.1.6 The Skull

While it is important to faithfully reproduce the geometry of the cranial cavity to simulate PBS, it is not necessary to reproduce the exact geometry or mechanical property variation within the body of the skull. Reproducing the skull in any sufficiently rigid material (stiffness in the GPa range) will replicate its function as an inflexible, shape-preserving container for the brain.

5.1.7 Summary

Shown in Table 5.1 is a summary of the features identified in the previous sections which are likely necessary to accurately simulate PBS in a brain-skull phantom. Together, they represent a much higher complexity than that found in previous phantoms.

Table 5.1: Features identified as necessary to replicate in a PBS simulating phantom.

Brain	*Geometry*	• All parts: cerebrum, cerebellum and brain stem. • Medial longitudinal fissure space. • Transverse cerebral fissure space. • All ventricular spaces. • Reduced sulci spaces.
	Mechanical Properties	• Homogenous and isotropic throughout. • Density within the 1.03 to 1.08 g/cm^3 range. • Stiffness within the 0.3 to 3.0 kPa range. • Realistic loading response at medium and low strain rates. • Sufficient porosity to allow fluid egress on loading.
PAC	*Geometry*	• Complete fluid filled subarachnoid space which is continuous with the ventricular spaces. • Complete pia layer. • Pia to skull tethering.
	Mechanical Properties	• CSF with density equal to 1.00 g/cm^3. • Pia with stiffness in the region of 6 MPa • Brain-skull tethering with tractional and shear stiffness in the ranges of 61-148 kPa and 11-22 kPa, respectively.
Dural Septa	*Geometry*	• Complete falx cerebri. • Complete tentorium cerebelli.
	Mechanical Properties	• Stiffness in the region of 70 MPa.
Skull	*Geometry*	• Complete neurocranium.
	Mechanical Properties	• Stiffness in the GPa range.

5.2 Forming a Tethered Model Design

This section details the attempt that was made towards forming a design that contained all the necessary features identified in the previous section, including the brain-skull tethering.

5.2.1 Identification of Fabrication Route

Recreating the complex relationship between the skull, dural septa (DS), PAC and brain with contemporary fabrication technologies is a difficult task and it was identified that it cannot be achieved through manual assembly of separately made model parts (traditional assembly route). The only feasible approach identified was to 3D print the skull, dural septa and PAC in a single print using a multi-material printer and to cast a brain surrogate into the printed model (Figure 5.2). In this workflow, the internal surface of the PAC (the pia) acts as the moulding surface in casting the brain.

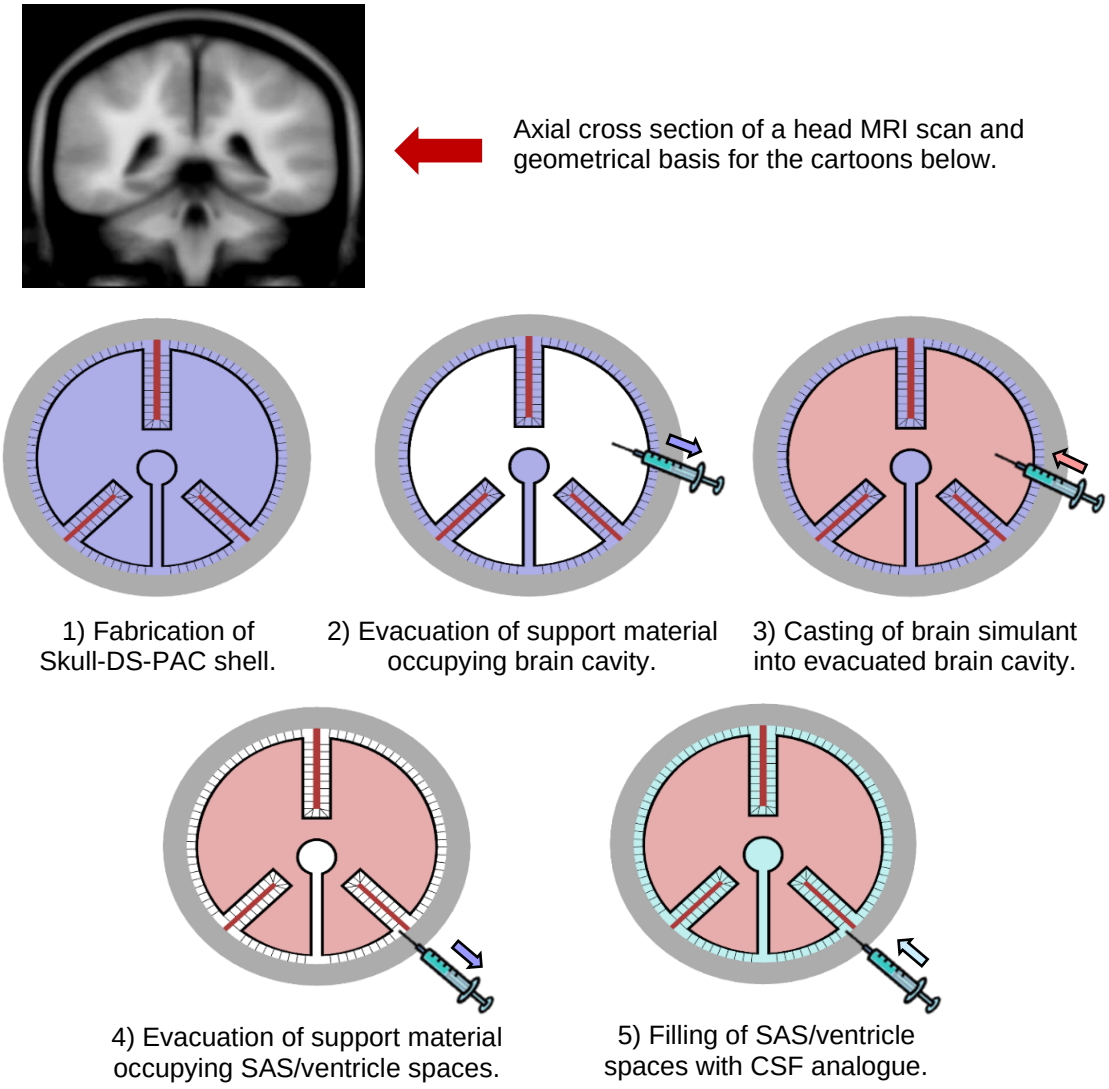

Figure 5.2: Identified workflow for the production of a tethered model. Dissolvable printing support is shown as purple; empty spaces are shown as white. Skull is shown in grey, pia and tethers in black, dural septa in red, CSF in blue and brain in pink.

For such a fabrication route to be viable, the printer needs to be capable of printing both rigid and soft materials and to utilise a support structure that can remain in the part whilst the brain is cast inside, but easily dissolved away once the support is no longer needed, such that it can be replaced with liquid to act as the CSF.

Illustrated in Figure 5.2 is the identified production workflow. First, the Skull-DS-PAC shell is built using a multi-material printer. Next, the support material occupying the brain cavity is evacuated and replaced with a brain simulant. Finally, to complete the model, the support material is evacuated from the SAS of the part and replaced with liquid.

5.2.2 Identification of Fabrication Technologies and Materials

5.2.2.1 The Skull-DS-PAC Part

Using a Connex multi-material 3D printer, it was identified that one could theoretically 3D print the Skull-DS-PAC part proposed in Section 5.2.1 in a single build, limiting geometrical error in fabrication to the dimensional accuracy of the printer.

The Connex line of Objet 3D printers (Polyjet technology) have the ability to print multiple materials in the same build such that they fuse together into a single part with discretely varying mechanical properties. They achieve this by blending two different photopolymers together at the point of deposition and UV curing the blend *in situ* alongside other deposited material. Similar to a traditional ink-jet printer, different blends can be deposited in different areas in a pixel-wise fashion. An example of properties attainable through the blending of primary and secondary photopolymers can be seen in Table 5.2. The primary and secondary materials themselves can also be printed individually.

Table 5.2: Mechanical properties of printed materials achieved through blending of primary and secondary photopolymers at the point of deposition. Here, Tangoblackplus (TB+) is the primary material and Veroclear (VC) is the secondary. In between these, vertically, are the blends (with FLX designation). Values taken from Reference 145.

Material	Tensile Strength (MPa)	Elongation at Break (%)	Shore Hardness	Tensile Tear Resistance (kg/cm)
TB+	0.8-1.5	170-220	A26-28	18-22
FLX9040	1.3-1.8	110-130	A35-40	5.5-7.5
FLX9050	1.9-3.0	95-110	A45-50	7.5-9.5
FLX9060	2.5-4.0	75-85	A57-63	11-13
FLX9070	3.5-5.0	65-80	A68-72	15.5-17.5
FLX9085	5.0-7.0	55-65	A80-85	23-25
FLX9095	8.5-10.0	35-45	A92-95	41-44
VC	50-65	10-25	D83-86	-

Considering the available simplifications discussed in Section 5.1 (p60), the layer system illustrated in Figure 5.3 was designed. Here, the dura and arachnoid are replaced as further skull material, instead having the arachnoid trabeculae attach directly to the skull or dural septa. Given the accuracy (~1 mm minimum feature size) of the Polyjet technology, the arachnoid trabeculae are reproduced as a fewer number of 1 mm diameter, gap-spanning tethers, spaced approximately 3 mm apart, attached to a 1 mm thick pia.

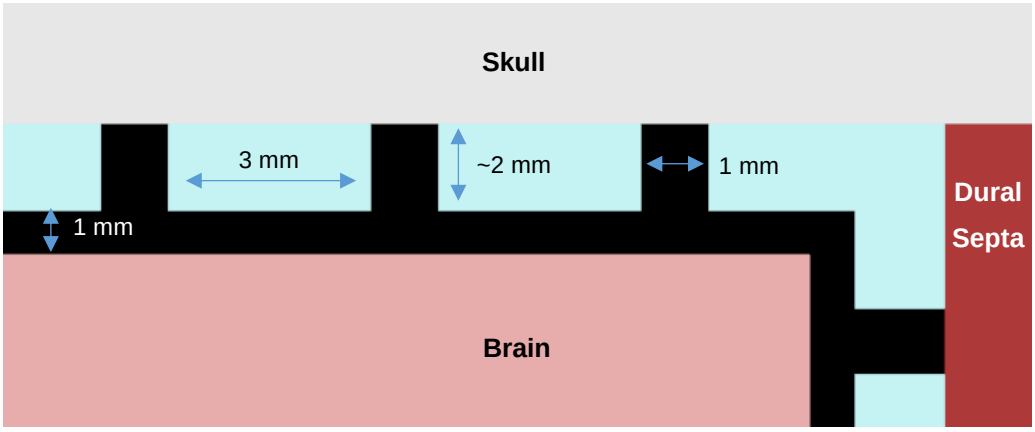

Figure 5.3: Layer system designed for the tethered model. SAS width is dictated by the anatomical width and therefore variable.

Assuming a constant SAS breadth, cylinders of 1 mm diameter spaced 3 mm apart achieves a material volume fraction of ~5%. When this fraction is applied to the nominal elastic modulus of the Tangoblack plus (TB+) material (~1 MPa), calculated using the Gent shore hardness conversion equation (Equation 5.1) (E = Young's modulus; s = shore A hardness) [145] and data from Table 5.2, an approximate tractional elastic modulus of 50 kPa is achieved. Similarly, by applying the 5% fraction to the TB+ materials shear modulus (G) (~0.33 MPa), calculated using Equation 5.2 (E = 1 MPa; Poisson's ratio, v = 0.5), an approximate shear modulus of 17 kPa is achieved. These values are within or sufficiently close to the ranges calculated by Jin et al. (61-148 kPa for tractional stiffness; 11-22 kPa for shear stiffness).

$$E\ (MPa) = \frac{0.0981(56 + 7.66s)}{0.137505(254 - 2.54s)} \tag{5.1}$$

$$G\ = \frac{E}{2(1 + v)} \tag{5.2}$$

With the minimum printing feature size (1 mm) being approximately 66 times greater than the pia's thickness (~0.015 mm), however, it was identified that an unrealistically stiff pia layer would have to be included. If softer materials were available, one could be chosen to account for the larger thickness, yet, the least stiff available Polyjet material (TB+, ~1 MPa stiffness) was identified as being in the same region of stiffness as the pia to begin with. Given that a pia is required in this design as both the casting container and the

tethering interface for the brain, the layer could not be removed from the design and so a 1 mm thick TB+ pia layer had to be selected. This was identified as a significant limitation of the design and is discussed further in Section 5.2.3. (p68).

For the dural septa, the FLX 9095 material was identified as a suitable surrogate, given its likely sufficient approximate elastic modulus of 33 MPa. Similarly for the skull, as a rigid plastic with a nominal elastic modulus of 2-3 GPa, the Veroclear material (VC designation) was identified as a suitable surrogate.

5.2.2.2 The Brain and CSF Simulant

In addition to the issues surrounding the pia, a further set of limitations were also encountered when it came to selecting the brain tissue surrogate. Ideally the CH would have been chosen, due to its high mechanical similarity to brain tissue (see Section 4.1, p52) across the properties identified as being necessary for simulating PBS, however, it was identified that the simulant would not be useable in this design for three reasons:

1. The curing process of the material needed to be compatible with the Skull-DS-PAC part (i.e. no freeze-thaw expansion).
2. The material needed to be long-lasting since the part can only be cast into once due to the fabrication workflow (the CH degrades after a few weeks).
3. The casting viscosity needed to be such that a suspension of markers can be achieved for the imaging of brain shift (as markers cannot be strung up inside the Skull-DS-PAC part).

Given these three critical requirements, 527 Sylgard silicone was identified as the only suitable established brain simulant for this design. This silicone is reported to be similar to brain tissue in compression at medium strain rates (0.83 mm/s), yet at quasi-static strain rates (0.00083 mm/s), it presents as a much stiffer material, with compressive stress at 0.3 strain being approximately four times higher than brain tissue [57]. This is partly because 527 Sylgard is not poroelastic and therefore unable to accurately capture the low strain rate loading response or relaxation behaviour of brain tissue. This is also further discussed in Section 5.2.3 (p68).

Nonetheless, with a forced selection of 527 Sylgard as the brain simulant (density of ~ 0.970 g/cm^3), it was next identified that the use of olive oil (density of ~ 0.920 g/cm^3) as the model's CSF would create a density differential of approximately 0.05 g/cm^3, which is within the identified biological range of 0.03 to 0.08 g/cm^3.

For the brain shift makers it was identified that a suspension of high impact polystyrene beads (density of ~ 1.030 to 1.060 g/cm^3) could likely be achieved in the silicone brain

(density of ~ 0.970 g/cm^3) to act as the imaging markers. These could be mixed in during casting and would likely stay suspended due to the high viscosity of the silicone.

5.2.3 Design Limitations

In attempting to make an all-inclusive design, it was discovered that the brain-skull tethering could not be recreated without reducing realism elsewhere in the pia and the brain. Specifically, it was found that the pia would have to be much thicker than in the anatomy and that the brain would have to be made using a silicone simulant that doesn't quite match the behaviour of brain tissue at low strain rates.

Having a pia with 66 times the thickness of the anatomical layer runs the risk of producing a model with an overly stiff brain boundary and, therefore, the risk that the model will not be able to reproduce the non-rigid element of PBS. Reproducing the brain in a material which does not redistribute fluid under load (like silicone) then also further increases the risk the brain will not deform realistically.

On the other hand, however, the omission of the PAC runs the risk that too much brain shift will occur in the form of rigid displacement. This is because, here, the brain motion is not restricted by the tethers at the top of the orientation (with respect to gravity), nor by the solid fraction of the SAS at the bottom of the orientation, and the brain is completely free to move in and out of the SAS. Thus, it was not clear that the omission of the PAC would be overall beneficial.

One other significant limitation was identified with the design, but in its practicality, rather than its ability to reproduce PBS. This was that the brain of the phantom cannot be replaced, since once the support material has been extracted out of the SAS, the PAC becomes deformable and cannot be used to re-cast the brain. This heavily restricts repeatability, as the cost of producing multiple large 3D printing builds with state-of-the-art technology is excessive.

5.3 Forming a Secondary Non-Tethered Model Design

In the previous section it was discovered that, to include the brain-skull tethering, significant concessions needed to be made in the realism other equally important model elements. It was not clear, however, that the concessions outweighed the inclusion of the PAC.

To account for this uncertainty, it was decided that a secondary non-tethered model would be designed. This secondary design would run the risk of over producing the rigid component of brain shift under gravitational loading, but would not run the counter risk of under producing the non-rigid component as in the tethered model design.

This section details the formation of a secondary non-tethered model design.

5.3.1 Identification of Fabrication Route

By omitting the tethers and pia and absorbing the dura and arachnoid into the geometry of the skull, it was identified that the model's components could be reduced to the skull, dural septa, fluid filled SAS and brain (see Figure 5.4). A key benefit of this simpler arrangement is that it permits the separate production of parts, allowing for them to be made out of a greater range of materials, including the biofidelic CH material for the brain.

While the fabrication route for the tethered model design was constraining with respect to material choice, it did side-step the problem of separately moulding a soft fragile brain and locating it into the skull without damage. This is a situation that becomes increasingly difficult when one considers the inclusion of the dural septa.

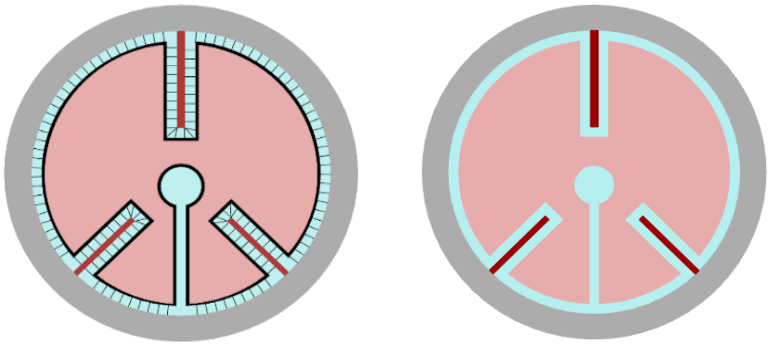

Figure 5.4: Comparison of elements present in the tethered (left) and non-tethered (right) model designs. Skull is shown in grey, pia and tethers in black, dural septa in red, CSF in blue and brain in pink.

Given the manner in which the dural septa compartmentalises the skull (Figure 2.15, p21), it was identified that it would not be possible to make a brain separately and introduce it into the skull with dural septa already attached. The only feasible route to fabrication that was identified, therefore, was to mould the brain separately, feed the dural septa into its fissures and transport the two into the skull simultaneously, using features to locate and fix the dural septa into its correct position.

Illustrated in Figure 5.5 (p70) is the mechanism which was devised for the location of the dural septa and brain into position in the skull. Here, cord is weaved between tabs added to the dural septa and corresponding sockets engineered into the skull. Once the brain has been cast and combined with the dural septa, the cord is pulled tight, drawing the dural septa tabs into their respective sockets and simultaneously locating all three solid elements of the model together.

Considering the realistic density, loading response and strain to failure of the CH (see Section 4.1, p52), it made sense to utilize the material over the other established brain simulants discussed in Section 4.2.1 (p57) for the model's brain. Given its casting profile, an expandable brain mould was required. This mould needed to be capable of moulding the complex external and internal geometry of the human brain.

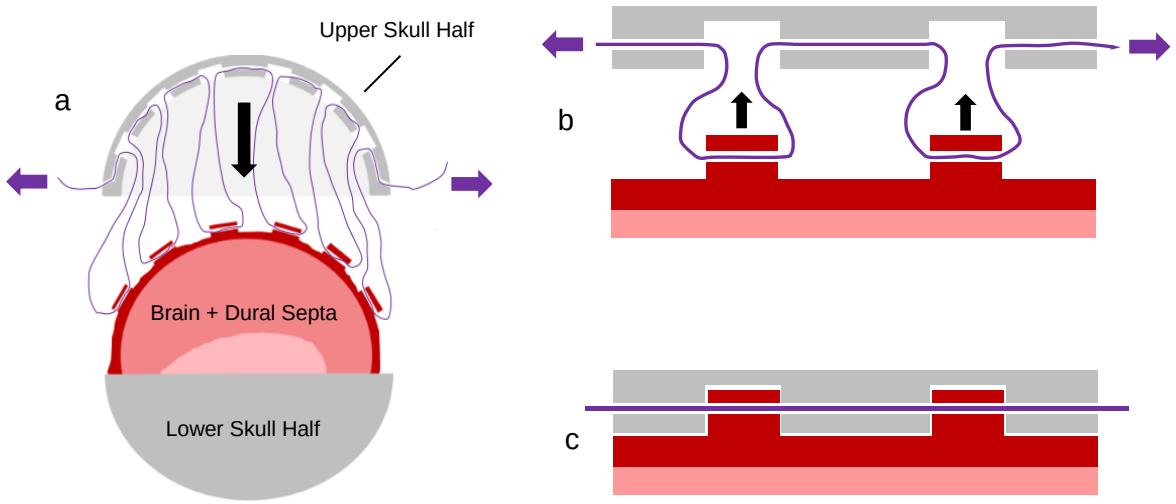

Figure 5.5: Cartoon representation of suggested dural septa and brain locating mechanism. a) sagittal cartoon of upper skull half and dural septa with brain being located together via interweaving cord tightening mechanism (with brain and dural septa already located in lower skull half via same mechanism); b) close-up of mechanism prior to cord tightening; c) close-up of mechanism following cord tightening.

Illustrated in Figure 5.6a (p71) is the initial mould design which was developed. This design consisted of two expandable silicone halves which contain slots for the attachment of rigid inserts. In this setup, the silicone halves provide for the moulding of a majority of the brain's external shape and the overall expansile capability of the mould, while the rigid inserts allow for the moulding of the fissures and the ventricles. Due to the complex shape of the ventricles, the insert defining this structure needed to be dissolvable and so the ventricle insert (gold) was designed to be formed form sugar glass and would be coated such that the CH casting solution does not dissolve the insert from within. It was identified that the fissure inserts (green) could be fabricated out of any sufficiently rigid plastic.

In this setup, when the hydrogel is poured into the cavity containing the inserts and placed in a freezer, the brain freezes around the inserts such that they become trapped (Figure 5.6a-c). At this stage, the solid brain with trapped inserts is removed from the mould (Figure 5.6d) and thawed in a bucket of water that supports the brain as it becomes soft and fragile. By positioning the frozen brain under a cap rigidly affixed to the bucket and placing the entire apparatus in an incubator (Figure 5.6e), the thawing rate is controlled. Once thawed, the fissure inserts are then physically removed and the ventricle insert is dissolved into the bucket's water, leading to a fully formed hydrogel brain with realistic fissure and ventricular spaces (Figure 5.6f).

With the brain ready for assembly, the dural septa is then combined with the brain and positioned into the skull using the aforementioned locating mechanism (Figure 5.6g-h). By doing this underwater in the bucket, a portion of the water is naturally scooped into the skull on assembly, acting as the model's CSF.

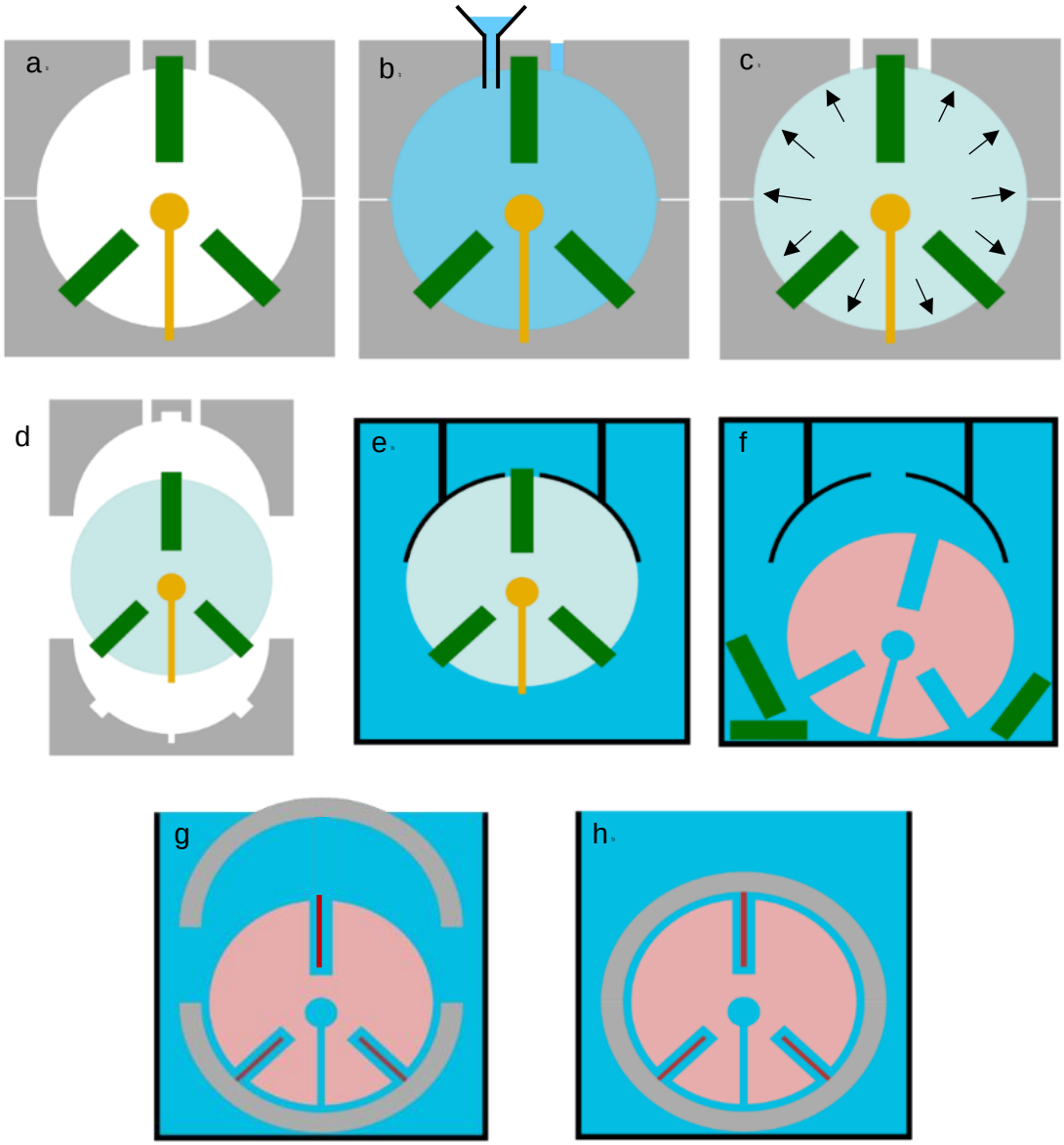

Figure 5.6: Suggested workflow for the production of the non-tethered model. a) assembled composite mould comprising expandable silicone halves (grey), rigid fissure inserts (green) and dissolvable ventricle insert (yellow); b) mould filled with hydrogel solution (blue); c) frozen mould with expanded frozen hydrogel solution (light blue); d) removal of frozen hydrogel together with trapped inserts; e) frozen hydrogel (light blue) with trapped inserts centered in bucket of water (blue); f) thawed hydrogel (pink) with freed/dissolved fissure and ventricle spaces; g) introduction of the thawed hydrogel into the skull (grey) with dural septa (red); h) completed model.

5.3.2 Identification of Fabrication Technologies and Materials

As discussed in Section 4.1 (p52), the CH presents as the best candidate for the brain simulant in an assembly phantom. The *[3.00% PVA : 0.43% PHY : 96.57% DI H_20]* formulation serves as a good starting point in obtaining the correct hydrogel stiffness, but it was identified that some experimentation would likely be required due to the materials dependency on thawing rate and the uncertainty in brain mechanical properties (identified in Section 2.4.1, p23).

With a density of 0.988 g/cm^3 [147], it was recognized that the use of deionised water as the model's CSF would create a density differential of only 0.017 g/cm^3, which is somewhat lower than the reported biological range of 0.03 and 0.08 g/cm^3. However, it was decided that additives could likely be added to either the brain formulation or the deionised water to raise the density differential, if necessary. This can be easily done with the design as the model can be freely disassembled and then reassembled with exchanged model parts.

Unlike for the silicone brain of the PAC featuring design, it was identified that a suspension of brain shift markers would be difficult to achieve due the lower casting viscosity of the CH. It was recognized, therefore, that markers would need to be positioned in the mould using a combination of lines strung across the cavity and rods cantilevered off of the mould walls. These positioning tools would need to be removable from the brain when thawed.

For the skull and dural septa, it was decided that the materials selected for the PAC featuring design remained suitable. These were the Veroclear material for the skull and the FLX 9095 material for the dural septa.

5.3.3 Design Limitations

In the tethered model design, the error in the fabrication of the SAS's geometry is limited to the dimensional accuracy of the printer (micron scale accuracy). However, in the non-tethered model design, the parts must be made separately with different technologies and assembled together, undoubtedly increasing the error. Having a smaller or larger SAS is highly likely to influence the extent of brain shift in a model, especially in one lacking the PAC. However, the separate production of all model parts means that each element can be reproduced if re-selection of material is required, adjustments are needed, or if damage occurs. Therefore, changes can be made to any of the parts to adjust their spatial relationships with one another.

The other limitations are that the non-tethered model design does of course not feature the pia layer boundary or the brain-skull tethering. The former may result in the brain undergoing excessive deformation at its surface, while the latter may result in the brain undergoing excessive levels of rigid shift.

5.4 Chapter Summary

Presented in this chapter has been an assessment of the features required to build a PBS simulating phantom, followed by the presentation of two model designs: a tethered model design and a non-tethered model design. Both designs and their associated fabrication workflows present as novel works, with complexity beyond those found in the literature (see Section 4.1, p52).

The tethered model design was created first, with the intention to include all mechanically important elements identified for the successful creation of a PBS simulating phantom. This included the brain-skull tethering, whose presence influences the mobility of the brain's surface and, therefore, the entire brain.

A novel design and fabrication workflow were identified for the production of a tethered model, however, it was discovered that in order to achieve the brain-skull tethering, significant concessions had to be made in the realism of the pia and the brain. The pia layer had to be made 66 times thicker than the anatomical layer (due to limitations of the necessary 3D printing technology), while the brain had to be made out of a silicone brain simulant that doesn't quite match the behaviour of brain tissue at low strain rates (due to *in situ* casting requirements). For the overly thick pia, it was identified that the brain boundary could end up being unrealistically stiff, leading to lower levels of non-rigid brain shift occurring in the model. Similarly, for the silicone brain, it was identified that the brain may not undergo realistic poroelastic deformation, again leading to lower levels of non-rigid brain shift.

However, it was not clear that these concessions outweighed the benefit of including the brain-skull tethering, since it was identified that its absence in a model runs a counter risk of too much rigid brain shift occurring due to free movement of the brain in and out of the SAS. To account for this uncertainty, it was decided that a secondary non-tethered model would be designed, with the aim to build both and compare their PBS simulating capacity.

It was identified that this second model had to be built through the traditional assembly route, which meant the development of a novel elaborate workflow for the separate production and subsequent assembly of individual parts. This, however, opened up the use of the biofidelic CH material identified in Chapter 4 and, without a pia layer, removed the risk of an over stiff brain boundary.

With two designs prepared, the next chapter details their construction. Here, it will be seen that there were problems in the fabrication of the Skull-DS-PAC part with the Polyjet technology.

6 PHANTOM CONSTRUCTION

The previous chapter identified two model designs for fabrication. Introduced by Figure 6.1, this chapter details the complete construction of the non-tethered model design and the steps taken towards fabricating the tethered model design. The following novel work is contained:

- The acquisition of realistic anatomical geometries from an averaged MRI dataset for the fabrication of the models.
- The computational design and subsequent production of the composite brain mould, thawing apparatus, dural septa and skull parts, described in Section 5.3, for the fabrication of the non-tethered model.
- The fabrication of the non-tethered model using the moulds, parts and workflows described in Section 5.3.
- The computational design and subsequent prototyping of the Skull-DS-PAC part described in Section 5.2, followed by the rationale for the abandonment of the tethered model.

Figure 6.1: Chapter storyboard showing casting of the non-tethered model's brain with the composite brain mould (left), the non-tethered model's formed brain with dural septa (middle) and assembled non-tethered model (right). Images are reshown and discussed later in the chapter.

6.1 Acquisition of Base Anatomical Geometries

The first step in fabricating the models was to acquire computational models of the brain, SAS, dural septa and skull. This section details the methods that were used to obtain them.

6.1.1 Sourcing the Anatomical Geometries

The MNI ICBM152 Average Brain Stereotaxic Registration Model (McConnell Brain Imaging Centre, Montreal Neurological Institute, McGill University) [148] was identified as being a suitable source for the geometries. This dataset is an average of 152 co-registered (spatially aligned) MRI scans (see Figure 6.2). Therefore, its use mitigates against irregularities that can arise in a single dataset due to patient specific geometry and/or sources of error in scanning (e.g. head orientation or patient motion in scanner). Furthermore, the use of the MNI ICBM152 datasets can be found in many projects concerning the development of phantom and *in silico* models of the brain-skull system [149,150,151].

Using image segmentation, models of the brain, SAS, dural septa and skull were extracted from the dataset. This was done primarily by the member of the brain shift research group developing the *in silico* model (Nicholas Bennion), with input from the author, using Simpleware ScanIP (Synopsys, Cradleain View, USA). To make the phantom and computer models as comparable as possible, the parts were segmented such that the same geometries could be utilised in both the synthetic model presented here and the concurrently developed *in silico* model.

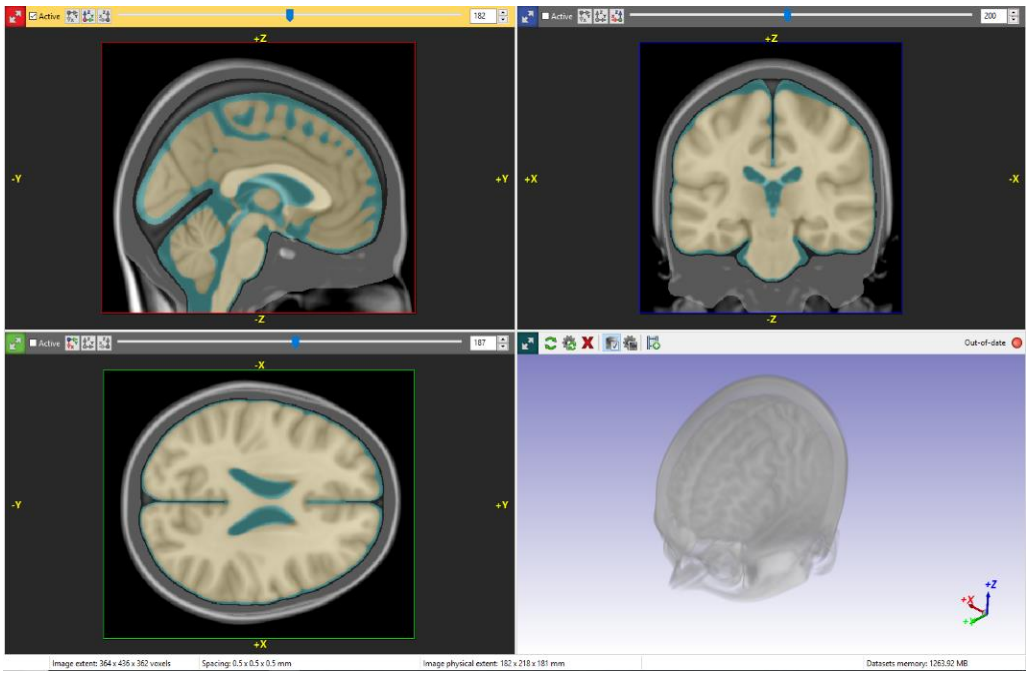

Figure 6.2: Segmentation of the MNI ICBM152 dataset's brain (yellow) and SAS/Ventricles (turquoise) in ScanIP.

Given that the MNI ICBM152 dataset was built through a combination of 152 co-registered supine scans, it was identified that the geometries extracted would be that of the brain-skull elements in a supine deformed state. However, as gravity cannot be abolished in MRI imaging, this prevented as an unavoidable limitation of this project.

The following sections further describe the segmentation process.

6.1.2 Segmentation of the Brain

The brain was segmented in a manner such that large fissures and cisterns were preserved, while the prominence of the sulci spaces were reduced (see Figure 6.2). The sylvian fissures were filled in as additional brain volume and the ventricles were artificially dilated and/or simplified in areas to make them more fabricable (see Figure 6.3). The posterior horn and inferior horn of the lateral ventricles could not be segmented due to loss of definition in the averaged dataset. The average dataset also contained an enlarged interthalamic adhesion (the tunnel located in the body of the third ventricle - see Figure 6.3); this was included in the segmentation.

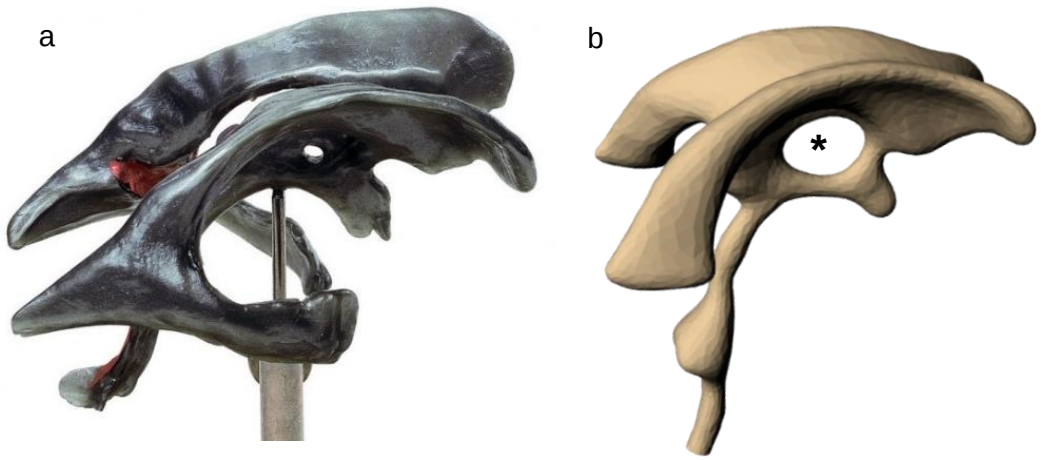

Figure 6.3: Comparison of segmented ventricles to commercial model. a) commercial model produced using a resin cast specimen (reproduced from Reference 152); b) ventricles segmented from the MNI ICBM152 dataset. Asterix indicates enlarged interthalamic adhesion.

6.1.3 Segmentation of the Dural Septa

The falx cerebri, cerebellar tentorium and the tentorium cerebelli were segmented as a single body (see Figure 6.4i-j). The diaphragm sellae was omitted for simplicity. To make the falx more fabricable, a large portion of the segmented structure was dilated and smoothed into a flat, 1.5 mm thick, vertical sheet. The cerebellar tentorium and tentorium cerebelli were segmented as they appeared (i.e. no alterations). Due to ill-definition of the anterior skull attachment point of the cerebellar tentorium, an estimation was made using artistic interpretations within the literature.

6.1.4 Segmentation of the Skull

The skull was segmented as it appeared in the dataset. Minimal smoothing was applied so as not to smooth away regions of the SAS. However, following segmentation, the generated skull mesh was imported into version 5 of the computer aided design (CAD) software Rhino (McNeel Europe) and disassembled into surface meshes defining the outer surface of the skull and the cranial cavity. The outer surface mesh was further smoothed for purely aesthetic purposes and subsequently recombined with the unaltered cranial cavity mesh.

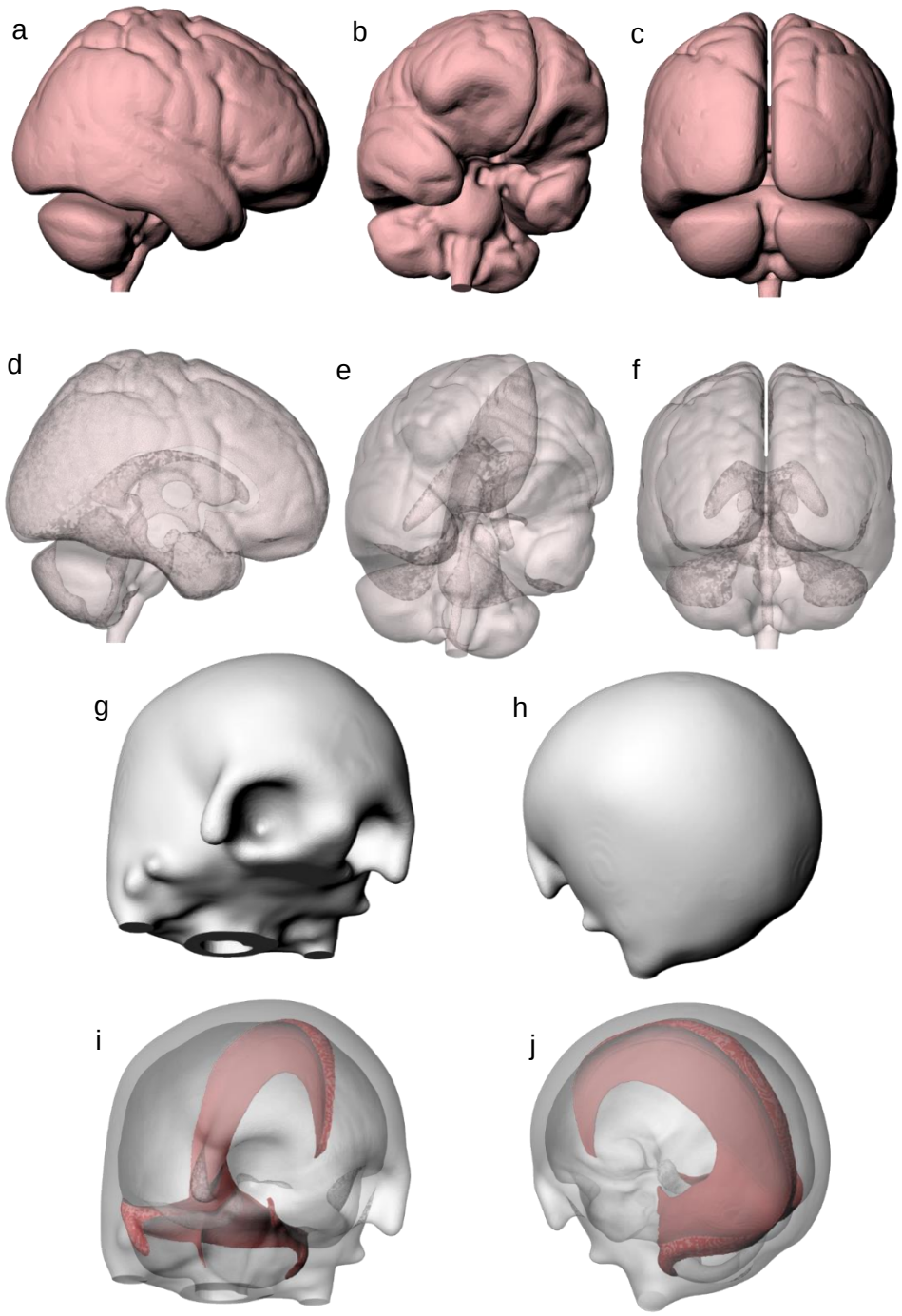

Figure 6.4: Segmented brain (pink), dural septa (red) and skull models (grey). a-c are views of the brain model; d-f are the same views but of the brain model but set translucent, showing the internal cavities; g-h are views of the skull model; i-j are the same views of the skull model but set translucent, showing the internal dural septa model.

6.1.5 Segmentation of the SAS

Given that the meningeal layers were not discernible in the MNI ICBM152 dataset, the SAS was assumed to be the space in-between the brain and the skull. PAC structures could not be seen and so no meshes were generated for them. Cross-sections showing the relationship between the segmented brain, dural septa and skull models are shown in Figure 6.5.

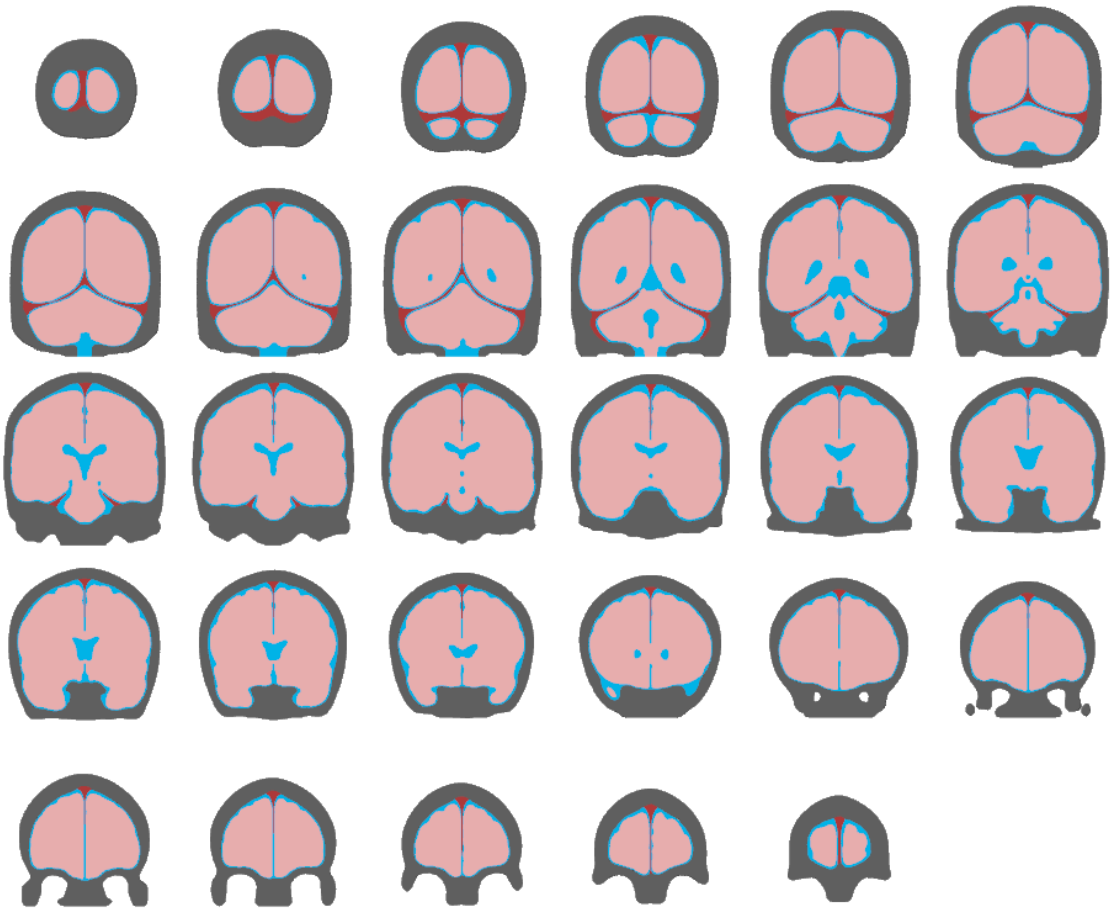

Figure 6.5: Posterior to anterior coronal cross-sections of segmented geometries. Pink = brain; blue = SAS and ventricles; red = dural septa; grey = skull.

6.2 Fabricating the Non-Tethered Model

This section describes the fabrication process for the building of the non-tethered model, using the base geometries acquired in Section 6.1.

Computational design of all parts in this section were performed in Rhino through the Grasshopper plugin (Robert McNeel & Associates) for enhanced workflow management and parametric design. In some instances, Meshlab was used to repair/alter meshes. With over 8500 components used, Grasshopper paths which define the geometries described within this section are not delineated due to their complexity. Instead, the general process by which the intermediates and end geometries are formed is described. However, the Grasshopper paths are shown in Appendix A and Appendix B.

6.2.1 Producing the Composite Brain Mould

This section details the computational design and fabrication of the composite brain mould (CBM) described in Section 5.3 (p68). Shown in Figure 6.6, is an overview of the entire process. The proceeding subsections describe the process in more depth.

The implementation of the marker delivery system was conducted towards the end of the model's development, after its primary construction and optimisation stages, and so is presented in Chapter 8 to avoid confusion.

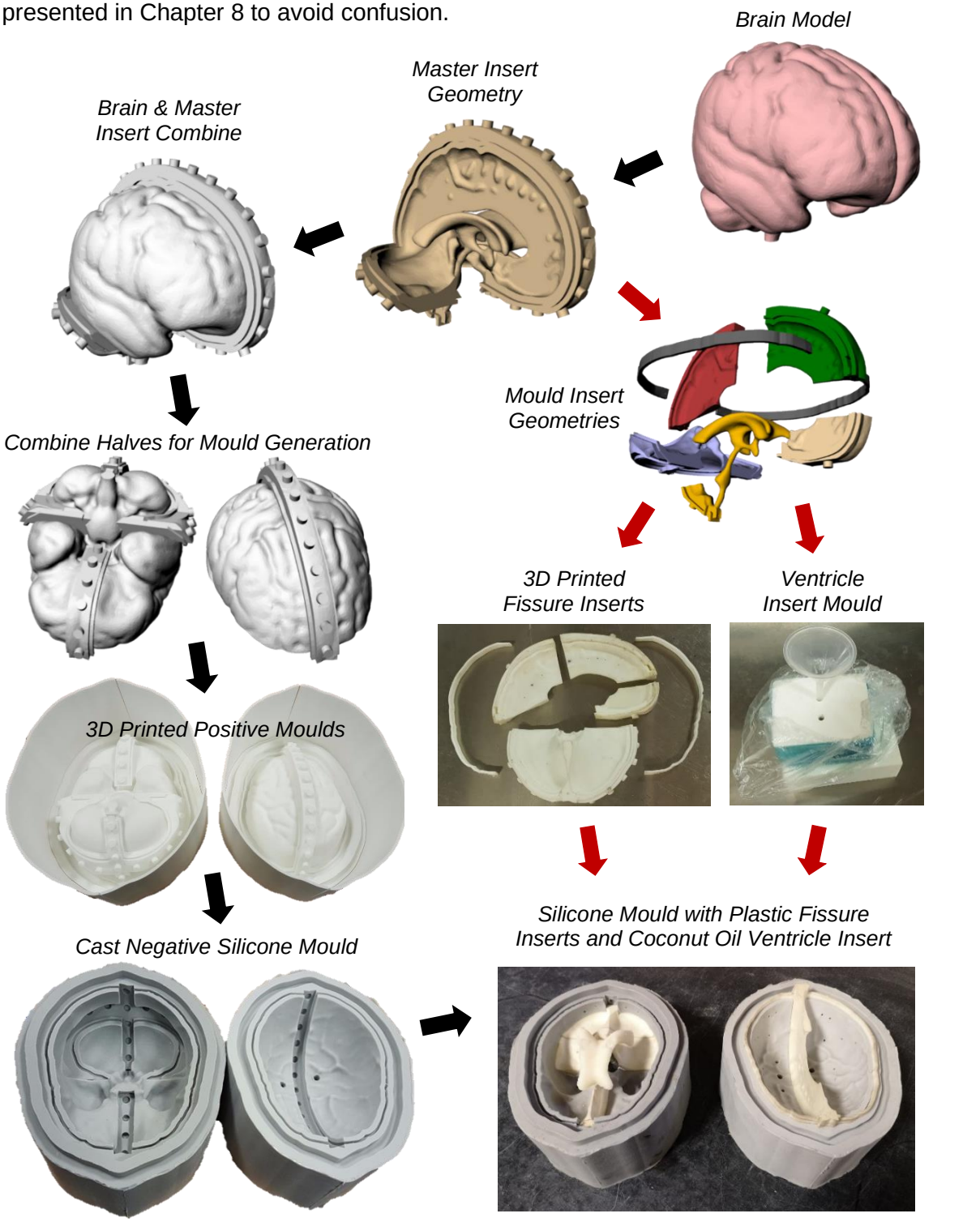

Figure 6.6: Overview of composite brain mould fabrication workflow. Major elements of the workflow are labelled, however, all are described and reshown in the proceeding sub-sections.

6.2.1.1 Producing the Expandable Silicone Halves

In producing the composite brain mould (CBM) described in Section 5.3 (p68), positive moulds to be 3D printed were first designed for the two silicone halves (Figure 6.7) in Rhino.

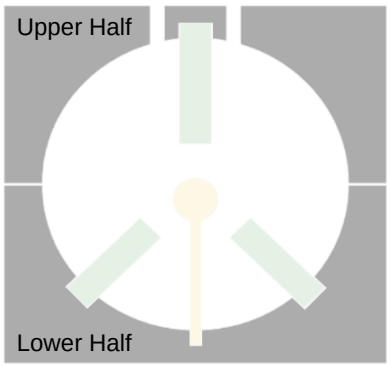

Figure 6.7: Cartoon depicting CBM's silicone halves.

The first step in achieving this was to produce the geometry that define the inserts (master insert geometry). To generate this geometry, a duplicate of the brain mesh was created and dilated by 15 mm. The dilated ventricle cavity of this mesh was then filled in before subtracting the original brain mesh from the result, creating a mesh of the SAS that is dilated externally but unchanged internally (Figure 6.8a, p81). This mesh was then intersected with a box construct (Figure 6.8b) created through the manual positioning of 19 boxes over regions of the fissure/ventricle spaces and combining them into a single part. A continuous 3x3 mm ridge and a collection of 33, 10 mm diameter studs (5 mm length) (Figure 6.8d) were finally combined with the intersection result (Figure 6.8c) to complete the insert geometry (Figure 6.8e).

The ridge was created through a) the offsetting of boundary curves of the individual planar surfaces of the insert geometry, b) the subsequent lofting of the offset boundary curves into walls defining the ridge at that section and, c) the combination of the lofted walls of all sections into a single closed solid (see Figure 6.9, p82 and Figure 6.10, p83). Included between (a) and (b) was a curve adjustment step, wherein offset curves where trimmed or projected such that they linked up with the corresponding curves of neighbouring surfaces.

The studs were created by taking cross-sections of the insert geometry and using the outer curve of the result to equally space build sites along the external curvature of the insert geometry. The position and curve normals at each site were then used to generate 10 mm diameter circles and extrude them into 5 mm long studs, normal to the mesh at that location.

The method by which the sagittal studs where made is shown in Figure 6.11 (p83). For the studs on the wings of the insert geometry (i.e. tentorial portion) a similar method was employed. Here a combination of horizontal and tilted horizontal sections were taken and the outermost curves of these were used to define build sites for the generation of equally spaced studs. Due to the complex curvature of the wings, the tentorial studs were individually angled to obtain optimal projection away from the mesh.

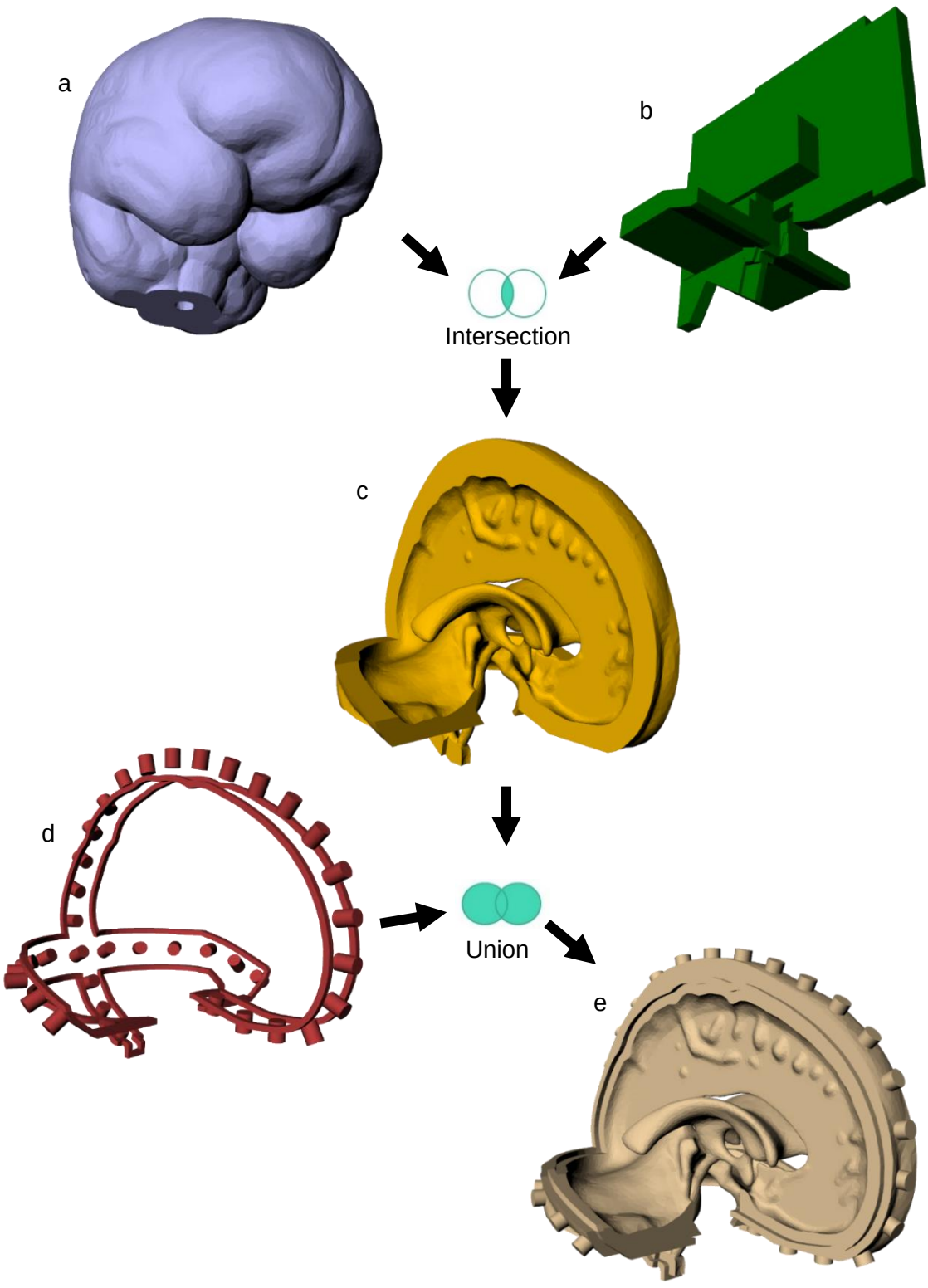

Figure 6.8: Generation of the master insert geometry defining fissure and ventricle spaces. a) dilated SAS mesh; b) box construct; c) intersection result; d) ridges and studs; e) union result / master insert geometry.

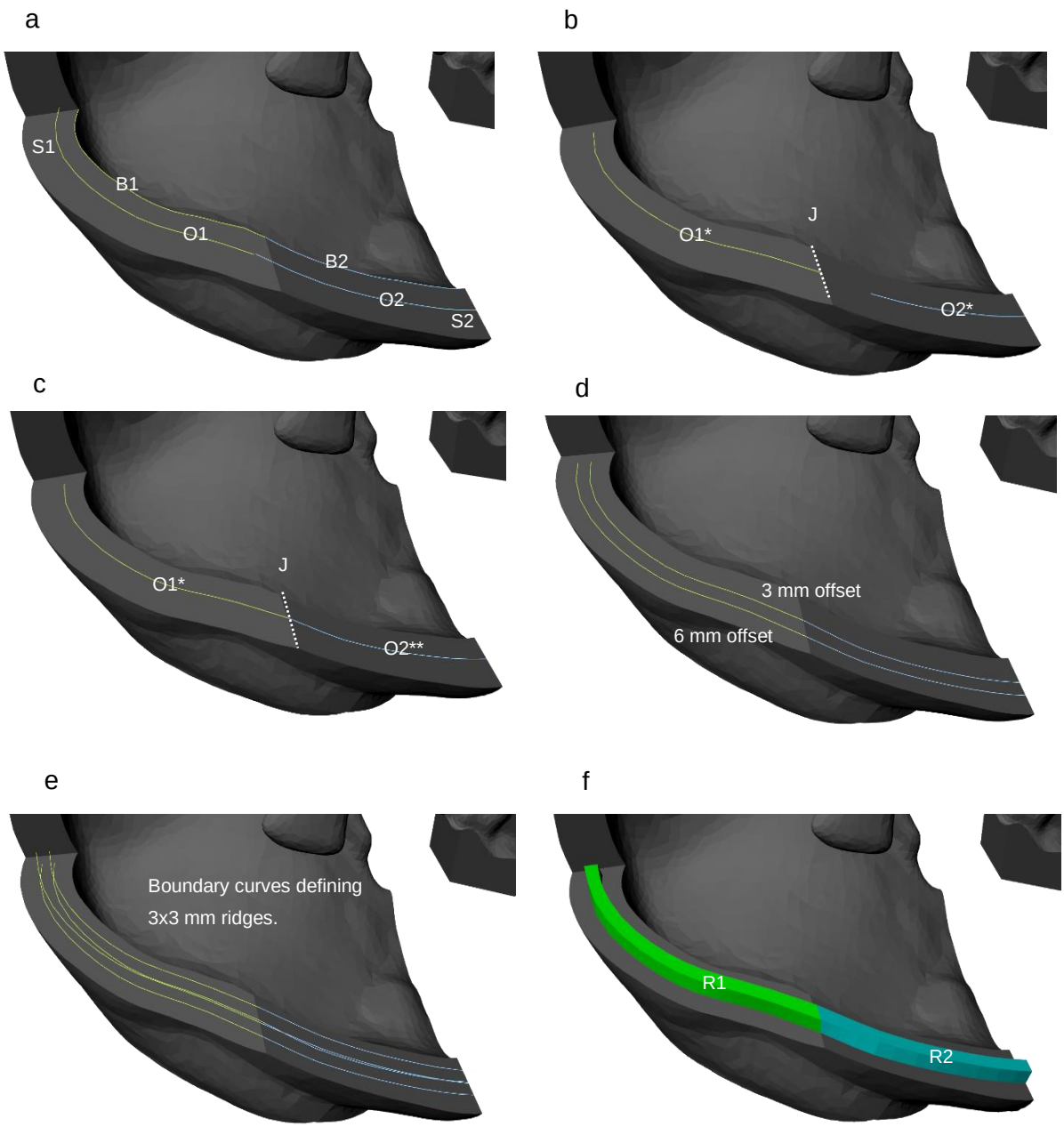

Figure 6.9: General method for formation of planar ridge sections which together form the continuous ridge. Shown here is the method by which R1 and R2 sections of the ridge are made and the junction between them. a) 3 mm offsetting of B1 to O1 and B2 to O2 along surfaces S1 and S2, respectively; b) extension of O1 to joining line J (forming O1) and shortening of O2 away from J (forming O2*); c) extrusion of O2* towards end point of O1* (forming O2**); d) Addition of 6mm offsets for B1 and B2 through same method; e) addition of 3 mm raised, 3 mm and 6 mm offsets; f) generation of R1 and R2 ridges through lofting of offsets.*

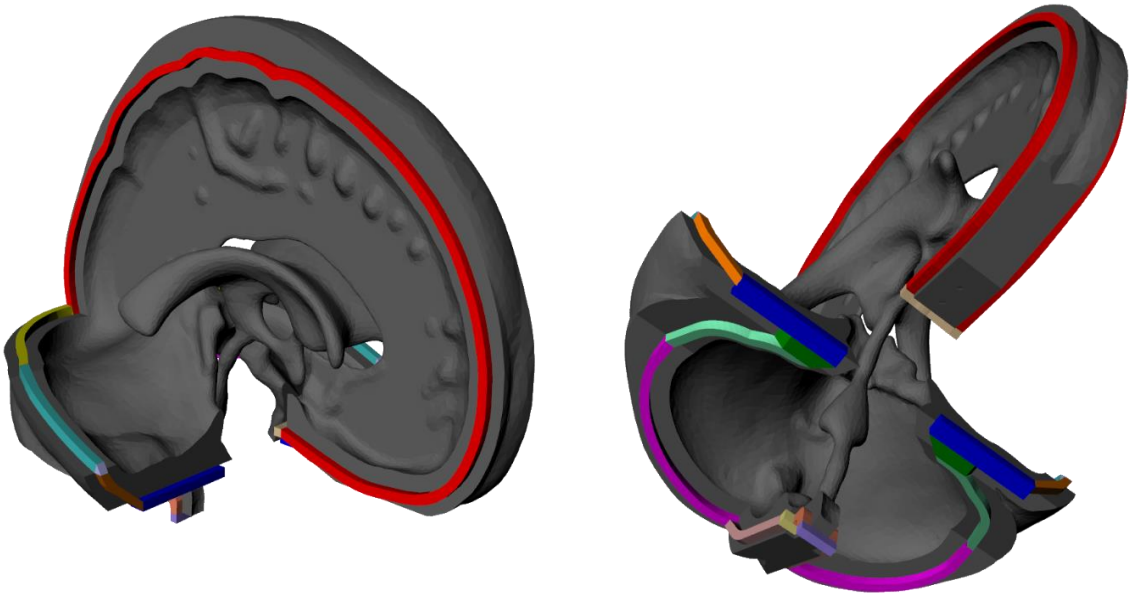

Figure 6.10: The 26 sections of the continuous ridge.

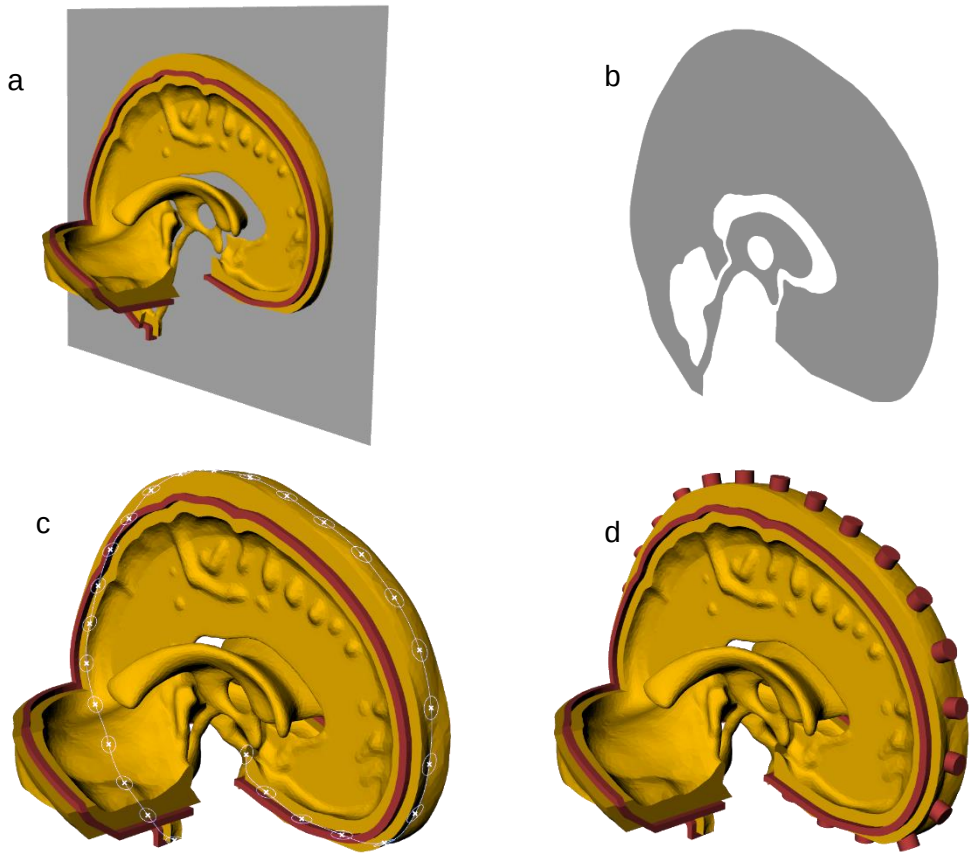

Figure 6.11: Positioning the sagittal studs. a) splitting of surface with insert mesh; b) resultant cross-section; c) division of cross-section boundary curve defining external geometry and generation of equally spaced circles on curve; d) extrusion of circles along normals into cylinders.

Following addition of the ridge and studs, the master insert geometry (Figure 6.12a) was combined with the brain mesh (Figure 6.12b) to produce the positive (Figure 6.12c) that would define the cavity of the silicone mould when cast. This positive was subsequently split in half 85 mm down from the top of the mesh to produce top (Figure 6.12d) and bottom (Figure 6.12e) positives. Bases and mould walls were then added to these positives (Figure 6.13, p85).

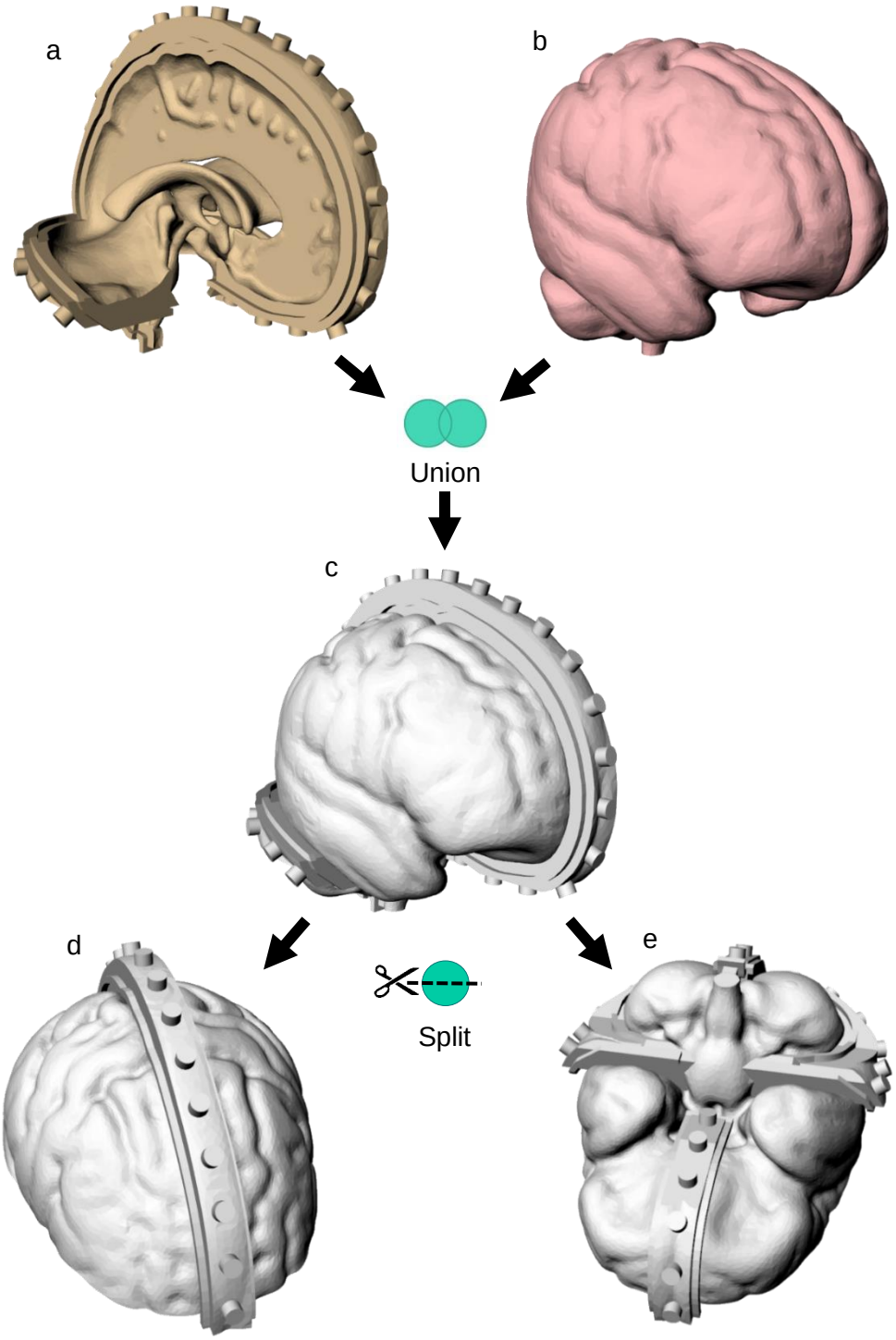

Figure 6.12: Unification of insert and brain meshes and separation of the result into two halves. a) insert geometry; b) brain mesh; c) union result; d) positive geometry of top mould; e) positive geometry of bottom mould.

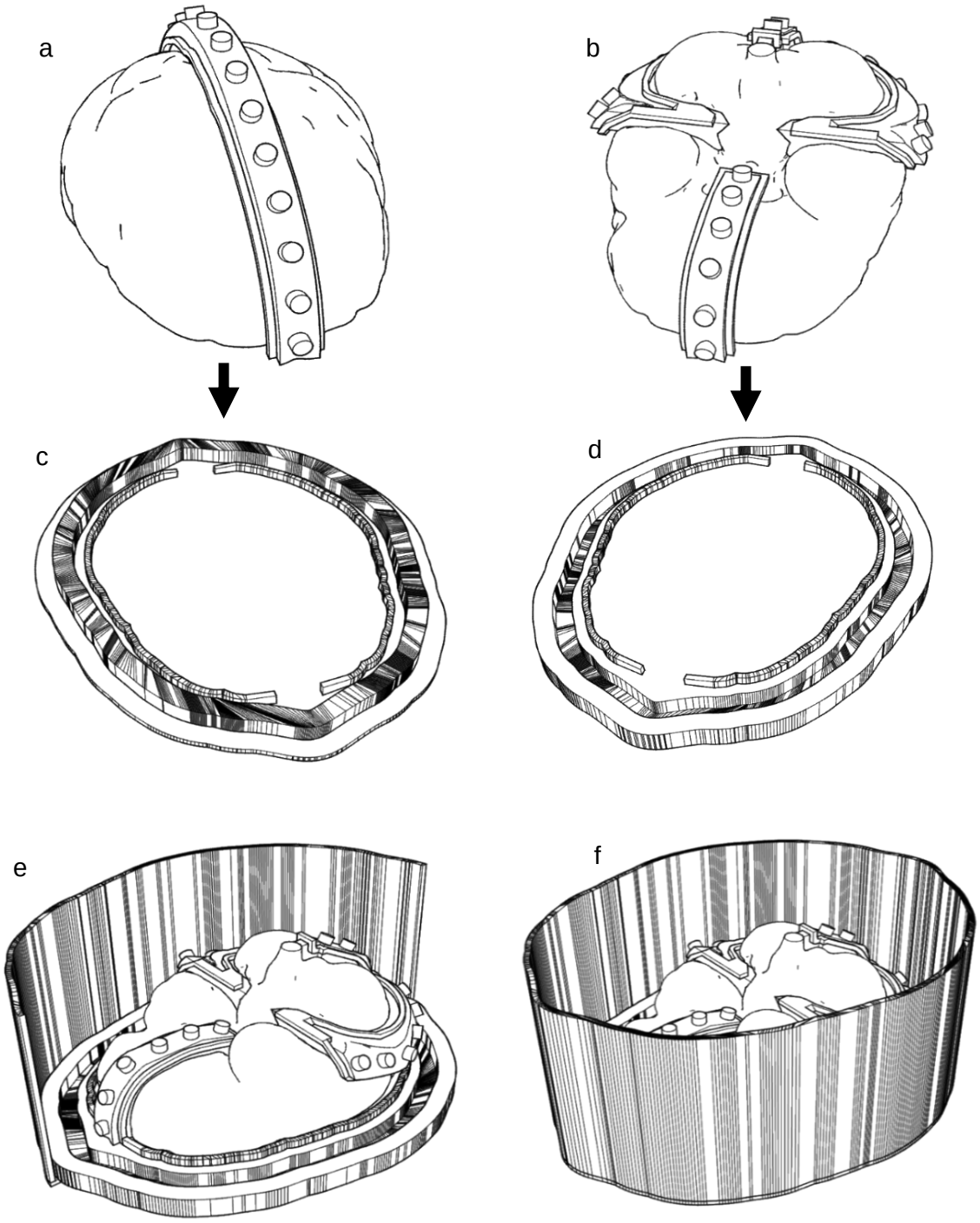

Figure 6.13: Addition of the mould bases and walls. a) top mould positive; b) bottom mould positive; c) top mould base; d) bottom mould base; e) bottom mould assembled with one wall; f) bottom mould assembled with both walls. Mould walls are not connected to the base.

The method by which the bases were created is shown in Figure 6.14. All curves which define the base were created using the cross-sectional curve of the positive at the level of the split (Figure 6.14a) through offsetting and smoothing operations. Engineered into the bases are a set of grooves and ridges for the moulding of features to help locate the two halves of the silicone mould when in use. These are best visualised in the silicone casts shown in Figure 6.16 (shown later on p88). The wide (15 x 20 mm) ridge of the bottom silicone half slots into the corresponding groove of the top half, whilst the minor grooves are occupied by the two locating bands of the rigid inserts (see later in Figure 6.18, p89).

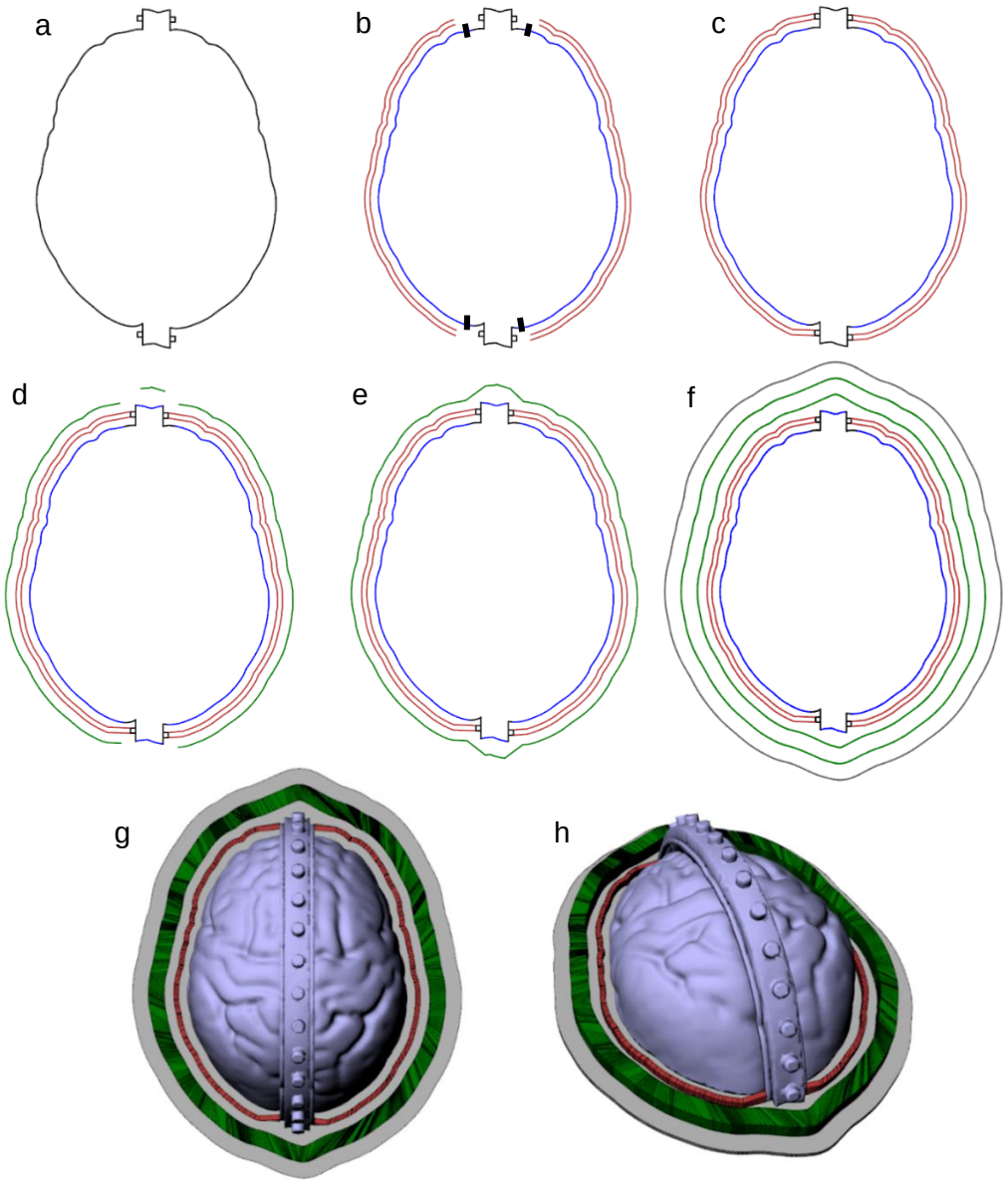

Figure 6.14: Formation of top positive mould base through the offsetting and lofting of curves. a) cross-sectional boundary curve at split; b) splitting of boundary curve at thick black lines to create blue curves and offsetting of blue curves by 5 and 8 mm to create red curves; c) extension of red curves to meet ridge curves; d) offsetting of blue curves by 13 mm to create green curves; e) joining of green curves; f) smoothing of joined green curves and offsetting of green curve by 10 and 20 mm to create second green curve and grey curve, respectively; g) lofting of green and red curves to create ridge surfaces of base and patching of grey line to create base surface; h) extrusion of lofted surfaces into volumes.

The walls of each positive mould were created by initially offsetting the outermost curve defining the base by 0.5 mm (for fit purposes). The curve was then offset by 3 mm and a surface was then lofted between them. This surface was then extruded to a height 20 mm above the top of the mould base and combined with a floor created by patching the 3 mm offset into a surface and extruding it down 3 mm. To make the walls more removable from the silicone when cast, this wall was then split down the long axis in the middle.

Now complete, the positive moulds were 3D printed on an EOS P700 SLS printer in the rigid DuraForm material with a layer thickness of 0.15 mm. Once built, the six parts (4 mould walls, top positive base and bottom positive base) were cleaned and treated with the sealing agent SuperSeal (Smooth-On Inc, UK) to prevent gripping of cast material in demoulding. Three coatings of SuperSeal was found to be sufficient.

The bases were then assembled together with their walls and sealed using butyl rubber tape, ready for silicone casting. CS25 Condensation Cure Silicone (Easy Composites, UK) was chosen as the silicone to fabricate the expandable mould in due to its appropriate stiffness (Shore A 25), high tear strength and low viscosity.

A 5/01 MCP vacuum caster (Renishaw plc, UK) was used to ensure close moulding of the silicone around the overhanging ridges of the moulds. Due to the limited capacity of the vacuum caster, each mould was filled in three sequential casts of 1200, 1200 and 1000 ml volume. For each cast volume, the silicone and its catalyst were added into the mixing vessel before placing the vessel into the vacuum caster. A vacuum was then created in the chamber before engaging the mixing arm for a total of 5 minutes to disperse the catalyst throughout the silicone. After the 5 minutes, the silicone (still under vacuum) was poured into the mould. The total casting time from initial contact of silicone with catalyst in the first cast to the final pour of the last cast was approximately 30 minutes. The silicone was then allowed to cure for 48 hours before demoulding, the result of which can be seen in Figure 6.16 (p88). Silicone volumes of 3310 and 3200 ml were used to form the top and bottom moulds, respectively.

Figure 6.15: 3D printed top (right) and (left) bottom positive moulds.

a

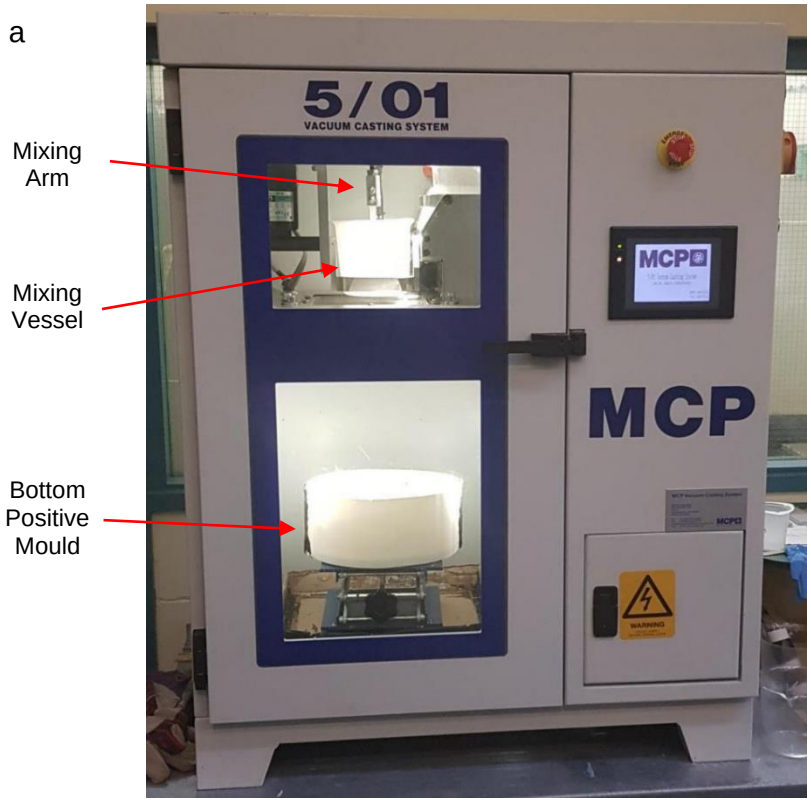

b

Figure 6.16: Casting of the expandable silicone halves. a) positive mould in vacuum caster; b) cast silicone top (right) and bottom (left) negative moulds.

6.2.1.2 Producing the Inserts

Figure 6.17: Cartoon depicting the CBM's inserts.

To produce the inserts for the CBM (Figure 6.17), the insert geometry presented in Figure 6.8 (p81), was first reproduced with a fewer number of studs (Figure 6.18a). This was done to make it easier to locate and remove the inserts, with the option of adding further studs later if required (due to slots being present on the mould already). Using the four red offsets of Figure 6.14c (p86), the mould locating bands were next built. These bands were built by extending the offsets by 10 mm into the insert geometry, lowering the curves by 2.5 mm, lofting between the inner and outer curve and extruding the result upwards by 5 mm to form a solid band. The final insert geometries (Figure 6.18b-d) were then produced by subtracting this band geometry from the reproduced insert geometry and splitting the result into five parts using manually positioned cutting surfaces. These geometries, minus the ventricle geometry, were 3D printed on the EOS P700 machine in the DuraForm material (Figure 6.19, p90).

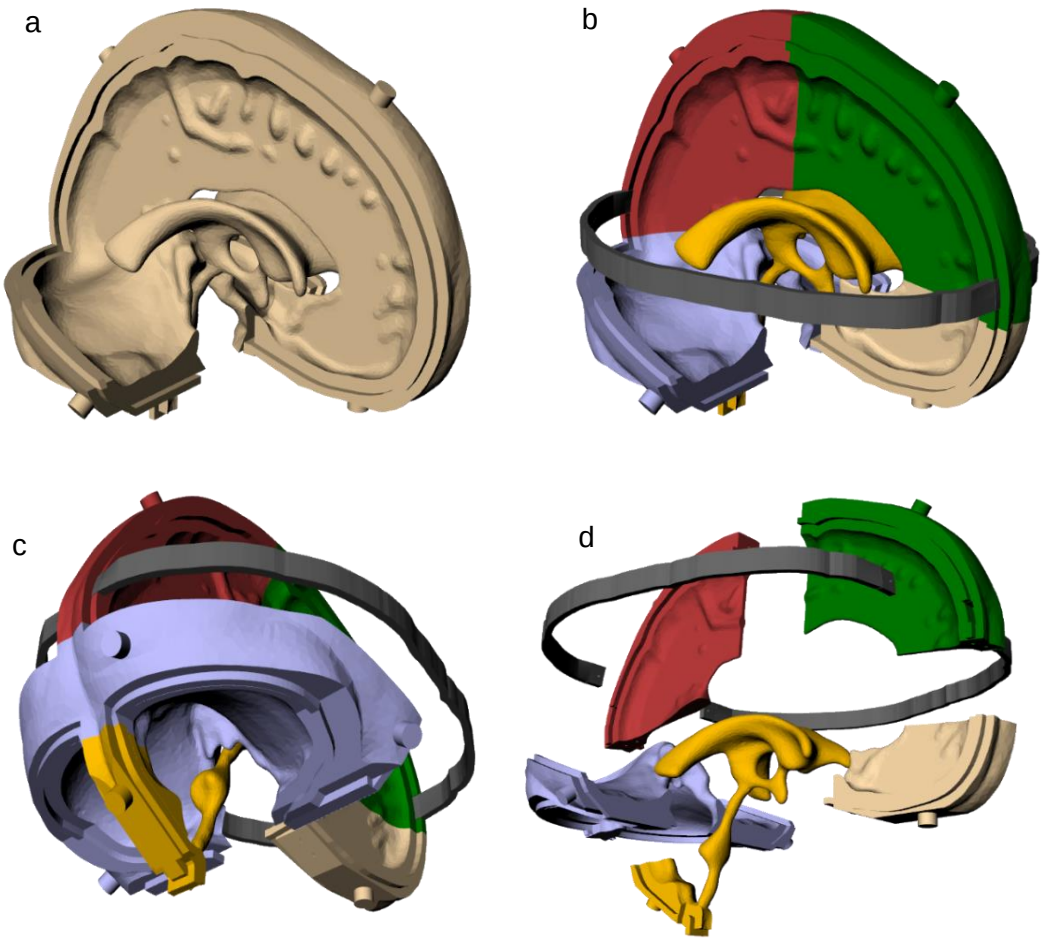

Figure 6.18: Producing the mould insert geometries from the master insert geometry. a) master insert geometry reproduced with fewer studs; b) master insert geometry split into 5 pieces with locating bands added; c) alternative view of (b); d) mould insert geometries and locating band.

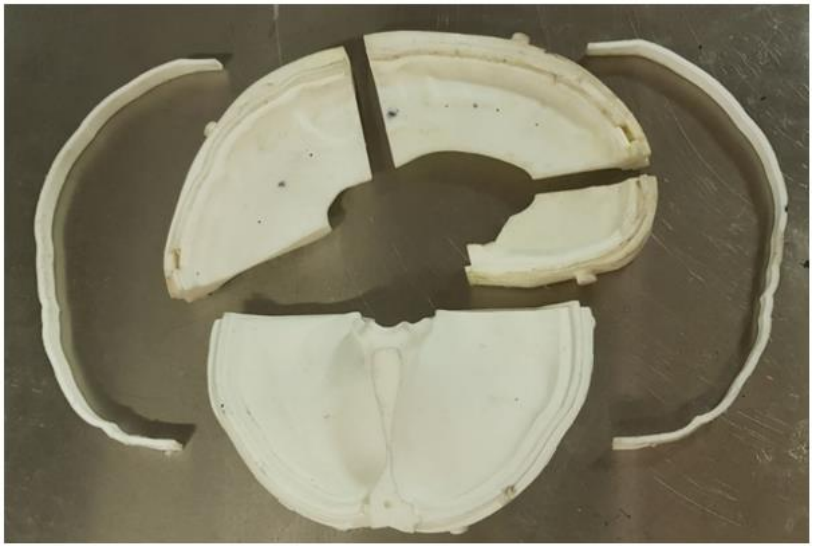

Figure 6.19: 3D printed fissure inserts and locating bands.

In producing the dissolvable ventricle insert, a mould structure was first decided upon. Given the complex shape of the cavity, a two-part mould was not deemed suitable for producing the ventricle and so a three-part silicone mould design was sought instead. This design is shown in Figure 6.20f (p91) and consists of a lower left (LL) section, a lower right (LR) section and an upper (U) section. The benefit of this design is that it removes the stresses that would otherwise be produced in a two-part mould when pulling the ventricles' curved horns out of the mould.

The method by which these splits were defined is shown in Figure 6.20a-e. To define the split running through the ventricle horns and body of 3rd ventricle a complex surface was built using four construction curves and two offsets. Two of these construction curves (C1 and C2 of Figure 6.20a) were produced by selecting vertices on the lateral horns, offsetting them from the mesh by 1 mm along their normals and drawing a polyline through them. The next two were created by manually positioning four points relative to the volume centroid of the ventricle geometry such that the resultant polyline drew through the points ran roughly through the center of ventricle head along the anterior-posterior axis; this curve was then offset 2 mm in each direction to produce two parallel central curves (C3 and C4 of Figure 6.20a).

Once defined, these initial construction curves were then extended in the anterior and posterior directions and two further curves (C1* and C2* of Figure 6.20b) were then produced through the offsetting of C1 and C2. A surface was then finally lofted between these curves (Figure 6.20c) and used to split a ventricle cavity-containing box geometry (Figure 6.20d) created by defining a bounding box over the ventricle mesh, dilating it by 15 mm and subtracting the ventricle mesh from it. Now split into upper and lower sections, a vertical surface was positioned over the lower half section and used to split it into left and right lower sections (Figure 6.20e).

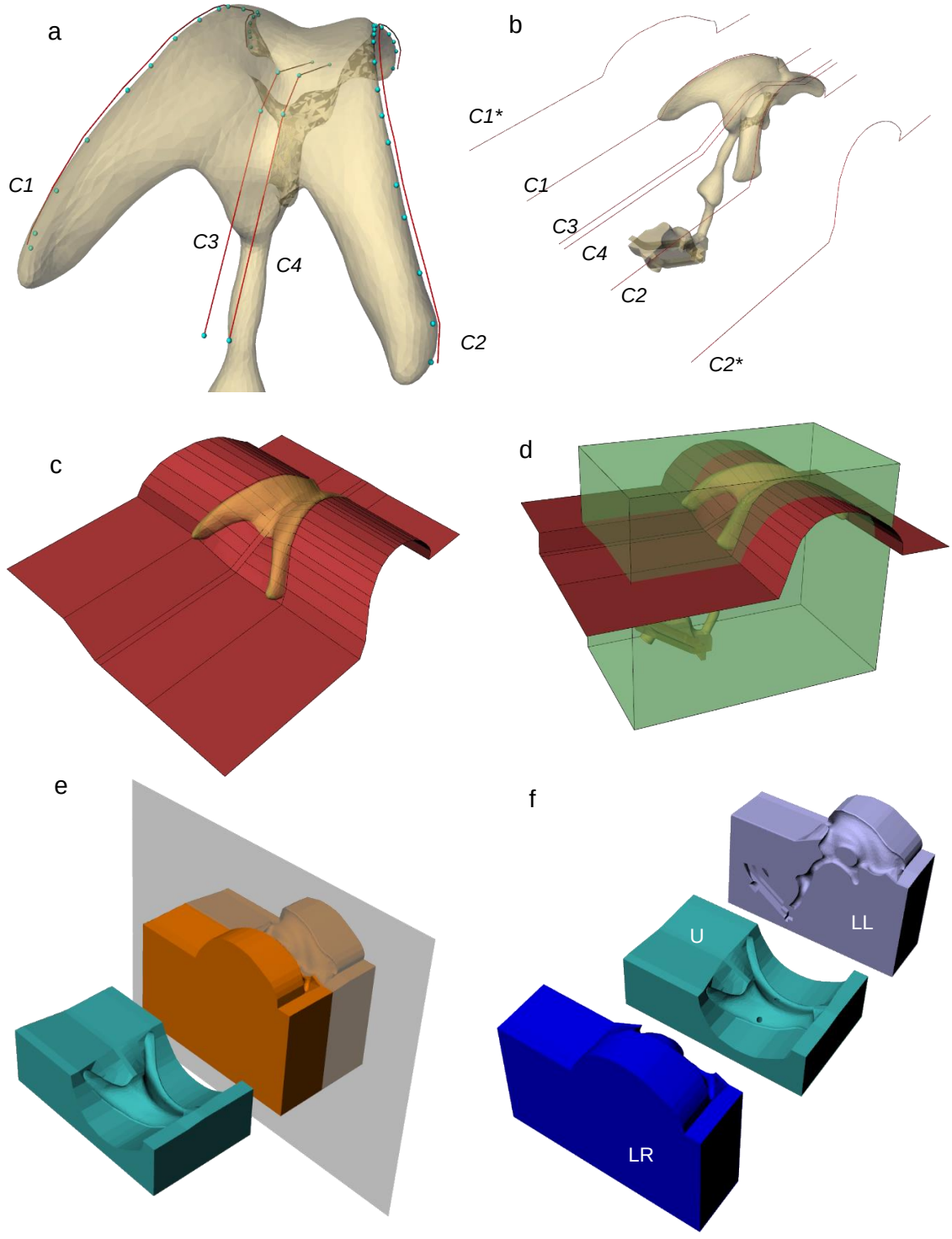

Figure 6.20: Designing the negative ventricle mould. a) definition of construction lines (red) from points (blue spheres); b) extension of construction lines and offsetting of C1 and C2 to C1 and C2*, respectively; c) lofting of construction lines and offsets to create ventricle splitting surface; d) subtraction of ventricle geometry from bounding box and splitting of box; e) splitting of lower portion of result with vertical plane; f) completed negative ventricle mould geometry (minus dowel pin slots) comprising lower left (LL), lower right (LR) and upper (U) sections.*

To fabricate the mould design in silicone, positive moulds were first produced. These were generated by first taking the positive geometry of the ventricle and cutting it in the same manner described in Figure 6.20. Mould bases and walls were then added to each section of the split ventricle, along with a collection of 15 mm diameter studs for the moulding of holes for mould section locating dowel pins. These three positive moulds were then fabricated with the EOS P700 machine in the DuraForm material. Finally, silicone negative moulds were cast with Mold Max 14 NV silicone rubber (Smooth-On, UK) (Figure 6.21).

6.2.1.3 Assessment of the Ventricle Mould

Upon fabrication, the ventricle mould was assembled for assessment. This was achieved by bringing the mould sections together and placing the assembly into a thin plastic freezer bag and tightly taping around the outside (Figure 6.21c-d and Figure 6.22).

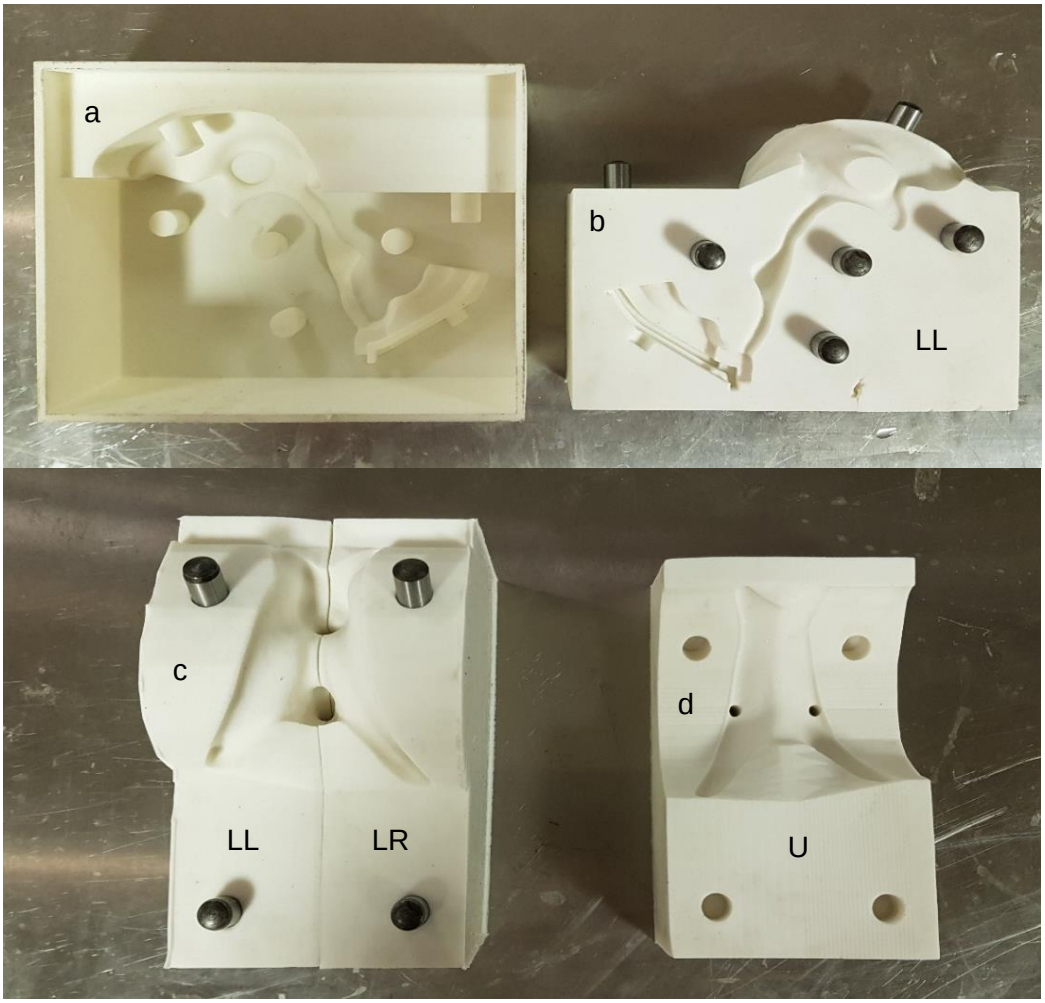

Figure 6.21: Fabricating the negative silicone ventricle mould. a) fabricated positive mould for the production of the LL section of the silicone negative mould; b) silicone cast LL section with locating dowel pins inserted; c) birds eye view of LL and LR sections assembled; d) U section.

Figure 6.22: Assembled ventricle mould. Shown is the assembled silicone mould within a plastic bag that has been wrapped tightly to the mould with tape. A funnel has also been inserted into the mould to show how material is cast into it.

Preliminary experimentation with dissolving a shape such as the ventricle through a thin long aperture (the ventricle stem) revealed it to be a long and involved process, even with a readily dissolvable material such as sugar glass. Consequently, a melting route was sought instead. Coconut oil (CO) was found to be the only suitable material due to its unique combination of high strength at low temperatures <10 °C, appropriate melting temperature (~25°C) and compatibility with the CH when in melted form (i.e. not damaging).

Although the traditional CH casting process involves casting the solution at >30°C (due to the ~28°C gelation temperature of the phytagel component), casting the solution at 5°C was found to be achievable, provided that the solution was vigorously mixed and then degassed with ultrasound (using an ultrasound bath) immediately prior to casting. Considering this, it was identified that both the brain mould and the CH solution could be chilled down to 5°C prior to casting, such that the ventricle insert would remain a strong solid during the formation of the brain's geometry (during freezing and the critical stages of thawing) but would soften as it came up to room temperature. Upon incubating the brain at ~27°C to fully melt the CO, the oil could then be washed out and replaced with water.

The ventricle mould was thus trialled with CO. The CO was first fully melted through heating in an oven and then poured into the mould. To maximise the strength of the CO material during demoulding, the mould was frozen down to -30°C before extracting the ventricle insert.

Upon demoulding, however, it was found that the ventricle would snap at two points along the stem (Figure 6.23a). Consequently, the mould was redesigned with a cavity to produce a ventricle with a reinforced stem and a space for a shorter plastic socket that the stem would set into (Figure 6.23b-e). This, however, did not stop the stem breaking and also appeared to cause an additional breakage at a level along one of the lateral horns (Figure 6.24a, p95).

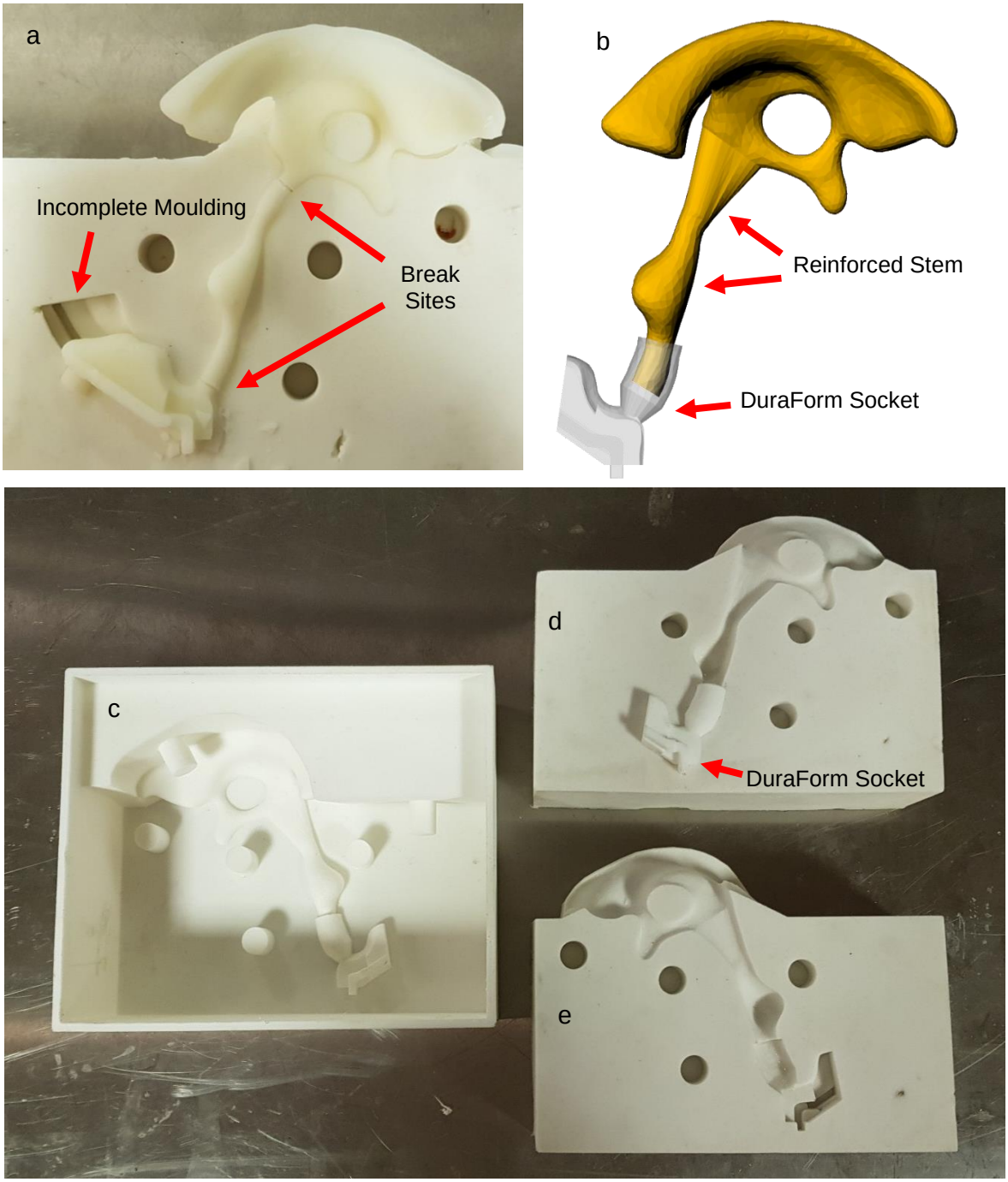

Figure 6.23: Redesigning the V1 ventricle mould into the V2 ventricle mould. a) breakage sites of V1 CO ventricles on demoulding; b) V2 ventricle design with reinforced stem and introduction of DuraForm socket; c) V2 LL positive mould; d) V2 LL section of negative mould with duraform socket in place; e) V2 LR section of negative mould.

In order to obtain a useable ventricle insert, the mould was revised once more. In this revision, the mould was redesigned to produce an insert comprised of a plastic (DuraForm) hex socket, a plastic (DuraForm) hex rod stem and a 1 mm dilated CO ventricle head with patched interthalamic adhesion (Figure 6.24b-f).

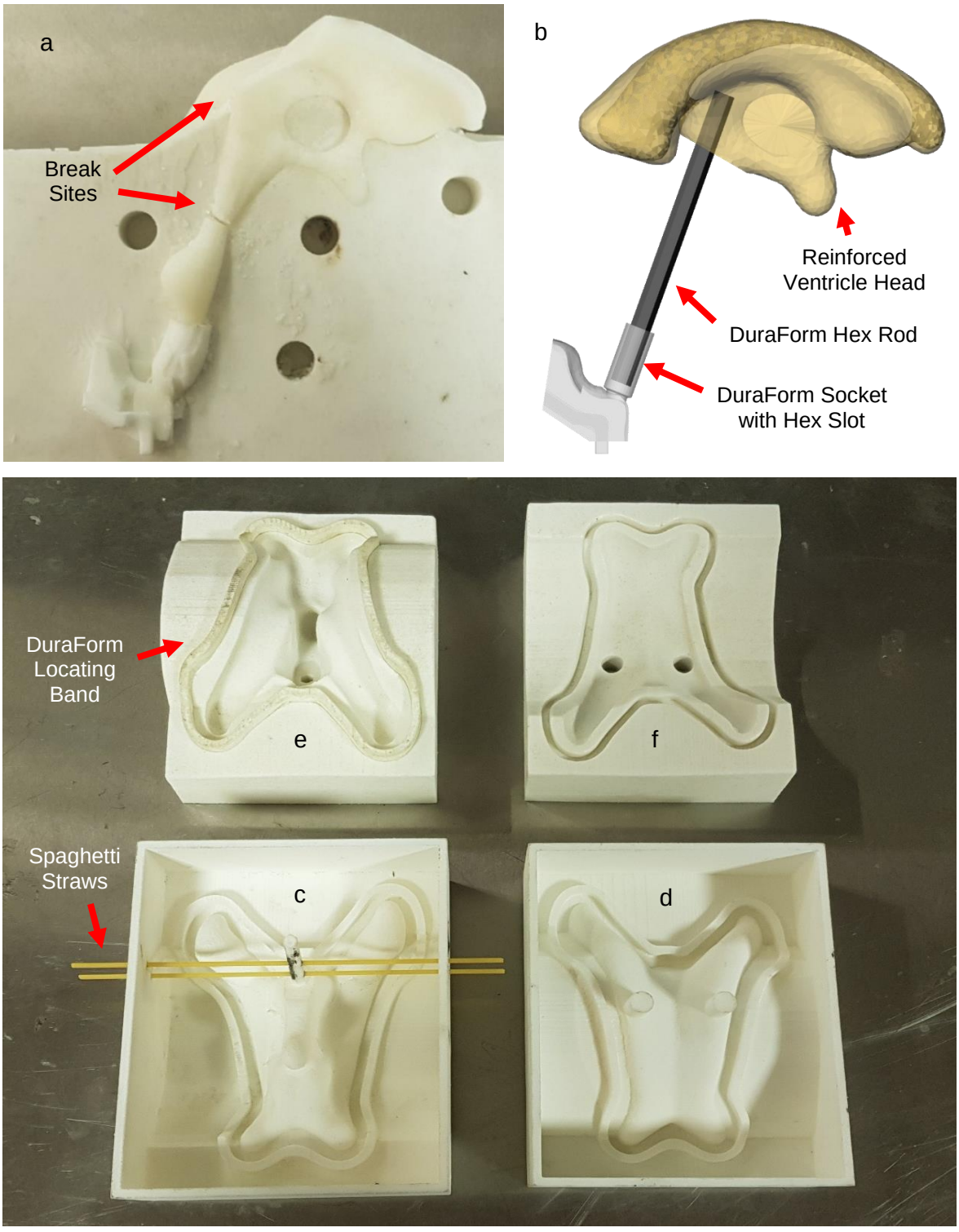

Figure 6.24: Redesigning the V2 ventricle mould into the V3 ventricle mould. a) breakage sites of V2 CO ventricles on demoulding; b) V3 ventricle design with reinforced ventricle head, DuraForm hex rod and socket; c) bottom positive mould for V3 ventricle mould with moulding spaghetti straws in place; d) top positive mould for V3 ventricle mould; e) bottom section of negative V3 mould with locating band in place; f) top section of negative V3 mould.

To produce this insert, a two-part silicone mould was produced for the moulding of the ventricle head onto the hex rod (Figure 6.24c-f). Designed into this mould are slots for a duraform locating band, a hex tunnel in the lower half for the hex rod to occupy and two tunnels intersecting the hex tunnel for spaghetti straws to occupy and lock the hex rod in place such that rod projects into the cavity (see Figure 6.25a-b). Spaghetti straws were used as locking rods due to their brittle nature, with the intention of them snapping on both sides of the hex rod upon retrieval of the ventricle from the lower mould half. Demoulding of this version of the ventricle proved to be successful (Figure 6.25d) and so was used going forward.

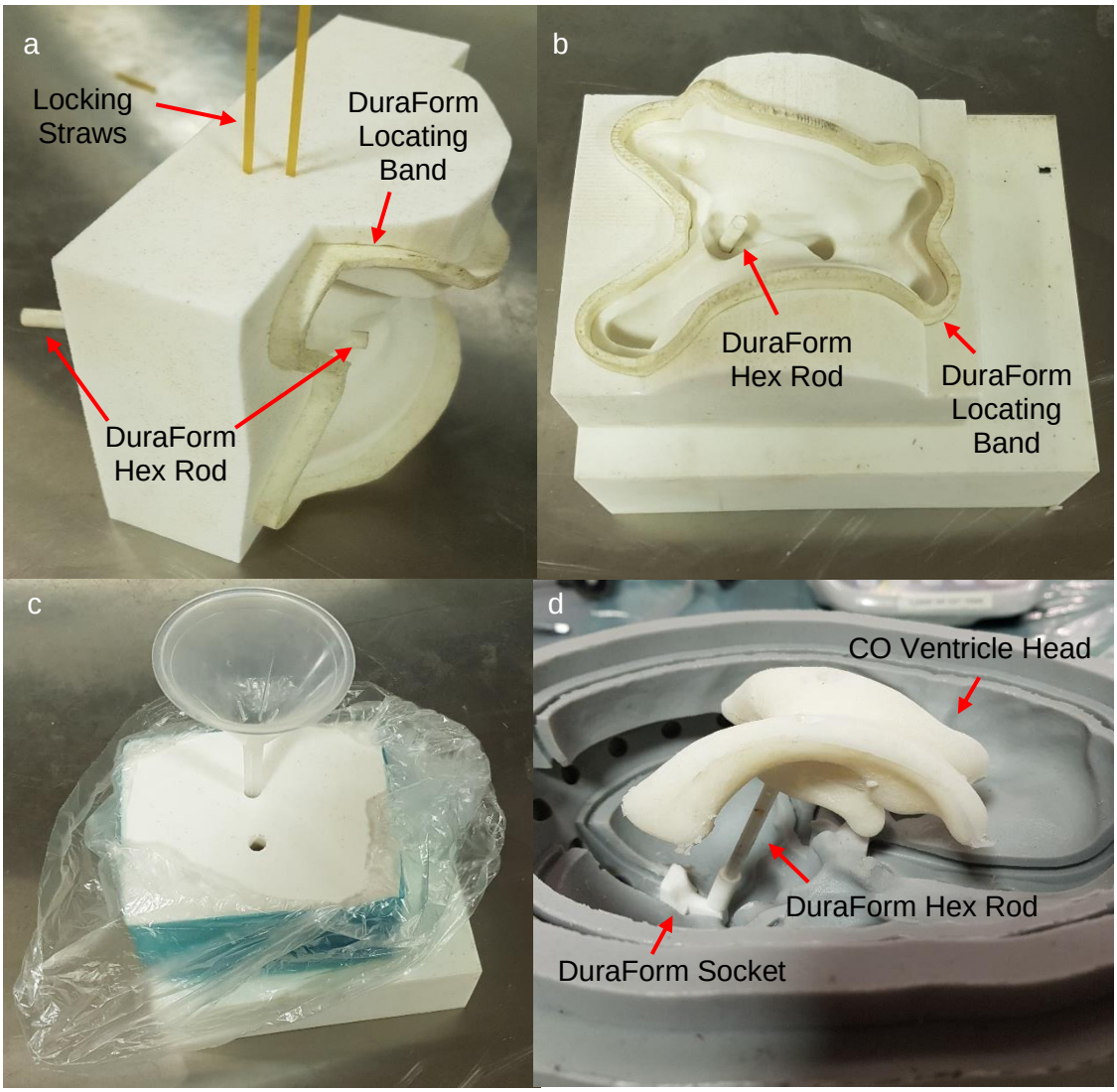

Figure 6.25: Mould assembly and successful demoulding of V3 ventricles. a) bottom section of V3 mould with locating band and hex rod in place; b) top-down view of bottom section of V3 mould; c) assembled mould on stand; d) cast ventricle inserted into lower half of CBM.

Due to the changes in the ventricle insert design, a linking insert piece was introduced to bridge the space between the tentorial insert and the ventricle insert. The changes from the original insert design to the final insert design are shown in Figure 6.26. Shown in Figure 6.27 are the silicone halves with all the 3D printed inserts and the CO ventricle insert in place.

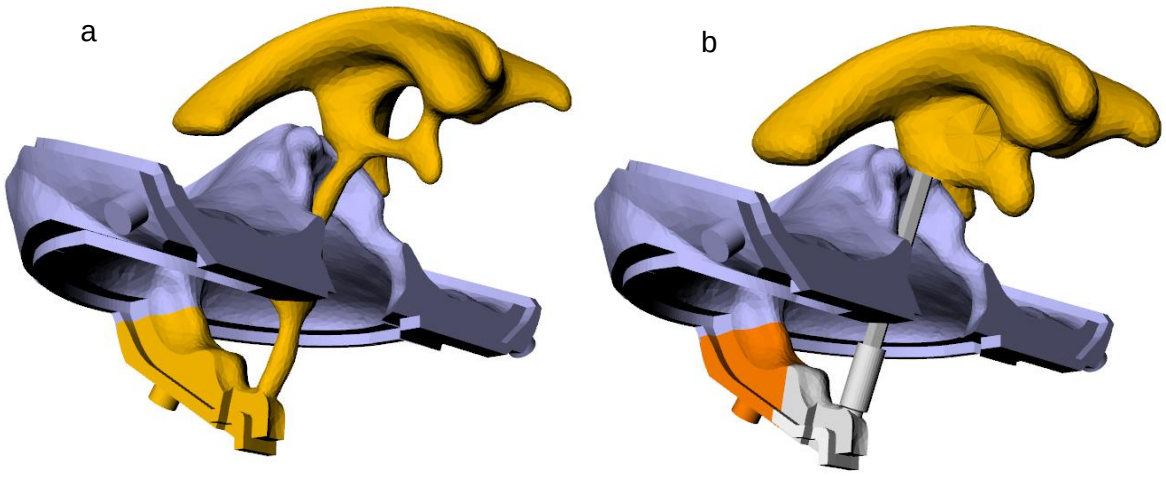

Figure 6.26: Changes to the ventricle insert. a) original design of ventricle insert (gold) and its relationship to the tentorial insert (purple); b) updated design featuring coconut oil ventricle (gold/grey) and its socket (grey), with linking piece (orange).

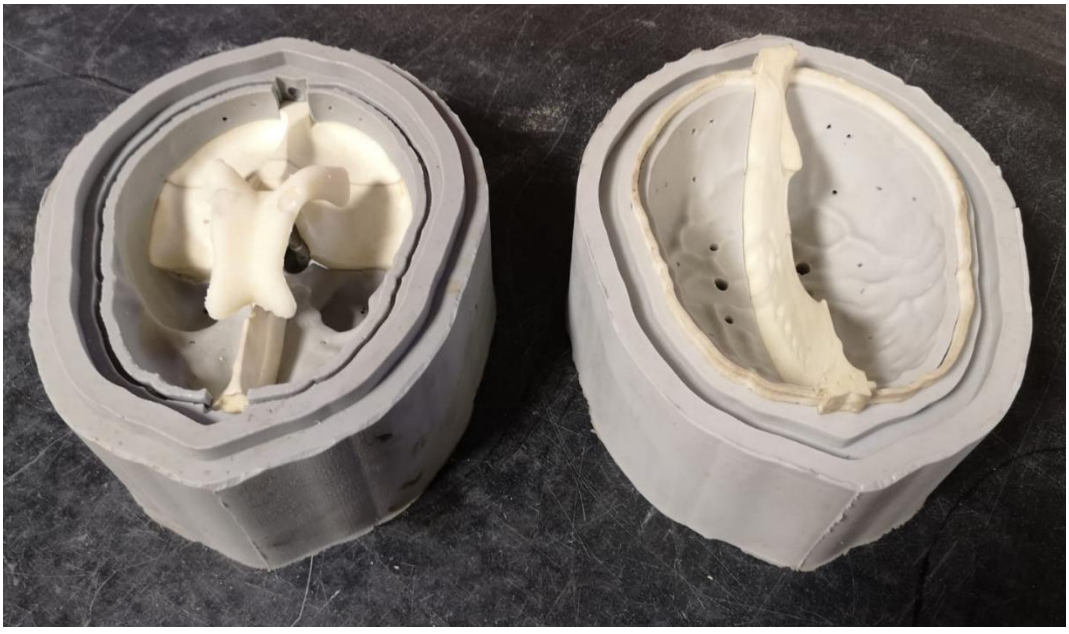

Figure 6.27: Upper (right) and lower (left) silicone halves with inserts in place.

6.2.2 Producing the Thawing Apparatus

This section details the computational design and fabrication of the thawing apparatus described in Section 5.3 (p68).

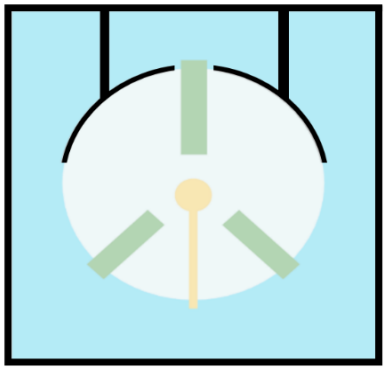

Figure 6.28: Cartoon depicting the thawing apparatus.

To produce the thawing apparatus (Figure 6.28), the thawing cap was first constructed. The mesh of the brain was taken and scaled by 8% to account for the volume change of the brain upon freezing and then thickened outwards into a 2 mm shell. This mesh was then split 87 mm up from the bottom of the mesh using a horizontal surface to create a lower and upper portion (Figure 6.29a). A box geometry, created by defining a bounding box over the falx segments of the insert geometry and thickening it on either side by 5 mm for tolerance purposes, was next subtracted from the upper shell mesh (Figure 6.29a). The resulting left and right caps (Figure 6.29b) were then finally connected through the addition of anterior and posterior fixation handles (Figure 6.29c). These were created through a) the generation of an initial curve connecting the two caps, b) the lofting of a surface between the curve and a 10 mm offset, c) the upwards extrusion of the surface by 10 mm and, d) the addition of two 5 mm hoops.

This thawing cap geometry was 3D printed on the EOS P700 machine in the DuraForm material (Figure 6.29d).

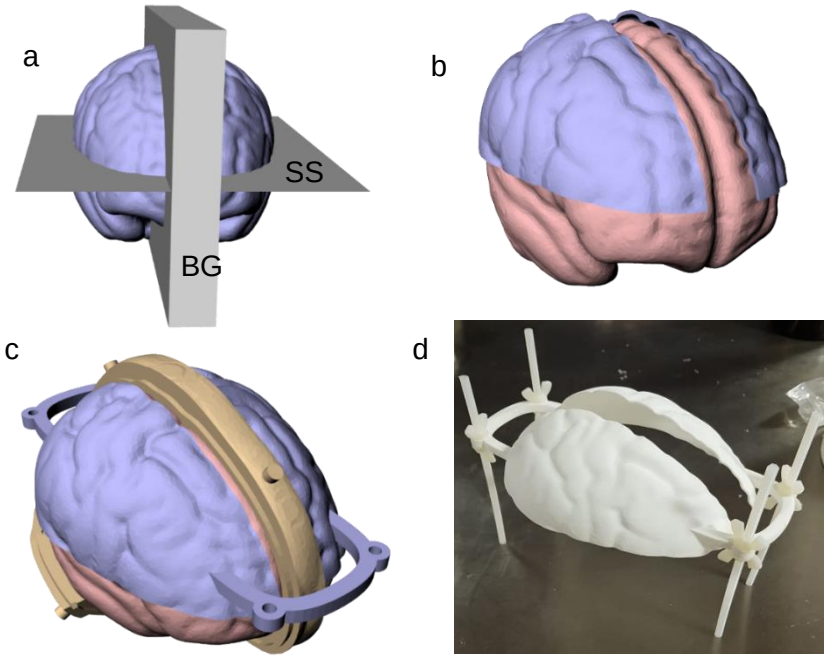

Figure 6.29: Production of the thawing cap. a) splitting of expanded shell brain mesh with splitting surface (SS) and subsequent subtraction of box geometry (BG) from top half of shell mesh; b) resulting left and right caps (purple) over brain mesh (pink); c) Addition of handles to caps with insert geometry positioned (gold) in place in brain fissures; d) Fabricated thawing cap with nylon rods and wing nuts.

An 8 litre bucket was next identified as a suitable container to thaw the brain in. Holes were made in the lid of the bucket, to which four 5 mm threaded nylon rods were threaded through and secured in place via nuts on either side of the lid. The thawing cap was then attached to the nylon rods via the hoops on the fixation handles and secured at a height that would centralise the brain in the bucket volume when placed in the cap (Figure 6.30).

Figure 6.30: Fabricated thawing cap attached to bucket lid through threaded nylon fixings and corresponding bucket.

6.2.3 Producing the Dural Septa and Skull

This section details the computational design and fabrication of the skull and dural septa parts described in Section 5.3 (p68).

In producing the dural septa part (Figure 6.31), construction curves were first produced for the definition of the skull locating tabs. These construction curves, illustrated in Figure 6.32a (p100), were each built by a) deconstructing the dural septa mesh into its vertices, b) manually selecting vertices lying along the center of the relevant aspect of the dural septa mesh and, c) stringing together the selected vertices into polylines. Three construction curves were generated using this method: a curve for the falx portion of the mesh, a curve for the left tentorial wing and a curve for the right tentorial wing.

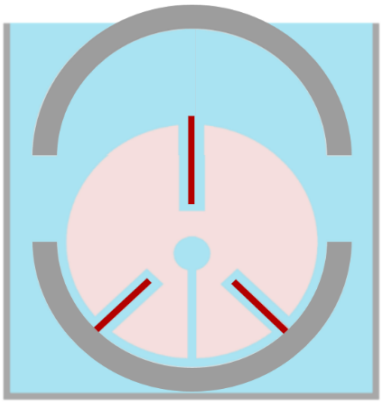

Figure 6.31: Cartoon depiction of skull and dural septa.

For each construction curve (cc), a tapered, continuous tab geometry was next generated (see Figure 6.32b). This was achieved by a) offsetting the cc by 1 mm inwards into the dural septa mesh and offsetting this curve left and right (relative to curve normals) by 3.3 mm to create o_1 and o_2, b) offsetting the cc outwards away from the dural septa mesh by 4.1 mm and offsetting this curve left and right by 2.3 mm to create o_3 and o_4, c) offsetting the cc

outwards away from the dural septa mesh by 5.6 mm and offsetting this curve left and right by 1.6 mm to create o_5 and o_6, d) offsetting the cc outwards away from the dural septa mesh by 6.1 mm to create o_7, e) lofting between o_1 and o_2 to create S_1, o_1 and o_3 to create S_2, o_2 and o_4 to create S_3 and o_3, o_4, o_5 o_6 and o_7 to create S_4 and, f) joining S_1, S_2, S_3 and S_4 surfaces into a single part and capping the resultant structure into a closed geometry.

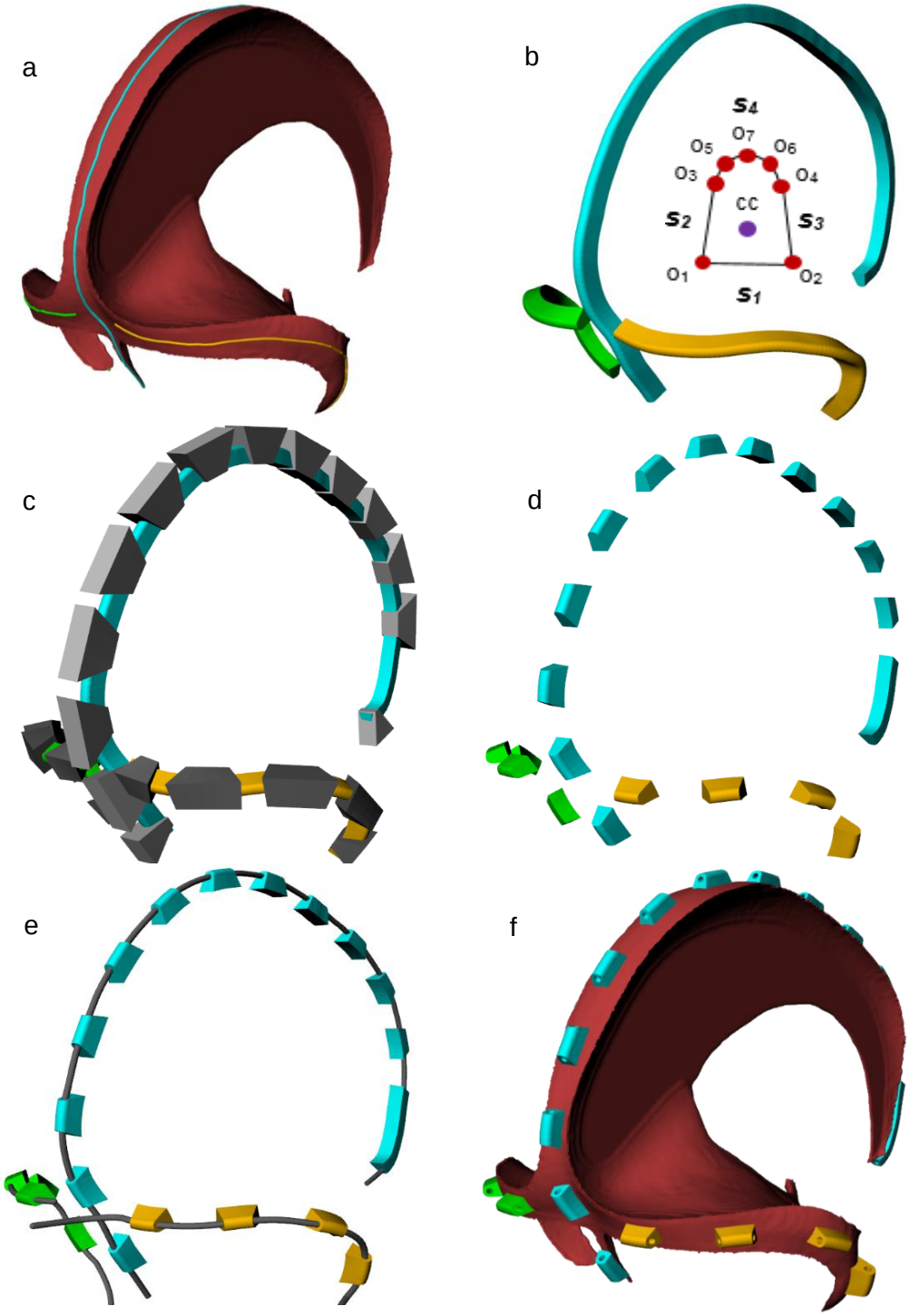

Figure 6.32: Definition of locating tabs for the dural septa part. a) construction curves used to build the falx tabs; b) continuous tab geometries built from construction curves with cross-section of construction curves used to generate geometry; c) wedge geometries (grey) positioned over continuous tab geometries (cyan, green and gold) for subtraction; d) subtraction result; e) pipe geometry (grey) prepared for subtraction from tabs (cyan, green and gold); f) falx (cyan), left tentorium (green) and right tentorium (gold) tabs with dural septa (red).

Each continuous tab geometry was next converted into a collection of discrete tabs by parametrically generating wedge structures along the construction curves and subtracting these from the continuous tab geometries (Figure 6.32c-d). To complete the tabs, pipe geometries were then subtracted from the tabs to generate tunnels for the string fastening system conceptualised in Figure 5.5 (p70). These pipes were created by offsetting each CC by 3.8 mm outwards away from the dural septa mesh and piping each offset into a 2 mm diameter pipe.

Upon completion of the tabs, anterior attachment features where next added. These were added to provide a means to attach the anterior most region of the tentorium to the skull in assembly. In creating these additions, the skull geometry was first split in half 94 mm down from the top of the mesh (Figure 6.33) to create an upper skull half (USH) and a lower skull half (LSH). Two box geometries were next built and intersected with the LSH at the locations shown in Figure 6.34a (p102), isolating the parts of the skull where the anterior-most regions of the tentorium attach to the skull. For each intersection result (Figure 6.34b), the boundary of the posterior surface was obtained, offset inwardly by 2 mm and smoothed into the curves shown in Figure 6.34c. These curves were then extruded downwards by 3 mm before adding two (6 x 5 mm) cuboid geometries with 2 mm tunnels engineered into them (Figure 6.34d), the former geometry serving as the plug for the eventual socket on the skull and the latter serving as a means to pull the plug down into the socket from the outside of the skull via some cord running out of the base of the LSH.

To complete the dural septa part, the tabs, anterior attachment features and dural septa mesh were finally combined into a single part (Figure 6.34e-f).

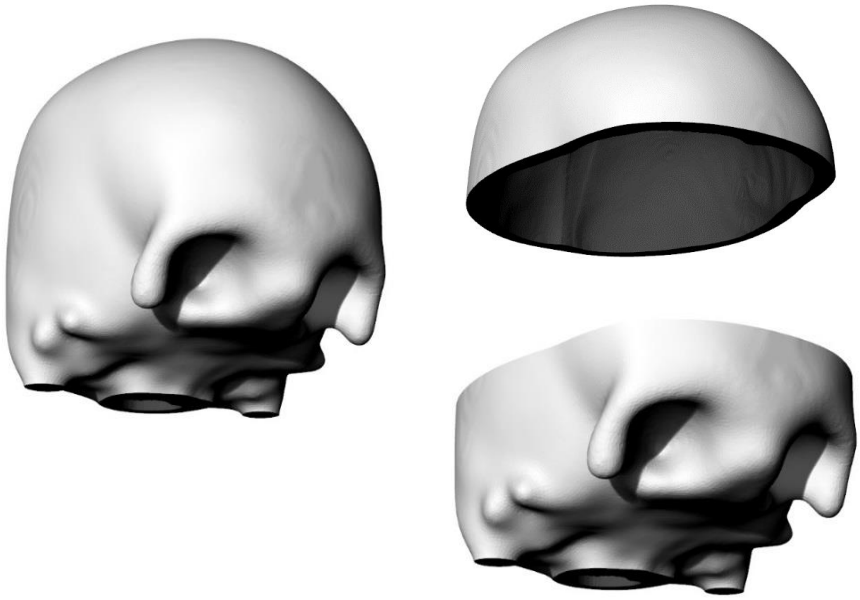

Figure 6.33: Splitting of skull into top and bottom halves.

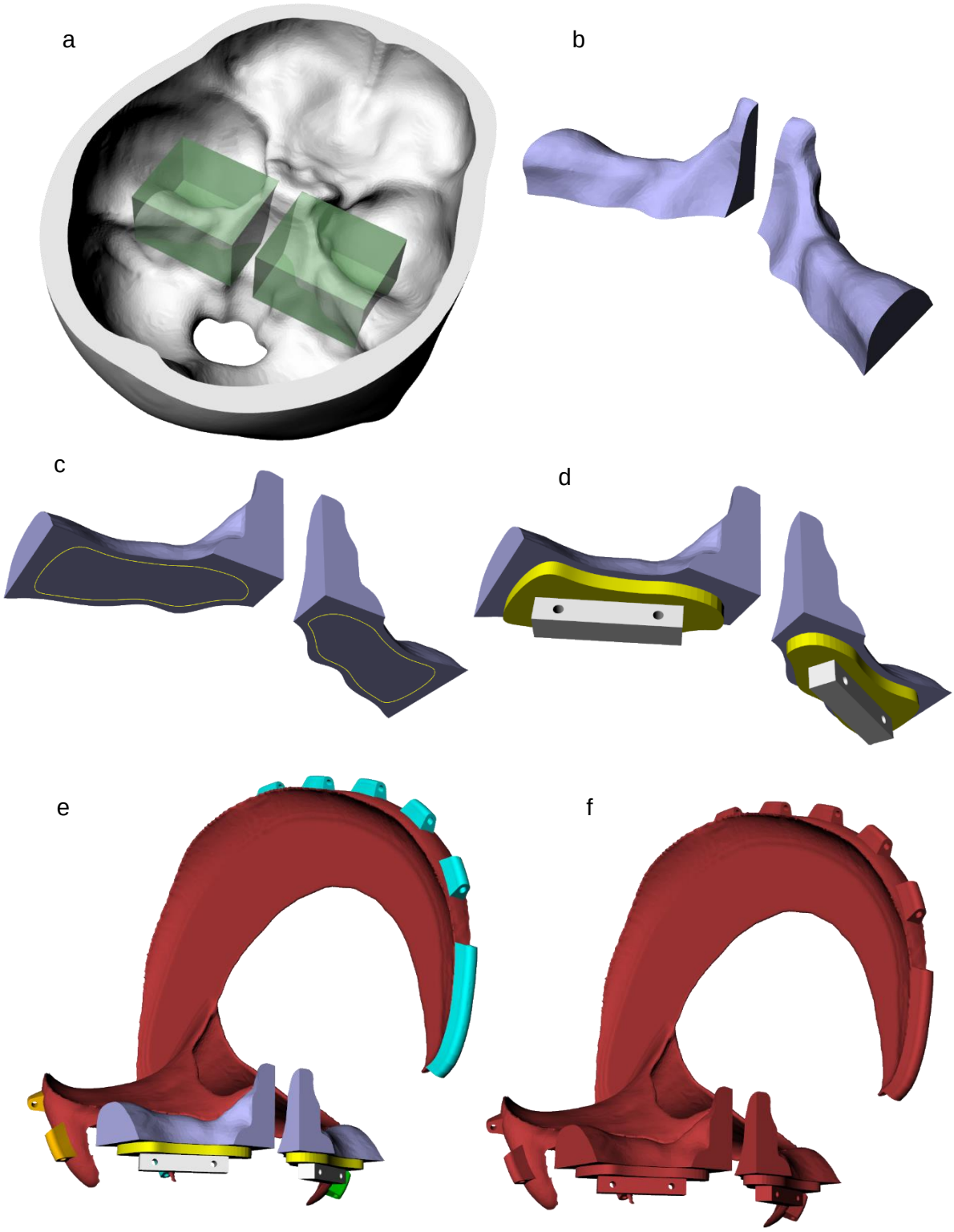

Figure 6.34: Completion of dural septa part through addition of anterior attachment features. a) boxes used to portion off segments of the cranial based for anterior attachment; b) result after intersection of boxes and lower skull half geometry; c) construction curve (yellow) created through offsetting and smoothing of inferior surface boundary; d) extrusion of boundary curve into step and addition of cuboid geometry with string attachment points. e) original dural septa geometry (red) with constructed tabs and anterior attachment features; f) complete dural septa part.

With the dural septa part complete, the lower and upper skull halves were next prepared.

For the LSH, corresponding features to the dural septa's added features (e.g. tabs) were first added. To achieve this, a complex of geometries (Figure 6.35b) was subtracted from the LSH (Figure 6.35a). This complex comprised: a) the geometries of Figure 6.32e (p100), but with tabs lengthened 3 mm either side and widened by 0.5 mm to allow the dural septa tabs to slide into position, b) the green boxes of Figure 6.34a combined with the yellow and grey (minus tunnels) geometries of Figure 6.34b, all dilated by 0.5 mm for fabrication tolerance purposes and, c) four additional 3 mm diameter tunnels projecting down away from the grey geometries of Figure 6.34d to serve as further string fixation tunnels. The result of the subtraction is shown in Figure 6.35c.

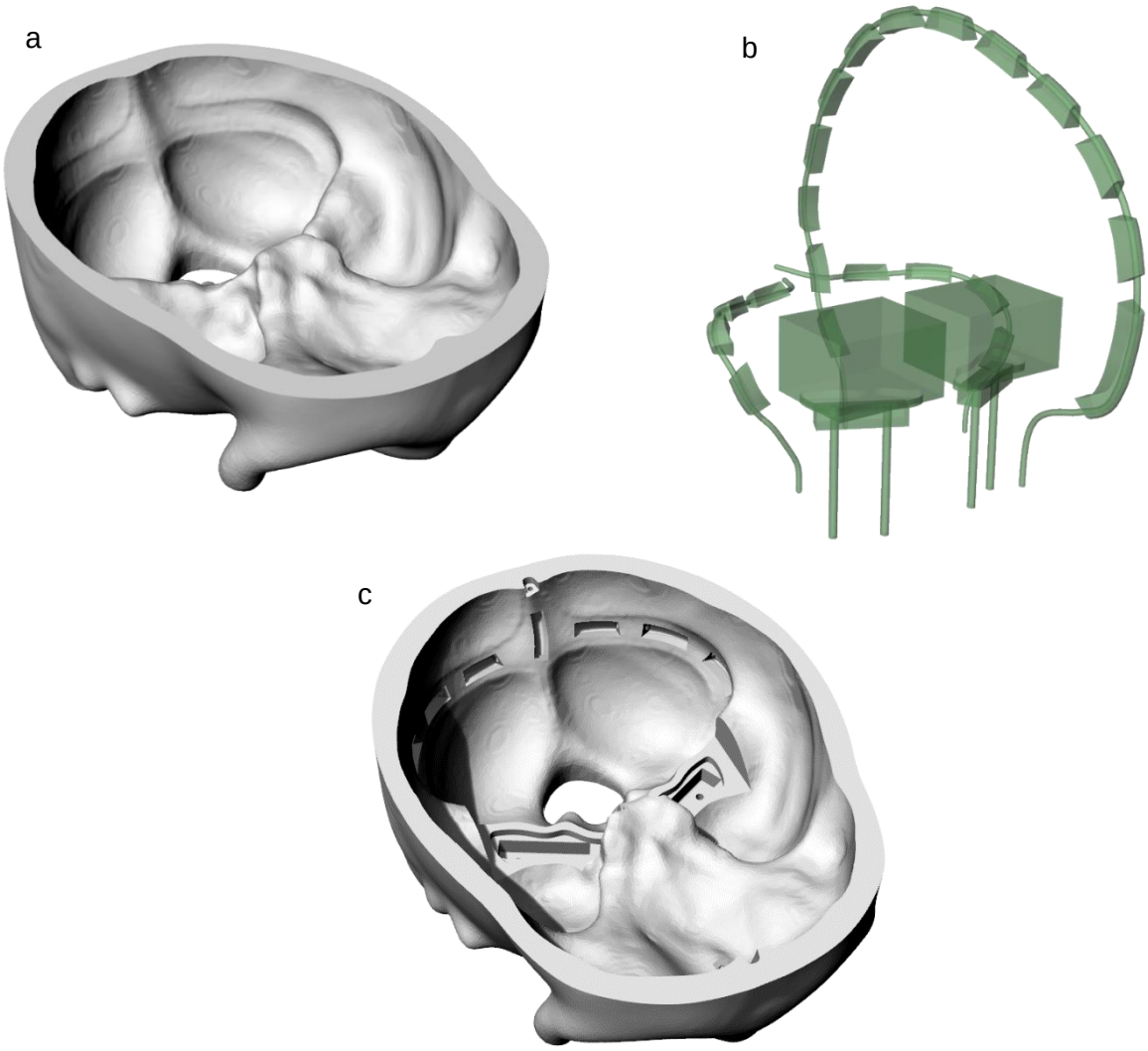

Figure 6.35: Addition of attachment features for the lower skull half: part 1. a) lower skull half; b) geometry prepared for subtraction from lower skull half; c) subtraction result.

With the dural septa attachment features added, the external geometries of Figure 6.36b were next added (Figure 6.36a-d). These comprised four fastening tubes (5 mm diameter) (red) for the fastening of the LSH to the USH via threaded nylon fixings, three hoops for tying down the string to the outside of the skull and three fixators (gold) to allow for mounting of the model for imaging, with the central fixator also providing a cap for the foramen magnum. Common to each fixator geometry is a 9 mm diameter, blind-ended tunnel, with a nut accepting slot opening out from its lateral aspect to allow for the use of a nut and bolt based fastening method (see Figure 6.37, p105) for the mounting of the model to a cradle.

On completion of the LSH, the previously described complex of geometries (Figure 6.35b) was next subtracted from the USH in order to create its corresponding features for the dural septa part (Figure 6.38a-c, p105). Four fastening tubes were then added to complete the USH part (Figure 6.38d).

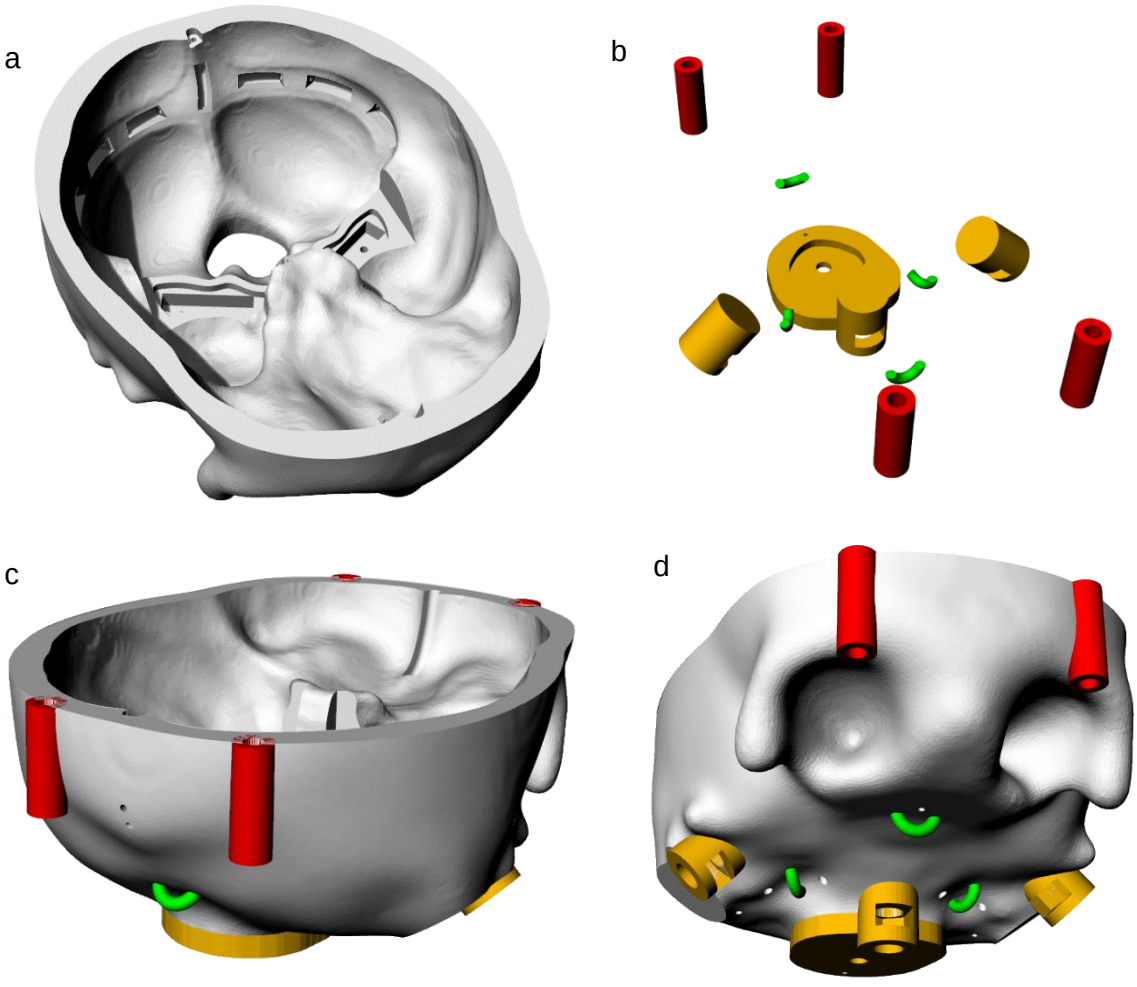

Figure 6.36: Addition of attachment features for the lower skull half: part 2. a) intersection result from Figure 6.35; b) fastening tubes (red), fixators (gold) and hoops (green); c) fastening tubes, fixators and hoops added to lower skull half; d) alternative view of (c).

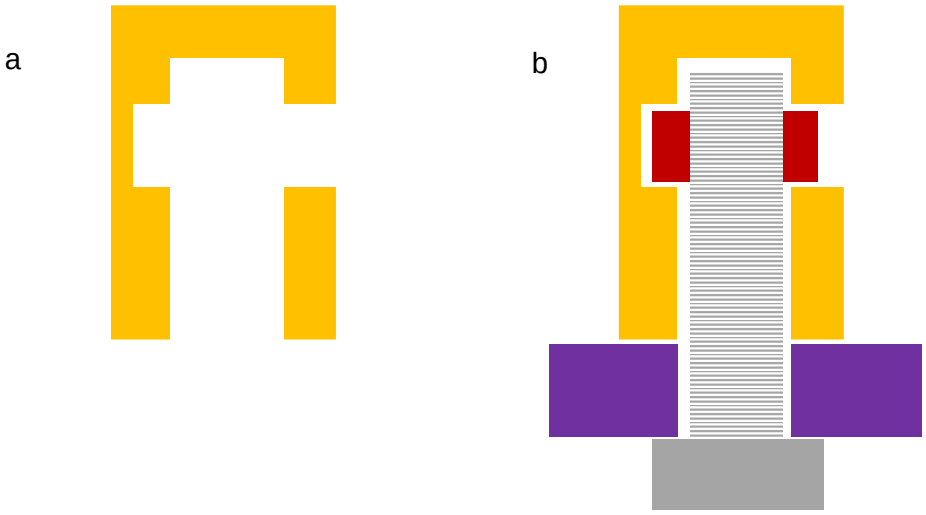

Figure 6.37: Principle of the fixator feature. a) fixator geometry; b) fixator geometry (gold) with portion of (yet to be described) phantom cradle (purple), bolt (grey) and nut (red).

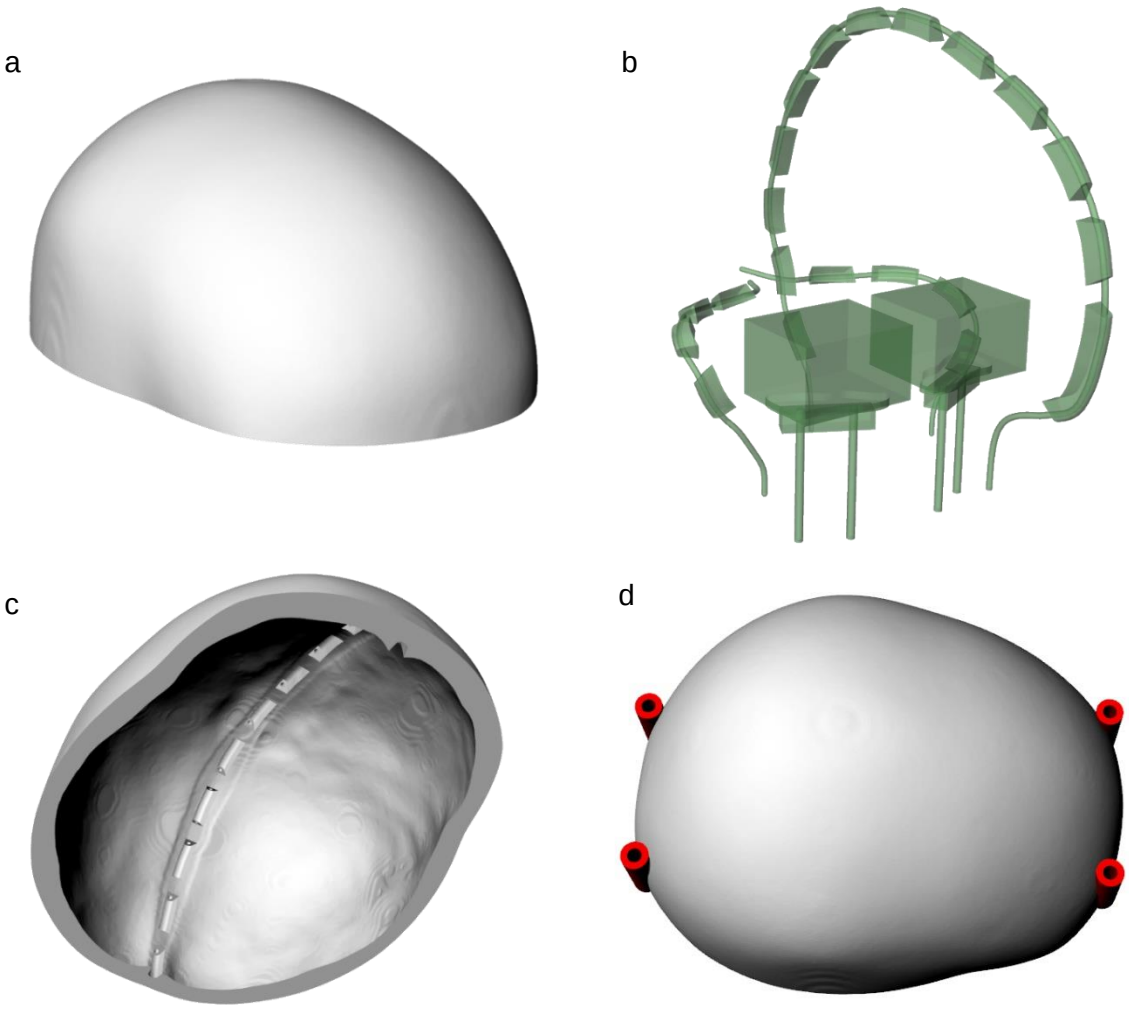

Figure 6.38: Addition of attachment feature for the upper skull half. a) upper skull half; b) geometry prepared for subtraction from upper skull half; c) subtraction result; d) upper skull half with added fastening tubes (red).

With the dural septa and the two skull halves complete (see Figure 6.39), the gasket mould was lastly prepared. This was achieved by first taking the surface of the LSH at the level of the split and extracting the inner and outer boundary curves. These curves were then offset and raised/lowered in various combinations to create the mould architecture displayed in Figure 6.40.

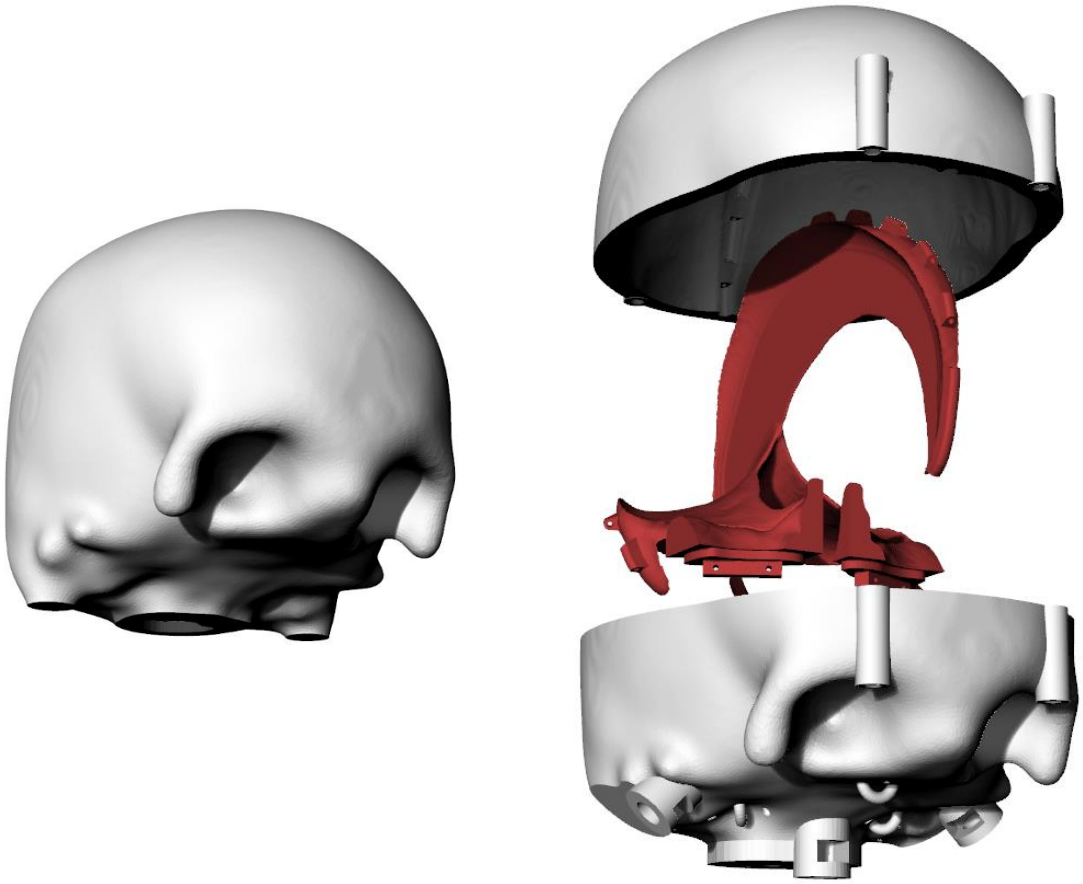

Figure 6.39: Completed skull halves and dural septa.

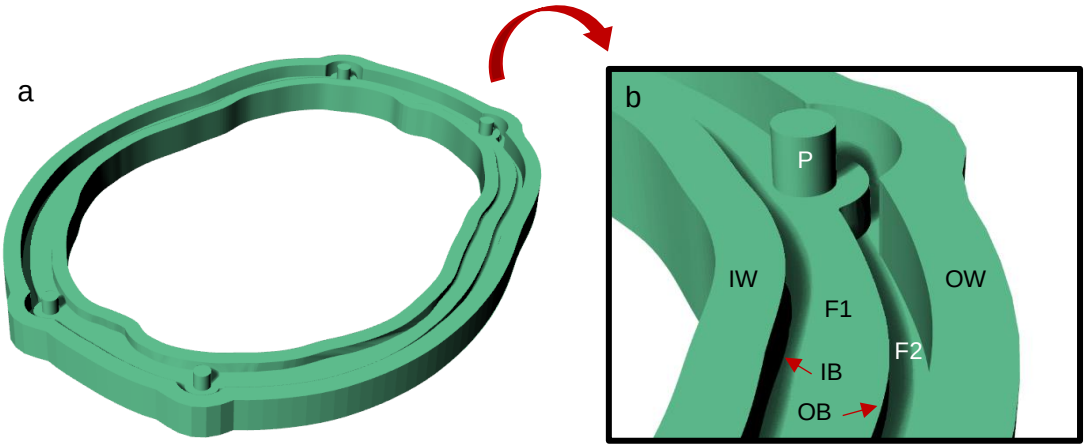

Figure 6.40: Mould for the fabrication of the silicone gasket. a) entire gasket mould; b) zoomed in view of mould cavity showing inner boundary (IB) of split surface, outer boundary of split surface, floor 1 of the mould (F1), floor 2 of the mould (F2), a pillar (P), inner wall (IW) and outer wall (OW).

With all parts defined, they were next fabricated. The USH, LSH and DS were all fabricated on a Connex 3 printer, with the USH and LSH being fabricated in the Veroclear material and the DS being fabricated in the FLX 9095 material. The gasket mould was 3D printed on an EOS P700 machine in the Duraform material.

Upon fabrication, the gasket mould was first treated with SuperSeal sealing agent and then used to cast the gasket. Mold Max 14 NV silicone rubber was chosen as the gasket material.

Due to fragility issues with the material, the FLX 9095 dural septa was immediately refabricated in a more durable material, DuraForm Flex, which has a tensional elastic modulus of 7.4 MPa [156]. The stiffness of this material is only a tenth of the anatomical stiffness, but again, it was considered to be sufficient as it is still many orders of magnitude stiffer than the brain. All fabricated parts are shown in Figure 6.41.

On inspection of the fabricated parts it was found that the dural septa could be manoeuvred into position in the skull reliably without the string fixation feature. In placing the dural septa into the LSH it was discovered that the tabs could be easily located into position by pressing down on the edges of the tentorial wing with a wooden tongue depressor. When the USH was then lowered onto the skull and dural septa it was found that the falx tabs naturally fell into place with only a small amount of force. Given the simplicity of this approach over the string fixation feature, the feature was abandoned going forward.

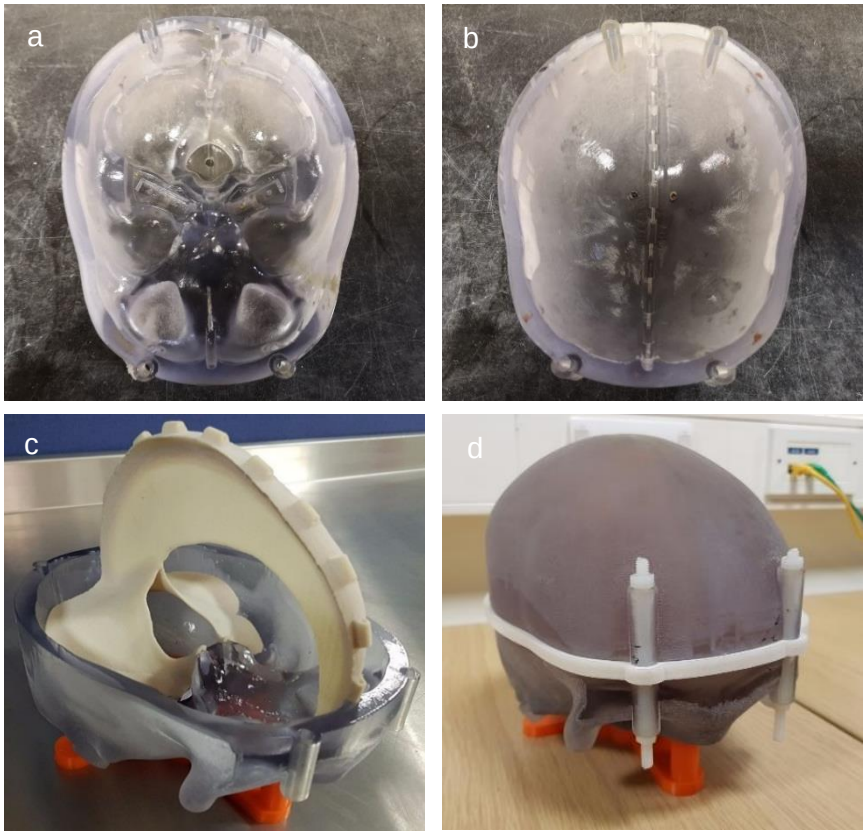

Figure 6.41: Fabricated skull and dural septa parts. a) lower skull half; b) upper skull half; c) lower skull half on orange stand with dural septa part in place; d) assembled skull resting on orange stand, showing white gasket and nylon fixings in fixation tubes.

6.2.4 Model Assembly

The previous sections detailed the fabrication of the elements required to build the non-tethered model. This section now details the method used for the model's construction.

The block diagram below (Figure 6.42) illustrates the general workflow that was used in the assembly. This can be considered as an updated version of the workflow conceived in Section 5.3 (p68), incorporating the changes necessitated by the change to CO ventricles.

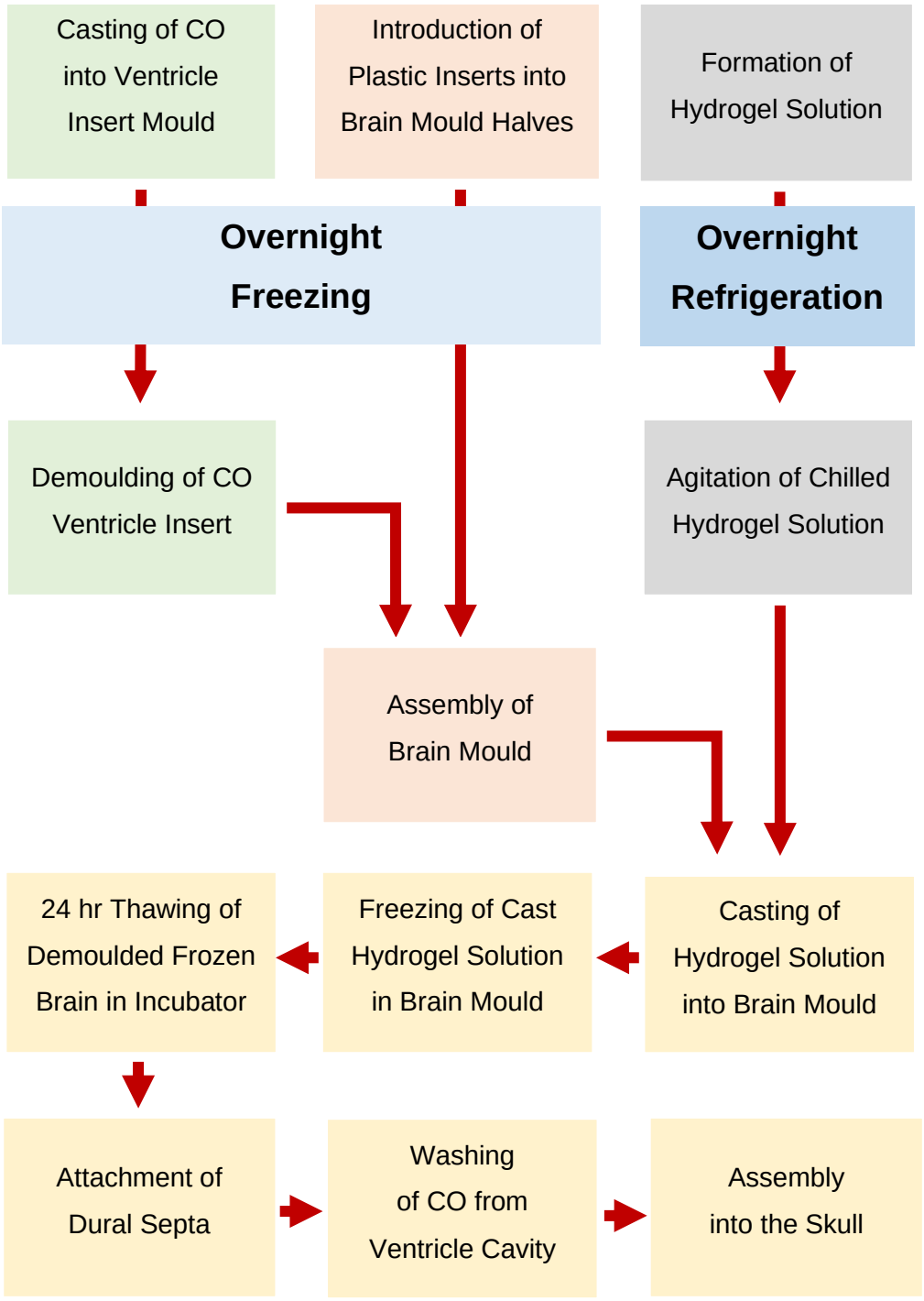

Figure 6.42: Block diagram of model assembly workflow.

6.2.4.1 Hydrogel Solution Preparation

Hydrogel solution preparation began the day before brain casting with the preparation of separate solutions of 6% PVA and 0.85% PHY, as detailed in [57]. When combined, as they are later on, these solutions work out to the *[3.00% PVA : 0.43% PHY : 96.57% DI $H_2$0]* formulation (rounded to 2 decimal places).

The PVA solution was created by adding 60 g of PVA (146 000 - 186 000 molecular weight, 99+% hydrolysed – Sigma Aldrich) to 940 g of vigorously stirring deionised water, heating to approximately 90°C, and mixing for 2hrs. A small 0.04 g quantity of gadopentic acid (an MRI contrast agent – Sigma Aldrich) was also added in an effort to increase the contrast between the brain and the water CSF.

The PHY solution was created by first slowly adding 8.5 g of PHY (Sigma Aldrich) to 991.5 g of vigorously stirring deionised water (at 20°C) to avoid clumping of the powder, before progressively heating the mixture to approximately 70°C for 2 hrs.

After 2 hrs of separate mixing, the two solutions were added together into a plastic container and mixed without heating until the solution reached room temperature. The container was then refrigerated to approximately 5°C overnight to chill the solution close to freezing such that, when cast the next day, the solution would freeze quickly around the CO ventricle insert. The next day, the container was removed from the refrigerator and placed into an ultrasound bath. The containers contents were then subjected to simultaneous agitation through ultrasound and a whisking motion (introduced with a pistol drill and whisk attachment) for approximately 5 minutes (Figure 6.43, p110), completing the solutions preparation. The use of the prepared solution is discussed later in Section 6.2.4.3.

6.2.4.2 Brain Mould Preparation

Brain mould preparation also began the day before brain casting. The plastic inserts, lightly coated in Vaseline to prevent adherence of the hydrogel material in demoulding, were first introduced into their respective mould halves. Once assembled, the two halves of the CBM were then placed into a -30°C freezer and left to freeze overnight, such that they reached approximately -25°C (the CH freezing temperature used in [57]) by the morning.

The CO ventricle insert was next prepared by melting CO and casting it into the mould depicted in Figure 6.25 (p96). The mould was then placed next to the CBM halves in the freezer and left to freeze overnight. The next day, the CO ventricle insert was retrieved from its mould and inserted into its socket already located into the lower half of the CBM (Figure 6.43a). The top CBM half was then positioned on top of the lower CBM half to complete its assembly (Figure 6.43b).

6.2.4.3 Brain Casting, Freezing and Demoulding

With the hydrogel solution and brain mould prepared, the solution, still at approximately 5°C, was poured into the mould (with the mould still sitting in the freezer) (Figure 6.43d). A heavy plate was then rested on top of the mould (to promote radial expansion of the cavity) before closing the freezer's lid and leaving the mould to freeze down to approximately -25°C over 24 hrs (Figure 6.43e), as detailed in [57] for the freezing of the CH solution, except with 6 hours extra freezing time to account for the larger size of the mould.

Figure 6.43: Casting, freezing and thawing of the hydrogel brain and assembly into the skull. a) assembled upper and lower mould halves and partially demoulded CO ventricle mould, all inside freezer; b) assembled mould in freezer, ready for casting; c) post-refrigeration agitation of hydrogel solution in ultrasound bath with whisking motion; d) casting of hydrogel into assembled brain mould; e) mould after 24 hour freezing with 20 kg weight on top; f) removal of top mould half after freezing and chiselling away of mould locating bands; g) frozen brain with trapped inserts placed into thawing cap; h) frozen brain and thawing cap inside water bucket, placed inside incubator; i) defrosted brain with trapped inserts replaced with dural septa (bucket drained for photo); j) defrosted brain and dural septa positioned into the top skull half for oil extraction; k) assembled skull.*

At the end of the freezing period, the top half of the mould was lifted off of the frozen brain, leaving behind its portion of the now trapped inserts (Figure 6.43f). Before fully removing the brain, undesired frozen material, such as the band spanning between the cavity and the locating bands (due to the seam of the mould), was chiselled off (Figure 6.43f). The frozen brain and trapped inserts where then extracted from the lower mould half and immediately placed into the thawing apparatus for defrosting (Figure 6.43g).

6.2.4.4 Brain Thawing and Oil Removal

Upon demoulding, the frozen brain with trapped inserts was immediately placed in the thawing cap and positioned into place in the 8 L thawing bucket, filled moments prior with 6.5 L of refrigerated (approximately 5°C) deionised water. The entire apparatus was then placed into a 10°C incubator for 24 hours to slowly thaw the brain (Figure 6.43h). At the end of the thawing period the fissure inserts were pulled away from the now soft brain and the hex rod of the ventricle insert was drawn out of the softened CO via its self-moulded tract in the brain (acting as the fourth ventricle - visible in Figure 6.43j).

With the brain preparation almost complete, the dural septa part was fed into its fissures (Figure 6.43i). The brain and dural septa were next positioned into the top half of the skull and allowed to rest upside down at the bottom of the bucket (still filled) (Figure 6.43j). The incubator was then set to 26°C (above melting temperature of CO but below melting temperature of phytagel) and the submerged brain left for 6 hrs to come up to temperature. After the incubation period, the melted oil of the ventricle insert was washed out of the moulded cavity by syringing some of the bucket's water in and out of the cavity. The evacuated oil was then skimmed off the top of the water, before drawing the brain and dural septa out of the top skull half, completing the preparation stages for the brain.

6.2.4.5 Assembly into the Skull

To assemble the brain into the skull, the lower skull half was first introduced into the bucket and rotated around to allow any trapped air to leave the part. The brain and dural septa were then drawn carefully into position in the lower skull half and the tabs of the septa were pressed into their respective sockets. The threaded nylon rods were next pushed into the fastening tubes on the lower skull half and the silicone gasket was positioned over the lower skull half and nylon rods. The upper skull half was then lowered down onto the lower skull half with brain and dural septa in place, using the threaded rods as guides. The skull halves were then finally fastened together using the nylon nuts, with the dural septa tabs naturally falling into position in the sockets of the upper skull half and a portion of the buckets water intentionally being trapped within the skull to act as the CSF (Figure 6.43k). This marked the completion of the non-tethered model's fabrication.

6.3 Fabricating the Tethered Phantom

This section details the steps taken towards fabricating the tethered phantom, using the base geometries acquired in Section 6.1. Its fabrication was eventually abandoned at the prototyping stage (see later).

6.3.1 Computer Generation of the Tethered Layer System

The first step that was taken towards fabricating the tethered phantom was to generate the computer model of the Skull-DS-PAC part. Described in Figures 6.44, 6.45 and 6.46 is the method that was used to construct the Skull-DS-PAC computer model with the segmented anatomical geometries. An axial cross-section of the model is used to present the method.

By combining the meshes defining the internal surface of the dural septa and the cranial cavity, a continuous surface was first produced (Figure 6.44a). This surface was then parameterised and isometrically re-meshed (Figure 6.44b) using the method described by Pietroni et al. [153], implemented in Meshlab.

Step 1:

Unification of meshes defining the cranial cavity and internal surface of dural septa.

Step 2:

Application of mesh parameterisation and isometric remeshing algorithms with iterative optimisation of input parameters to achieve ~ 4 mm spacing.

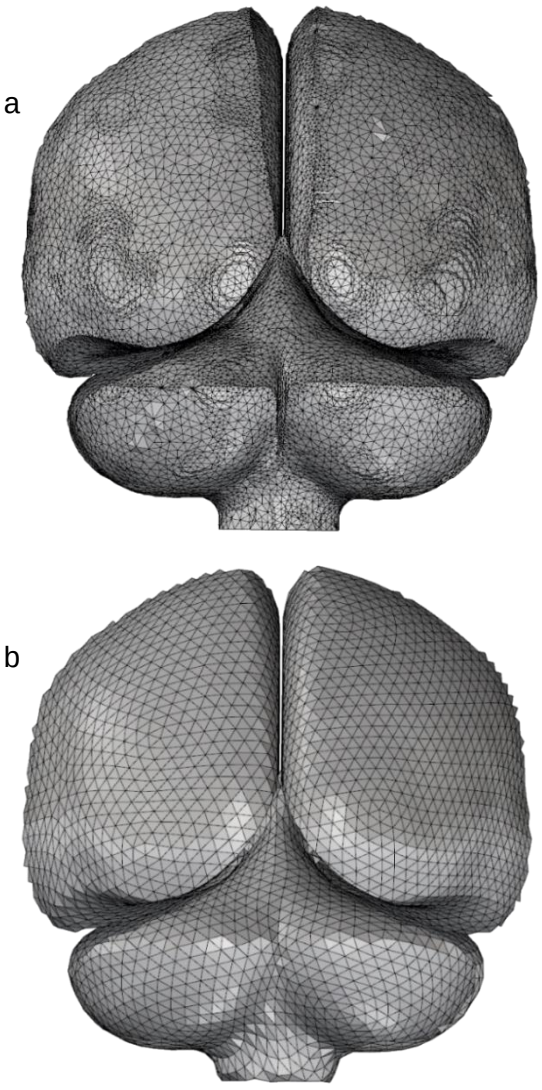

Figure 6.44: Generating the layer system: part 1. a) unified mesh of cranial cavity and dural septa with native vertex spacing (axial cross-sectional view); b) result of isometric parameterisation.

Following isotropic remeshing, 1 mm diameter cylinders of appropriate length were then positioned on the now isotropically spaced vertices and orientated towards the brain mesh using the vertex normals and mesh-ray intersection events (Figure 6.45). A length rule was imposed here to avoid the generation of a tangle of tethers in the cistern regions.

Step 3:

Inward projection of a pseudo-infinite line (ray) normal to each vertex.

Step 4:

Computation of intersection events between each ray and the brain mesh.

Step 5:

Generation of lines spanning between vertex points and their respective ray intersection events.

Step 6:

Dilation of lines into 1 mm diameter cylinders, capped with hemispherical ends.

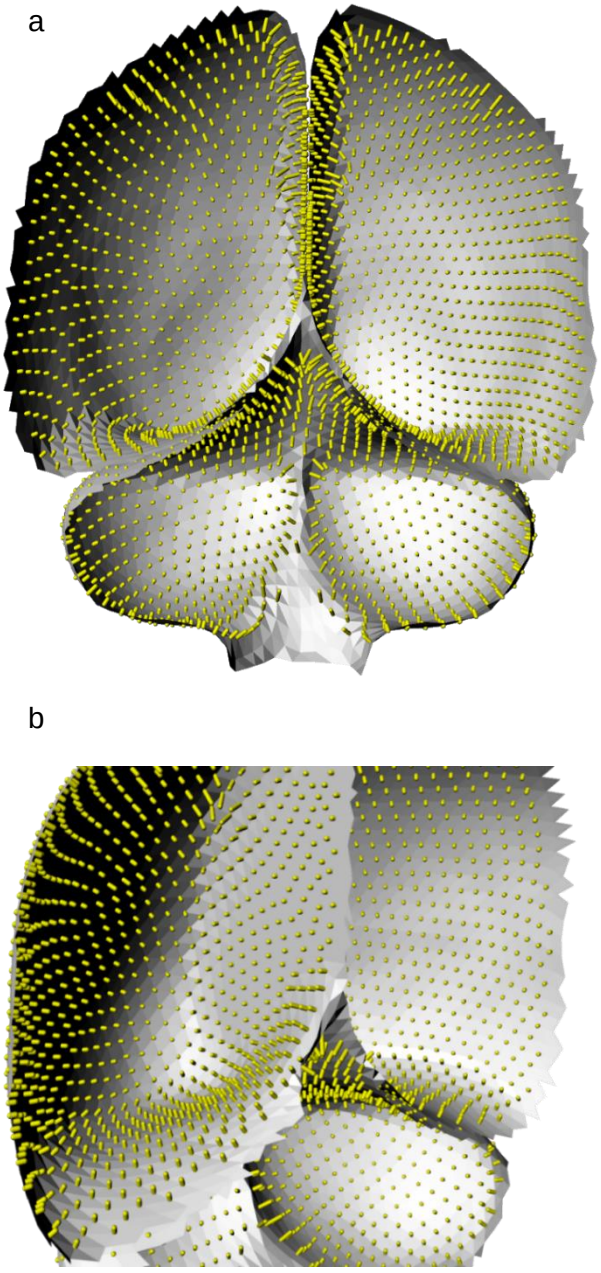

Figure 6.45: Generating the layer system: part 2. a) 1 mm diameter, inward projecting cylinders, positioned on vertices of parameterised mesh; b) alternate view of mesh and cylinders.

Once the tethers were generated, the parameterised mesh was removed. The skull and dural septa meshes were then introduced along with a pia layer which was created by thickening the surface mesh of the brain inwards by 1 mm. This completed the Skull-DS-PAC model (Figure 6.46).

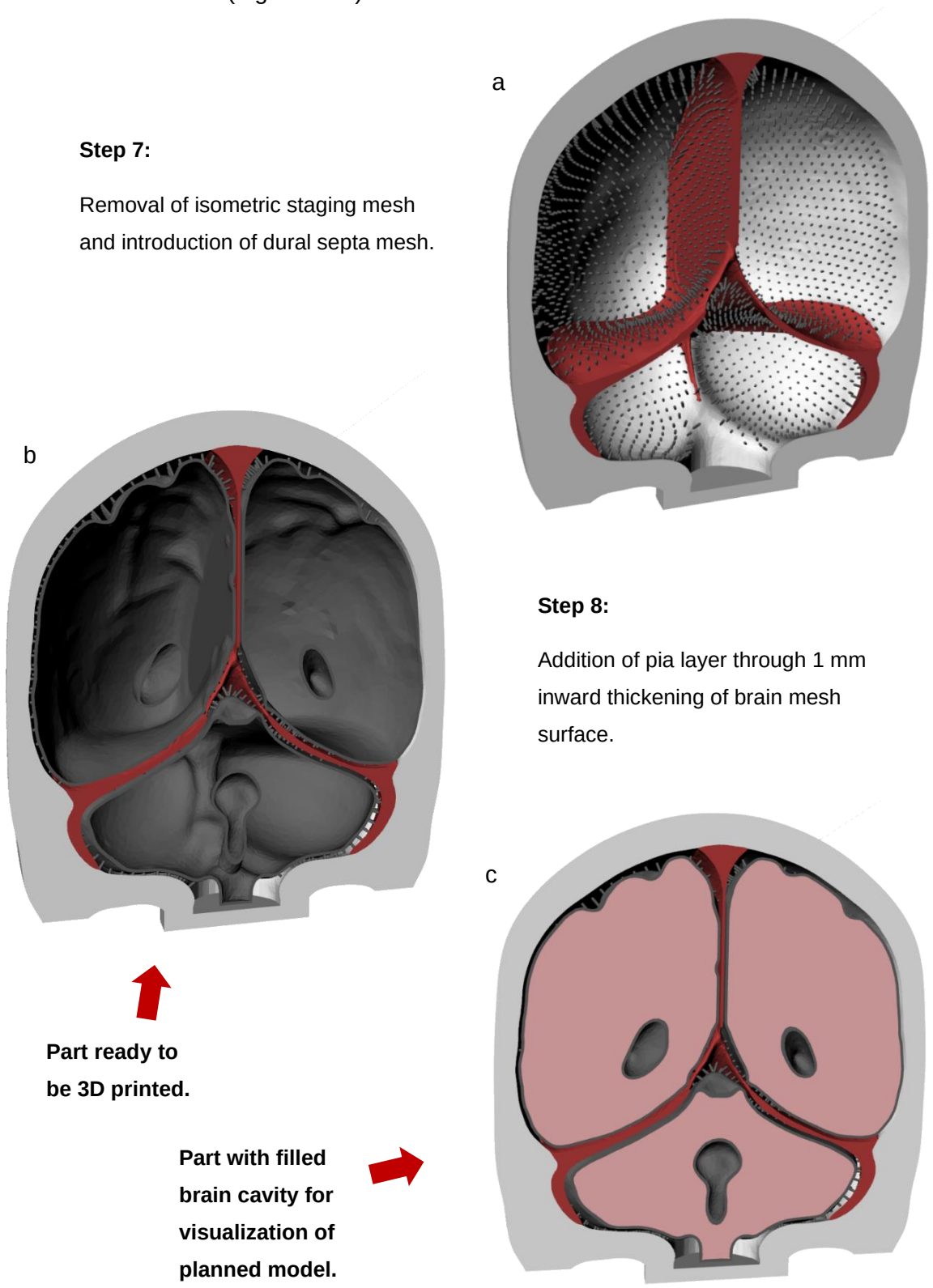

Figure 6.46: Generating the layer system: part 3. a) cylinders alongside skull and dural septa meshes; b) addition of 1 mm pia layer, completing the part; c) completed model (b) with filled brain cavity for visualization (CSF not included).

6.3.2 Problems Encountered in Prototyping

Before printing the Skull-DS-PAC part, prototype specimens (Figure 6.47) were fabricated to assess the feasibility of the fabrication workflow. These specimens were created with a Polyjet printer lacking the soluble support module and so an altered design featuring holes in the now 2 mm skull layer and 2 mm tethers spaced 4 mm apart, instead of 1 mm tethers spaced 3 mm apart (see Figure 6.47). These changes were made to provide the means and architectural strength to manipulate out the traditional break-away (brittle) Polyjet support material which was in use with the printer immediately available for prototyping.

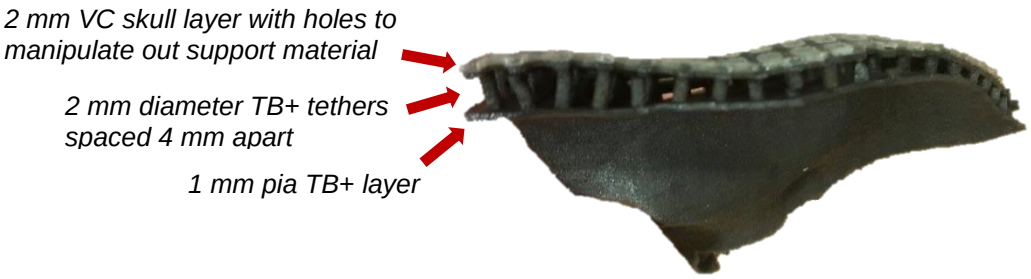

Figure 6.47: Prototype specimen of Skull-DS-PAC part with altered dimensions for production feasibility. Geometry of the specimen is a segment of the model presented in Figure 6.46b.

Unfortunately, however, it was immediately found that, even at 2 mm, the tethers were exceedingly fragile where they connected with the pia and skull layer, indicating that the smaller 1 mm tethers of the tethered model design would very unlikely survive the washing forces when fabricating the full model. This was not confirmed by printing the full part as it was quoted to cost ~£4500 and funds needed to be managed between the two models.

It was identified that this fragility may have been in part due to the bitmap approximation of curves the Polyjet technology makes in printing, which has been found to significantly lower the strength of TB+ specimens below the material's nominal strength (due to stress concentration) [154]. Considering the high surface to volume ratio and variable orientation of the tethers, it is possible that these features suffer especially from the bitmap approximation issue.

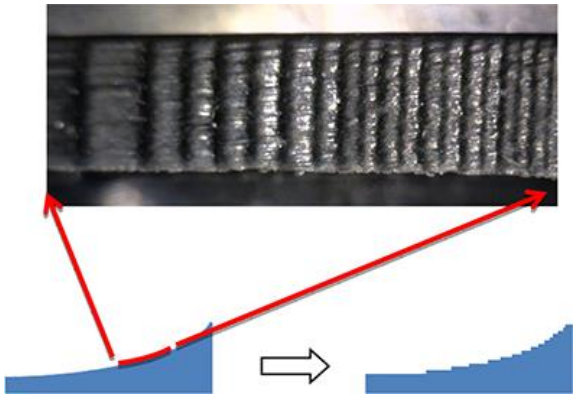

Figure 6.48: Polyjet bitmap approximation of curves. Top image is a view of the stepped side of a TB+ dog bone specimen. Reproduced from Moore and Williams [154].

It has also been found that the TB+ material is particularly prone to the accumulation of microscopic voids at print layer and print head boundaries and that the multi-material interface has very erratic fatigue behaviour that leads occasionally to “very premature fatigue failure” [154].

However, the fragility could also be due to the geometries of the Skull-DS-PAC part being at the lowest end of the technologies printing capability and it is not uncommon to see those experienced with the technology recommending higher minimum feature sizes than the manufacturers recommendation. Yet, even the use of a 1 mm minimum feature size proved problematic in the design of certain elements of the tethered model (e.g. the pia).

Regardless, the encountered fragility presented as an insurmountable obstacle in the fabrication of the tethered model. Given that no other printing technology was capable of printing the Skull-DS-PAC part and that no other route to fabrication could be identified other than the *in situ* casting route, it was decided that the development of the tethered model would be discontinued (within the scope of this project).

6.4 Chapter Summary

This chapter began with the acquisition of the anatomical geometries necessary for the construction of the tethered and non-tethered models. These were segmented from an averaged dataset of 152 human MRI scans. The construction of the non-tethered model was next presented.

All parts of the non-tethered model design were fabricated, however, a few changes were made to the production workflow (due to the necessity of using CO as the sacrificial ventricle insert material) and the string-fixation feature was also abandoned due to it being unnecessary. The composite brain mould, thawing apparatus and fabrication workflow were found to be successful in producing a geometrically and mechanically realistic (biofidelic) brain, and the dural septa, skull and assembly workflow were also found to be successful in assembling the brain into the larger phantom (the inspection of the realism is presented in the next chapter).

At the time of writing, the non-tethered model is the first to combine a biofidelic brain with fluid filled ventricles, biofidelic dural septa, biofidelic fluid filled SAS and biofidelic cranial cavity. This was made possible by the development of an entirely novel set of moulds (composite brain mould and ventricle mould), parts (dural septa, skull and thawing apparatus) and fabrication/assembly workflows.

When it came to fabricating the tethered model design, however, it was identified during prototyping that the tethers of the Skull-DS-PAC were exceedingly fragile and that they

would unlikely survive the washing forces involved in forming the full model. Given that the no other means of fabrication could be identified, the development of the tethered model was discontinued.

However, the computational design of the Skull-DS-PAC part still presents as a significant novel step in the production of a PAC featuring model. The model is theoretically fabricable and the technological limitations that need to be overcome are relatively small. Most 3D printing technologies currently struggle to print sub-mm features, but with the upward trend of resolution and accuracy in 3D printing, it is not unreasonable to assume that features of the Skull-DS-PAC part will be able to be printed effortlessly in the future and in a much larger range of materials. Multi-material silicone printing technologies [155], in particular, are promising, as these may even be able to print materials as soft as the brain one day. This would allow for the entire printing of the tethered model (Figure 6.49) in a single build, with only the uncured silicone support needing to be drained and replaced with a suitable fluid afterwards.

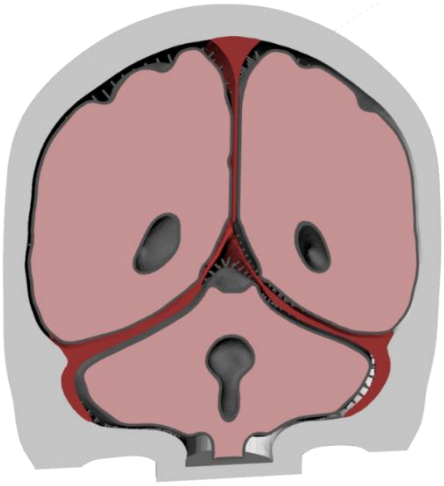

Figure 6.49: SAS-DS-PAC computer model with additional brain volume.

In building two models it was hoped that an answer could be reached on the question of the influence of the brain-skull tethering in PBS. However, it was identified that an answer could still be obtained through the comparison of the non-tethered model's PBS to that of the *in silico* project's computational model. This model was formed from the same base geometries as the non-tethered model, but with the inclusion of a mathematically defined brain-skull tethering feature (see later in Chapter 9).

The next step, however, was to assess the geometric and mechanical realism of the non-tethered model. This is presented in the next chapter.

7 PHANTOM REFINEMENT

The previous chapter detailed the construction of the non-tethered model, hereafter referred to as simply “the phantom”. Introduced by Figure 7.1, this chapter details its initial assessment and optimisation prior to its use as a research tool and contains the following novel work:

- An assessment of the phantom’s assembled geometry through MR imaging.
- Improvements to the tentorial insert to mitigate against cerebellar tearing on brain demoulding.
- Improvements to the ventricle insert to mitigate against trapped oil in ventricle washing.
- An assessment of the brain’s stiffness through indentation testing of cerebral sections.
- Improvements to the brain’s stiffness through changes in hydrogel formulation and thaw rate and measurement of hydrogel density.

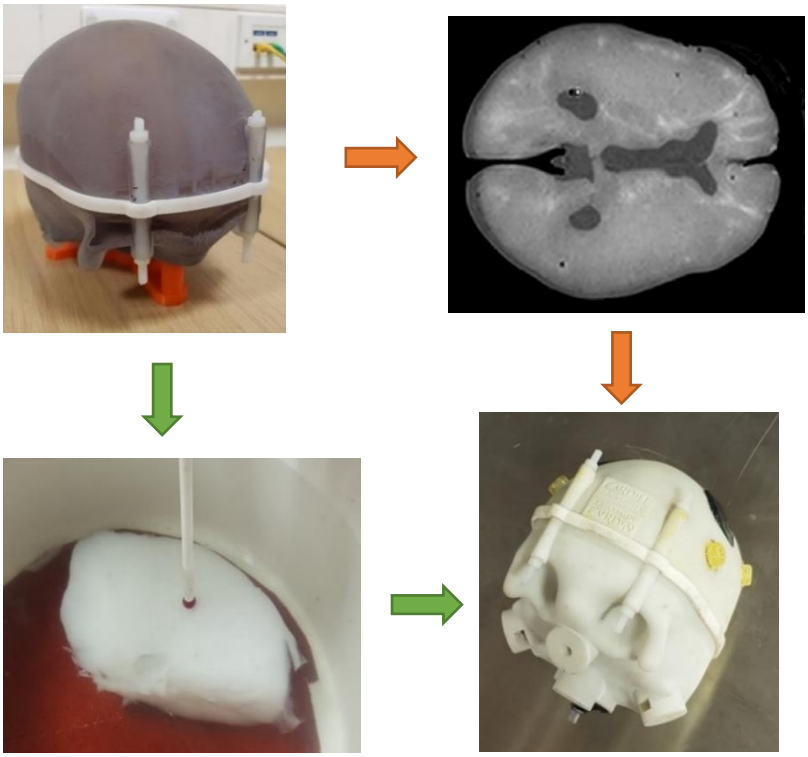

Figure 7.1: Chapter storyboard showing the refinement of V1 phantom (top-left) to the V2 phantom (bottom-right) following mechanical (bottom-left) and imaging (top-right) assessment. Images are reshown and discussed later in the chapter.

7.1 Construction Quality

This section details the assessment of the phantom's construction through MR imaging and the subsequent improvements that were made to optimise it prior to use. All MR imaging was performed at the Cardiff University Brain Research Imaging Centre (CUBRIC).

7.1.1 MRI Assessment of the Phantom

To assess its construction, the phantom was placed inside a Siemens 3T Prisma MRI system and scanned to obtain cross-sectional images. MRI was used for this purpose as CT images of the phantom were found to have no contrast between the hydrogel brain and the water CSF (see later in Section 8.2.3, p146).

In the knowledge a multi-axis cradle would be later required for imaging the phantom in different positions, scanning sequences were developed around the use of a single channel head coil, due to its simple cylindrical cavity (see later in Figure 8.2, p138). For these initial imaging sessions, however, the phantom was simply rested in the supine position on its four posterior fastening tubes.

A variety of scanning sequences were trialled with the phantom. A T1-weighted, gradient echo scanning sequence with 0.71 x 0.71 x 0.71 mm voxel size and three scan averages was empirically found to produce the best images for assessment of the phantom. This sequence produced the best trade-off between voxel size, image noise and geometrical distortion, due to stark magnetic susceptibility differences between phantom materials. Figure 7.2 (p120) and Figure 7.3 (p121) display a selection of axial, sagittal and coronal images produced from the imaging sequence. In these images it can be seen that the desired geometrical relationships were largely achieved. The following sub-sections provide a discussion of the individual elements.

7.1.1.1 The Brain

On assembly, the hydrogel brain was noted to be unrealistically stiff (further analysis in Section 7.2, p128). In terms of geometry, however, it formed more or less as intended according to the MR images (Figure 7.2 and Figure 7.3) and the subsequent segmentation of the brain (performed in the image processing software 3D Slicer) (Figure 7.4, p122), showing well defined lobes, fissures and cavities. It can be seen that, while slightly oversized, the ventricular cavity is similar in shape to that of the anatomical version. Due to the poor contrast at the boundary of the brain, the segmentation should only be considered an approximation. The addition of the MR contrast agent gadopentic acid was intended to mitigate against this type of problem, however, it can be seen to have concentrated in specific areas of the hydrogel during freezing. Consequently, the use of contrast agent was abandoned going forward.

A near complete-tear can be seen between the brain stem and cerebrum. This was produced on removal of the tentorial insert during assembly.

7.1.1.2 The SAS

A SAS of variable width is clearly present around the perimeter of the brain. Its precise dimensions, however, are difficult to measure due to boundary artifacts, signal drop-off away from the isocenter and image noise. Nonetheless, a SAS width roughly in the region of 1-2 mm can be found in the parietal, temporal and frontal regions. The occipital SAS width, however, appears to be greater, growing up to approximately 6 mm in some regions. This may be due to the noted unrealistic stiffness of the brain not allowing the brain to sit correctly in the cavity, rather than an issue with its moulded shape.

7.1.1.3 The Dural Septa and Cranial Cavity

The MR images show that the dural septa locates correctly in the cranial cavity without the cord fixation mechanism. Except for some buckling, it can be seen that the dural septa takes on a similar conformation within the cranial cavity to that of the anatomical septa (see Figure 7.3), creating realistic anatomical partitions.

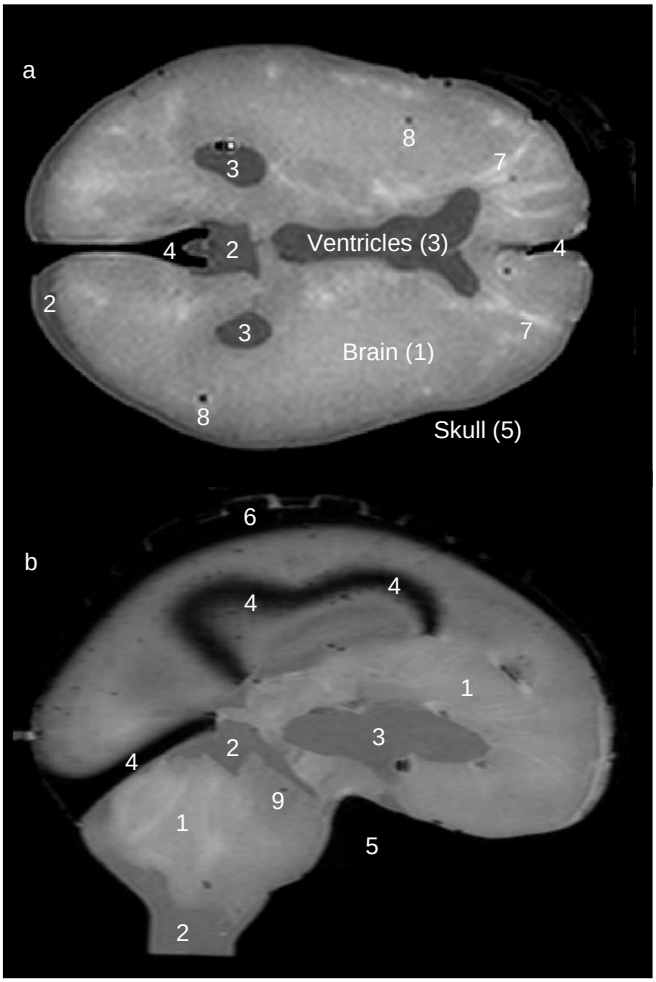

1) *Hydrogel brain*

2) *SAS (water)*

3) *Ventricle cavity (water)*

4) *Dural septa (no signal)*

5) *Skull (no signal)*

6) *Dural septa tab in groove*

7) *Gadolinium streak*

8) *Air bubble*

9) *Tear in hydrogel*

Figure 7.2: Labelled MR images of the V1 phantom. a) axial image; b) sagittal image.

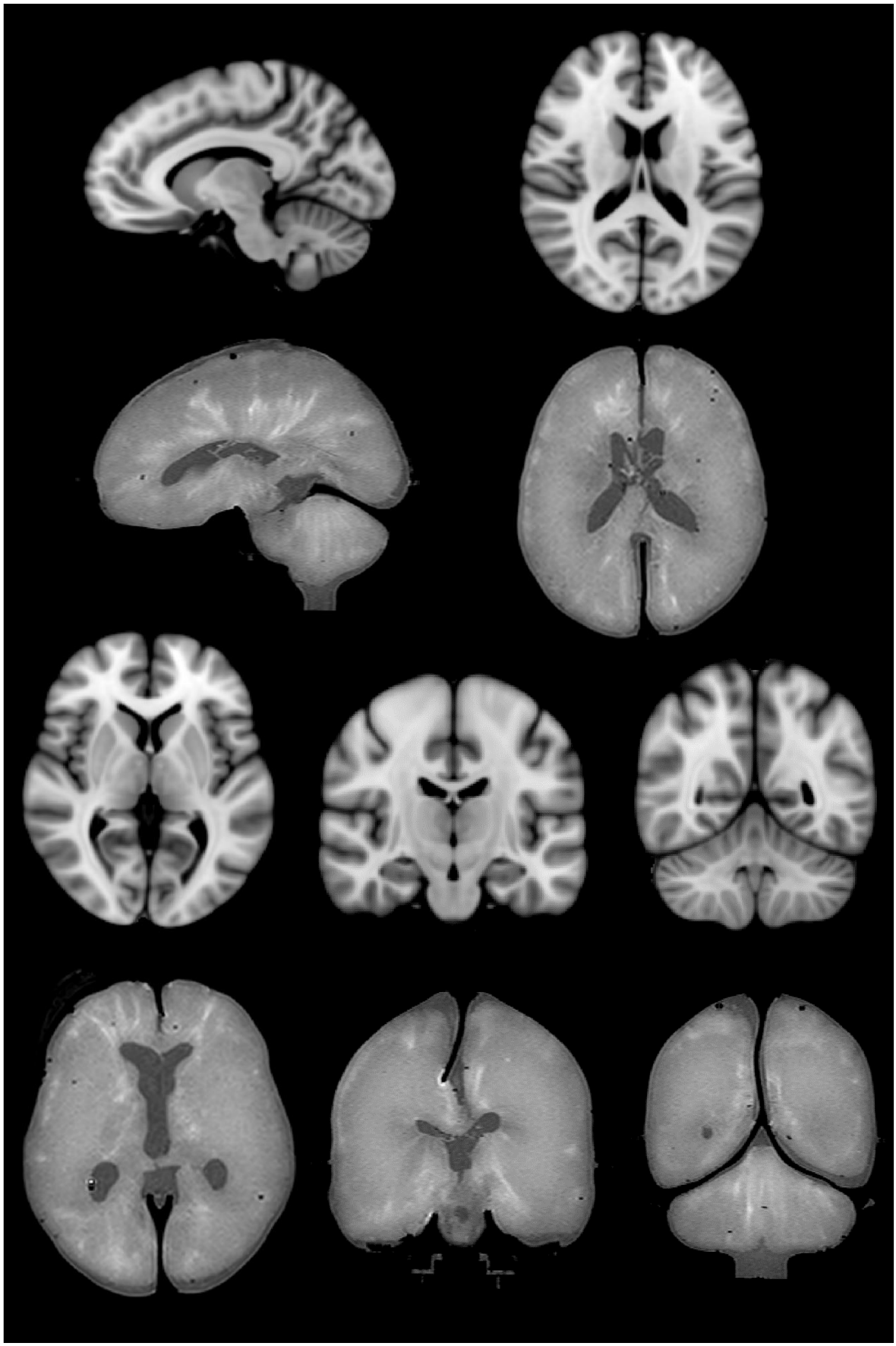

Figure 7.3: Comparison between the MNI ICBM152 and V1 phantom MR images. MNI ICBM152 images sit on top of corresponding phantom images. See dural septa buckling in last two images.

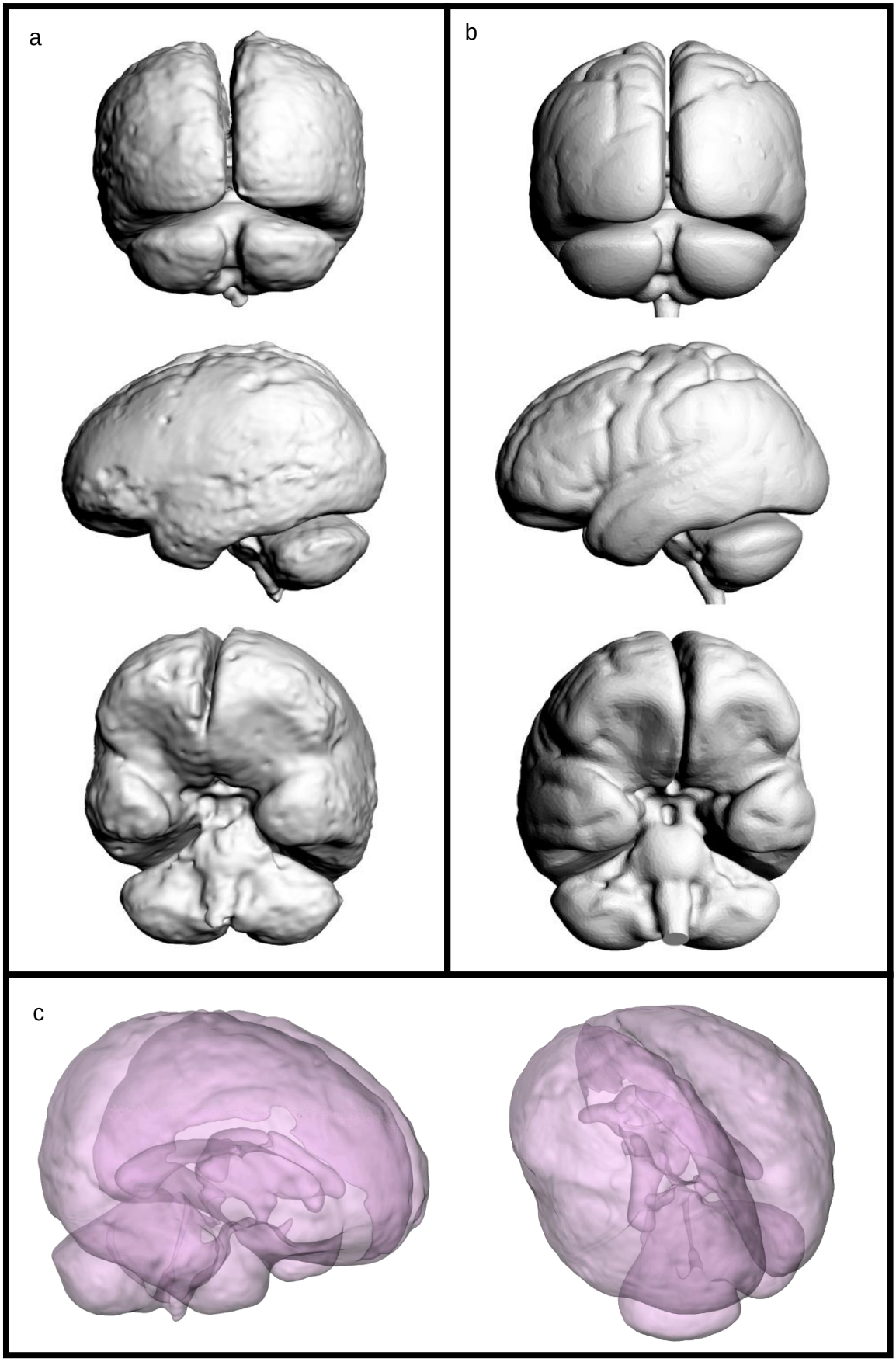

Figure 7.4: Comparison of geometry between brains segmented from the phantom and MNI ICBM152 datasets. a) three views of the phantom's MRI segmented brain obtained through thresholding only (no smoothing); b) three views of the MNI dataset's segmented brain; c) two translucent views of segmented phantom brain.

7.1.2 Improvements to the Tentorial and Ventricle inserts

Following the observation of the hydrogel tear in the initial phantom, improvements to the tentorial insert were made (Figure 7.5). This tear came about due to gripping of the hydrogel material around the protrusions and sharp edges of the insert (see Figure 7.5a). The insert was consequently remade with a design that lessened these features. In redesigning the CAD model, the protrusions were first smoothed away and the sharp edges removed. The linking piece was then absorbed into the geometry of the altered tentorial insert, before splitting the resultant geometry into two to further aid in its removal.

The phantom was next remade a few times with the redesigned tentorial insert and no subsequent tears were found. On remaking the phantom, however, it was revealed that the full removal of the oil in the initial phantom was merely a chance result, as trapped oil was found in the ventricles of all subsequent phantoms (usually in one of the lateral horns). This occurrence was likely due to the varying morphology of hydrogel bridges that can be seen bridging across the ventricle cavity in all phantoms (see Figure 7.6b, p124). These hydrogel bridges are likely a result of the CO positive snapping during freezing which, more often than not, lead to full partitioning of the cavity by hydrogel material, preventing removal of oil on washing.

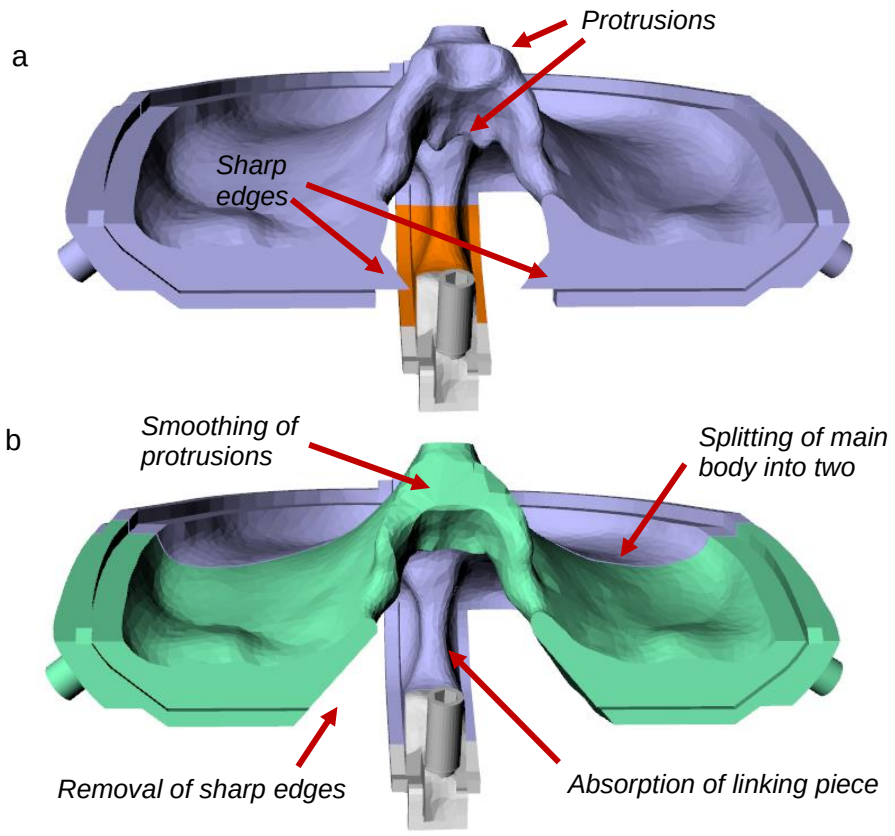

Figure 7.5: Splitting and smoothing of the tentorial insert. a) V2 insert after accommodation of the coconut oil ventricle; b) V3 insert after splitting of the tentorial insert into two pieces, removal of the sharp jaws, absorption of the linking piece and smoothing of the protrusions.

Trapped oil in the phantom reduces its mechanical realism because, if not removed when liquefied at 26°C, it will revert to a solid and remain as such in the ventricle cavity, reducing its collapsibility and altering the delicate density differential between the brain and its fluid.

In an attempt to solve this problem, ice ventricles were trialled with the CBM. These were made using deionised water and the CO ventricle mould. While producing a slightly different shape to that of the CO ventricles (see Figure 7.6d), it was found that ice ventricles could be used to successfully mould a ventricular cavity without the problems associated with the CO ventricle and so were used going forward.

The different ventricular shape created through using the ice ventricles is suggested to be due to the +5°C hydrogel solution instantly freezing around the -25°C ventricle positive on casting, and then thawing as temperature evens out throughout the cavity, creating a formed solid hydrogel barrier between the ventricle insert and the remaining hydrogel solution. Given that the contents of the mould cavity likely stays above 0°C for at least a couple of hours after casting, the ventricle positive then either completely or partially melts. However, with a hydrogel barrier encapsulating the ventricle positive, the melt water likely redistributes inside the solid barrier under expansive forces from the outside-in freezing of the hydrogel solution (creating the different moulded ventricle shape), rather than flowing out and locally deconcentrating the hydrogel solution.

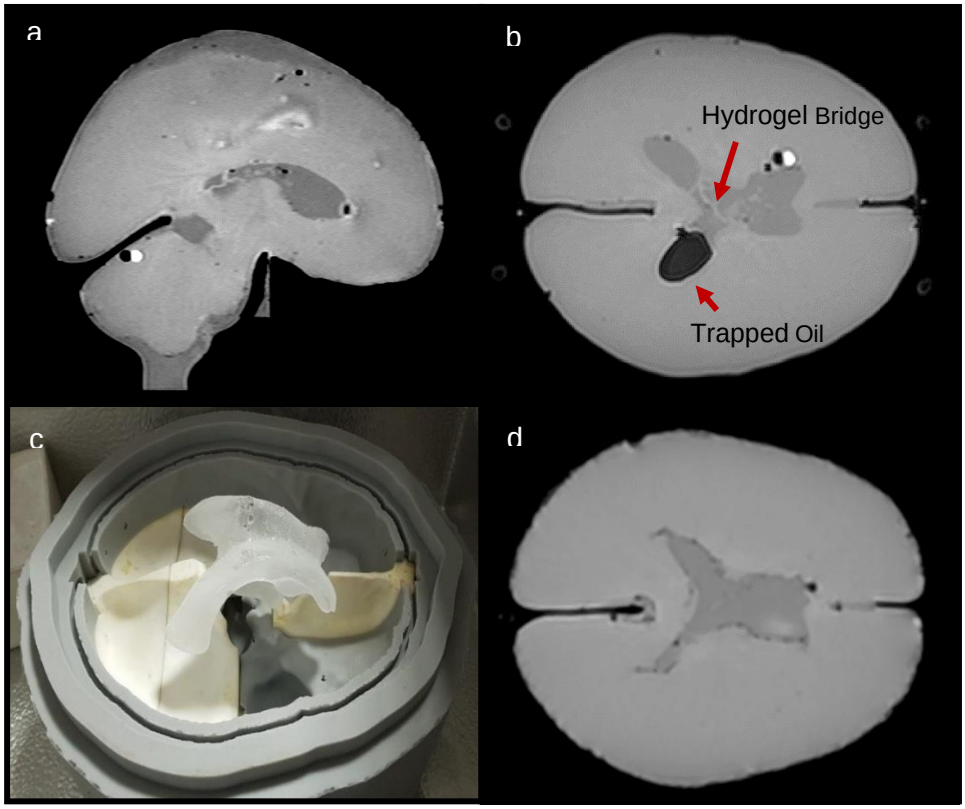

Figure 7.6: Addressing the brain stem tearing and trapped oil. a) MR image of the phantom created using the redesigned insert showing no brain stem tear; b) MR image of the phantom with oil trapped in the right lateral horn, showing hydrogel bridge; c) lower half of the CBM assembled with ice ventricles; d) MR image of the phantom created with ice ventricles.

This hypothesis would explain why the hydrogel material appears well formed in the vicinity of the ventricle cavity despite evident melting and shape change of the ice ventricle insert during the casting process. It is also consistent with the end shape of the ventricle cavity which features shrunken projections such as the lateral horns and a fatter body (see Figure 7.7). At 32 ml, however, the overall volume of the cavity is still within the normal range for the anatomical ventricles (see Section 2.1.4, p11).

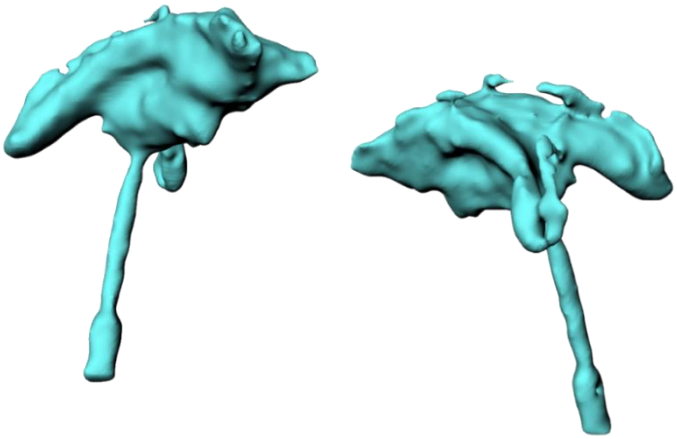

Figure 7.7: MR segmented model of the ventricle cavity moulded with the ice ventricle insert. Total mesh volume equal to 32 ml.

These morphological changes to the phantom's ventricle cavity are not ideal but are certainly an improvement over the problems associated with the CO ventricles. Use of the ice ventricle insert also removes a messy six hour step (brain incubation to 26°C and ventricle washing) in the original production workflow.

7.1.3 Improvements to the Dural Septa

Buckling of the dural septa in the assembled phantom was deemed to largely be due to swelling of the structure inside the fluid environment of the skull rather than due to issues with fit. To mitigate against this, the dural septa part was remade and sealed with polyvinyl acetate sealant solution. The part was also infiltrated with black dye prior to sealant to aid easier identification of the part in underwater assembly.

Prior to refabrication, however, a few design changes were made to the dural septa to make the part more practical (Figure 7.8). Firstly, roughly half of the tabs were removed to make it easier to locate the part into the skull. The tunnel running through each tab was also removed. Secondly, the anterior portion of the tentorium with its anterior attachment features was removed due to unreliable attachment of the plugs to the skull sockets. Thirdly, the falx was split and a hinge-like mechanism was added for easier introduction of the dural septa part into the fragile brain. This mechanism featured a lace-up system that allowed for the part to be introduced into the fragile brain with the scythe-like portion of the falx hinged away (Figure 7.8b), before being laced back together when in place (Figure 7.8c).

This redesigned part was tested in a number of subsequent assemblies and was found to adopt a less buckled conformation than the first design. This is illustrated in Figure 7.8d, which shows two views of an MR image segmentation of the V2 dural septa. Here, it can be seen that the falx remains relatively flat when assembled in the skull.

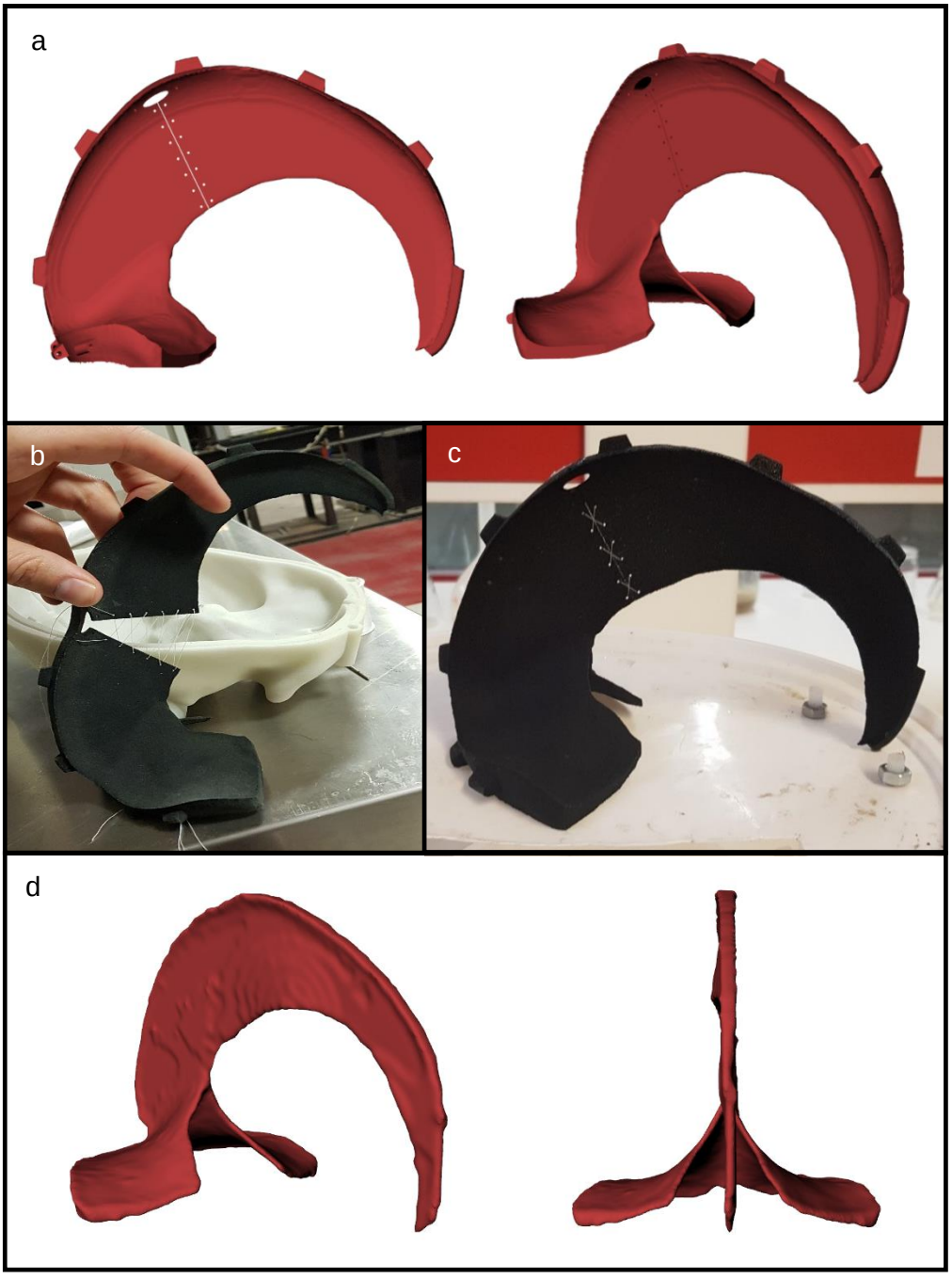

Figure 7.8: Improving the dural septa. a) the redesigned CAD model; b) V2 dural septa in hinged position; c) V2 dural septa laced-up; d) MRI segmentation of the V2 dural septa in assembled phantom, showing minimal buckling.

7.1.4 Improvements to the Skull

With abandonment of the cord fixation system and the removal of the dural septa's anterior attachment features, the corresponding features on the skull also needed to be removed. Consequently, all tunnels of the skull were removed along with the relevant dural septa tab grooves. The portion of the skull base donated to the dural septa part for the anterior attachment features was then returned to the lower skull half geometry.

In using the phantom, two problems had been identified with the Veroclear skull. The first was that the material was brittle and prone to breaking (with general wear and tear) in external regions such as the fixators. The second was that residual support material proved difficult to remove from the internal surfaces of the part and would often flake off into the phantom's SAS in assembly, contaminating the MR signal.

To address these problems, the redesigned upper and lower skull halves were remade in glass-filled DuraForm, a SLS material with a nominal tensional elastic modulus of approximately 4 GPa [157]. The walls of the fixators were also thickened by an extra 3 mm to prevent any further breakages of these important features.

Once fabricated, six multi-modal fiducials (Beekley Medical, USA) were then added to the upper skull half (Figure 7.9) to aid rigid registration of images of the phantom (see later in Chapter 8). A one-way Luer Lock port was also added to the foramen magnum cap to allow for a syringe to introduce additional water if necessary post-assembly (with sealable exit holes drilled into the upper skull half to allow any trapped air to leave the interior).

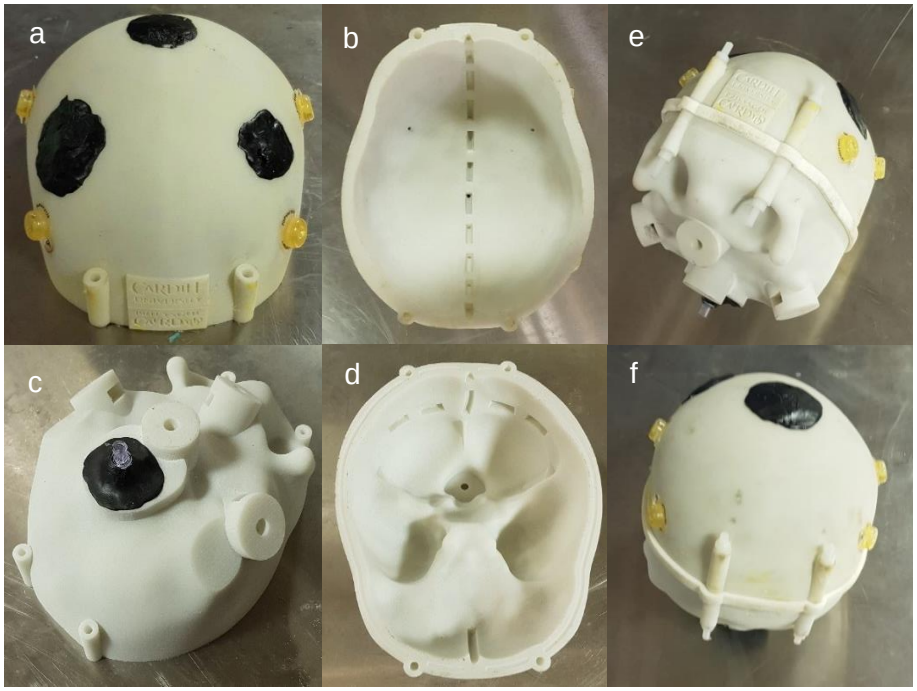

Figure 7.9: The V2 skull. a) external view of the top skull half; b) internal view of the top skull half; c) external view of the lower skull half; d) internal view of lower skull half; e) assembled skull; f) alternate view of assembled skull. Yellow attachments are the multi-modal fiducials. Black material is rubber sealant.

7.2 Brain Stiffness

As discussed in Section 7.1.1.1 (p119), the hydrogel produced through the method described in Section 6.2.4 (p108) was found to be overly stiff (on palpation), despite using the same formulation as in [57]: *[3.00% PVA : 0.43% PHY : 97.24% Di H20]*. This was not overly surprising, however, as the mechanical properties are known to be strongly influenced by the thawing rate, and the thawing environment used here is substantially different due to the different mold architecture and the different thawing setup.

To obtain a hydrogel with closer properties to those obtained by Forte et al. [57], a trial and error approach was next taken. In this process, a number of brains were made with hydrogel formulations containing varying concentrations of PVA and PHY. Rather than quantitatively assessing each brain produced (of which there were many), a qualitative assessment through palpation was first made to rule out formulations that produced brains overtly too stiff. Rejected formulations are not presented here for brevity.

On palpation, the formulation *[2.20% PVA : 0.26% PHY : 97.54% Di H20]* (initial formulation, IF) was found to produce a brain with seemingly realistic softness. To confirm this quantitatively, cerebral segments were next harvested from the brain and indented.

In obtaining cerebral segments, the left cerebral hemisphere was first isolated from the rest of the brain (Figure 7.10a, p129). This hemisphere was then cut in half (with a long pair of scissors) along the vertical seam created by the falx inserts (solid line of Figure 7.10a). The anterior portion of the split was then cut along an imaginary line parallel to the seam which intersects the anterior tip of the corpus callosum (P1 of Figure 7.10a). Similarly, the posterior portion of the split was cut along another imaginary parallel line, this line intersecting a point a third of the way along a further imaginary perpendicular line (dotted line of Figure 7.10a) projecting from the posterior tip of the corpus callosum (P2 of Figure 7.10a) to the posterior tip of the cerebral hemisphere. The anterior and posterior most segments were finally discarded leaving behind two flat central segments (segments A and B) (Figure 7.10b), of which three of the four surfaces (S1, S2 and S3) (Figure 7.10c) were then used for indentation (Figure 7.10e-f).

The *[2.20% PVA : 0.26% PHY : 97.54% Di H20]* formulation was found to produce a very porous brain gel which, even when reduced to flat cerebral segments, would expel a significant proportion of its water content under its own weight. To assess the mechanical properties of the hydrogel material in an unloaded state, or as close to it as possible, the cerebral segments were indented underwater in a bucket of room temperature deionised water.

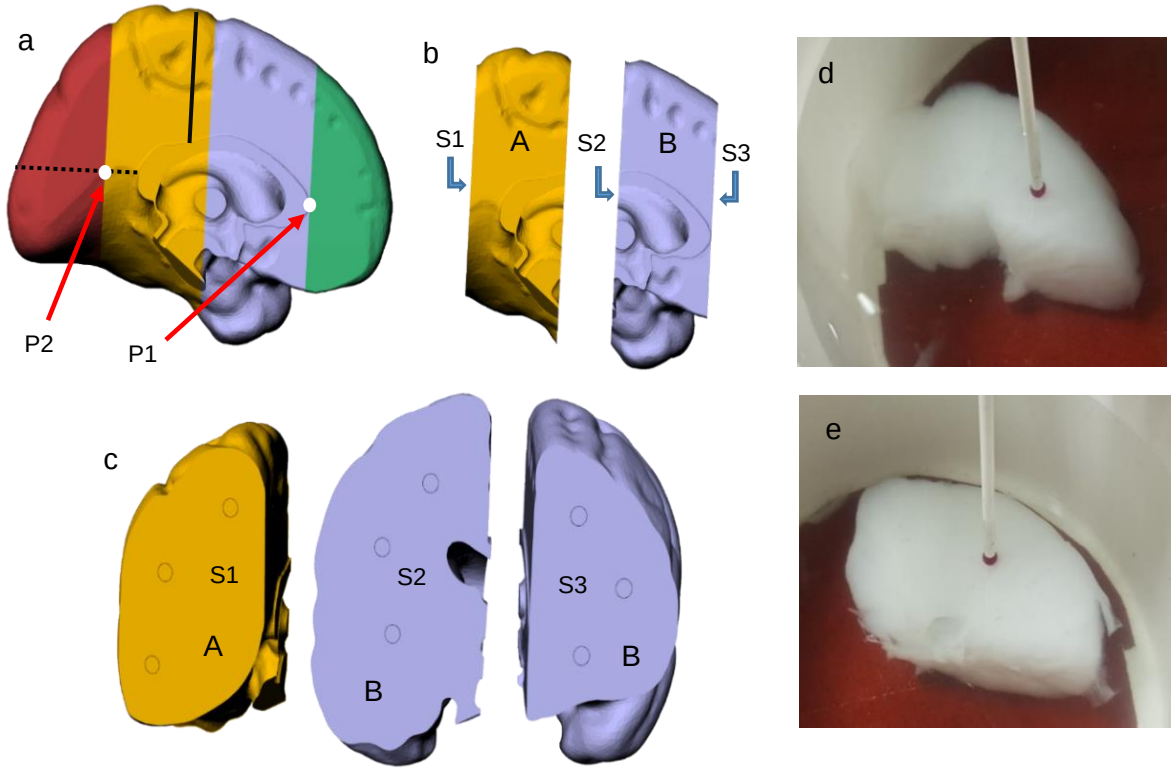

Figure 7.10: Generation and underwater indentation of flat cerebral segments. a) CAD model representation of the harvested left cerebrum, showing landmarks used for segment cutting; b) CAD model representation of harvested cerebral segments (A and B); c) illustration of the approximate indentation sites for the segments; d) underwater indentation of segment A; e) underwater indentation of segment B.

With the segments prepared, the indentation protocol utilized in [142] was next adopted to indent three sites on each surface. The protocol of [142] was used over the protocol of [57] due to the possession of a 6 mm diameter indenter. This second study [142] concerned an altered CH formula (ACH) developed to match soft tissue needle insertion, but it also contained indentation of brain tissue. Therefore, in using the same protocol, the force-displacement data of the hydrogel developed here and the brain tissue measured in [142] could be directly compared.

For each test, therefore, a 6 mm diameter spherical indenter was driven down towards the cerebral segment until a touching load was found. At this point the indenter was then driven down 6 mm at a rate of 1 mm/s and held at 6 mm depth for 500 seconds, as detailed in [142]. The results for the nine tests are shown in Figure 7.11 and Figure 7.12.

In the absence of similar instrumentation to that used by [142] a 10 N load cell was used to indent the segments. Although accurate to approximately ±0.5 μN this load cell presents as a much cruder measuring tool than the 1.5 N load cell used in [142] and consequently a similar touching load proved difficult to identify. This process was made further difficult by the activity in the workshop which disturbed the water in the bucket.

The most consistent approach in identifying a touching load with the 10 N load cell was found empirically to be in manually lowering the indenter at a rate of approximately 0.08 mm/s until a consistent climb towards 3 μN was observed. At 3 μN the test was then manually triggered. As can be seen in Figure 7.11, this protocol produced acceptable curves with minimal inconsistencies at the start.

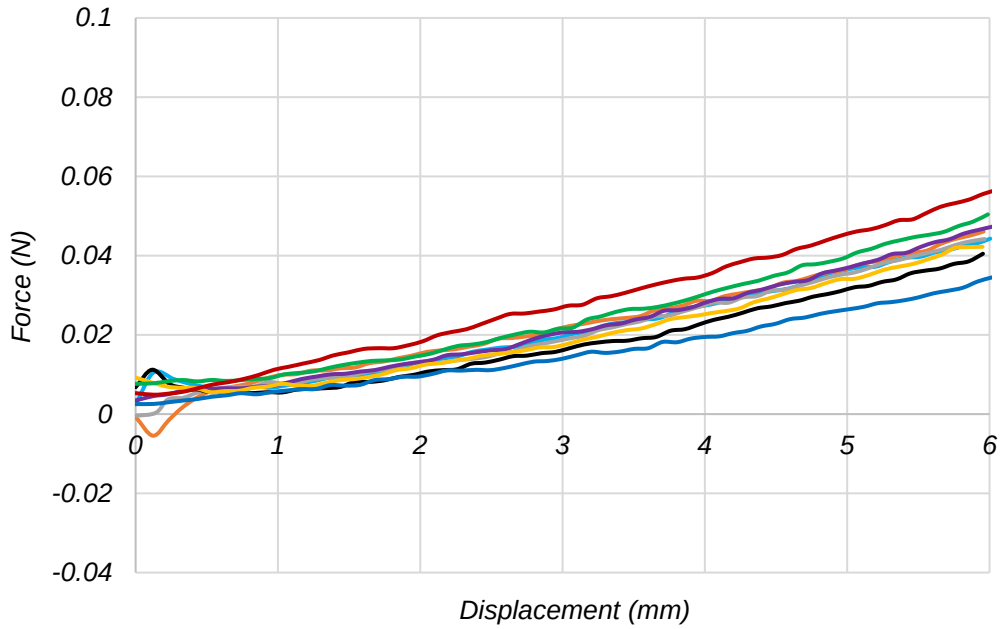

Figure 7.11: Force-displacement curves of the IF indentation tests.

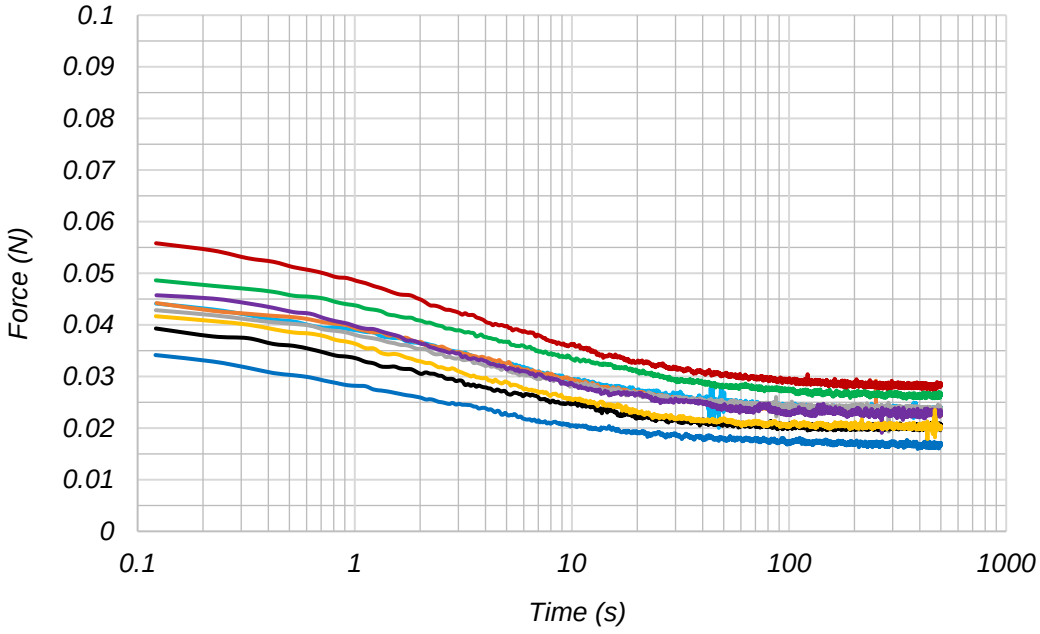

Figure 7.12: Logarithmic time-relaxation curves of the IF indentation tests.

The indentation tests produced similarly shaped force-displacement curves to the curves generated by [142] for brain tissue, with peak loads of between 350 to 600 μN at approximate 6 mm depth measured. By comparison, peak loads of roughly 1000 μN (Figure 7.13) were measured for brain tissue by [142]. The loads measured for the IF hydrogel are, therefore, slightly lesser than this particular measurement of brain tissue.

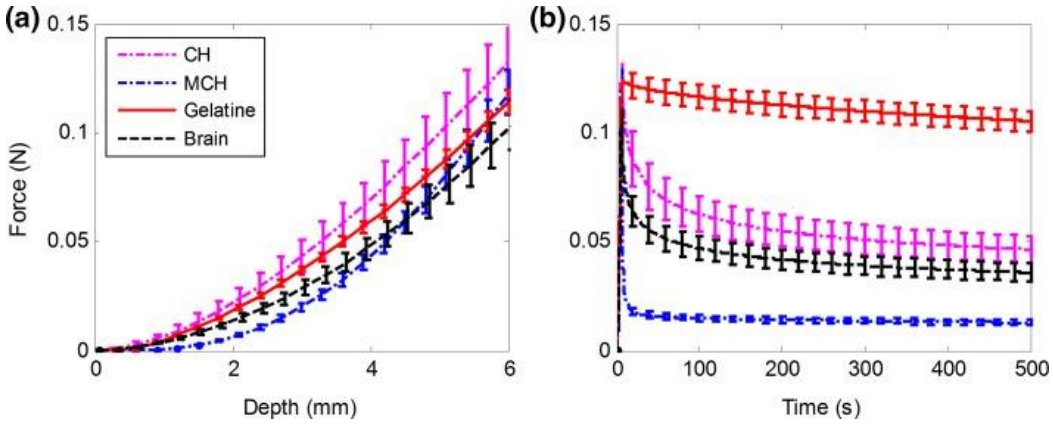

Figure 7.13: Force-displacement curves from brain indentation tests and three gels performed by Leibenger et al. [142]. a) force-displacement (depth) curves from indenting to 6 mm depth at 1 mm/s. b) relaxation curves after indenter held at 6 mm depth for 500 seconds. Reproduced from Leibenger et al. [142].

Using the indentation force-displacement to elastic modulus conversion equation developed by Czerner et al. [158], however, an elastic modulus of between 0.7 and 1.4 kPa can be estimated for the IF hydrogel, which is still well within the 0.3 - 3.0 kPa range reported for brain tissue (see Section 2.4.1, p23). This conversion equation, rearranged from its presented format in [158], is shown in Equation 7.1, where E is the elastic modulus, r is the radius of the indenter, h is the height (depth/displacement) of the indenter and P is the force measured at the depth. Force/displacement data at 4 mm depth for the steepest and flattest curve was used to garner the 0.70 to 1.41 kPa range.

$$E\ (Pa) = \frac{9(P)}{16(r^{1/2}\ h^{3/2})} \tag{7.1}$$

Interestingly, the IF is very close to the ACH formulation developed in [142] for needle insertion, *[2.50% PVA : 0.26% PHY : 97.24% DI H20],* although again the freezing profile used to form the gels is substantially different. Despite producing approximately half the peak loads than the ACH (pink dotted line of Figure 7.13), the shape of the curves can be seen to be very similar in both the initial loading portion and the holding stage, with the material relaxing very quickly and dropping to give approximately half the load after 200 seconds. The same relaxation behaviour can be seen for brain tissue.

The minimal variance in the curves of the individual tests indicates a reasonable level of homogeneity throughout the IF hydrogel. This is an achievement in the production workflow design, as uniform properties in large volumes of freeze-thaw hydrogel have previously been found to be difficult to achieve [159].

7.3 Brain Density

Following stiffness, the quantification of density was next sought. To measure the density, however, it was discovered that a non-traditional protocol of mass and volume measurement needed to be developed. This is because the traditional methods were found to be difficult to apply to the hydrogel and/or too insensitive to measure the density to the three decimal places required to accurately calculate a comparable density differential between the hydrogel brain and the water CSF (comparable to the anatomical differential).

To determine the volume of a castable material sample, either the sample can be moulded to a known shape, the sample can be moulded to an unknown shape and then scanned, or the sample can be submerged to displace a known volume of liquid. Due to the irregular freezing expansion characteristics of the hydrogel, however, moulding a known shape is difficult, and scanning its highly translucent, watery surface optically or with MR/CT would not lead to an accurate result, making the displacement route the only viable method of volume determination.

With the displacement method being the only viable route, the determination of mass then becomes difficult as well. This is because traditional mass determination involves placing the sample on a weighing machine and the hydrogel expels its water easily under gravity or manipulation (e.g. extracting it from its mould). In weighing the sample prior to volume determination, therefore, it is difficult to avoid decreasing its volume prior to determination by displacement. Weighing the sample after volume determination is equally problematic, because in transferring the sample from a liquid to the scales it becomes difficult to determine what liquid actually belongs to the hydrogel.

Considering these difficulties, a protocol for mass and volume determination of hydrogel samples was developed which exploited the frozen intermediary stage of the casting profile. This protocol involved: 1) the freezing of a pseudo-cylinder sample of hydrogel solution, 2) the extraction and weighing of the frozen sample, 3) the addition of the frozen sample to a known volume of deionised water and, 4) the calculation of volume by displacement when thawed to room temperature.

In measuring the IF hydrogel's density, five 60 ml enteric syringes with sawn off tops were used to create five 50 ml pseudo-cylindrical frozen samples. This was done by arranging the syringes upright with their plungers maximally retracted and casting the prepared solution into them and freezing them overnight in the same -30°C freezer used to form the phantom's brain (Figure 7.14a). For each sample, a 100ml (1ml graduated) measuring cylinder was prepared with approximately 30ml of deionised water (exact measurement is read - v_1) and placed on a weighing scale which was then zeroed (Figure 7.14c). The frozen sample (Figure 7.14b) was then plunged out of the syringe directly into the water in the measuring cylinder and the mass of the sample was recorded (m). The sample was allowed to thaw (Figure 7.14d-e) and come to room temperature over 3 hours before recording the volume of the water and the thawed hydrogel (v_2). To obtain the density of the sample, the mass (m) was then divided by the volume change (v_2-v_1).

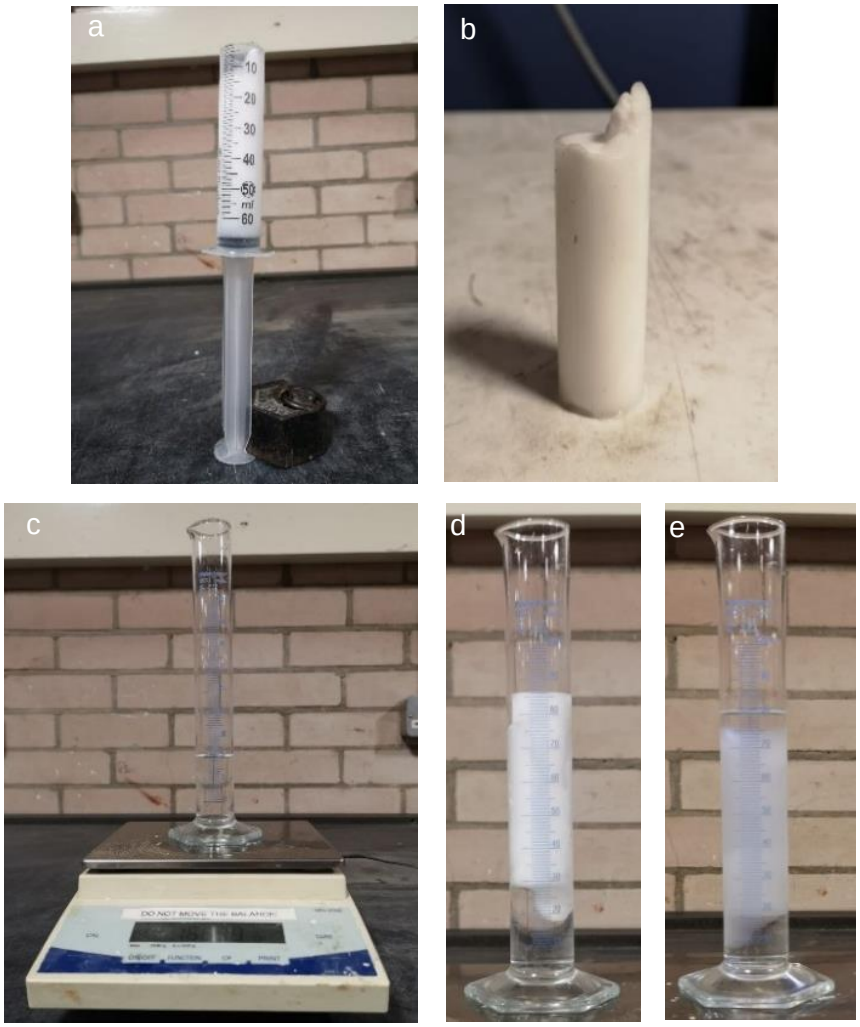

Figure 7.14: Hydrogel sample preparation and mass/volume determination. a) modified syringe with frozen pseudo-cylinder sample inside; b) example of frozen sample extracted from syringe; c) 100 ml measuring cylinder with measured ~30 ml DiH_20 water volume (v_1), resting on tared weighing machine; d) measuring cylinder with frozen sample added (weight is recorded – m); e) thawed sample partially sunk in cylinder (volume is read again – v_2). The thawed sample does not fully sink due to deformation into the walls of the cylinder under its own weight, creating suction/friction effects.

Measuring cylinders are only accurate to the size of their gradations, however, sub-gradation estimates to a tenth of the graduation size are still considered significant. As such, the volume was read to one decimal place. Assuming a reasonable sub-gradation accuracy of 0.5 ml in volume measurement, for an approximate 50 g sample, the error in density measurement can be assumed to be approximately 0.01 g/cm^3. This is not ideal, however, a measurement method without a similar degree of error arising somewhere from its process could not be devised. Density measurement by density gradient column was considered as an alternative to mass/volume measurement, however, a similar degree of error presents in the calibration of the column and the measurement with it. A similar argument can be made for the calibration and measurement with buoyancy measuring devices.

Regardless, with the described measurement method, the density of the IF hydrogel was found to have a mean density of 1.004 ± 0.003 g/cm^3. This is somewhat lower than the 1.015 ± 0.013 g/cm^3 density measured by Forte et al. [131] for their formulation of the CH, but consistent with the lower concentrations of PVA and PHY used in the IF. The low standard deviation is somewhat reassuring in the accuracy of the measurement method.

With a brain density of 1.004 g/cm^3 and a Di H20 CSF density of 0.998 g/cm^3, a density differential of 0.006 g/cm^3 is produced. This gives the phantom's brain (1480 ml volume) a submerged weight of approximately 9 grams, which is quite a small fraction of the 40-100 grams estimated for the human brain. Without further development, it is, therefore, unlikely that the phantom's brain will recreate a similar magnitude of brain shift to the anatomy under gravitational loading. This was determined through simulation of the S→P brain shift event and is presented in the next chapter.

7.4 Chapter Summary

This chapter began with an assessment of the phantom's construction. Here it was shown that the parts and production workflow devised produced a brain-skull phantom with similar morphology to that of the anatomical system. A number of improvements to the parts and production workflow were then made to improve this similarity further.

The geometry and spatial relationships of parts within the brain-skull phantom can be seen to be a considerable improvement over existing phantom models. Not only is the complete brain geometry recreated, but also the important compartmentalisation of the cranial cavity by the dural septa, in addition to the fluid support offered by the CSF surrogate.

Following the assessment of construction, an assessment of the mechanical realism of the phantom's hydrogel brain was next made. On observing the formulation comprising *[3.00% PVA : 0.43% PHY : 97.24% Di H_20]* to be too stiff when made with the long thawing

times associated with the workflow, a new formulation was sought. A formulation comprising *[2.20% PVA : 0.26% PHY : 97.54% Di H_20]* was subsequently found to produce a brain with similar stiffness to that reported for brain tissue. The density of the stiffness matched formulation, however, was found to produce a hydrogel with considerably lower density to that of the anatomical brain.

It was identified that the density could be raised using additives, however, it was decided that it would be best to first trial simulating the PBS event with the current brain stiffness and density differential combination. This is because it was recognized that the use of additives can be problematic in hydrogel formation and that the combination might already be sufficient to simulate the PBS event.

This investigation is presented in the next chapter, following the opening sections which detail the construction of the phantom orientating cradle and the implementation of the phantom's PBS imaging marker system.

[Blank Page]

8 BRAIN SHIFT TUNING

The previous chapter addressed the refinement of the phantom following MR imaging and mechanical testing. Introduced by Figure 8.1, this chapter details the tuning of the phantom to match literature accounts of PBS and includes the following novel work:

- The construction of a cradle for orientation of the phantom in MR and CT environments.
- The development of a marker system to measure positional brain shift in the phantom's hydrogel brain.
- An assessment of the phantom's marker system in MR and CT imaging and selection of brain shift imaging modality.
- The measurement of supine to prone PBS in two phantoms of differing brain stiffness and density differential.
- An assessment of observed PBS and selection of appropriate brain formulation for PBS modelling.

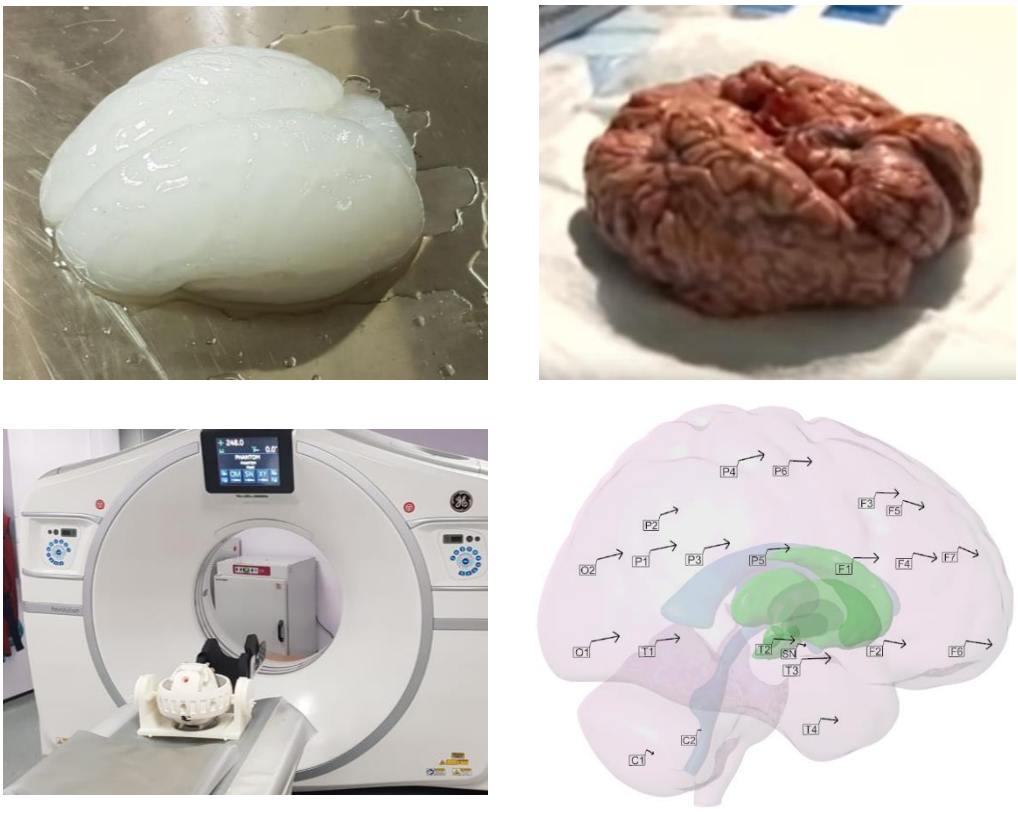

Figure 8.1: Chapter storyboard showing the tuning of the hydrogel to obtain realistic properties and to better match literature accounts of positional brain shift. Images are reshown and discussed later in the chapter.

8.1 Fabrication of Phantom Cradle for PBS Imaging

Before PBS assessment could be undertaken in the developed phantom, a brain shift measurement system needed to be developed and a phantom orientating cradle needed to be built for accurate positioning of the phantom with respect to gravity. The fabrication of the cradle is addressed in this section and the development of the marker system is addressed in the next.

The cradle was built to be compatible in both MR and CT imaging machines, but the difficulty in designing the apparatus was in finding a way to fit a robust orientating cradle within one of the tight fitting (anatomy matching) head coils necessary for MR imaging the phantom. Since the bores of CT machines are much larger than the bores of MR head coils, it was identified that anything designed for MR imaging would be simultaneously compatible (geometrically) with CT machines.

As discussed in Section 7.1.1 (p119), the only suitable head coil for this project was deemed to be a single channel head coil due to it being the only available coil with a large enough cavity to fit the phantom and cradle. The more advanced coils tend to have a cavity which closely matches the contours of the head and neck (for comfort and image quality purposes) which leaves little space for an appropriately robust orientating cradle.

The main benefit of using a multi-channel head coil is reduced image noise, as more signal sampling can occur during an acquisition, however, a similar result can be achieved when using a single channel coil by taking a number of sequential scans and averaging their output. Thus, it was identified that the use of the single channel head coil would not present as a significant limitation with the phantom. This is evident in the MR images presented in Figure 7.2 (p120) which feature minimal noise when using three averages.

The bore of the single channel head coil (used with the same Prisma MR system described in Section 7.1.1, p119) presents as a cylinder with a diameter of 30 cm and a length of 32 cm. A cradle capable of rotating the phantom around the coronal and sagittal axes was therefore designed to fit within this volume (Figure 8.2).

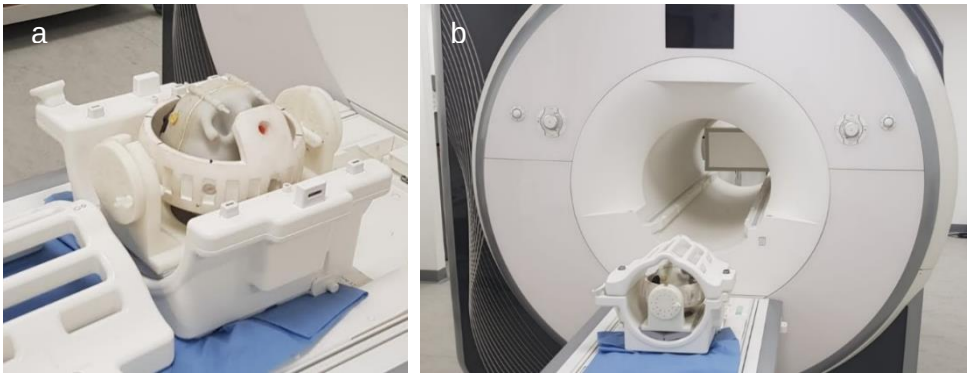

Figure 8.2: Phantom and cradle positioned in the single channel head coil. a) phantom placed in base of single channel head coil; b) phantom being loaded into a mock Prisma 3T MR scanner.

This cradle system developed features three main parts: a fixation ring (Figure 8.3a), a pair of wheel arms (Figure 8.3d) and a frame (Figure 8.3f). The phantom is mounted inside the fixation ring which encircles the phantom in the coronal plane (Figure 8.3a-c). The wheel arms are then used to levitate the phantom in the center of the frame by slotting into the frame and engaging the fixation ring either side via a radial set of grooves (Figure 8.3e). These grooves are spaced at 15 degree intervals allowing for the phantom to rest at one of 12 coronal orientations.

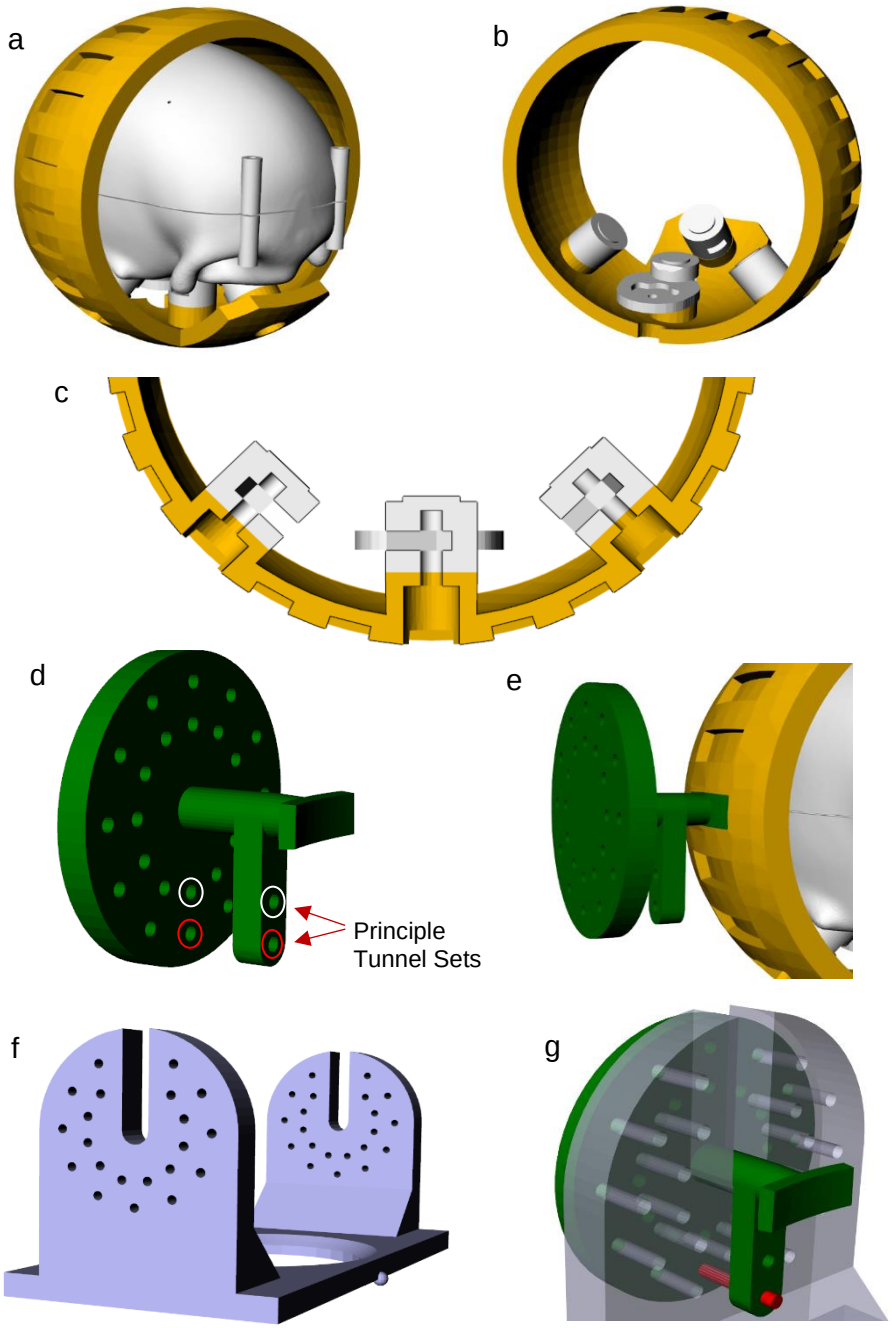

Figure 8.3: Parts and features of the phantom cradle. a) phantom mounted inside the fixation ring; b) reduced view emphasizing docking structures of the fixation ring and the phantom; c) cross-sectional view of the fixation rings central docking features and the phantoms central fixation features; d) wheel arm; e) wheel arm engaged in groove of fixation ring; f) cradling frame; g) wheel locked into a sagittal orientation with locking rod.

Featured where each wheel arm slots into the frame is a two-tiered radial system of tunnels (see Figure 8.3f). Together, the two tiers provide 21 sagittal locking positions at 15 degree intervals for the wheel arms which are free to rotate around in their slots. When the phantom, fixation ring and wheel arms are all rotated together to one of the available sagittal orientations, one of the two principle tunnel sets on each wheel arm becomes aligned with a tunnel on the frame (see Figure 8.3g and Figure 8.4a-c). At this point a rod can then be threaded through the aligned holes to lock the wheel in position. Further rods can also be threaded through the non-principle tunnel sets to further brace the wheel arms.

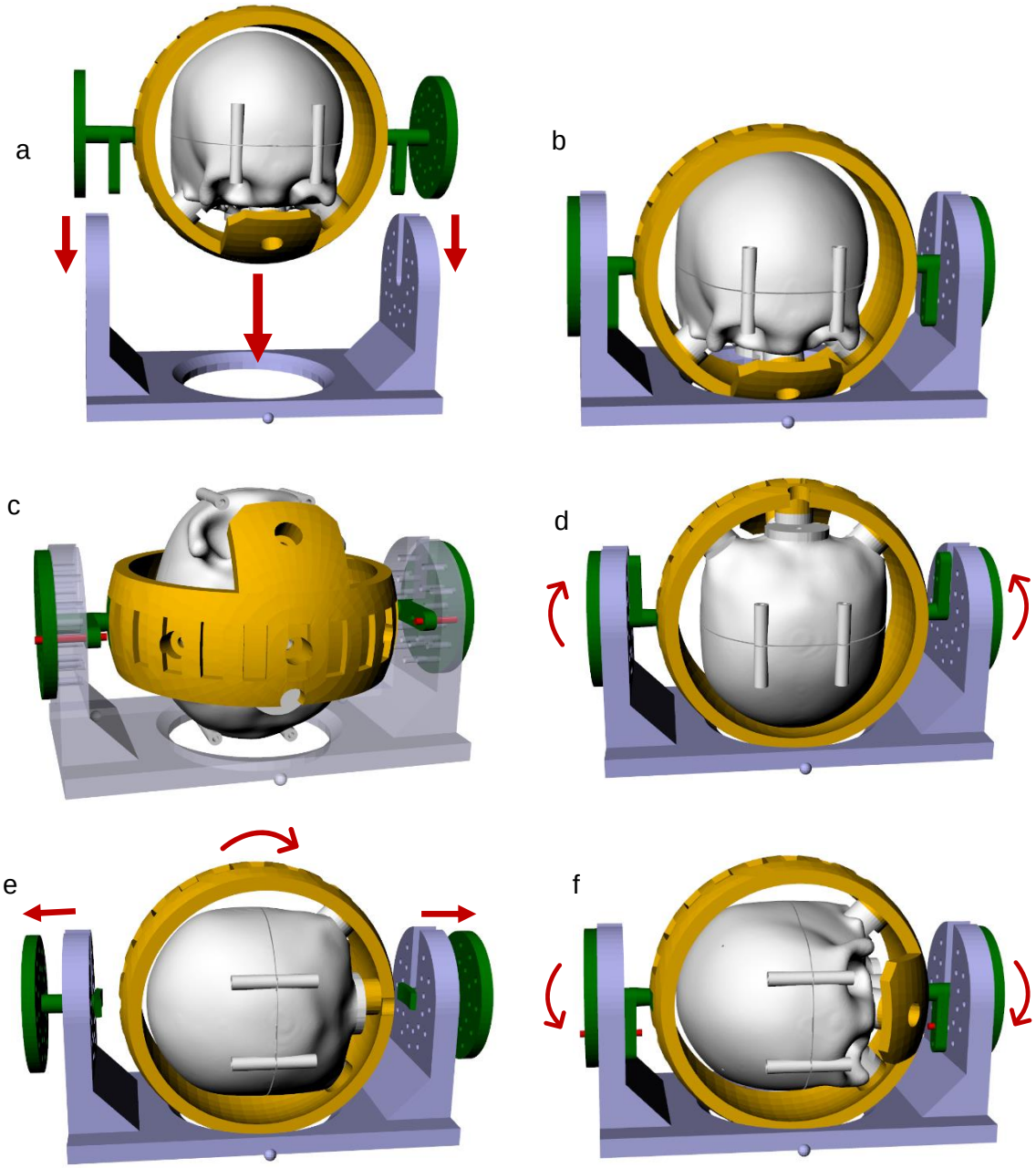

Figure 8.4: Loading the phantom cradle. a) lowering of fixation ring and wheel arms onto frame; b) fixation ring and wheel arms in place on frame; c) phantom rotated around the sagittal plane and locked into the supine position; d) phantom rotated upside down to disengage wheel arms; e) wheel arms disengaged from fixation ring and phantom rotated round around the coronal plane to engage grooves corresponding to right decubitus position; e) wheel arms re-engaged with fixation ring and rotated round 180 degrees to lock phantom in right decubitus position.

When mounted into the frame, as shown in Figure 8.4c, the phantom is quickly repositioned in the sagittal plane by simply removing the locking rods and rotating the wheel arms. To change the coronal position, however, the phantom is rotated upside down so that the wheel arms can disengage the ring (Figure 8.4d). Once disengaged, a new coronal orientation can then be achieved by rotating the fixation ring in the coronal plane, reengaging the wheel arms, and rotating back down (Figure 8.4e-f). Given that the brain has very limited mobility in the skull, the up-turning of the phantom was not deemed to be an issue.

Shown in Figure 8.5 is the phantom mounted in the supine position and the left decubitus position, ready for loading into an MR or CT imaging machine. The fixation ring was fabricated in the DuraForm material, while the wheel arms and cradle frame were fabricated in the stereolithography SOMOS GP Plus 14122 material on a 3D Systems 5000 3D printer, as large SLS parts are susceptible to thermal warping. A threaded nylon rod with a wing nut on one end was used as the locking rod. The entire system of materials is both MR and CT compatible.

Due to the tolerances of the interacting parts of the phantom and the cradle, some error was naturally found in the orientating capability of the apparatus. However, a phantom orientating error of only ± 1 degree was measured, and so the cradle was considered to be accurate enough for the purposes of PBS simulation.

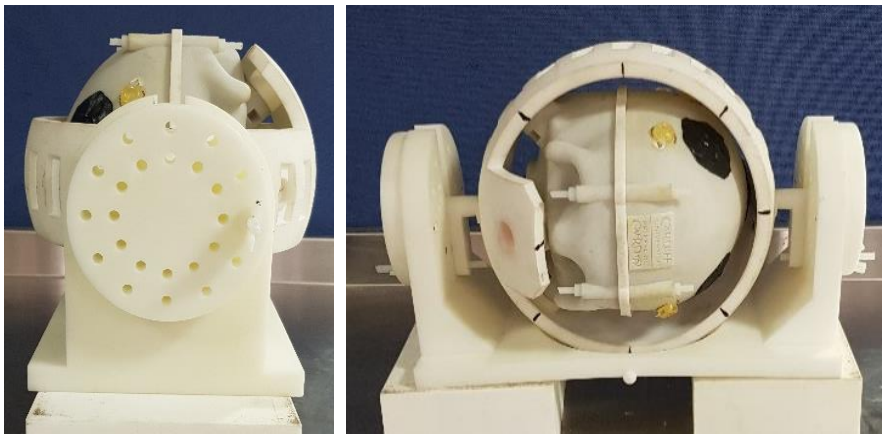

Figure 8.5: Phantom loaded into the multi-axis cradle in the supine (left) and left decubitus (right) positions. Black marks on the fixation ring indicate 45-degree intervals.

8.2 Development of Brain Shift Measurement System

8.2.1 Development of Marker System

In developing a brain shift measurement system, a marker delivery system needed to first be developed for the phantom's brain fabrication workflow. This is because the homogenous CH brain was found to not naturally produce any trackable elements when imaged with MR or CT (see Section 7.1 - p119 for MR and later for CT). This is unlike the human brain, which produces many trackable elements when scanned due to the many

tissue boundaries throughout its body (e.g. grey-white and brain-vessel interfaces). PBS measurement in the human brain is, therefore, simply the case of tracking these elements between scans taken in one position and scans taken in another.

The first marker system trialled with the phantom was a simple dispersion of markers throughout the hydrogel material. This could be obtained through adding markers of similar density to the hydrogel solution, prior to casting, such that a stable suspension is achieved in the mould during freezing.

A stable marker suspension was initially found to be achievable with small plastic objects such as high impact polystyrene pellets (density of ~1.03 to 1.06 g/cm^3) (Figure 8.6). However, as the PVA/PHY content was lowered during the hydrogel tuning stage, the viscosity also dropped to a point where no suspension could be achieved. Therefore, this marker system was deemed unsuitable.

Figure 8.6: Suspension of plastic pellets in hydrogel solution.

The next marker system trialled was one that utilised map pins and fishing line in order to suspend a number of 4 mm diameter glass beads (with 0.5 - 1 mm diameter tunnel) in the mould cavity. In this system, prior to hydrogel solution casting, glass beads were either placed on the tips of map pins embedded in the mould walls of the CBM or threaded along line (fishing line) drawn taught across the mould cavity (Figure 8.7 and Figure 8.8). When frozen down and removed from the CBM, the map pins and fishing line can then be drawn out of the frozen brain with pliers, leaving behind the trapped beads.

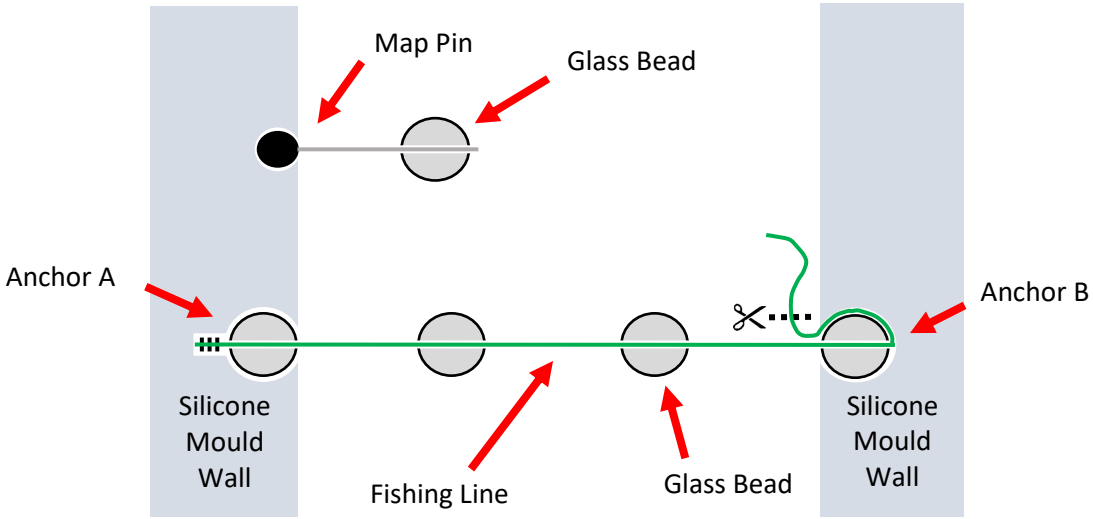

Figure 8.7: Illustration of map pin and fishing line marker positioning methods. Terminal glass beads of fishing line method are used to anchor the fishing line in the mould walls. Anchor A is knotted, while anchor B uses friction to hold the line taught when a desired tension is achieved.

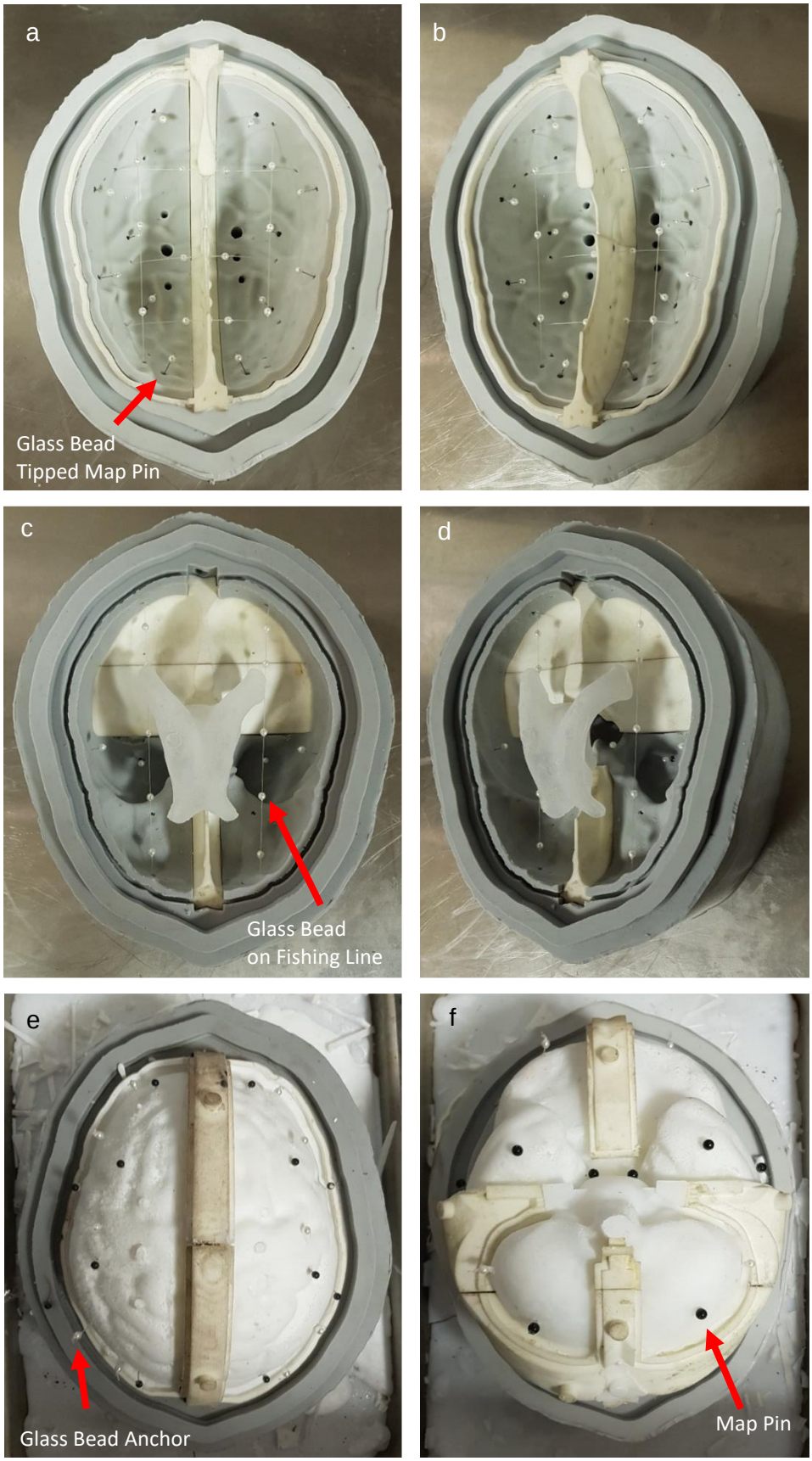

Figure 8.8: Map pin and fishing line maker positioning method. a) assembled upper mould half; b) alternate view of assembled upper mould half; c) assembled lower mould half; d) alternative view of assembled lower mould half; e) top half of demoulded brain (frozen) showing exposed heads of map pins and fishing line bead anchors; f) bottom half of demoulded brain showing exposed heads of map pins and fishing line bead anchors.

The system of map pins and bridging lines shown in Figure 8.8 was built progressively, cast after cast, by drilling new sockets into the silicone walls of the CBM. Initially a much smaller system of ~20 markers was trialled, due to fears surrounding the tearing of the hydrogel, however, a system of 44 markers was eventually achieved. This system utilized 18 map pins and 8 bridging lines to position the markers.

On dissection, the glass beads proved to be remarkably integrated with the hydrogel material, with no identifiable space between bead and hydrogel. Furthermore, little evidence could be found of the map pins or bridging lines used to position the beads.

The success of this marker positioning method is likely due to the manner in which the map pins and bridging line are removed. Doing so whilst the brain is frozen allows for the map pins and bridging line to be pulled out of a block of ice rather than a soft, fragile hydrogel material which tends to grip strongly to surfaces through suction effects. It is also possible that the hydrogel material occludes the very small tracts created by the map pins and bridging line as it forms during thawing.

8.2.2 Assessment of the Marker System in MR Imaging

With a potential delivery system identified, a phantom containing the marker set was next taken for MR and CT imaging to assess the distribution produced by the delivery method and the reliability of each imaging modality in tracking the markers between images and, therefore, in measuring PBS. The MR imaging assessment was performed first.

Unfortunately, it was quickly revealed when imaging with the 3D GRE sequence (identified in Section 7.1.1, p119) that the shape of the glass bead markers were being distorted by the magnetic susceptibility artifact, which occurred due to contrasting magnetic susceptibility (a material property) between the hydrogel and the glass bead markers (see Figure 8.9). This type of artifact arises due to local magnetic field inhomogeneities which results in erroneous localisation of the signal.

Shape distortion in the markers is not inherently a problem provided the distorted shape remains constant, however, a feature of the magnetic susceptibility artifact is that the distortion predominantly propagates along the phase encoding direction of the sequence employed. Given that this direction can only be set parallel or perpendicular to the main magnetic field of the scanner, the orientation of distortion changes with respect to the anatomical axis of the phantom when scanned in different positions. The consequence of this is that the apparent segmented shape of each marker also changes, leading to error in the determination of the marker centroids. In the phantom's case, it was identified that this would lead to the centroids of the markers shifting with respect to the orientation of the phantom within the scanner.

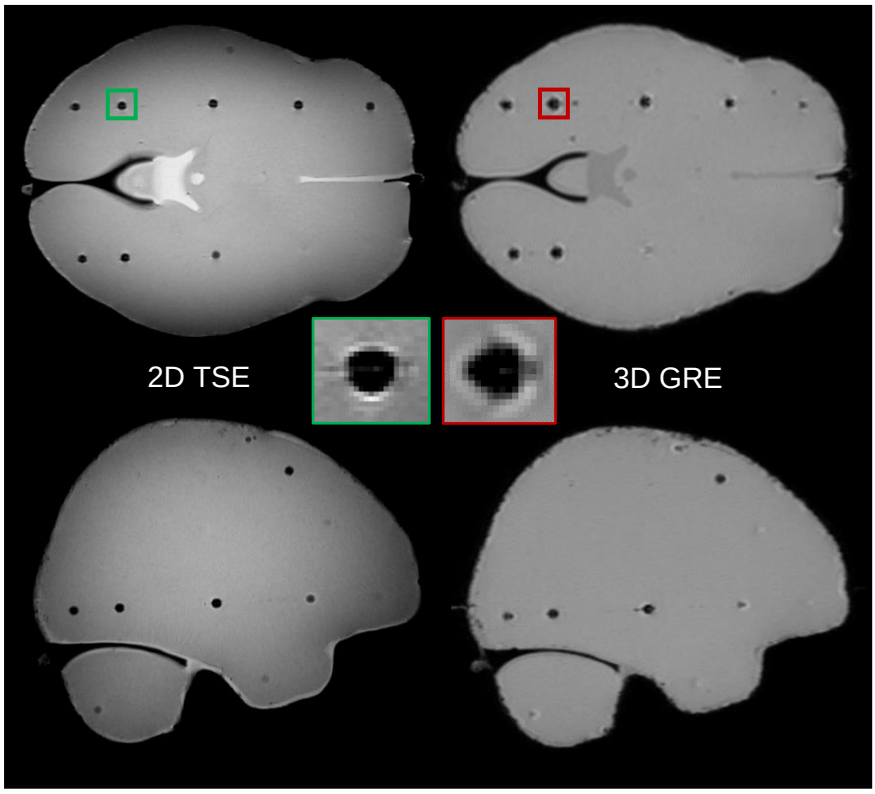

Figure 8.9: Comparison between images produced by the 2D TSE sequence (left) and the 3D GRE sequence (right), including blown up view of one marker of the set for each sequence. Top and bottom TSE images belong to different 2D scans taken in different planes.

This directional distortion is evident in the segmented dimensions of the supine imaged markers which present with mean *x*, *y* and *z* (phase encoding direction = *z*) diameters of 4.3 ± 0.2 mm, 5.1 ± 0.5 mm and 5.7 ± 0.3 mm, respectively. These were segmented in the 3D Slicer software using the threshold function.

Given the source of the distortion, a spin echo (SE) sequence was next trialled in place of the GRE sequence. This type of sequence mitigates against magnetic field inhomogeneities through the use of inverted phase direction refocusing pulses [160]. Yet, an appropriate 3D SE sequence could not be found, as although improvements in hydrogel-bead boundary distortion could be achieved, this invariably came at the cost of either voxel size, image noise or skull-region signal drop-off.

A T2-weighted, 2D turbo spin echo sequence was identified, however, as a useful tool for revealing the distortion within the GRE images and as a better sequence for determining correct phantom construction. This sequence produced images with 0.43 x 0.43 mm in-plane voxel dimensions and a 2D slice thickness of 3.25 mm.

Given that the artifact is a function of contrasting magnetic susceptibility between materials, it was identified that some of the hydrogel-bead boundary distortion could have been reduced by using beads with a closer magnetic susceptibility to that of water, such as acrylic. However, this would not entirely remove that source of the artifact and the distortion is likely to be in part due to air trapped in the tunnels of the beads which is unavoidable.

Another important limitation of MRI to consider with regards to image distortion is the system geometric distortion, which is a product of hardware related gradient non-linearities, rather than material heterogeneity. Although corrected for in post-processing with distortion correction algorithms, studies have repeatedly shown that residual geometrical distortion still exists in corrected images and that the severity of distortion varies depending on which imaging sequence is used and field strength (see Section 3.1, p33). Typical residual distortion appears to range roughly between 0 and 2 mm for 3T imaging sequences (see Figure 3.3, p35).

The significance of this is that while it may be possible to minimize image distortion due to material inhomogeneity through reselection of phantom materials, system distortion will remain. System distortion varies throughout the magnetic field and so if the phantom were to be rotated around in the magnetic field, any given region of the phantom would find itself in a different region of the distortional landscape (Figure 8.10).

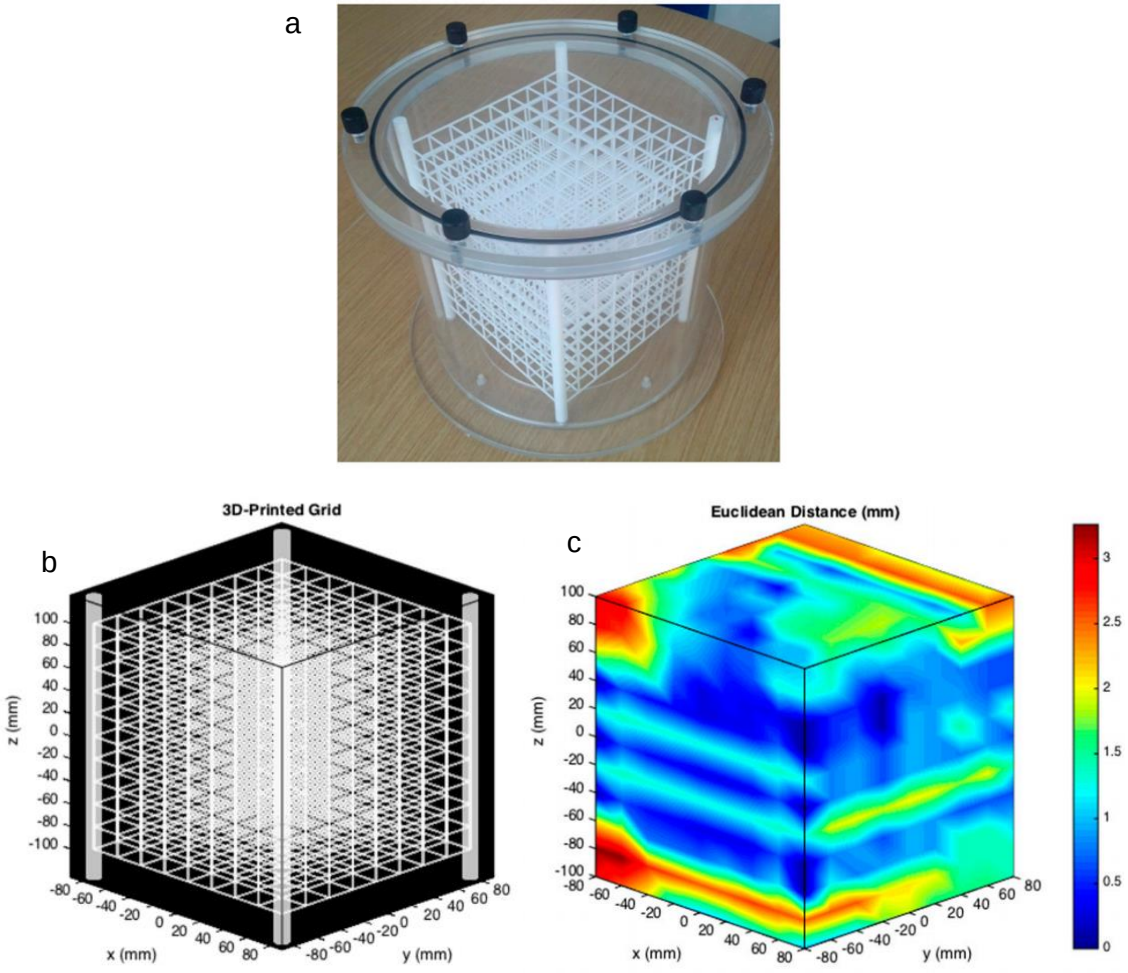

Figure 8.10: 3D residual distortion map measured in a 3T Prisma MRI scanner with a grid phantom, showing variable distortion throughout the field of view even after application of vendor distortion algorithm. a) grid phantom; b) computer model of grid phantom; c) residual MR distortion field measured with grid phantom and applied to (b). Adapted from [161].

8.2.3 Assessment of the Marker System in CT Imaging

Following assessment in MR imaging, the phantom and its marker set were next assessed for use with CT imaging.

For this project, a Discovery PET/CT 690 VCT system (GE Healthcare) based at the Wales Research and Diagnostic PET Imaging Centre (PETIC) at University Hospital Wales (Cardiff, UK) was used primarily in the CT scanning of the phantom (Figure 8.11a).

A Revolution HD CT system (GE Healthcare) based at Velindre Cancer Centre (Cardiff, UK) (Figure 8.11b) was also used during the phantom's development, due to variable availability of the Discovery system. This scanner was available daily but was not suitable for long experiments due to availability being restricted to 1hr slots during breaks in clinical scanning.

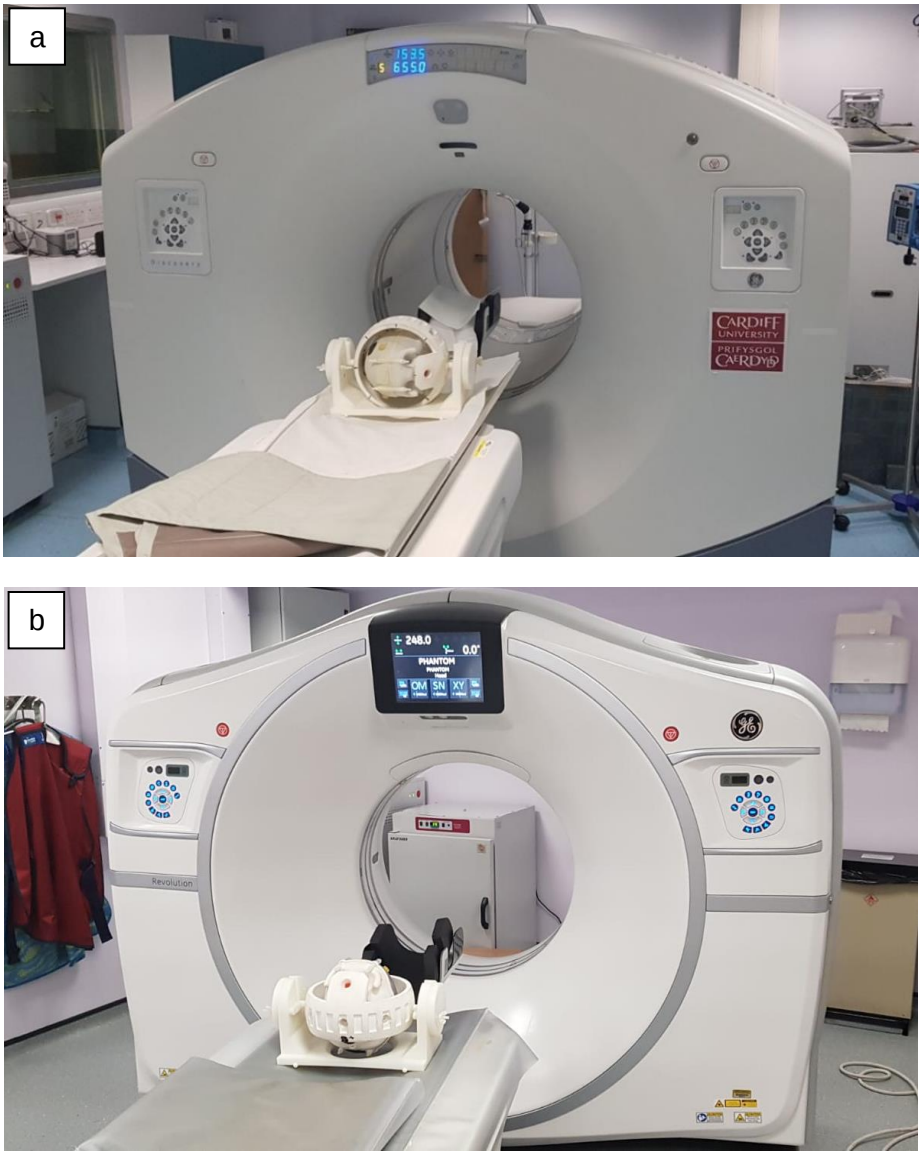

Figure 8.11: CT systems used in project. a) phantom prepared for right decubitus imaging with the Discovery PET/CT 690 VCT system; b) phantom prepared for supine imaging with the Revolution HD CT system.

Figure 8.12 shows a sagittal and axial slice of the CT scan that was captured with the Discovery system for marker system assessment. This scan was captured with 0.63 mm^3 isotropic voxel size.

Immediately, it can be seen that, while contrast is lost between the brain, dural septa, SAS and ventricles of the phantom, the remaining boundaries appear much clearer. Conveniently, it is these boundaries that are critical to the measurement of brain shift, with unambiguous skull boundaries being important to the rigid registration of differently orientated images and unambiguous hydrogel-bead boundaries being important for the segmentation of the markers and determination of their centroids.

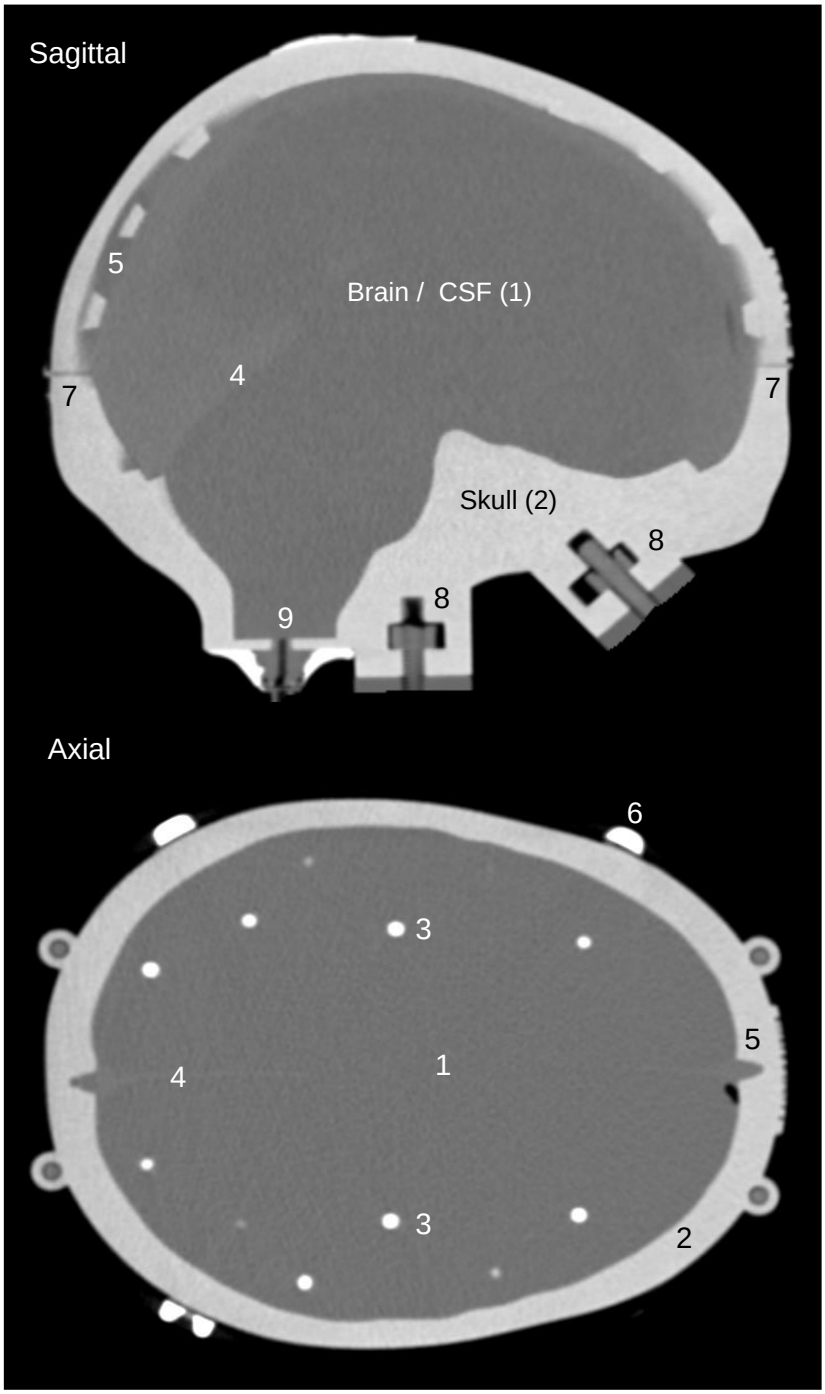

1) *Brain/CSF*

2) *Skull*

3) *Glass Bead Marker*

4) *Feint Image of Dural Septa*

5) *Dural Septa Skull Groove*

6) *Registration Fiducial*

7) *Gasket*

8) *Skull Fixation Features*

9) *Luer Lock Port*

Figure 8.12: Raw CT images of the V2 phantom.

In registering supine and prone scans together, it was found that the unambiguous skull boundaries indeed provided strong features for the rigid registration of differently orientated scans. This is illustrated in the checkerboard fusion of the supine and registered prone scans shown in Figure 8.13, which shows no identifiable misalignment of the skull. Evidently there is some signal difference between the anterior and posterior regions of the two scans, but this appears to be the only discrepancy.

Rigid registration was performed in 3D Slicer using the BRAINSFit module. Six degrees of freedom (translation and rotation only) were found to be sufficient in registering the prone and supine scans, provided the scans were first smoothed with a median image filter (2x2x2 pixel search) to reduce image noise.

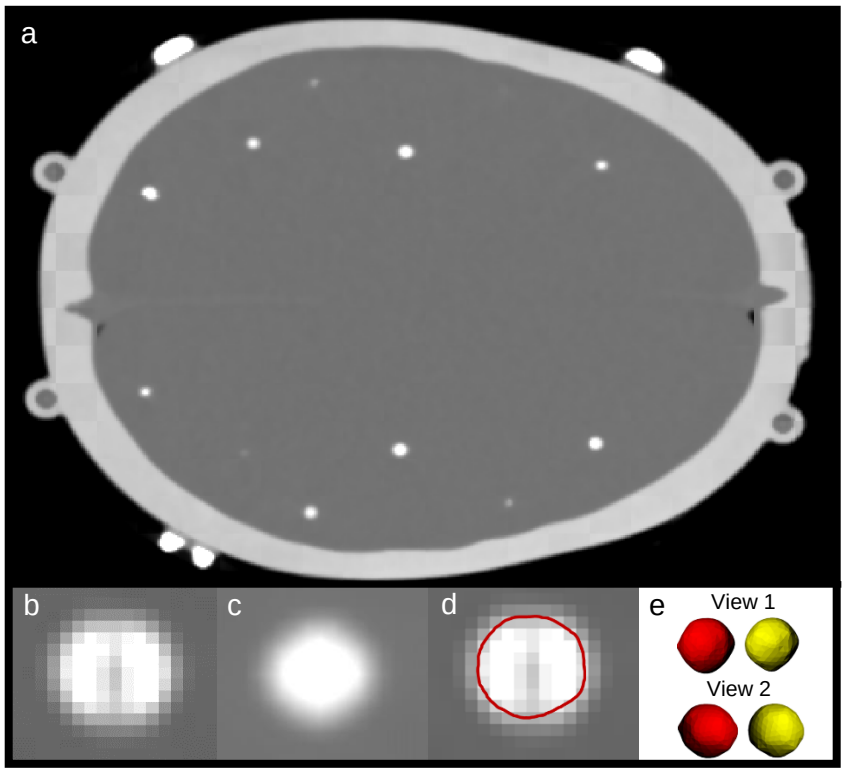

Figure 8.13: Checkerboard fusion of registered scans and segmentation of markers. a) checkerboard fusion of supine scan and registered prone scan; b) appearance of a marker in the unsmoothed supine scan; c) appearance of a marker in the supine scan after median smoothing; d) outline of marker model (superimposed on b) created through thresholding (c) to 300 pixel value and converting to 3D model (with 3D Slicers export to model function); e) two orthogonal views of the model segmented in (d) and the corresponding model of the marker in the prone scan.

In segmenting the markers, it was found that the clear hydrogel-bead boundary allowed for decent reconstruction of the 4 mm diameter beads. Thresholding of the smoothed supine scan to a pixel value of 300 and the subsequent conversion to model with the “export to model function” was found to reconstruct the supine markers with mean *x*, *y* and *z* diameters of 4.6 ± 0.1, 4.4 ± 0.1 and 4.3 ± 0.1 mm, respectively. Similarly, the prone markers presented with mean *x*, *y* and *z* diameters of 4.7 ± 0.2, 4.4 ± 0.1, and 4.3 ± 0.1 mm, respectively, demonstrating reliable segmentation of the markers.

To further assess the reliability of the registration and segmentation methods, the phantom was scanned in the supine position and then twice re-scanned after being nudged forward by a few mm in the scanner. The two re-scans were then registered to the initial scan to compare any discrepancy in marker centroid location after segmentation. Mean volume centroid discrepancies of 0.06 ± 0.03 mm and 0.05 ± 0.02 mm were found for the first and second re-scans, respectively, indicating good reliability in the registration and segmentation methods.

Illustrated in Figure 8.14 are the reconstructed models of all the markers within the particular phantom taken for CT scanning. Here the consistency of the reconstruction method can be seen visually across the complete marker set. It can also be seen that a good distribution of markers is achieved throughout the brain with the map pin and bridging line system that was developed.

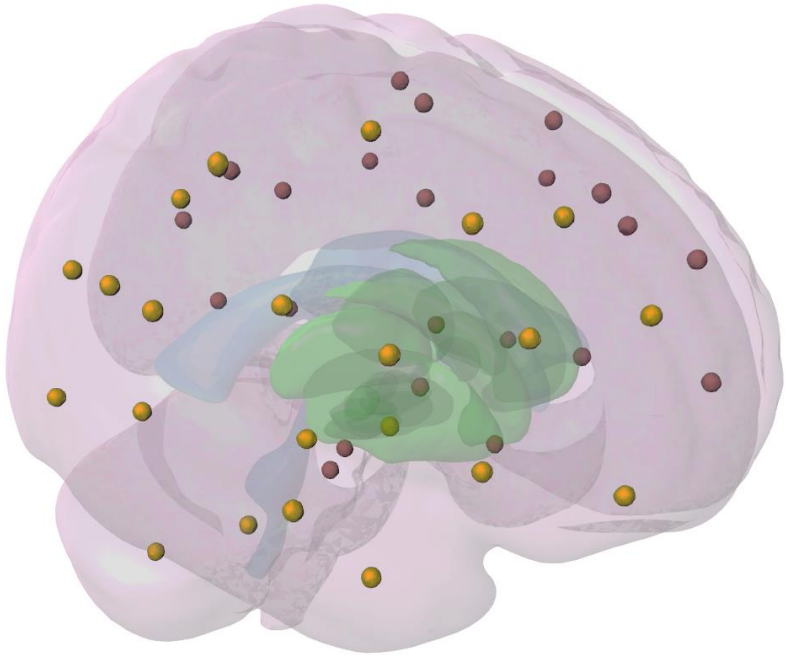

Figure 8.14: Reconstructed marker set. Left-hand set is coloured red; right-hand set is coloured gold. See Figure 8.15 for detailed marker distribution maps. Overlaid brain (pink) and ventricle (blue) geometries are the original segmentations of the MNI-ICBM dataset. Overlaid subcortical structures (green) are segmentations of the MNI PD-25 dataset after rigid registration to the MNI-ICBM dataset (which did not contain sub-cortical structural segmentations), which were added to provide additional positional context.

Figure 8.15 presents a distribution map for the marker set. Here the markers are split into left-hand and right-hand marker sets which are pseudo-symmetrical with respect to the central sagittal plane of the brain. Depending on their approximate location in the brain, the markers of each marker set are then further categorized. As illustrated, each side of the brain contains 2 cerebellar markers, 2 occipital markers, 6 parietal markers, 4 temporal markers, 7 frontal markers and one marker with close relationship to the substantia nigra, termed sub-nucleal (SN). The green sub-cortical structures were added here to provide additional context to the position of the markers.

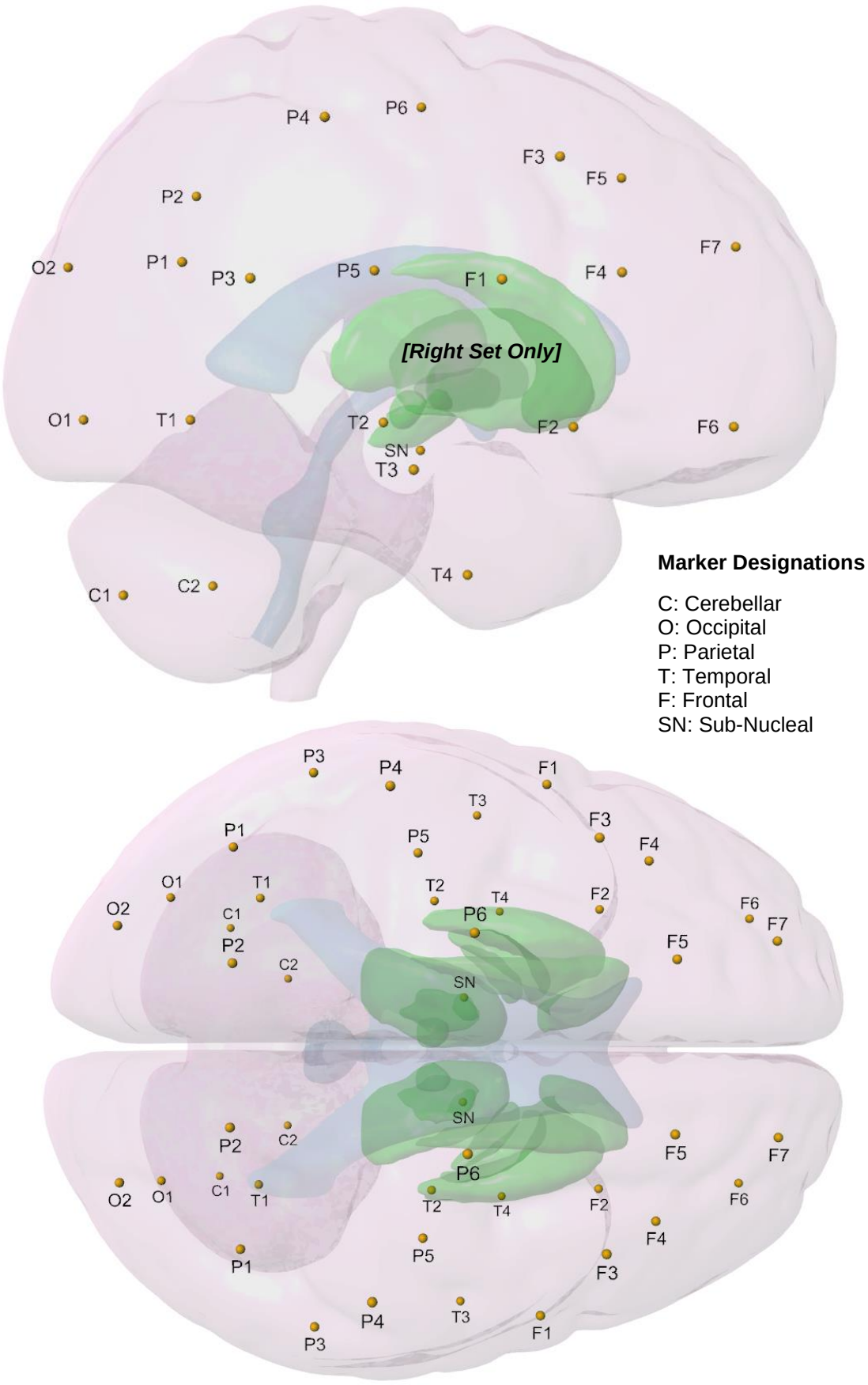

Figure 8.15: Distribution maps of marker set. Top image shows distribution of the right-hand marker set in the sagittal plane. Bottom image shows the distribution of the left- and right-hand marker sets in the axial plane. Marker designations are assigned to markers based on approximately which brain lobe they lie in, except for the SN markers which lie beneath the grey matter nuclei, particularly the substantia nigra.

A final note to be made regarding the CT imaging assessment of the phantom is that it can be seen that the recreation of the geometry of the cranial cavity and its compartmentalization by the dural septa is realistic (Figure 8.16). This assessment was difficult to achieve with the ambiguous boundaries and geometrical distortion prevalent in the MR images of the phantom.

This assessment was achieved through fitting the MNI ICBM152 skull model to the skull of the phantom's CT scan and then using the same transform to fit the dural septa.

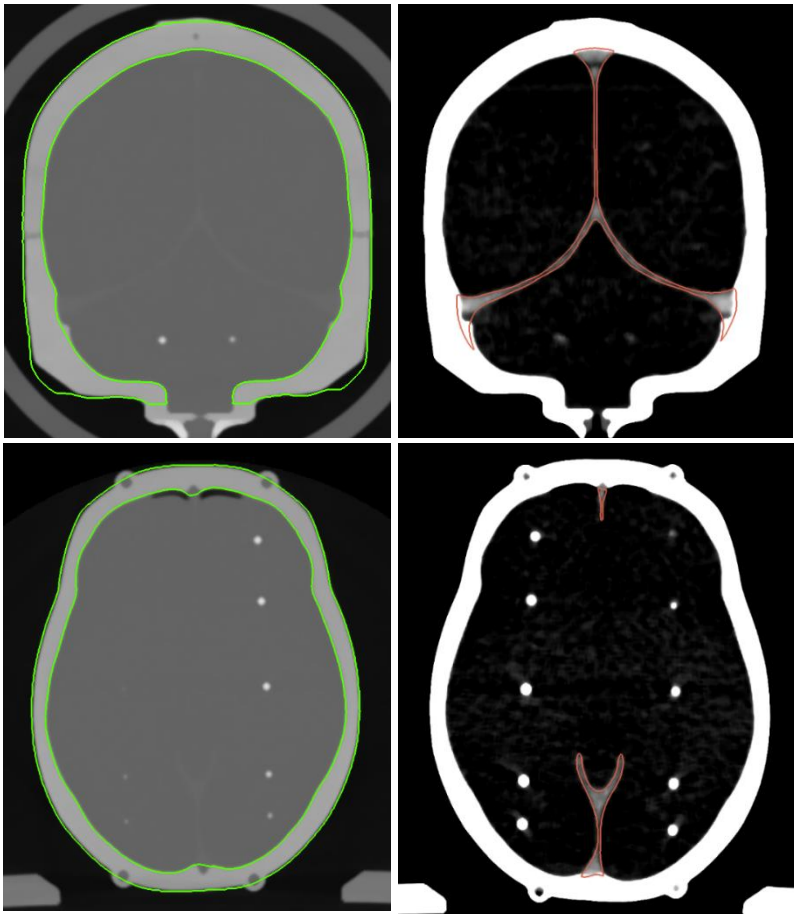

Figure 8.16: Comparison of boundaries between original segmented models of skull (green) and dural septa (red) from MNI dataset and the CT scan of the fabricated phantom. Contrast of right hand images are set to best view the barely detectable dural septa.

8.2.4 Selection of Brain Shift Imaging Modality

The glass bead marker system was found to function poorly with MR imaging but successfully with CT imaging. Reliable high precision segmentation of the beads was found to be achievable between differently orientated scans and the registration using the phantom's skull was found to be robust.

Consequently, CT was chosen as the imaging modality for measurement of brain shift. However, it was identified that MRI would still be needed (due to loss of anatomical contrast in CT) to image the construction of the phantom, as confirmation is needed to properly draw conclusions from any brain shift measured.

8.3 Supine to Prone Brain Shift Assessment

8.3.1 Positional Brain Shift with the Initial Hydrogel Formulation

With a brain shift measurement process determined, PBS within the developed phantom was next assessed and compared to that reported in the literature for the supine to prone transition (S→P). This particular transition was chosen to validate/tune the phantom due to it being the transition with by far the most *in vivo* data available for comparison.

To assess S→P brain shift, a fresh phantom was made with the IF and taken for CT scanning. This phantom, hereafter referred to as the IF phantom, was then scanned once in the supine position and once in the prone position, with a 10 minute settling time prior to each scan. With the positions imaged, the prone scan was then rigidly registered to the supine scan, before segmenting the markers out of the respective scans and determining the displacement of the marker centroids from the supine scan to the prone scan. Following the acquisition of PBS data, the brain of the phantom was sacrificed and indented in the same manner described in Section 7.2 (p128), except this time both hemispheres were indented. The time between defrosting the brain to indentation of the brain was kept under a week for this experiment and all subsequent experiments.

As illustrated in Figure 8.17, the loading response of the 2nd production of the IF hydrogel was found to be practically the same as the 1st production (see Figure 7.11 and Figure 7.12, p131). Larger variability can be seen in the data, but as both hemispheres were indented there is twice the opportunity for the variability to manifest. In this particular indentation session, the delicate touching load was also found to be especially difficult to find due to activity in the large multi-occupancy engineering lab. This activity manifested itself as sudden spikes in the load cells output. Two extreme examples can be seen in the solid green relaxation curve. The anomalous grey-dashed curve was deemed a result of uncertainty in touching load rather than as a result of any anomalous stiffness at that indentation site.

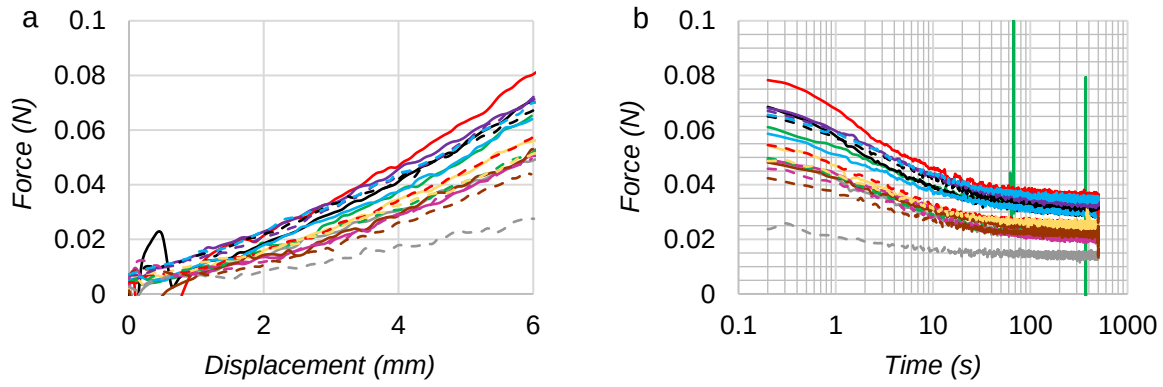

Figure 8.17: Indentation data for the brain used in the IF phantom. a) force-displacement data; b) logarithmic time-relaxation data. Solid and dashed curves pertain to tests of the left and right hemispheres, respectively.

No statistical assessment was made between the loading response of the left and right hemisphere indentation sites due to sufficient uncertainty in indentation depth across the measurements, however there does not appear to be any obvious difference between the left (solid curves) and right (dashed curves) loading responses.

Displayed in Table 8.1 are a collection of metrics which describe the depth and symmetry of the markers within the marker set that was present in the IF phantom. The depth metric describes the distance from each marker to its closest point on the skull, while the *x*, *y* and *z* mirrored difference metrics describe the discrepancy in position between the left-hand (LH) markers and the right-hand (RH) markers after mirroring the RH markers across the central sagittal plane to the left hand side (i.e. a measure of symmetry).

Overall, these metrics show that the LH and RH marker sets were reasonably symmetrical in the IF. The mean, standard deviation and range for the LH and RH marker sets are practically the same and the *x*, *y* and *z* mirrored differences all have means of only a few tenths of a mm and standard deviations less than 2.2 mm.

Table 8.1: Depth and symmetry metrics of the marker set in the IF phantom. Mirrored difference describes the discrepancy in position between the left-hand markers and the right hand markers after mirroring across the central sagittal plane.

Marker Site	Left Depth (mm)	Right Depth (mm)	Mirrored *x* Difference (mm)	Mirrored *y* Difference (mm)	Mirrored *z* Difference (mm)
C1	9.9	9.7	1.1	1.3	-2.4
C2	18.5	19.6	1.2	-0.3	1.1
O1	15.2	13.3	-3.1	1.5	3.4
O2	8.9	8.4	4.5	-1.4	-0.1
P1	18.2	16.3	1.1	-2.9	-0.5
P2	26.2	26.1	0.7	0.0	0.3
P3	9.1	8.9	1.1	-1.8	1.1
P4	7.3	7.8	-0.5	2.2	-0.2
P5	28.2	27.3	-0.9	-2.1	-0.1
P6	18.7	18.8	-0.5	0.8	-0.5
T1	27.5	24.3	-2.7	-0.4	2.9
T2	25.3	28.0	-1.6	-0.1	3.2
T3	10.0	11.2	2.5	2.8	-4.0
T4	10.5	9.0	0.7	-1.1	-1.8
SN	4.9	4.3	-0.3	0.0	-1.2
F1	7.6	8.7	0.5	0.3	2.8
F2	16.7	20.2	-0.8	-0.5	3.7
F3	7.8	7.8	-0.2	-2.4	4.0
F4	16.2	15.4	-3.7	-2.0	0.9
F5	14.7	16.8	-0.7	0.5	-2.1
F6	7.4	11.0	-0.7	1.5	3.8
F7	8.3	8.3	-4.8	-0.3	-1.1
Mean ± Sd	14.4 ± 7.1	14.6 ± 7.0	-0.3 ± 2.0	-0.2 ± 1.5	0.6 ± 2.2
Range	4.9 to 28.2	4.3 to 28.0	-4.8 to 4.5	-2.9 to 2.8	-4.0 to 4.0

Presented in Figure 8.18, Figure 8.19 and Figure 8.20 is the brain shift data extracted from the S→P imaging session with the IF phantom.

Figure 8.18 shows a collection of metrics for the magnitude of displacement which manifested in the IF phantom. Immediately it can be seen that the brain shift which manifested in the IF phantom was very muted with a mean marker displacement of only 0.19 ± 0.09 mm and a range of 0.04 - 0.44 mm. What little shift there was, however, appeared to manifest reasonably symmetrically as exhibited by the "individual marker displacements" radar graph. It should be noted that the connecting lines of the radar plots in this thesis serve only to help the reader more easily identify the individual data points. This is especially necessary for the busier plots of Chapter 9 (e.g. Figure 9.12 - p182).

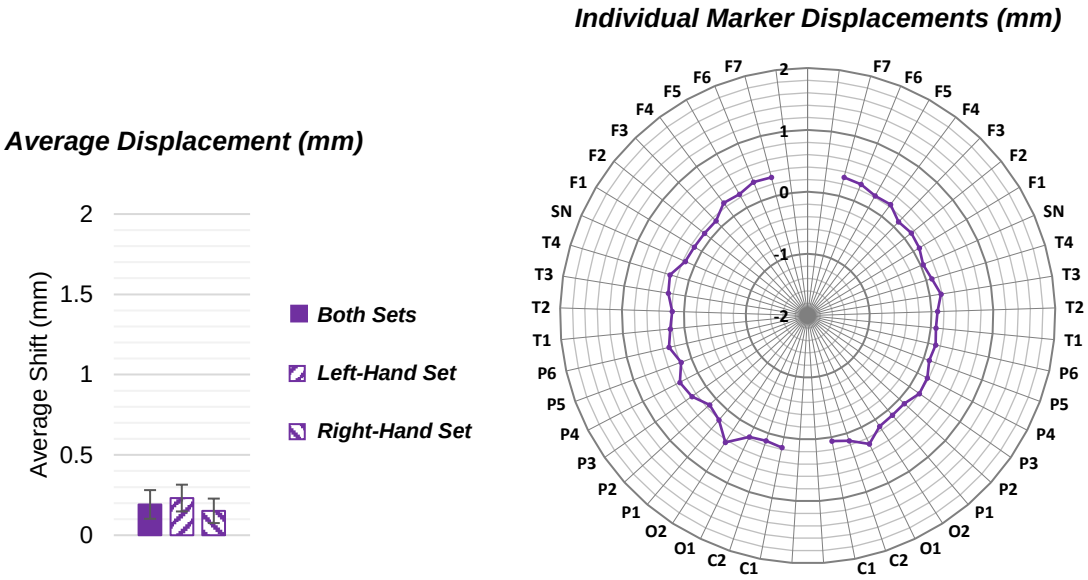

Figure 8.18: Displacement of markers upon transition from the supine position to the prone position in the IF phantom.

Figure 8.19 and Figure 8.20 present the shift data in vector format in the sagittal plane and axial plane, respectively. For easier later comparison, these graphics share the same format as those that will be displayed for the multi-positional study (see Figure 9.13 - p184 and Figure 9.14 - p185) and, therefore, spaces can be seen for the shift upon transition to positions other than prone. In these graphs (Figure 8.19 and Figure 8.20), it can also be seen that the manifested shift is very small and, critically, much smaller than that reported by the PBS studies reviewed in Section 3.5 (p45) (approximately 0-2 mm for a majority of the brain shift). MR images of the phantom taken prior to indentation of the brain showed the phantom to have a SAS of sufficient size to accommodate shifts of mm magnitude, suggesting that the muted shift likely had more to do with the unrealistically small density differential between the IF hydrogel brain and Di H_20 CSF. Therefore, it was identified that the density differential needed to be improved in order to simulate PBS, as predicted earlier on in the phantom's development (see Section 7.3, p132).

[IF Phantom]

Sagittal Plane Displacement upon Transition from the Supine Position to:

Prone (P)

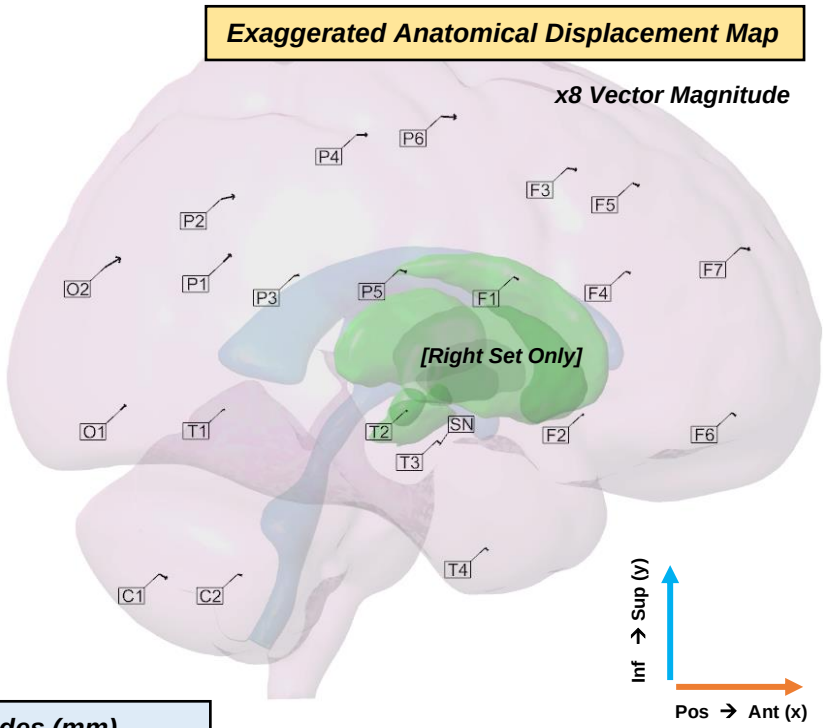

True Component Magnitudes (mm)

L-C1	L-C2	L-O1	L-O2	L-P1	L-P2
x +0.08 y +0.01	+0.12 +0.00	+0.18 +0.29	+0.34 +0.17	+0.29 +0.13	+0.28 +0.17
R-C1	R-C2	R-O1	R-O2	R-P1	R-P2
+0.21 -0.12	+0.12 -0.04	+0.13 +0.14	+0.42 +0.25	+0.20 +0.22	+0.37 +0.08
L-P3	L-P4	L-P5	L-P6	L-T1	L-T2
+0.12 +0.14	+0.21 +0.05	+0.12 +0.12	+0.30 +0.01	+0.03 +0.08	+0.08 -0.00
R-P3	R-P4	R-P5	R-P6	R-T1	R-T2
+0.13 +0.03	+0.29 -0.00	+0.20 -0.06	+0.42 -0.02	+0.02 -0.03	+0.02 -0.04
L-T3	L-T4	L-SN	L-F1	L-F2	L-F3
-0.05 +0.08	+0.02 +0.04	-0.05 +0.02	+0.10 +0.14	+0.06 +0.05	+0.16 +0.05
R-T3	R-T4	R-SN	R-F1	R-F2	R-F3
+0.10 -0.09	+0.07 -0.07	-0.01 +0.00	+0.13 -0.07	-0.02 -0.06	+0.25 -0.05
L-F4	L-F5	L-F6	L-F7		
+0.19 +0.06	+0.15 +0.04	+0.09 +0.03	+0.22 +0.05		
R-F4	R-F5	R-F6	R-F7		
+0.13 -0.05	+0.18 -0.08	+0.10 -0.08	+0.26 -0.04		

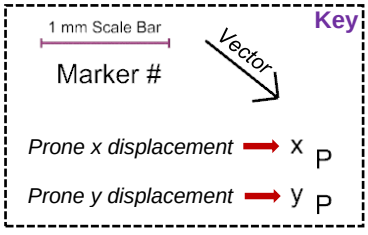

Figure 8.19: Sagittal plane marker displacement in the IF phantom upon transition from the supine position to prone. Shown in the Exaggerated Anatomical Displacement Map graphic are the displacement vectors with length exaggerated by a factor of eight but with real anatomical start position. Shown in the Actual Component Magnitudes graphic are the displacement vectors repositioned onto a grid with real component magnitudes listed below (see key). L and R stand for left and right, respectively (e.g. R-C1 = right C1 marker).

[IF Phantom]

Axial Plane Displacement upon Transition from the Supine Position to:

Prone (P)

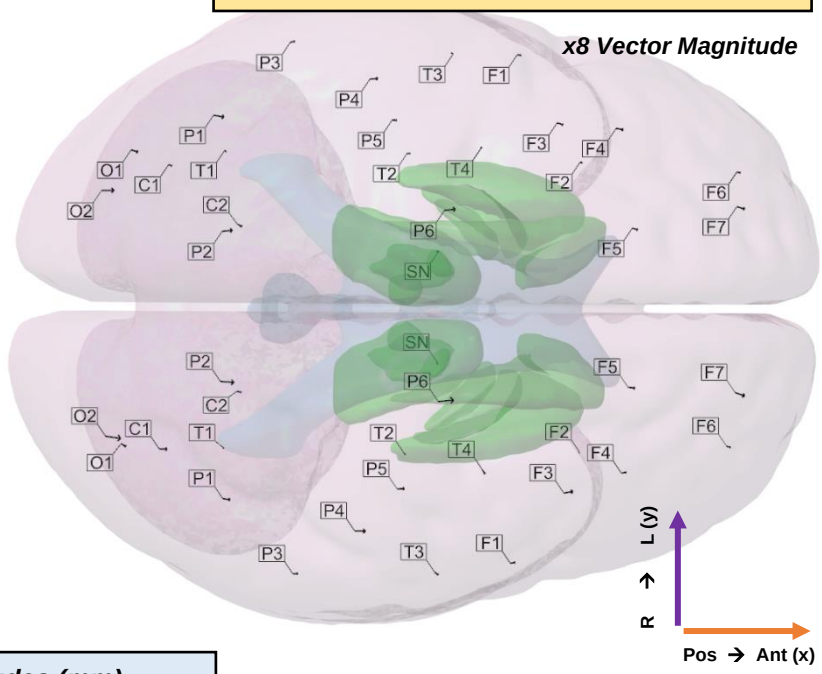

True Component Magnitudes (mm)

L-C1	L-C2	L-O1	L-O2	L-P1	L-P2
+0.08 -0.04	+0.12 -0.07	+0.18 -0.06	+0.34 +0.01	+0.29 -0.05	+0.28 +0.03
R-C1	R-C2	R-O1	R-O2	R-P1	R-P2
+0.21 -0.01	+0.12 -0.03	+0.13 -0.08	+0.42 -0.06	+0.20 -0.03	+0.37 -0.02
L-P3	L-P4	L-P5	L-P6	L-T1	L-T2
+0.12 +0.02	+0.21 +0.01	+0.12 -0.00	+0.30 +0.03	+0.03 -0.05	+0.08 -0.00
R-P3	R-P4	R-P5	R-P6	R-T1	R-T2
+0.13 +0.00	+0.29 -0.01	+0.20 +0.01	+0.42 +0.04	+0.02 -0.03	+0.02 -0.04
L-T3	L-T4	L-SN	L-F1	L-F2	L-F3
-0.05 +0.04	+0.02 +0.04	-0.05 -0.03	+0.10 -0.01	+0.06 -0.03	+0.16 -0.05
R-T3	R-T4	R-SN	R-F1	R-F2	R-F3
+0.10 -0.08	+0.07 -0.11	-0.01 -0.04	+0.13 +0.02	-0.02 -0.02	+0.25 +0.04
L-F4	L-F5	L-F6	L-F7		
+0.19 -0.04	+0.15 -0.04	+0.09 -0.03	+0.22 -0.07		
R-F4	R-F5	R-F6	R-F7		
+0.13 +0.02	+0.18 -0.03	+0.10 -0.03	+0.26 -0.09		

Key
1 mm Scale Bar
Marker #
Vector
Prone x displacement → x P
Prone y displacement → y P

Figure 8.20: Axial plane marker displacement in the IF phantom upon transition from the supine position to prone. Shown in the Exaggerated Anatomical Displacement Map graphic are the displacement vectors with length exaggerated by a factor of eight but with real anatomical start position. Shown in the Actual Component Magnitudes graphic are the displacement vectors repositioned onto a grid with real component magnitudes listed below (see key). L and R stand for left and right, respectively (e.g. R-C1 = right C1 marker).

8.3.2 Positional Brain Shift with an Altered Hydrogel Formulation

In an effort to manifest a greater magnitude of brain shift in the phantom, an attempt was next made to increase the hydrogel's density so that a greater density differential was achieved between the phantom's brain and its CSF surrogate.

Since stable sugar solutions can be created in a similar heating and cooling process to that found in the hydrogel preparation protocol, the addition of granulated white sugar to the hydrogel formulation was trialled. Approximately 99% of white sugar is sucrose which has a considerably higher density (1.58 g/cm^3) to that of deionised water [162].

A number of formulations where trialled, incorporated into phantoms and investigated for suitability in the same approach detailed in the previous section. The formulation comprising *[2.15% PVA : 0.25% PHY : 2.45% Sugar : 95.15% Di H_20]* (sugar formulation - SF) was eventually found to produce a phantom capable of manifesting brain shift with a magnitude similar to that reported in PBS studies (approximately 0-2 mm).

As can be seen in Figure 8.21, the hydrogel material manufactured with the SF turned out to be considerably softer than that manufactured with the IF, with peak loads being approximately halved from 350 - 600 μN to 215 - 340 μN. The oscillations visible in the force-displacement curves of Figure 8.21a were considered to be a result of an unintended inclusion of less water in the bucket containing the cerebral segments, thus creating an environment wherein minute but nonetheless impactful waves are more easily generated around the indenter. Although the water level was lesser in these measurements, it still remained approximately 2 cm above the end of the indenter and so likely was not a surface tension problem.

With an elastic modulus of approximately 0.65 to 0.86 kPa, when calculated again with the conversation equation from [158], the SF hydrogel still presents with a stiffness within the range reported for brain tissue 0.3 - 3.0 kPa, albeit at the lower end.

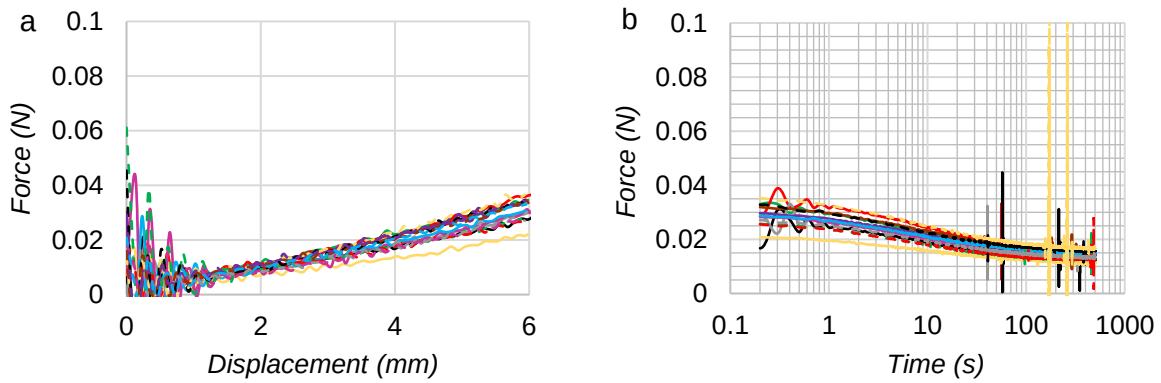

Figure 8.21: Indentation data for the brain used in the SF phantom. a) force-displacement data; b) logarithmic time-relaxation data. Solid and dashed curves pertain to tests of the left and right hemispheres, respectively.

Using the same method described in Section 7.3 (p132), the density of the SF formulation was measured to be 1.010 ± 0.008 g/cm^3, doubling the submerged weight of the IF brain from approximately 9 to 18 g. This is still a small fraction of the anatomical submerged weight, however, together with the approximately halved stiffness of the brain it was found to be sufficient to recreate the shift magnitude seen in S→P brain shift.

As can be seen in Table 8.2, the depth and symmetry measures for the SF phantom are largely similar to that of the IF phantom, except for the left cerebellar markers (C1 and C2). On disassembly of this phantom it appeared that the left cerebellar lobe had become pinched between the dural septa and the skull in assembly, leading the left cerebellar markers to present in a significantly different position to that of the IF phantom. Excluding the cerebellar markers (left and right to keep population size the same), however, it can be seen that the depth and symmetry profiles are similar for both phantoms.

Table 8.2: Depth and symmetry metrics of the marker set in the SF phantom. Mirrored difference describes the discrepancy in position between the left-hand markers and the right-hand markers after mirroring across the central sagittal plane. C1 and C2 markers were not used in the calculation of mean, standard deviation or range.

Marker Site	Left Depth (mm)	Right Depth (mm)	Mirrored *x* Difference (mm)	Mirrored *y* Difference (mm)	Mirrored *z* Difference (mm)
C1	7.7	14.4	-12.8	21.9	7.3
C2	11.6	14.2	-5.1	9.4	5.5
O1	11.0	11.3	-2.5	3.5	3.0
O2	11.1	12.0	1.6	-1.0	-1.1
P1	16.6	16.7	2.4	0.0	2.0
P2	25.0	25.7	3.2	-0.5	1.0
P3	11.2	12.3	1.6	-0.8	7.5
P4	9.1	6.2	6.1	1.3	1.7
P5	28.6	28.5	0.7	-0.7	4.0
P6	20.6	20.3	3.3	0.8	1.0
T1	23.4	24.6	-1.8	2.1	3.8
T2	30.5	27.1	0.1	2.5	5.1
T3	10.3	8.9	3.0	5.2	0.8
T4	14.8	14.4	-2.5	0.1	1.4
SN	9.4	8.0	2.5	-1.3	1.9
F1	7.5	10.7	-2.4	-3.6	11.0
F2	21.0	18.3	0.5	1.0	3.8
F3	10.7	11.7	3.1	-4.3	8.0
F4	13.6	15.4	-1.3	-0.8	4.8
F5	16.9	15.5	2.1	0.6	-0.7
F6	11.9	9.2	0.7	2.8	3.2
F7	11.1	12.2	-5.1	-0.5	0.8
Mean ± Sd	15.7 ± 6.7	15.5 ± 6.5	0.8 ± 2.6	0.3 ± 2.2	3.2 ± 2.9
Range	7.5 to 30.5	6.2 to 28.5	-5.1 to 6.1	-4.3 to 5.2	-1.1 to 11.0

Table 8.3 shows the difference in position between the markers of the IF phantom and the SF phantom after co-registration. Here it can be seen that the location of the markers differ to a small degree. This is unsurprising given the nature of the marker positioning methods and the complex dynamics of freezing that takes place in the mould. However, with only an average discrepancy of 6.9 ± 3.4 and 4.3 ± 1.3 mm for the left and right marker sets, respectively, the variation in position does not make inter-phantom comparison impossible.

Table 8.3: Difference between marker positions of the IF and SF phantoms after co-registration. C1 and C2 markers were not used in calculation of mean, standard deviation or range.

Marker Site	Total Difference (mm)		*x* Difference (mm)		*y* Difference (mm)		*z* Difference (mm)	
	Left	Right	Left	Right	Left	Right	Left	Right
C1	29.0	10.9	4.4	7.8	-27.7	-7.2	-7.6	2.4
C2	19.5	11.8	-3.0	8.0	-17.9	-8.3	-7.1	-2.5
O1	2.5	4.8	1.9	-3.5	1.0	2.9	-1.4	-1.7
O2	3.3	3.2	-0.4	2.2	-2.4	-2.1	2.2	1.2
P1	4.4	3.9	-2.4	0.1	1.1	3.7	-3.6	-1.0
P2	6.2	2.9	-5.8	2.5	2.2	1.4	-0.6	0.2
P3	12.2	5.9	-4.3	3.1	-0.2	0.3	-11.4	-5.0
P4	11.1	4.5	-8.9	1.6	3.7	2.2	-5.5	-3.6
P5	7.5	3.4	-2.0	-0.3	0.7	1.6	-7.2	-3.0
P6	10.2	5.6	-9.6	5.2	2.0	1.5	-3.1	-1.5
T1	2.8	4.0	1.1	-2.8	0.1	2.4	-2.6	-1.6
T2	4.4	3.2	-0.3	-2.0	-1.5	0.9	-4.2	-2.3
T3	9.6	4.4	-0.8	-0.3	-3.1	-1.1	-9.0	-4.2
T4	8.9	5.1	4.3	-1.7	0.4	1.5	-7.8	-4.6
SN	9.7	6.4	-3.3	0.1	-0.3	-1.8	-9.1	-6.2
F1	10.4	5.3	-1.7	4.2	1.7	-2.6	-10.1	-1.9
F2	2.8	2.6	-0.1	-1.6	-1.7	-0.4	-2.2	-2.1
F3	11.8	7.2	-10.7	7.1	1.8	-0.7	-4.5	-0.7
F4	7.2	2.5	-3.4	0.6	-2.2	-1.3	-5.9	-2.0
F5	7.4	4.1	-6.6	3.6	0.9	0.8	-3.2	-1.7
F6	1.3	3.0	0.1	-1.6	1.0	2.0	-0.8	-1.5
F7	4.5	4.2	-0.3	0.5	4.4	4.0	-0.8	1.2
Mean ± Sd	6.9 ± 3.4	4.3 ± 1.3	-2.7 ± 3.9	1.5 ± 3.3	0.5 ± 1.9	0.0 ± 3.0	-4.5 ± 3.6	-1.9 ± 2.0
Range	1.3 to 12.2	2.7 to 7.2	-10.7 to 4.3	-3.5 to 8	-3.1 to 4.4	-8.3 to 4.0	-11.4 to 2.2	-6.2 to 2.4

Presented in Figure 8.22, Figure 8.23 and Figure 8.24 is the brain shift data extracted from the supine to prone imaging session with the SF phantom.

In Figure 8.22 it can be seen that the displacement which manifested in the SF phantom is much greater than that which manifested in the IF phantom, with an average of 1.07 ± 0.32 mm and a range of 0.22 - 1.66 mm. This is a similar displacement magnitude to that reported in the studies by Rice et al. [39], Schnaudigel et al. [123], Monea et al. [124], and Mikkonen and Laakso [125]. It can also be seen in the average displacement and the individual marker displacement graphs that the brain shift which manifested in this phantom was largely symmetrical (as observed in the IF phantom).

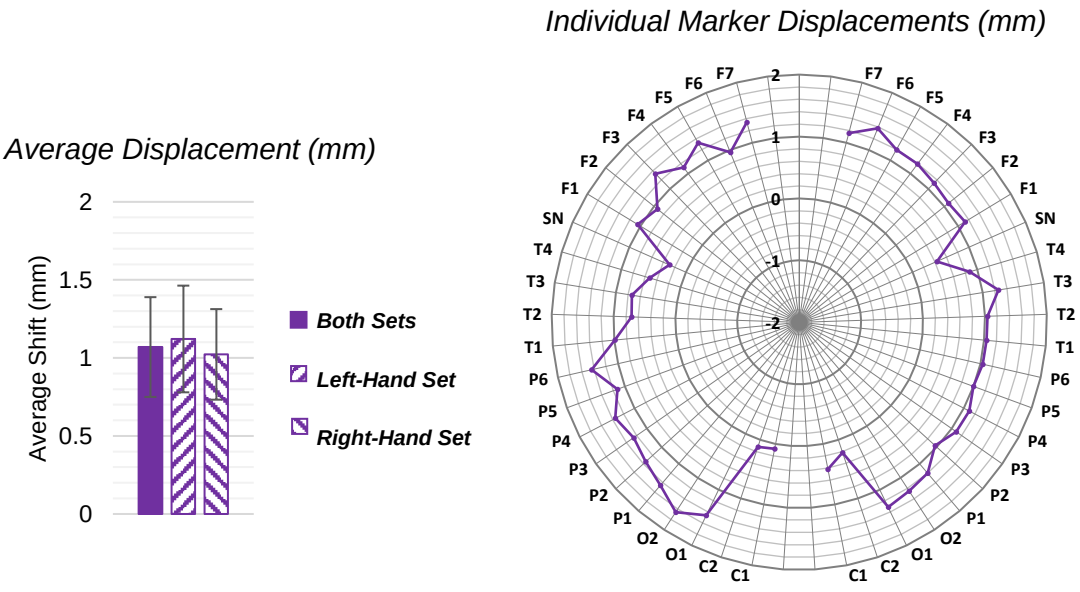

Figure 8.22: Displacement of markers upon transition from the supine position to the prone position in the SF phantom.

In Figure 8.23 and Figure 8.24 it can be seen that the direction and magnitude of displacement between markers is highly variable, indicating a realistic non-rigid shift.

Within these figures it can be seen that the greatest shift took place within the occipital, parietal and frontal regions of the brain. In comparison, Monea et al. observed greatest shift in the inferolateral aspects of the brain, while Mikkonen and Laakso observed greatest shift in the parietal regions. Although it might seem that the displacement within the SF phantom is somewhat in agreement with the observations made by Mikkonen and Laakso, the direction of displacement is very dissimilar, with their observed shift being predominantly inferiorly (see Figure 3.18, p48) and the SF phantom shift being predominantly anteriorly. However, it seems more realistic for the brain to shift predominantly anteriorly in the direction of gravity, as it does in the SF phantom, than perpendicular to the direction of gravity, as it appears to do in Mikkonen and Laakso's measurements.

[SF Phantom]

Sagittal Plane Displacement upon Transition from the Supine Position to:

Prone (P)

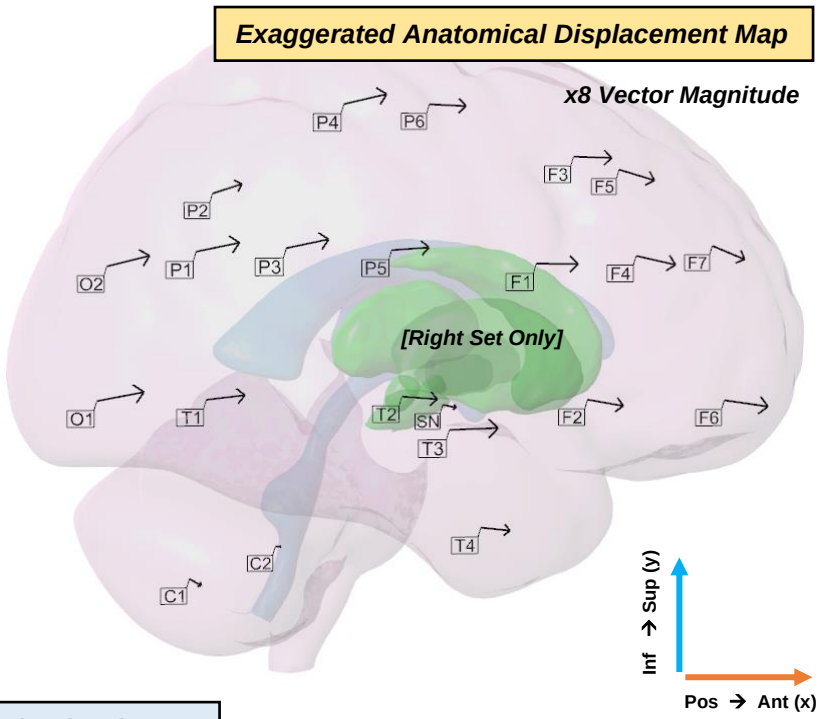

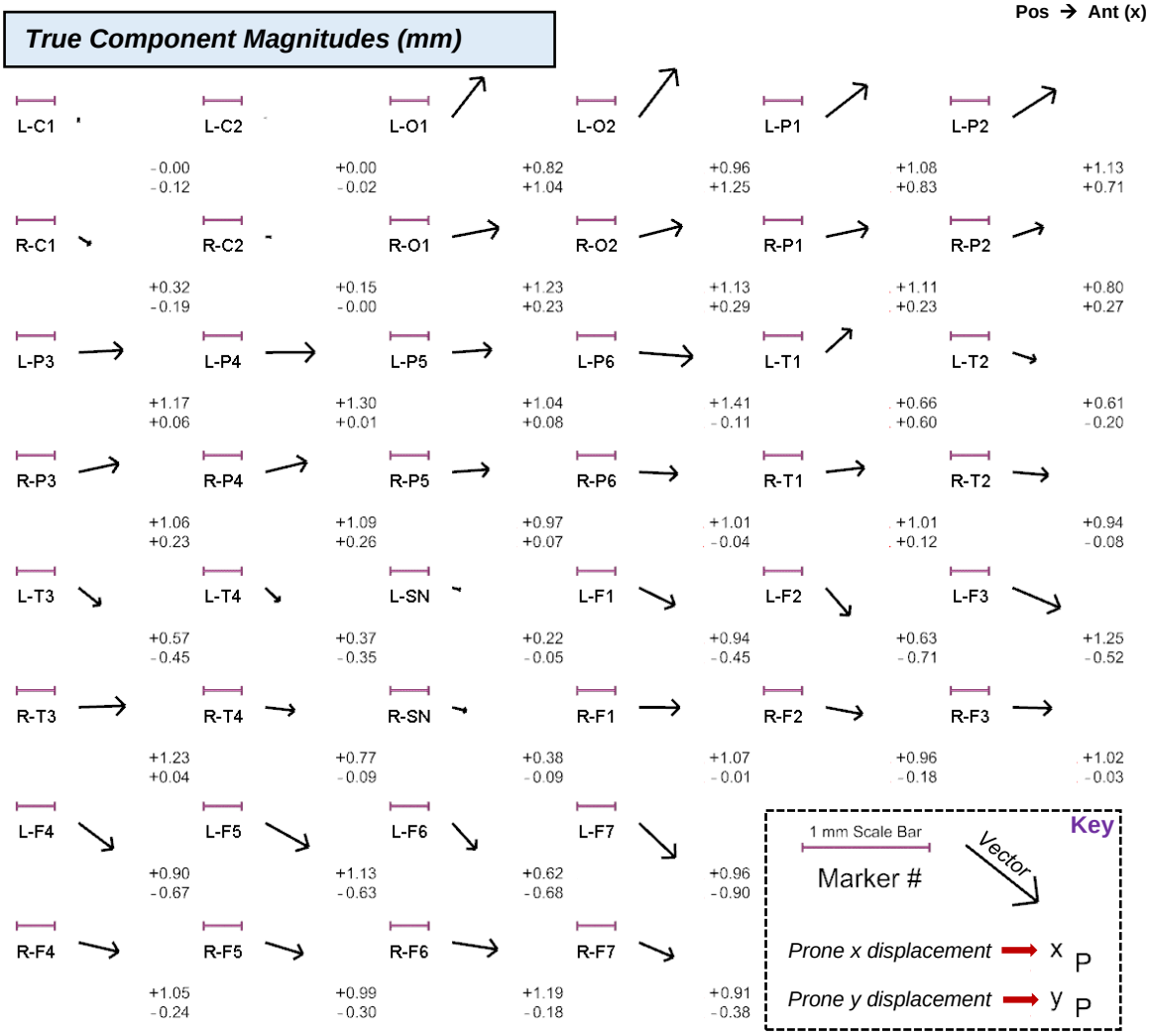

Figure 8.23: Sagittal plane marker displacement in the SF Phantom upon transition from the supine position to prone. Shown in the Exaggerated Anatomical Displacement Map graphic are the displacement vectors with length exaggerated by a factor of eight but with real anatomical start position. Shown in the Actual Component Magnitudes graphic are the displacement vectors repositioned onto a grid with real component magnitudes listed below (see key). L and R stand for left and right, respectively (e.g. R-C1 = right C1 marker).

[SF Phantom]

Axial Plane Displacement upon Transition from the Supine Position to:

Prone (P)

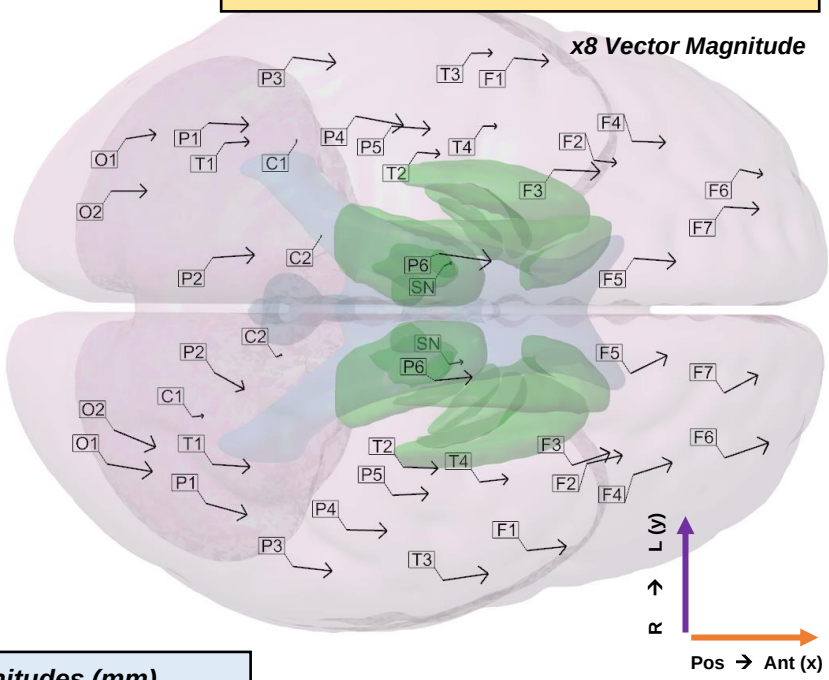

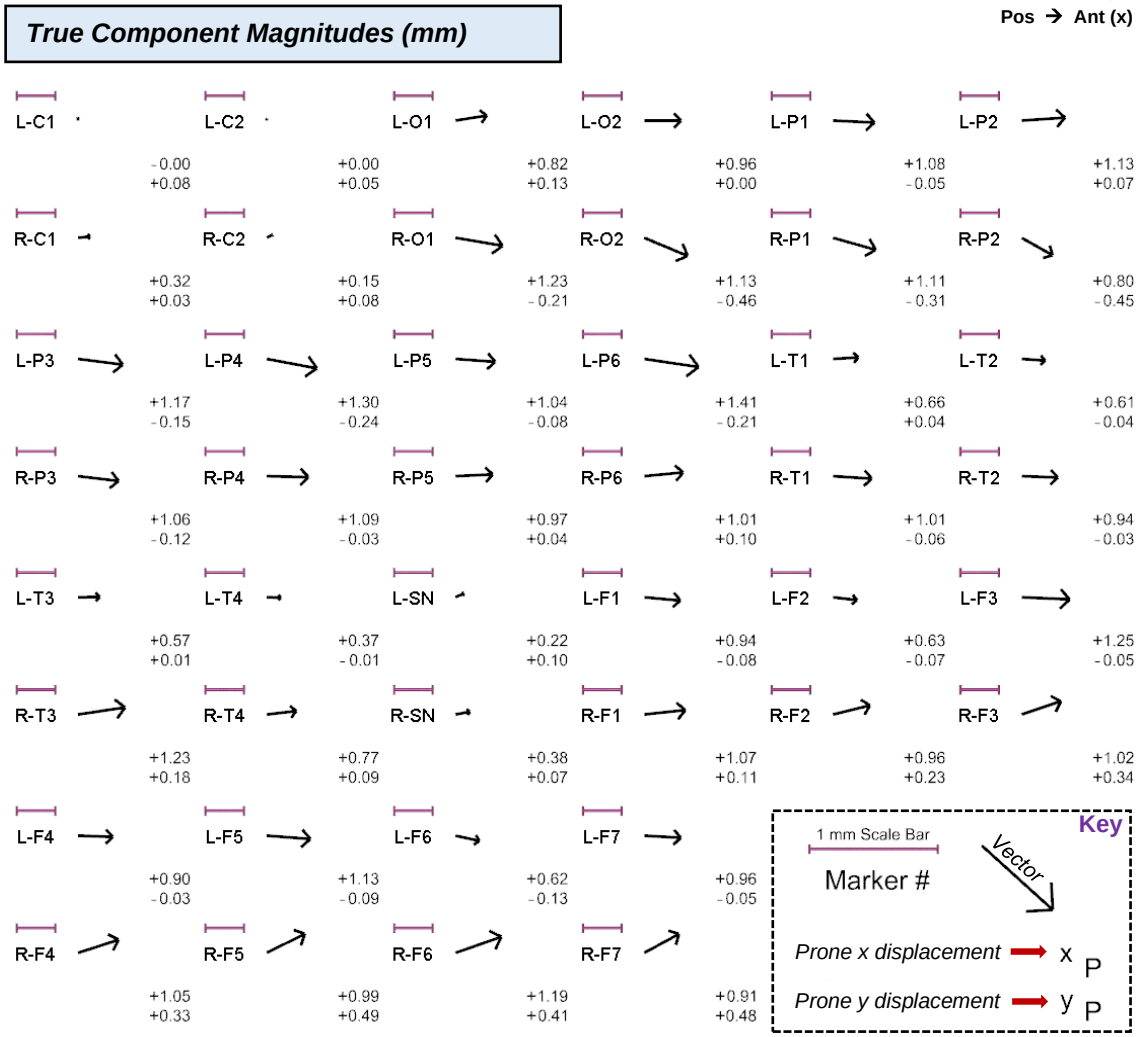

Figure 8.24: Axial plane marker displacement in the SF Phantom upon transition from the supine position to prone (black). Shown in the Exaggerated Anatomical Displacement Map graphic are the displacement vectors with length exaggerated by a factor of eight but with real anatomical start position. Shown in the Actual Component Magnitudes graphic are the displacement vectors repositioned onto a grid with real component magnitudes listed below (see key). L and R stand for left and right, respectively (e.g. R-C1 = right C1 marker).

Looking at the sagittal plane displacement, one can see a degree of rotation to the brain shift, with the center of rotation lying towards the top of the brain stem. This slight rotation is likely due to the absence of cerebral tethering and the cradling of the brain stem by the tentorium, and is likely the artificial result of omitting the arachnoid tethering.

Yet, despite some discrepancies in shift pattern, the use of the SF appears to produce a phantom with realistic S→P brain shift magnitude. Given that the phantom brain-CSF density differential and brain stiffness are low, relative to that measured for the anatomy, it could be inferred that either the higher density measurements or lower stiffness measurements for brain tissue (or both) are incorrect.

When placed on a table, in a similar manner to the unfixed brain in Figure 8.25, it can be seen that the SF brain adopts a similarly heavily deformed conformation, suggesting that the elastic properties of the two are somewhat matched. This, however, is only a qualitative comparison.

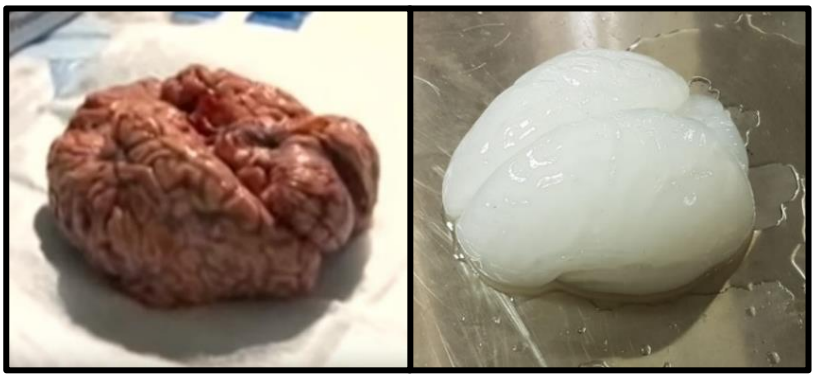

Figure 8.25: Freshly excised brain (left) and SF phantom brain (right) resting unsupported on a table, showing similar deformation. Image of the human brain is a still extracted from a YouTube video featuring a brain autopsy at the Banner Sun Health Research Institute [143].

Regardless, the SF phantom was shown to be capable of reproducing the S→P brain shift event. Therefore, going forward, the SF hydrogel was used as the phantom's brain simulant.

8.4 Chapter Summary

This chapter began with the preparation of the phantom for multi-position brain shift imaging. This involved the fabrication of an orientating cradle and the development of a brain shift measurement system for the phantom.

The cradle that was built was designed for both MR and CT imaging, but specifically to fit in a single-channel MRI head coil. This was done because MR head coils are invariably smaller than the bore of a CT scanner and because the single-channel head coil presented as the only coil large enough for an appropriately robust cradle. The built cradle presents as a novel device for orientating a head phantom in MR and CT imaging environments, with no similar device to be found in the literature.

A delivery method was next developed for the positioning of 44 glass bead markers within the phantom's hydrogel brain. This method involved the use of pins and line in the composite brain mould (removable when frozen) to position the 44 glass beads in a pseudo-symmetrical and pseudo-repeatable fashion. This method presents as a further novel technique in the context of cryo-moulding and in the non-random positioning of markers in a moulded brain.

Upon assessment of the phantom's marker set in MR and CT imaging, it was found that the marker set was incompatible with MR due to distortion difficulties at the brain-bead interface. With no means of abolishing this and with little distortion found to take place in CT imaging, it was decided that CT alone would be used to image the brain shift in the phantom. Although brain-bead contrast was found to be maximised in CT, contrast between other elements was lost. Therefore, it was identified that MR would still be necessary to confirm the construction of the phantom so that proper conclusions could be drawn from brain shift measurements. A superior 2D turbo spin echo sequence was identified to image the construction of the phantom, producing much greater detail with less distortion and artifacts than the 3D GRE sequence.

In CT imaging, the delivery method was found to produce a decent coverage throughout the brain and the markers were found to be repeatable in their segmentation and reconstruction between scans taken of the phantom in different positions (supine and prone). The rigid registration was found to be particularly robust due to the unambiguous boundaries of the skull.

Ready for use, the phantom and its cradle were next taken for CT scanning to assess whether the S→P brain shift event could be recreated, with respect to quantitative measurements of the event in the literature. Here it was found that the use of the IF (identified in the previous chapter) produced unrealistically low levels of brain shift.

In an effort to raise the general level of shift within the phantom, a new sugar containing formulation was developed with increased density and lowered stiffness. Use of this formulation doubled the submerged weight of the brain and, together with the lowered stiffness, was found to manifest a realistic level shift at around 0-2 mm as a result. This is comparable to measurements of S→P brain shift in the literature and so the phantom was decided to be somewhat validated in PBS simulation at this point.

At this stage, it was identified that the phantom could be used to investigate PBS beyond the S→P transition. The next and final stage of the project was to perform a multi-positional brain shift study with the phantom to generate a novel comprehensive PBS dataset that characterises a broader representative range of the spectrum of possible positional transitions in neurosurgery. This is presented in the next chapter.

[Blank Page]

9 MULTI-POSITIONAL BRAIN SHIFT STUDY

The previous chapter addressed the preparation of the phantom for PBS simulation and the tuning of the hydrogel brain to better match literature accounts of PBS. Introduced by Figure 9.1, this chapter contains a multi-positional study of PBS and includes the following novel work:

- The definition and description of a study to investigate PBS across a discrete representation of the continuous spectrum of possible positional transitions in neurosurgery.
- An account of the methods used to carry out the study.
- An analysis and discussion of the results, with comparison to the emerging data from the concurrent *in silico* and *in vivo* projects.

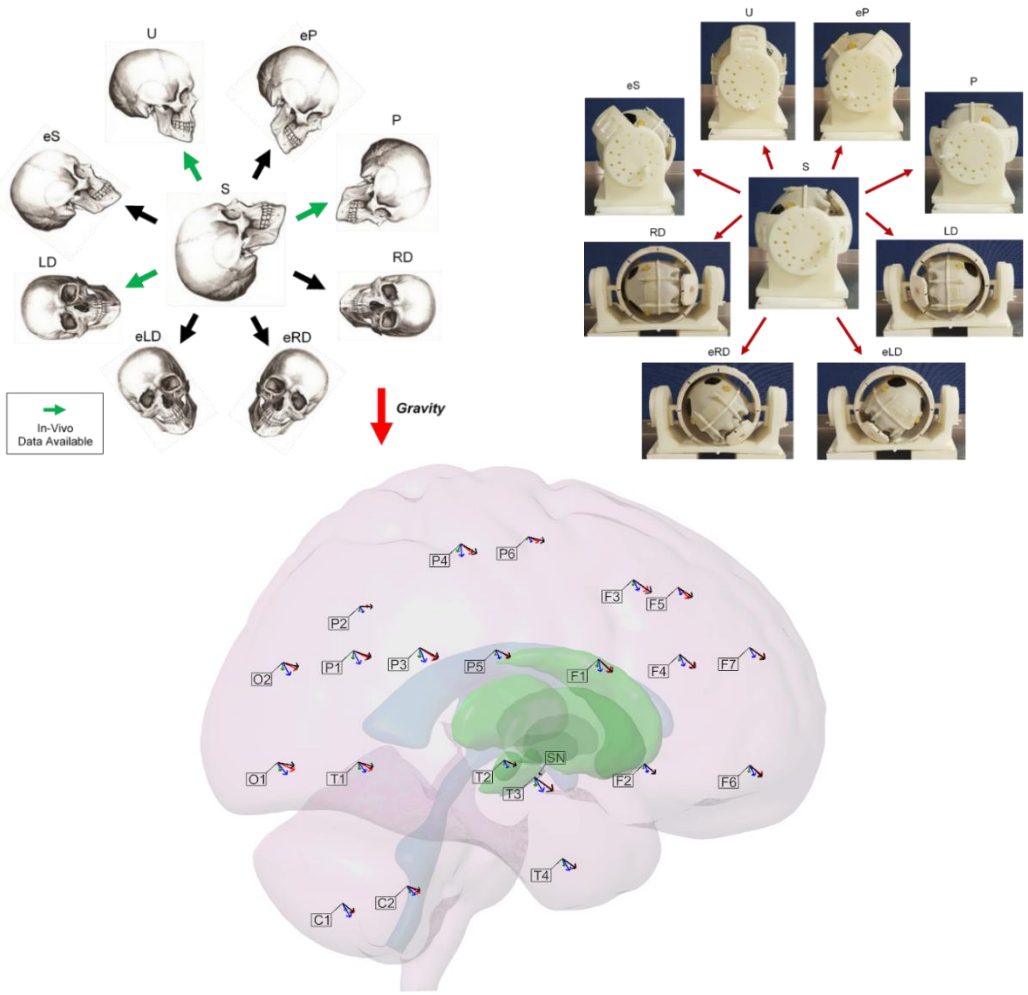

Figure 9.1: Chapter storyboard showing the selection of eight non-supine imaging positions (top-left and top-right images) and, in this particular image, the sagittal plane displacement upon transition to the elevated supine, upright, elevated prone and prone positions (bottom image). Images are reshown and discussed later in the chapter.

9.1 Introduction

As explored in Section 3.6 (p50), patients are routinely positioned across a continuous spectrum of head positions when operated on using the stereotactic method. This is because individual surgical cases come with individual logistical requirements, something which is especially true for interventions related to the treatment of pathology which can manifest anywhere in the brain, such as cancer.

Much of the work on PBS to date has focused on the measurement of brain shift upon transition from the supine to prone position. This measurement is important, but only produces actionable PBS information for a small fraction of stereotactic cases. The purpose of this study, therefore, was to produce novel PBS information for a discrete representation of the continuous spectrum of possible positional transitions in neurosurgery.

9.2 Methods

9.2.1 Selection of Head Positions

Shown in Figure 9.2 (p169) are the eight, non-supine, head positions chosen for study in this project. These include the elevated supine position (eS), the upright position (U), the elevated prone position, (eP) the prone position (P), the left decubitus position (LD), the elevated left decubitus position (eLD), the elevated right decubitus position (eRD) and the right decubitus position (RD). In this context, the “elevated” prefix term refers to a 45-degree rotation or elevation from whatever position term it precedes (e.g. supine of elevated supine). Elevated supine, therefore, refers to the position achieved through rotating the head 45 degrees from the supine position (S) towards the upright position. The elevated positions can also therefore be considered as midway positions.

The transitions marked by the green arrows in Figure 9.2 (p169) indicate transitions for which in-vivo brain shift data is available (see Section 3.5, p45). These are the transitions to the upright, prone and left decubitus positions. Although these transitions were not used to tune the phantom, they will be used when discussing the measurements of the same transitions made with the phantom.

Illustrated in Figure 9.3 (p169) is the phantom loaded into its cradle in the supine position and the eight non-supine positions. As identified in Section 8.1 (p138), an orientation error of ±1 degree exists within the cradle and so should be assumed for any of the positions mentioned in this study.

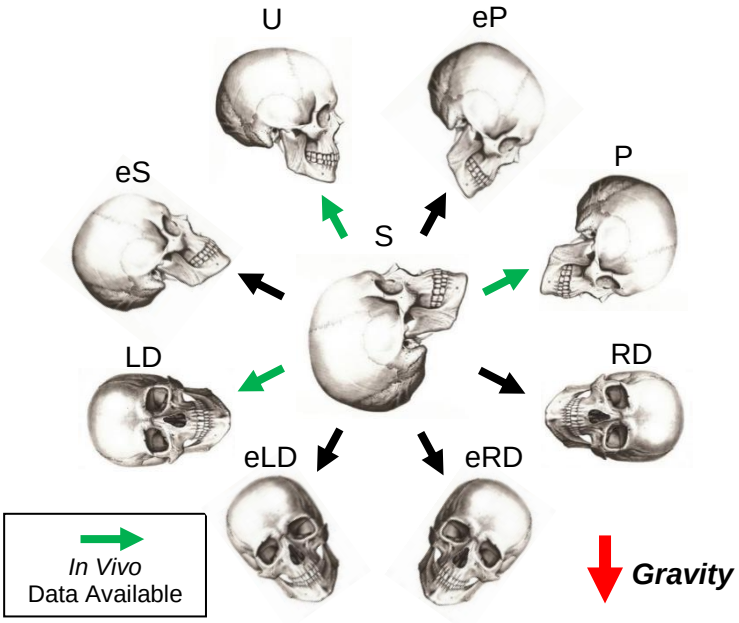

Figure 9.2: Map of the eight selected positions for positional brain shift measurement. S = supine; eS = elevated supine; U = upright; eP = elevated prone; P = prone; LD = left decubitus; eLD = elevated left decubitus; RD = right decubitus; eRD = elevated right decubitus. Green arrows represent transitions for which brain shift has been measured in humans using MRI or CT; black arrows represent transitions for which there is currently no in vivo data.

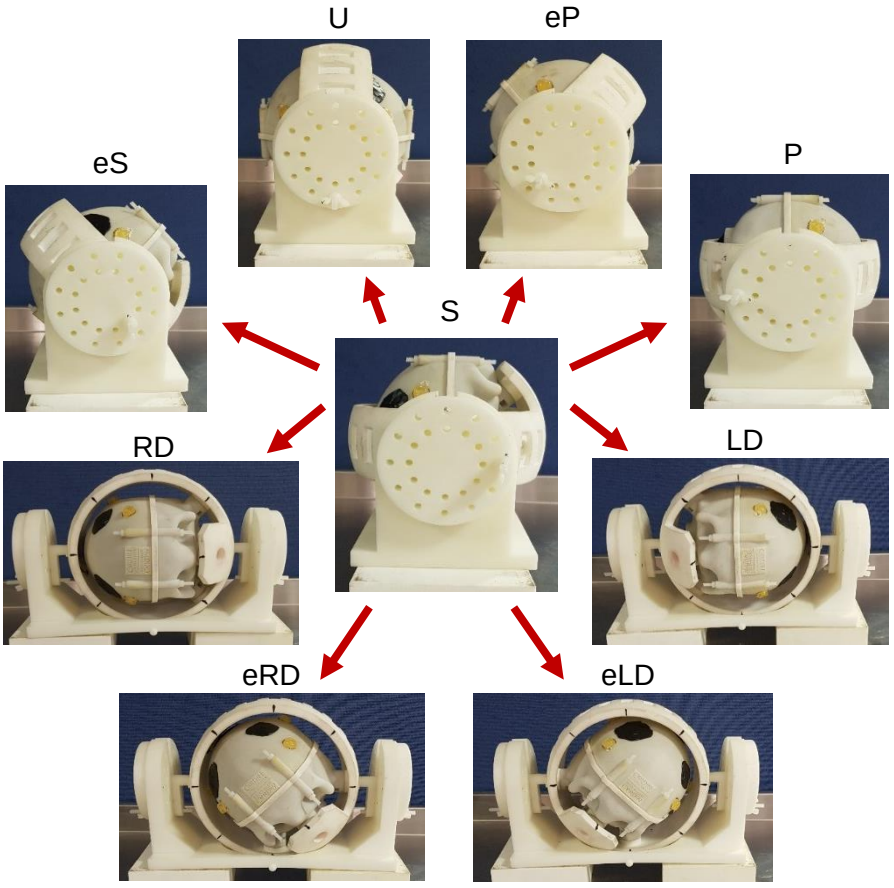

Figure 9.3: Phantom loaded into the cradle in the supine (S), elevated supine (eS), upright (U), elevated prone (eP), right decubitus (RD), elevated right decubitus (eRD), elevated left decubitus (eLD) and left decubitus (LD) positions.

9.2.2 Estimation of Phantom Settling Time

During the brain shift tuning of the phantom it was assumed that the brain would have settled after 10 minutes and so a settling period of 10 minutes was employed before taking the supine and prone scans. Before embarking on a longer set of experiments, however, a better estimation of the settling time was sought.

To achieve this, a phantom was taken for CT scanning and scanned once in the supine position after a 10 minute settling period and then repositioned to prone and scanned at 2.5, 4.5 and 9.5 minutes. The 4.5 and 9.5 minute prone scans were each then rigidly registered to the 2.5 minute prone scan and the displacement of the markers were extracted.

Mean displacement magnitude between the 2.5 and 4.5 minute scans and the 2.5 and 9.5 minute scans were 0.06 ± 0.02 and 0.03 ± 0.01 mm, respectively, indicating that brain shift within the phantom had settled by 2.5 minutes. To account for error in time monitoring, the settling time used going forward was then changed and rounded up to 3 minutes.

9.2.3 Image Acquisition Protocol

To measure PBS upon transition to the eight selected non-supine positions, a fresh phantom made with the SF was CT scanned in six rounds with the Discovery PET/CT 690 VCT system. A settling time of 3 minutes was used prior to scanning in each position. The first three rounds were used to measure PBS upon transition to the elevated supine, upright, elevated prone and prone positions, while the second three rounds measured PBS upon transition to the right decubitus, elevated right decubitus, elevated left decubitus and left decubitus positions. These will be referred to as the sagittal and coronal sessions/positions, respectively, as the phantom is effectively being rotated around the normal axis of these planes.

In each round of the sagittal session, the phantom was placed in the supine position (S) and scanned. Following this, the phantom was rotated progressively to the elevated supine (eS), upright (U), elevated prone (eP) and prone (P) positions and rescanned at each position. The phantom was then rotated back to the supine position for the next round. Three rounds were carried out to achieve an estimation of the repeatability of the PBS measurement. The same process was then performed for the coronal sessions, with the phantom being initially scanned in the supine position for each round, repositioned to the right decubitus (RD) position and then progressively rotated to the elevated right decubitus position (eRD), elevated left decubitus position (eLD) and left decubitus position (LD), rescanning at each position.

Displayed in Figure 9.4 is an illustration of the six imaging rounds and the designation used for each scan. The number after the position indicator indicates the imaging round of which it belongs to.

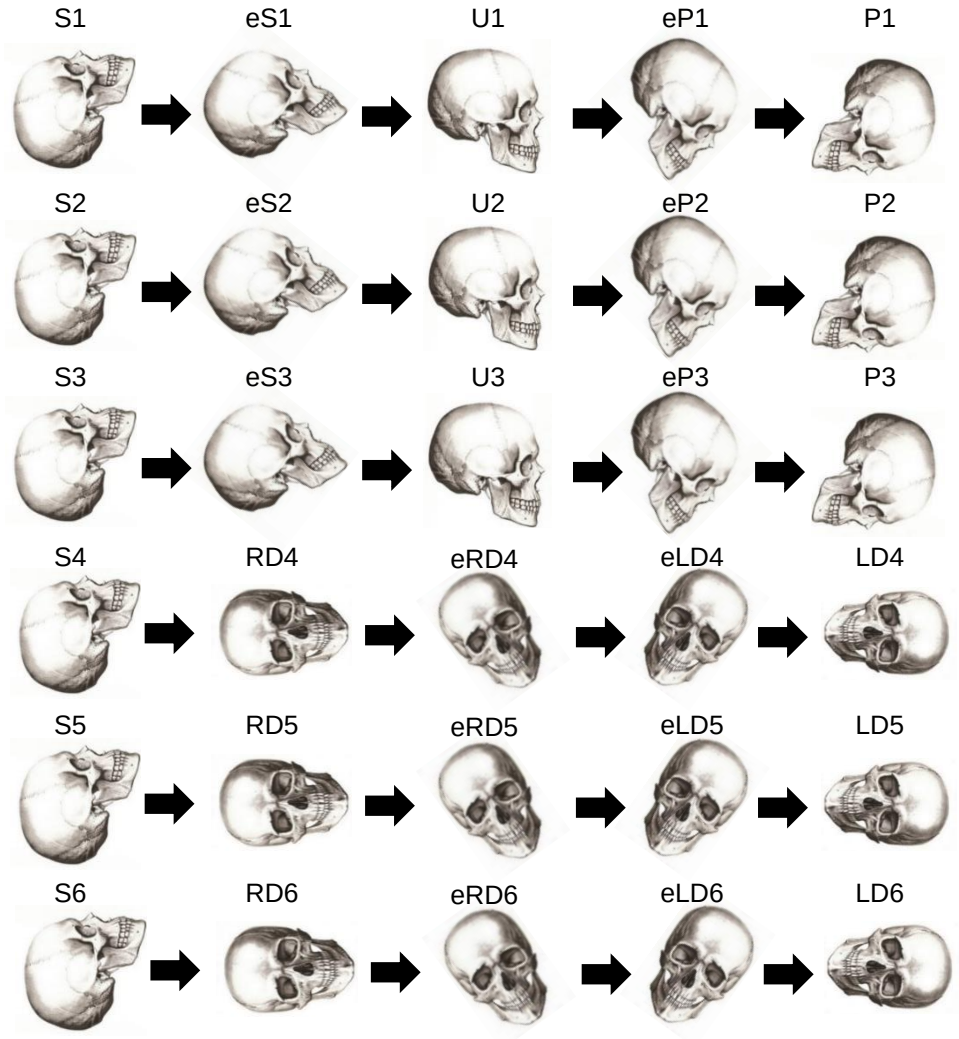

Figure 9.4: The 6 imaging rounds and the 30 imaging positions.

9.2.4 Marker Distribution Measurement

As with the IF and SF phantoms, the distribution of the marker set was analysed. Depth and right-left position discrepancy was quantified within the study phantom's marker set, along with position discrepancy quantification between the study phantom and the co-registered SF phantom.

Depth of the markers were calculated by segmenting out the S1 markers and quantifying the distance between their volume centroids and their closest point on an extracted 3D model of the cranial cavity. Right-left discrepancy was calculated by mirroring the centroid of the markers right hand markers across the central sagittal plane of the cranial cavity model. Inter-phantom marker position discrepancy between the study phantom and SF phantom was calculated by co-registering the supine scan of the SF phantom and the S1 scan of the study phantom and calculating the distance between the markers.

9.2.5 Brain Shift Measurement

Quantification of brain shift was performed by first rigidly registering the scan of each non-supine position to the supine scan of the round in which it was part of. This was performed in 3D Slicer with the BRAINSFit module. Prior to registration, each image was smoothed with the median image filter (2x2x2 pixel search) function. A mask covering the skull, dilated a few mm either side, was also used to focus the registration (Figure 9.5), with all voxels contained within the mask used in the registration.

Although a 6 degree of freedom registration (translation and rotation only) was attempted between all images, it was found that a 10 degree of freedom registration (translation, rotation, scale and skew) was required to properly align the coronal position images to the supine position images. It is unclear why this was necessary for these positions and not the sagittal positions. Aside from the use of mean squared error as the cost metric and changing the minimum step length to 0.00001, all remaining default parameters/modules were used.

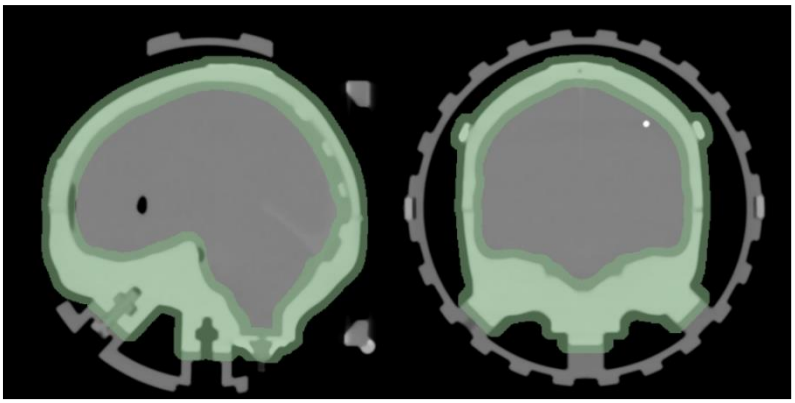

Figure 9.5: Mask (green) used to focus registration.

For each transition, the supine and non-supine images were each thresholded to 300 greyscale pixel value in order to gain a segmentation of the markers. The supine and non-supine marker segmentation label maps were then converted into 3D models with the "export to model" function of 3D Slicer. The two marker sets were then finally exported to Rhino, wherein the volume centroids were determined and the per-marker displacement between the supine and non-supine images was extracted. Displacement of the markers between the different supine scans was also ascertained using the same process.

9.2.6 Intracranial Air Measurement

Unlike the IF and SF phantoms, which contained a negligible quantity (< 2 ml) of intracranial air from assembly, viewing of the study phantom's CT scans revealed a small but clinically relevant volume of intracranial air with varying distribution across the head positions. To quantify the volume of air and to produce qualitative images of its distribution, the air volume was first segmented out of the three sets of co-registered supine, prone, right decubitus and left decubitus images with a threshold function. The segmentations were then converted

into 3D models and imported into Rhino, where the volumes were quantified and images were taken with the air models overlaid over the original MNI ICBM152 segmented brain model, transformed into the phantom's coordinate system using transform data outputted from the registration of the MNI ICBM152 dataset to the S1 supine scan.

9.2.7 Post-Experiment Indentation of the Brain

As for the IF phantom and the SF phantom, the brain of the study phantom was harvested after scanning, chopped into coronal sections and indented at 18 locations. The same methods for specimen harvesting and indentation of the other phantoms were employed with the study phantom and are described in Section 7.2 (p128).

9.2.8 Overview of Methods used in the Presented *In Vivo* Project Work

Part of the emerging work from the *in vivo* project is a study measuring prone to supine PBS in human subjects with MRI. At the time of writing, the results from an initial study of three subjects was available. This data was used in analysis of the measurements obtained with the phantom and so a brief description of the studies methods is given here.

Declaration of appropriate accreditation:

> *The in vivo measurements of prone to supine brain shift presented in this chapter is part of the in vivo project being carried out by Stefano Zappalá and forms part of the work to be submitted for his doctoral thesis. This work should therefore be credited to him only.*

The initial human study, carried out in conjunction with the Cardiff University Brain Imaging Research Centre (CUBRIC), was approved by the Ethical Committee of the Cardiff University School of Psychology and informed consent was obtained from all participants prior to scanning. Three healthy male subjects (aged 20, 30 and 60) were scanned using the Supine Head Inversion methodology. Here, participants were first placed in a prone position outside of the scanner for 30 minutes to ensure the brain had completely settled. Following this, one prone image was taken before repositioning the subject to the supine position. Once in the supine position, three consecutive scans were taken over a period of approximately 30 minutes to assess the time dependency of brain shift. Structural T1 weighted scans of 1 mm^3 voxel size were obtained from the same Siemens 3T Prisma scanner for all subjects in all positions.

This preliminary study was performed to assess the practicality of the methods described above, and as such, only a limited number of subjects were imaged with no rigorous consideration of factors such as age or sex. However, it will be later seen that the measurements exhibit minimal inter-subject variation and were, therefore, considered suitable for the purpose of analysing the general pattern of brain shift in the phantom.

The reason subjects where scanned prone to supine rather than supine to prone was due to comfort issues with the head coils, which are designed for supine scanning. By having the first position as prone, the subject was free to shuffle around during the pre-scanning settling period, only having to remain still for the 5 minute duration of the scan. If the second position was prone, the subject would have had to remain still for 30 minutes in discomfort.

To measure displacement within the brain, affine registration was first used to align the skulls of each patient's prone and supine images. Elastic registration was next carried out between the prone and supine images, generating a vector displacement field over the entire brain volume.

9.2.9 Overview of Methods used in the Presented *In Silico* Project Work

Part of the emerging work from the *in silico* project is a finite element computational model of the brain-skull system. At the time of writing, the results from a number of prone to supine simulations were available. This data was used in analysis of the measurements obtained with the phantom and so a brief description of the studies methods is given here.

Declaration of appropriate accreditation:

> *The in silico measurements of prone to supine brain shift presented in this chapter is part of the in silico project being carried out by Nicholas Bennion and forms part of the work to be submitted for his doctoral thesis. This work should therefore be credited to him only.*

The computer model of the brain-skull system was developed in FEBio, an implicit, non-linear finite element solver. Geometries of the model (Figure 9.6) were the same as those used to develop the phantom, however, the skull was omitted. In place of the skull, the inner boundary of the cranial cavity was connected with the dural septa and thickened outwards into a 1 mm layer. The external boundary of this dura layer was then rigidly constrained mathematically in simulation.

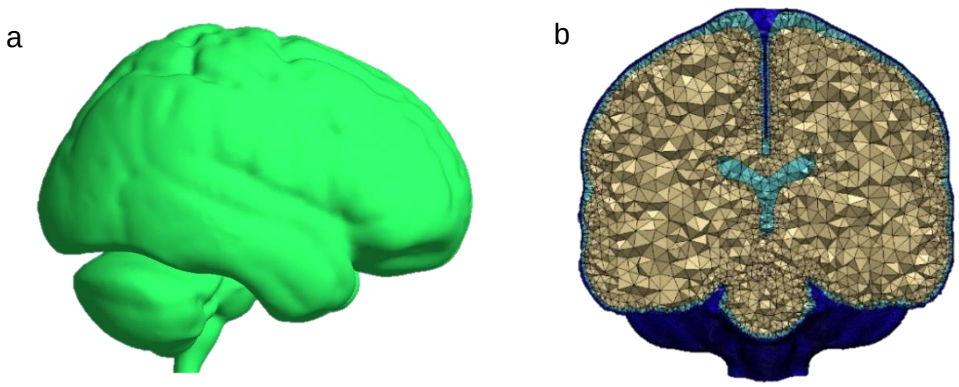

Figure 9.6: Elements of the computational model of the brain-skull system. a) lateral view of the brain/pia mater with arachnoid trabeculae springs removed; b) coronal section of the dura (dark blue), CSF region (light blue) and brain (beige). Springs are not visible.

A fluid structure interaction representation of the subarachnoid space (and ventricles) and discrete spring element representation of the arachnoid trabeculae was developed to best replicate the mechanics of the PAC. This inclusion of brain-skull tethering is a notable difference between the phantom and the *in silico* model.

Material parameter identification and sensitivity analysis were next performed using statistical software, comparing FE results to the initial human *in vivo* measurements from the *in vivo* project.

The model was loaded from the neutral segmentation position with a body force equivalent to gravity to represent the prone and supine positions. Sixty combinations of material parameters were then computed, with values over an initial range estimated from the literature and used in the parameter identification and sensitivity analysis. The parameters gathered from the analysis were then used in the simulation that provided the results in this chapter.

9.2.10 Comparison to *In Vivo* and *In Silico* Displacement Fields

In order to compare the discrete supine to prone brain shift dataset of the phantom to the more continuous displacement fields of the *in vivo* and *in silico* studies, the displacement fields needed to first be transformed into the phantom coordinate system. For both the *in vivo* and *in silico* displacement fields, this was achieved by extracting a mask of the cranial cavity and registering it to a mask of the phantom's cranial cavity in 3D slicer (see Figure 9.7). The transforms outputted by the respective registrations were then applied to the displacement fields to transform them into the phantom's coordinate system.

Following their transformation, the displacement at the marker sites of the phantom needed to be extracted from the displacement fields. To achieve this, the vectors were first decomposed into their start and end coordinates. Then, for each marker, all the vectors with start coordinates within a 5 mm radius of the markers coordinate were averaged to obtain a single comparable vector. Standard deviation measures were also collected in this process. The 5 mm radius was chosen arbitrarily since raising or lowering the radius by a few mm had no significant effect on the averaged vector obtained.

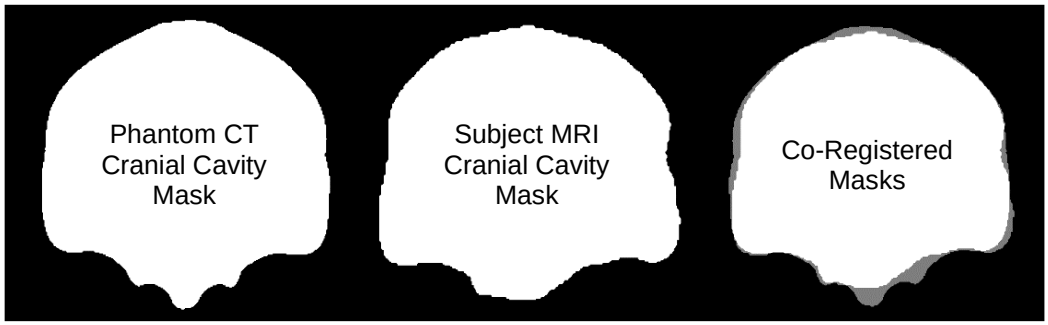

Figure 9.7: Registration of phantom CT cranial cavity mask and subject MRI cranial cavity mask.

9.3 Results

9.3.1 Phantom Structure

MR images of the study phantom (Figure 9.8) showed that, like the previous phantoms built, a reasonable approximation of the biological anatomy had been achieved. Realistic compartmentation of the cranial cavity was achieved by the dural septa and a reasonable recreation of the ventricles and fissures can be seen. Due to the signal drop off towards the periphery and the close association of hydrogel and plastic, and the resulting boundary artifacts which are generated, it was difficult to assess the gap between the brain and the skull, as discovered with previous phantoms (see Section 7.1.1, p119), and so no quantitative measurement was made.

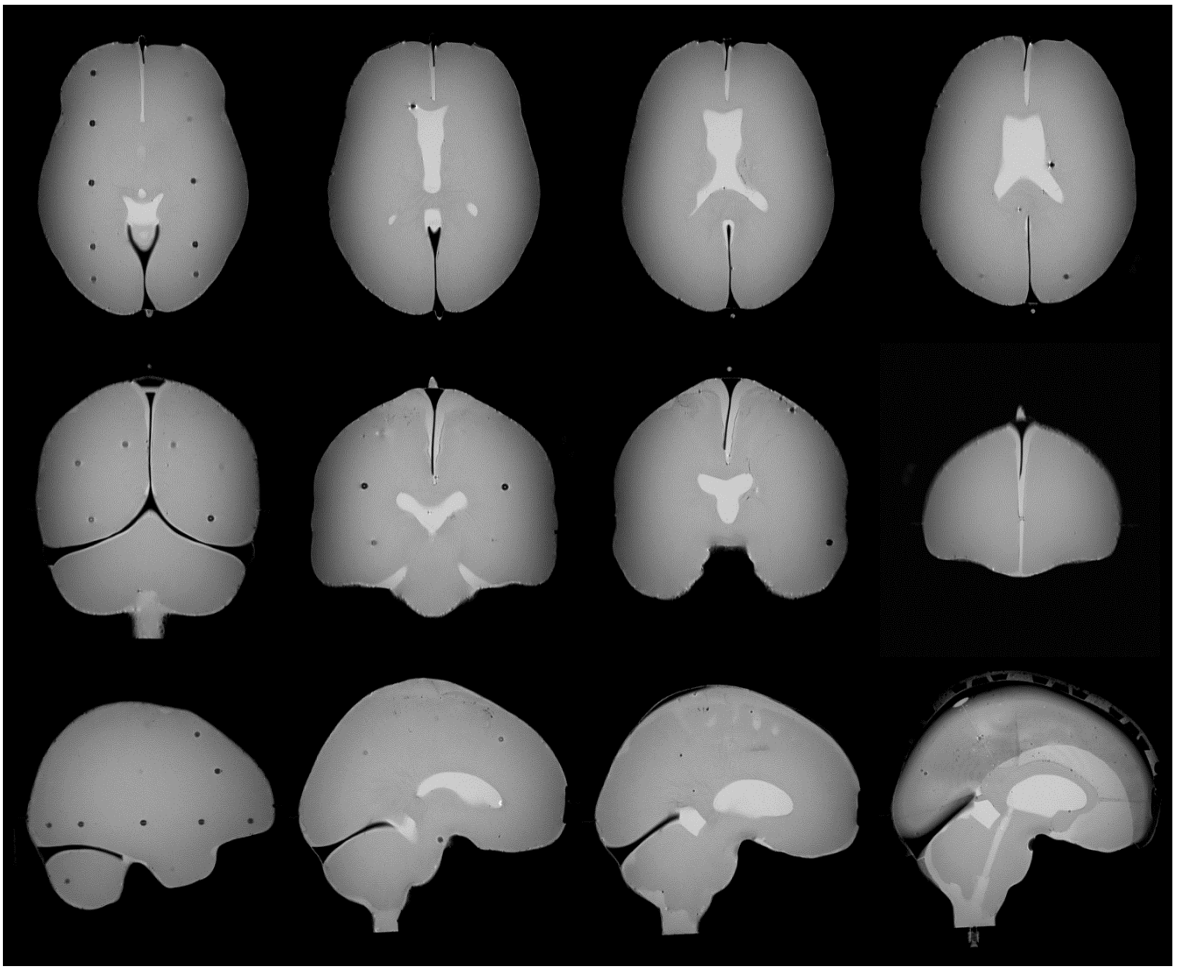

Figure 9.8: MR images of the study phantom. Top row shows a selection of axial images in order of inferior to superior; middle row shows a selection of coronal images in order of posterior to anterior; bottom images show a selection of sagittal images in order of the left to the centre.

9.3.2 Phantom Marker Distribution

As can be seen in Table 9.1, the depth and symmetry markers for the study phantom are largely similar to that of the SF phantom (except again for the left C1 and C2 cerebellar markers) and, as with the comparison between the IF phantom and the SF phantom, it can be seen that between the SF and the study phantom the depth and symmetry profiles were again very similar (see Table 8.2, p159).

Table 9.1: Depth and symmetry metrics of the marker set in the study phantom. Mirrored difference describes the discrepancy in position between the left-hand markers and the right-hand markers after mirroring across the central sagittal plane of the cranial cavity.

Marker Site	Left Depth (mm)	Right Depth (mm)	Mirrored *x* Difference (mm)	Mirrored *y* Difference (mm)	Mirrored *z* Difference (mm)
C1	10.5	8.8	1.0	0.4	-4.2
C2	17.6	17.8	1.1	-0.7	0.4
O1	12.4	11.8	-2.2	2.7	0.4
O2	11.4	11.8	5.8	-0.9	-0.8
P1	17.6	16.2	1.4	-1.9	-1.9
P2	25.6	25.5	1.8	-0.7	-0.3
P3	10.9	8.4	0.1	-2.7	6.3
P4	11.4	10.6	3.0	3.1	3.0
P5	28.3	28.6	0.4	-2.1	0.1
P6	20.0	20.4	1.6	-0.9	-0.1
T1	24.2	22.9	-1.2	1.3	1.1
T2	26.2	28.0	0.8	0.9	2.2
T3	10.2	10.2	0.9	5.1	-2.9
T4	11.6	12.2	0.4	2.3	1.0
SN	4.9	6.1	1.8	-2.4	-0.3
F1	10.6	10.4	-0.4	-3.8	4.0
F2	19.1	21.2	2.3	2.4	3.5
F3	7.8	11.2	2.3	-4.3	0.3
F4	15.7	13.9	-2.0	-1.1	2.5
F5	15.7	16.4	-0.6	-0.1	-0.8
F6	8.5	12.9	3.3	-1.1	4.2
F7	10.8	10.8	-3.6	-1.8	0.3
Mean ± Sd	15.1 ± 6.6	15.5 ± 6.5	0.8 ± 2.1	-0.3 ± 2.4	1.1 ± 2.2
Range	4.9 to 28.3	6.1 to 28.6	-3.6 to 5.8	-4.3 to 5.1	-2.9 to 6.3

The comparative metrics of the marker sets in the SF phantom and study phantom displayed in Table 9.2 show that only small (> 1 cm) differences exist between a majority of the markers of these two phantoms. The mm scale difference in position is likely to make a difference when considering sub-mm scale displacements but, as asserted before, it should not make inter-phantom comparison impossible.

Table 9.2: Difference between marker positions of the SF and study phantoms after co-registration. C1 and C2 markers are not used in calculation of mean, standard deviation or range.

Marker Site	Total Difference (mm)		*x* Difference (mm)		*y* Difference (mm)		*z* Difference (mm)	
	Left	Right	Left	Right	Left	Right	Left	Right
C1	11.0	30.2	4.5	8.2	-28.7	-6.6	-8.3	3.4
C2	9.9	20.3	0.6	4.7	-18.4	-8.1	-8.5	-3.3
O1	1.5	2.7	1.2	-1.0	-0.3	1.1	-2.4	0.2
O2	3.5	1.0	0.8	3.3	0.5	0.8	-0.1	-0.4
P1	2.4	2.6	-0.6	-0.8	-0.7	1.8	-2.5	1.4
P2	0.6	2.6	-2.3	0.5	0.1	0.3	-1.1	0.1
P3	3.9	6.1	-3.5	1.4	-1.6	1.0	-4.7	-3.5
P4	5.4	3.0	0.1	-4.2	2.3	1.0	-1.9	-3.3
P5	1.5	3.2	-0.8	-0.6	-1.0	1.0	-3.0	0.9
P6	1.0	3.6	-3.3	0.4	-1.0	0.9	-1.2	-0.1
T1	1.3	3.7	0.8	-0.8	-2.4	-1.0	-2.7	0.0
T2	1.5	5.0	0.0	-0.5	-3.2	-1.1	-3.8	-0.8
T3	2.4	6.0	-2.5	-0.9	-3.0	-2.0	-4.5	-0.9
T4	3.7	4.6	1.0	0.6	1.9	0.4	-4.0	-3.6
SN	9.1	11.7	-1.7	-0.2	-4.4	-3.1	-10.7	-8.6
F1	2.9	8.5	-0.3	0.9	-3.7	-2.7	-7.6	-0.6
F2	2.8	2.0	0.6	-0.6	-1.7	-2.6	-0.9	-0.6
F3	4.6	6.4	-5.1	2.7	-0.5	-0.2	-3.9	3.7
F4	1.3	3.0	-2.0	-0.5	-1.7	-0.8	-1.4	0.8
F5	0.7	4.0	-3.9	-0.7	-0.8	0.1	-0.1	0.0
F6	0.8	4.8	0.4	-0.1	-4.8	-0.5	0.4	-0.6
F7	2.3	1.9	-1.4	0.8	0.3	2.0	-1.2	-0.7
Mean ± Sd	4.3 ± 2.4	2.6 ± 2.0	-1.1 ± 1.8	0.0 ± 1.5	-1.3 ± 1.9	-0.2 ± 1.5	-2.9 ± 2.6	-0.8 ± 2.4
Range	1.0 to 11.7	0.6 to 9.1	-5.1 to 1.2	-4.2 to 3.3	-4.8 to 2.3	-3.1 to 2.0	-10.7 to 0.4	-8.6 to 3.7

9.3.3 Intracranial Air Assessment

A collection of air measuring approximately 4 ml in total volume was measured consistently across the three sets of supine, prone, right decubitus and left decubitus scans of the phantom. This further evidences the repeatability of the segmentation process with the phantom and CT imaging.

The distribution of air among the supine and prone scans (Figure 9.9) was found to lie primarily towards the top of the scanning orientation, with little intra-position variation. However, some of the air could be seen to be trapped around the brain stem and inside the ventricles (asterix marked volumes). The air distribution manifested itself asymmetrically with the air volume on the left side (gold) of the cranial cavity being approximately twice as large than the right side (blue).

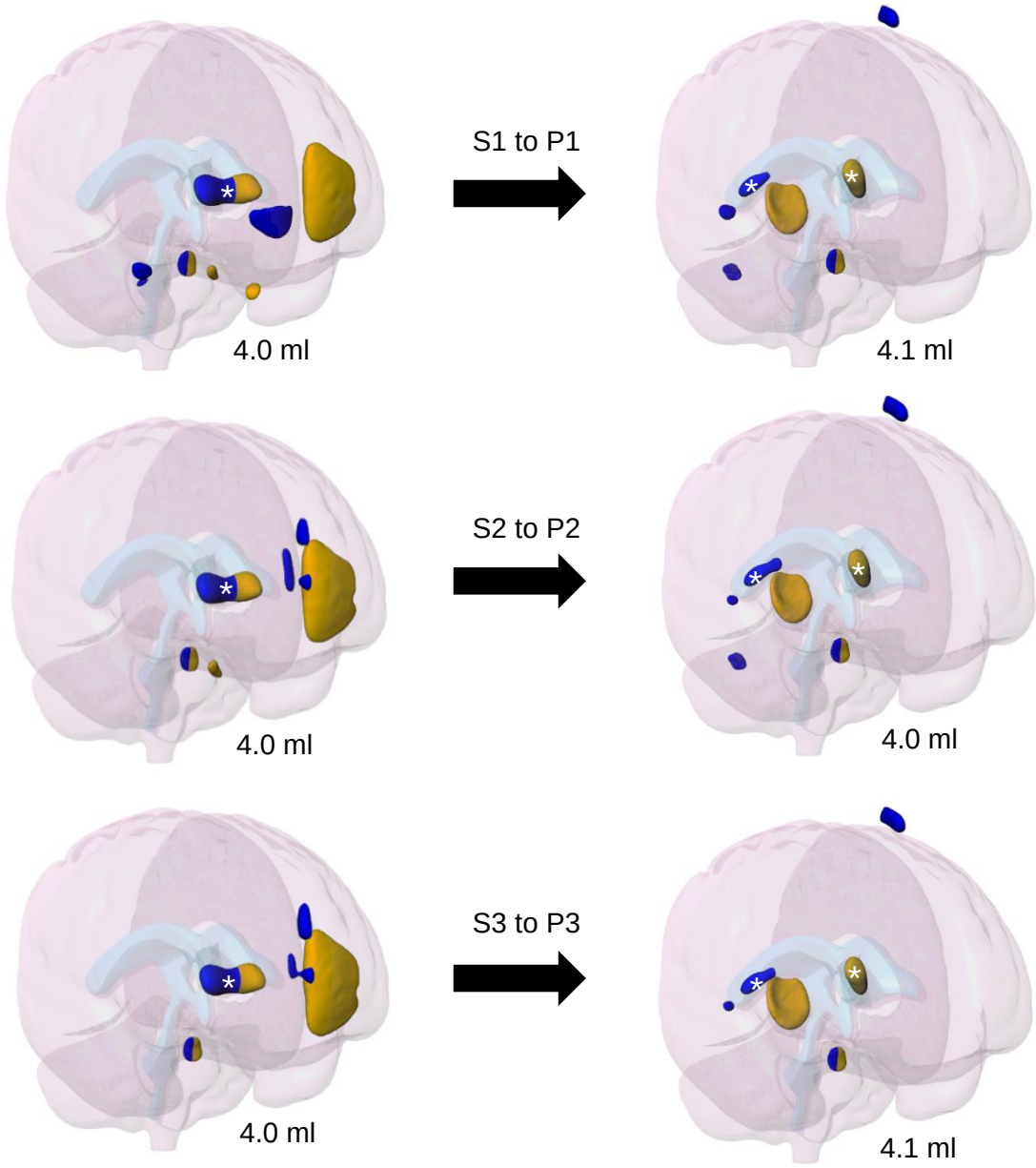

Figure 9.9: Measured intracranial air in the phantom across the three supine images and the three prone images. Ventricular volumes are indicated by asterix; left-side air volumes are gold; right-side volumes are blue. Bottom-right values are the total air volume for each position.

The distribution of air among the right decubitus and left decubitus scans (Figure 9.10) was found to be much more variable across both intra-position and inter-position scans. For the right decubitus scans, the air appeared to lie primarily towards the top of the scanning orientation (with respect to gravity). However, for the left decubitus scans, a large portion of the air appeared to gather near the falx in the medial longitudinal fissure (chevron marked volumes), reducing the amount which could collect towards the top of the orientation.

Ventricular air could be seen in the round 4 decubitus scans but appeared to have escaped into the subarachnoid space during the round 5 imaging sessions.

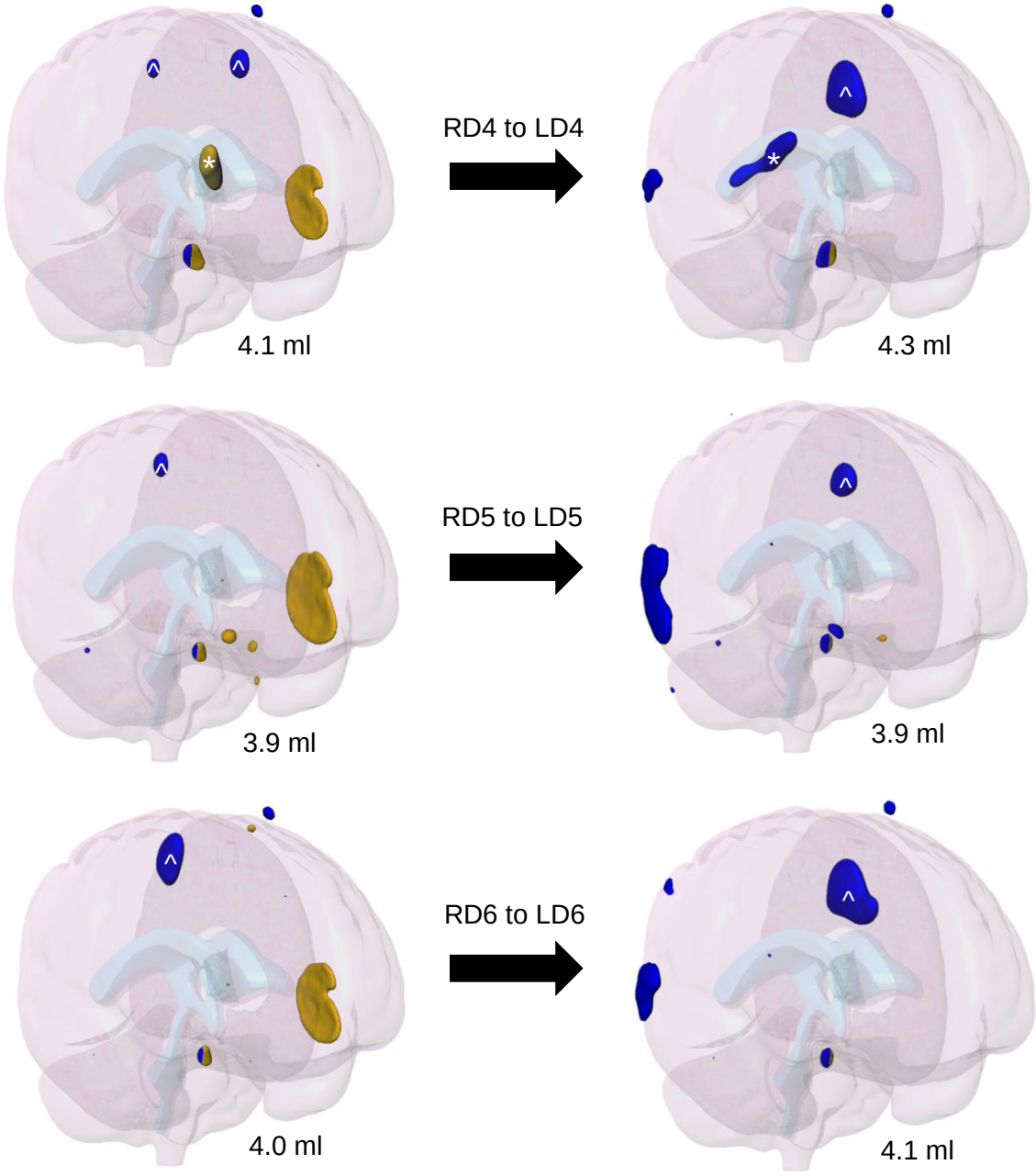

Figure 9.10: Measured intracranial air in the phantom across the three right decubitus images and the three left decubitus images. Ventricular volumes are indicated by asterix; medial longitudinal fissure volumes are indicated by chevron; left-side air volumes are gold; right-side volumes are blue. Bottom-right values are the total air volume for each position.

9.3.4 Indentation Assessment

The indentation response of the coronal sections harvested from the study phantom, shown in Figure 9.11, displays a similar loading response to that of the sections harvested from the SF phantom (see Figure 8.21, p158), with peak force range of 214 to 411 μN being measured at 6 mm depth. No obvious difference in the variance of the two datasets can be seen, but again, no statistical measurements were performed due to sufficient uncertainty in indentation depth.

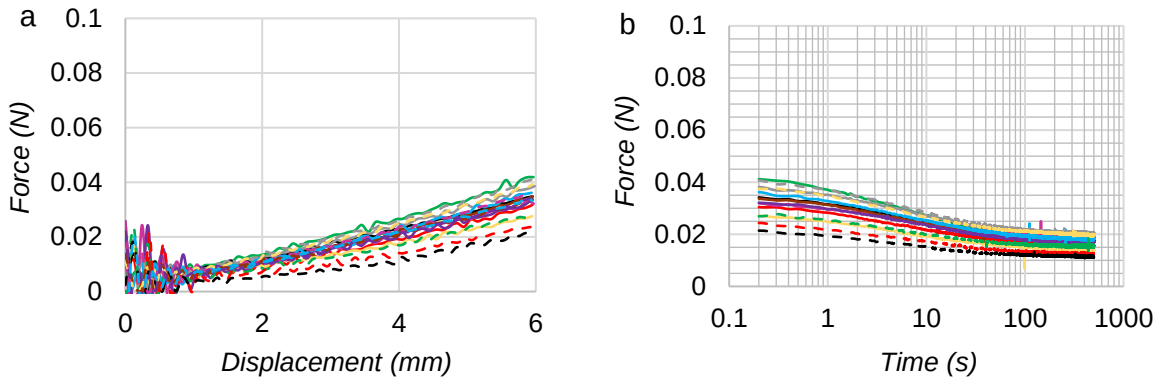

Figure 9.11: Indentation data for the brain used in the study phantom. a) force-displacement data; b) logarithmic time-relaxation data. Solid and dashed curves pertain to tests of the left and right hemispheres, respectively.

9.3.5 Inter-Supine Phantom Brain Shift

Displayed in Figure 9.12 is the total displacement and component displacement of markers measured between the supine position of the first imaging round, designated S1, and the subsequent supine scans of the 5 further imaging rounds, designated S2, S3, S4, S5 and S6, with S1-S3 belonging to the sagittal imaging sessions and S4-S6 belonging to the coronal imaging sessions. Here it can be seen that the markers do not return to rest at exactly the same location within the cranial cavity when placed in the supine position, with inter-supine displacement reaching as high as approximately 0.9 mm for some of the markers. Mean displacement between the S1 and S2, S3, S4, S5 and S6 images was calculated to be 0.30 ± 0.16, 0.17 ± 0.10, 0.38 ± 0.26 and 0.38 ± 0.16 mm, respectively.

The inter-supine brain displacement appears to be rotation dominant with a random pattern that can be explained by a combination of free brain rotation, complex container geometry and weak loading.

The largest displacements can be seen between S1 and S5 and S1 and S6. A possible explanation for this observation is the upturning of the phantom which occurred a number of times between S4 and S6, as necessitated by the design of the cradle in the changing of coronal positions (see Figure 8.4, p140).

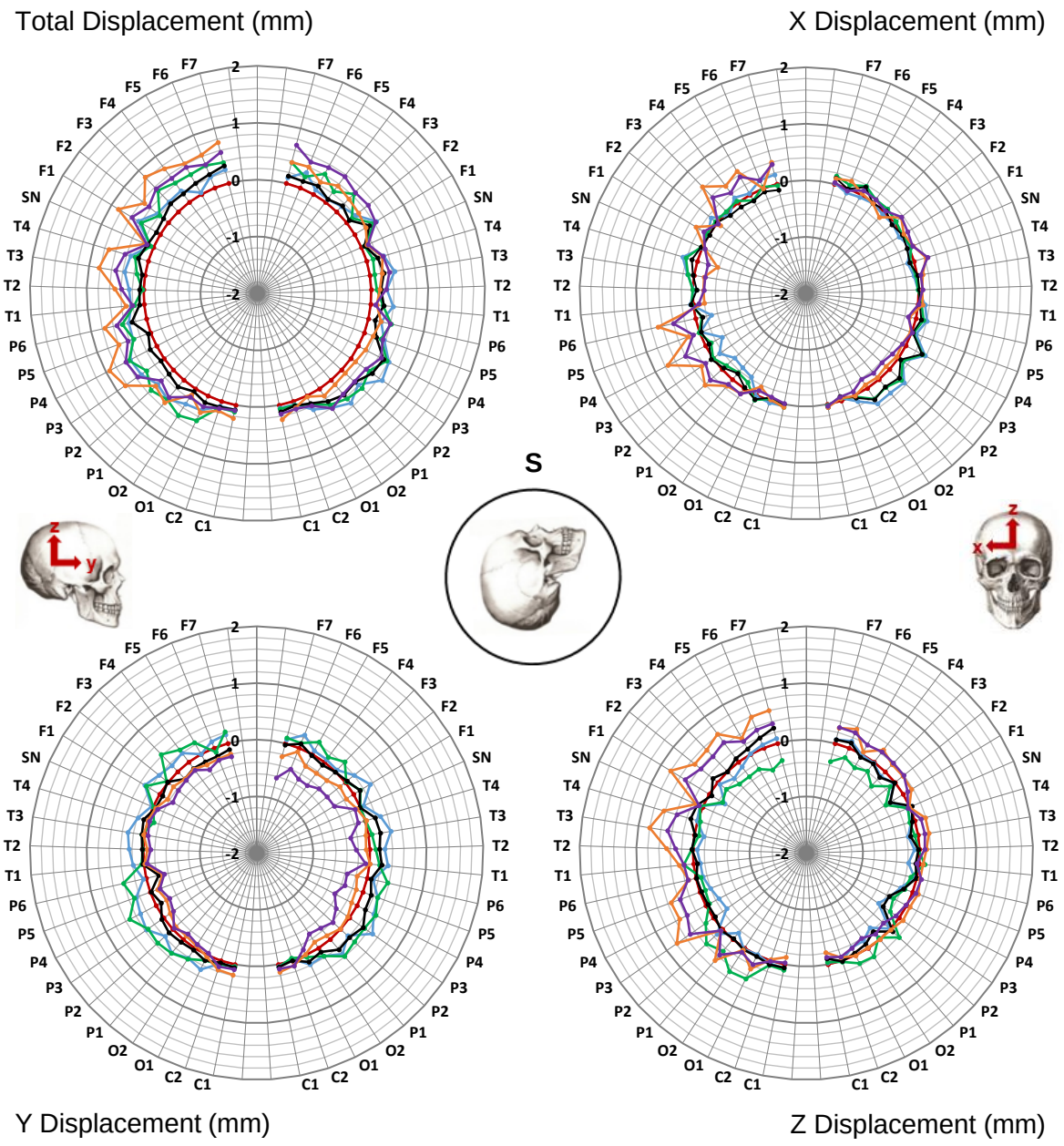

Figure 9.12: Displacement of markers between starting supine position (S1) and subsequent supine repeats: S2, S3, S4, S5, S6. Top-left radar graph shows total displacement, top-right shows displacement along the x axis, bottom-left shows displacement along the y axis and bottom-right shows displacement along the z axis. The x axis points towards the right side of the head, the y axis points anteriorly and the z axis points superiorly.

9.3.6 Inter-Position Phantom Brain Shift

Displayed in Figure 9.13 (p184) and Figure 9.14 (p185) are presentations of the elevated supine, upright, elevated prone and prone shift data in vector format in the sagittal plane and axial plane, respectively. Displayed in Figure 9.15 (p186) and Figure 9.16 (p187) are presentations of the right decubitus, elevated right decubitus, elevated left decubitus and left decubitus shift data in vector format in the sagittal plane and axial plane, respectively. These presentations are used to show the general brain shift and, therefore, only the average across the three repeats for each position is shown (variability is shown in later images).

Collectively, these presentations show that the phantom's brain undergoes a non-rigid, position-dependent shift which varies in both magnitude and direction. Marker displacement in the elevated supine position, for example, appears to point predominantly inferiorly with relatively small magnitude, whereas marker displacement in the prone position appears to point predominantly anteriorly with relatively large magnitude.

Generally, an evolution of direction and magnitude can be seen in the sagittal plane upon progressive rotation from the elevated supine position to the prone position. It is interesting to note, however, that not all markers moved in the gravitational direction for any given position. The left parietal markers of the prone position, for example, appear to move predominantly anteriorly in the direction of gravity, while the right frontal markers appear to move in the direction of gravity for the elevated prone position. This displacement of markers in the gravitational directions of other positions appears to take place across all the positions.

The displacement across the right decubitus, elevated right decubitus, elevated left decubitus and left decubitus positions all contained an unexpectedly large anterior component which offsets the direction of displacement away from the gravitational direction. The displacement magnitude for all these positions was also relatively large with the elevated right decubitus position containing the greatest displacements across the eight non-supine positions. The displacement pattern in the left decubitus and elevated left decubitus positions, however, does not appear to be strictly symmetrical with respect to the right decubitus and elevated right decubitus positions, as one might expect.

The absence of symmetry among the right and left decubitus positions may be a result of the generally asymmetric displacement that can be seen in the data. Across all the positions, the displacement can be seen to be larger on the left side of the brain. This is particularly evident when comparing the displacement of the right and left parietal markers and the right and left frontal markers.

[Study Phantom]

Average Sagittal Plane Displacement upon Transition from the Supine Position to:

Elevated Supine (eS)

Upright (U)

Elevated Prone (eP)

Prone (P)

Exaggerated Anatomical Displacement Map

x8 Vector Magnitude

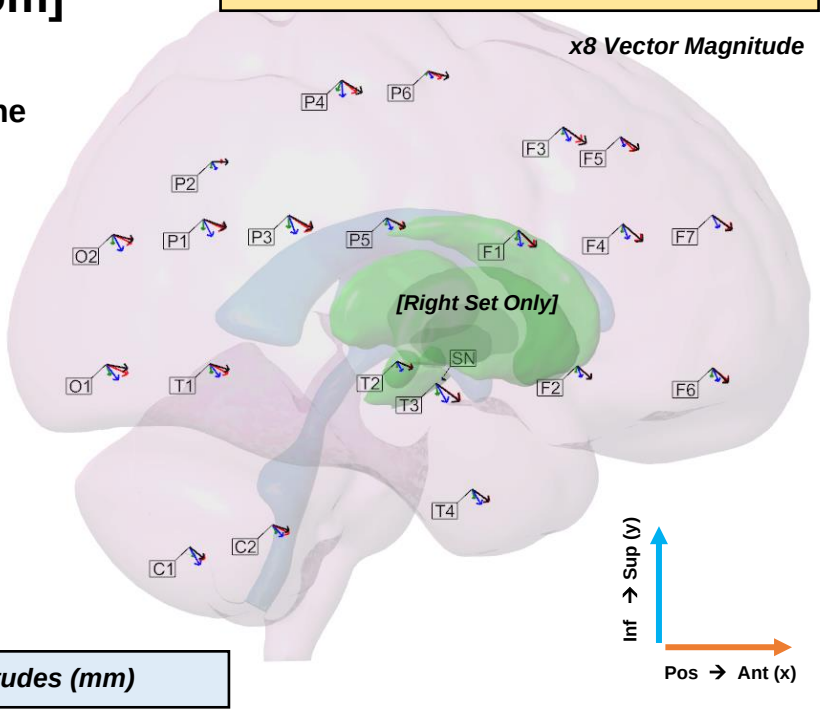

True Component Magnitudes (mm)

L-C1	L-C2	L-O1	L-O2	L-P1	L-P2
+0.11 +0.30 +0.46 +0.44 -0.23 -0.38 -0.23 -0.07	+0.09 +0.26 +0.45 +0.45 -0.19 -0.33 -0.17 -0.06	+0.07 +0.29 +0.72 +0.76 -0.47 -0.54 -0.33 +0.17	+0.02 +0.20 +0.60 +0.74 -0.34 -0.34 -0.08 +0.38	+0.01 +0.25 +0.82 +0.88 -0.48 -0.55 -0.42 +0.09	+0.02 +0.19 +0.52 +0.72 -0.25 -0.23 -0.02 +0.28
R-C1	R-C2	R-O1	R-O2	R-P1	R-P2
+0.12 +0.28 +0.42 +0.39 -0.27 -0.50 -0.34 -0.31	+0.12 +0.29 +0.46 +0.46 -0.24 -0.32 -0.24 -0.15	+0.11 +0.33 +0.60 +0.59 -0.30 -0.43 -0.26 -0.11	-0.01 +0.25 +0.52 +0.56 -0.27 -0.46 -0.24 -0.15	-0.01 +0.23 +0.58 +0.63 -0.30 -0.47 -0.28 -0.23	-0.03 +0.13 +0.30 +0.45 -0.17 -0.21 +0.01 -0.00
L-P3	L-P4	L-P5	L-P6	L-T1	L-T2
-0.04 +0.21 +0.90 +0.93 -0.57 -0.71 -0.66 -0.17	-0.10 +0.17 +0.92 +1.02 -0.43 -0.56 -0.52 -0.24	-0.03 +0.19 +0.74 +0.84 -0.35 -0.42 -0.43 -0.15	+0.06 +0.27 +0.72 +0.99 -0.25 -0.24 -0.34 -0.12	+0.05 +0.26 +0.64 +0.65 -0.44 -0.53 -0.34 +0.05	+0.07 +0.30 +0.60 +0.71 -0.33 -0.37 -0.31 -0.11
R-P3	R-P4	R-P5	R-P6	R-T1	R-T2
+0.01 +0.19 +0.62 +0.66 -0.36 -0.52 -0.42 -0.36	-0.12 +0.04 +0.42 +0.56 -0.29 -0.47 -0.34 -0.34	-0.01 +0.14 +0.48 +0.52 -0.20 -0.32 -0.23 -0.27	-0.05 +0.13 +0.38 +0.58 -0.10 -0.19 -0.18 -0.16	+0.05 +0.27 +0.50 +0.53 -0.27 -0.36 -0.27 -0.17	+0.01 +0.15 +0.42 +0.44 -0.17 -0.27 -0.17 -0.19
L-T3	L-T4	L-SN	L-F1	L-F2	L-F3
+0.07 +0.32 +0.79 +0.84 -0.66 -0.75 -0.74 -0.31	+0.05 +0.31 +0.58 +0.57 -0.50 -0.57 -0.55 -0.28	-0.01 +0.00 +0.10 +0.13 -0.05 -0.05 -0.03 +0.01	-0.12 +0.18 +0.88 +0.89 -0.46 -0.60 -0.64 -0.35	+0.11 +0.36 +0.73 +0.77 -0.37 -0.50 -0.53 -0.40	-0.01 +0.32 +0.95 +1.07 -0.47 -0.58 -0.65 -0.48
R-T3	R-T4	R-SN	R-F1	R-F2	R-F3
+0.05 +0.30 +0.66 +0.64 -0.33 -0.52 -0.48 -0.49	+0.07 +0.25 +0.48 +0.47 -0.27 -0.42 -0.34 -0.33	+0.01 +0.02 +0.07 +0.09 +0.03 -0.06 -0.02 -0.04	-0.06 +0.07 +0.43 +0.49 -0.28 -0.45 -0.43 -0.46	-0.04 +0.12 +0.39 +0.39 -0.18 -0.31 -0.34 -0.36	+0.00 +0.19 +0.52 +0.64 -0.21 -0.39 -0.39 -0.46
L-F4	L-F5	L-F6	L-F7		
+0.00 +0.30 +0.85 +0.94 -0.49 -0.63 -0.72 -0.58	+0.22 +0.39 +0.85 +1.01 -0.32 -0.40 -0.56 -0.45	+0.30 +0.58 +1.01 +0.99 -0.46 -0.58 -0.64 -0.57	+0.11 +0.39 +0.97 +1.00 -0.49 -0.57 -0.66 -0.62		
R-F4	R-F5	R-F6	R-F7		
-0.02 +0.15 +0.51 +0.55 -0.24 -0.41 -0.44 -0.47	+0.03 +0.12 +0.40 +0.52 -0.07 -0.27 -0.39 -0.35	-0.03 +0.17 +0.44 +0.43 -0.26 -0.37 -0.36 -0.41	+0.06 +0.18 +0.53 +0.55 -0.11 -0.36 -0.37 -0.41		

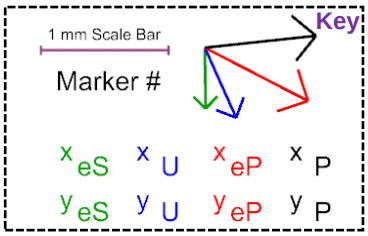

Figure 9.13: Average (n=3) sagittal plane marker displacement in the study phantom upon transition from the supine position to elevated supine (green), upright (blue), elevated prone (red) and prone (black). Please refer back to Figure 8.19 (p156) for a greater description of the figure's general format and its key. [x_{eS} x_U x_{eP} x_P] and [y_{eS} y_U y_{eP} y_P] represent the x and y displacement, respectively, in the elevated supine (eS), upright (U), elevated prone (eP) and prone (P) positions.

[Study Phantom]

Average Axial Plane Displacement upon Transition from the Supine Position to:

Elevated Supine (eS)

Upright (U)

Elevated Prone (eP)

Prone (P)

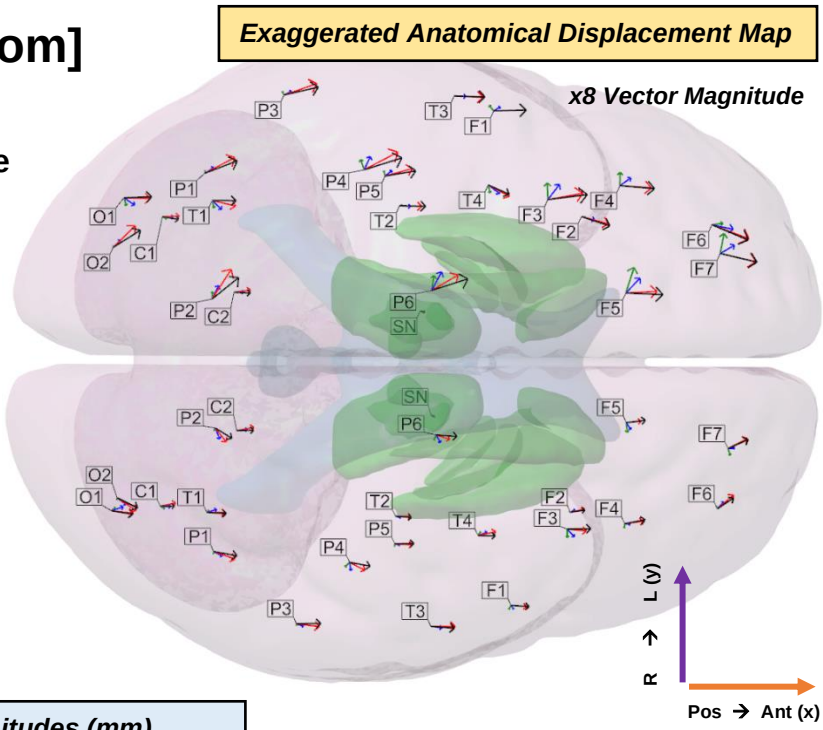

True Component Magnitudes (mm)

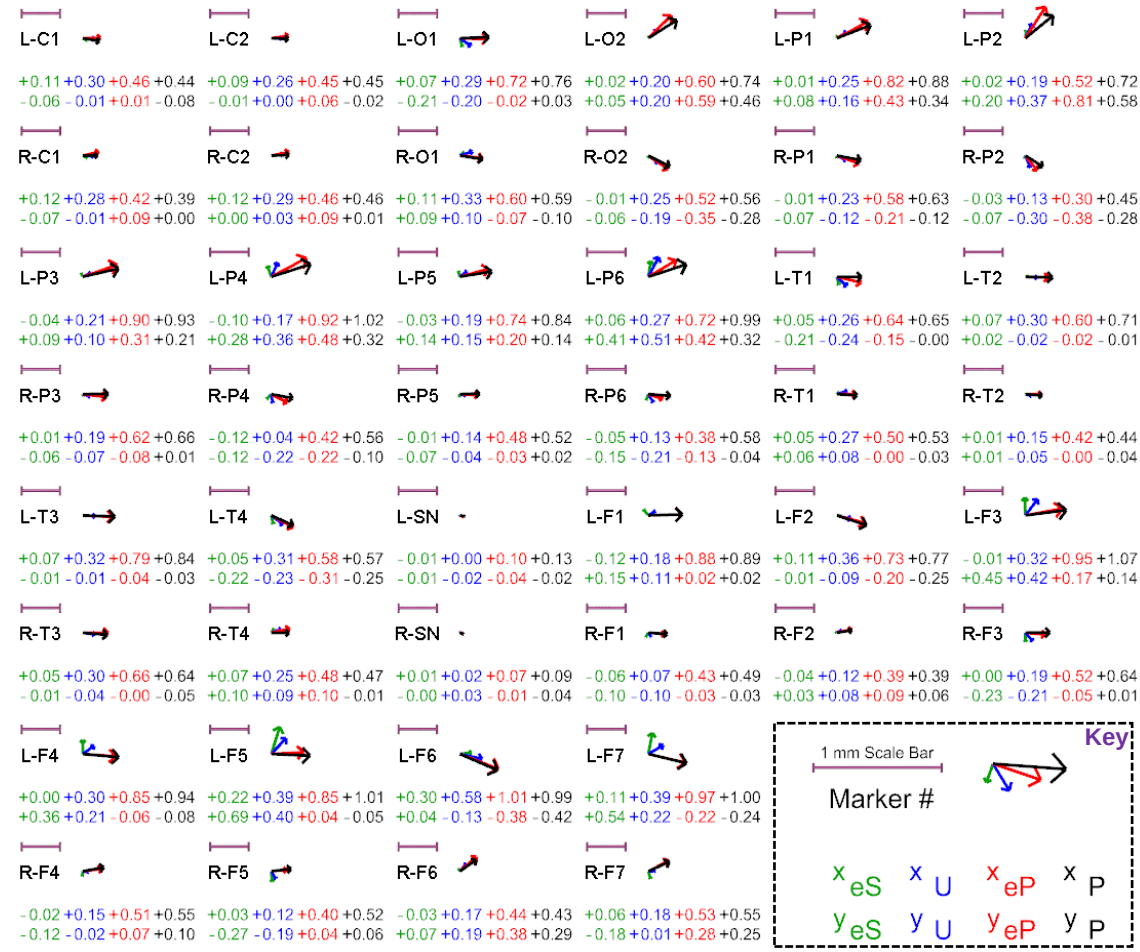

Figure 9.14: Average (n=3) axial plane marker displacement in the study phantom upon transition from the supine position to elevated supine (green), upright (blue), elevated prone (red) and prone (black). Please refer back to Figure 8.19 (p156) for a greater description of the figure's general format and its key. [x_{eS} x_U x_{eP} x_P] and [y_{eS} y_U y_{eP} y_P] represent the x and y displacement, respectively, in the elevated supine (eS), upright (U), elevated prone (eP) and prone (P) positions.

[Study Phantom]

Average Sagittal Plane Displacement upon Transition from the Supine Position to:

Right Decubitus (RD)

Elevated Right Decubitus (eRD)

Elevated Left Decubitus (eLD)

Left Decubitus (LD)

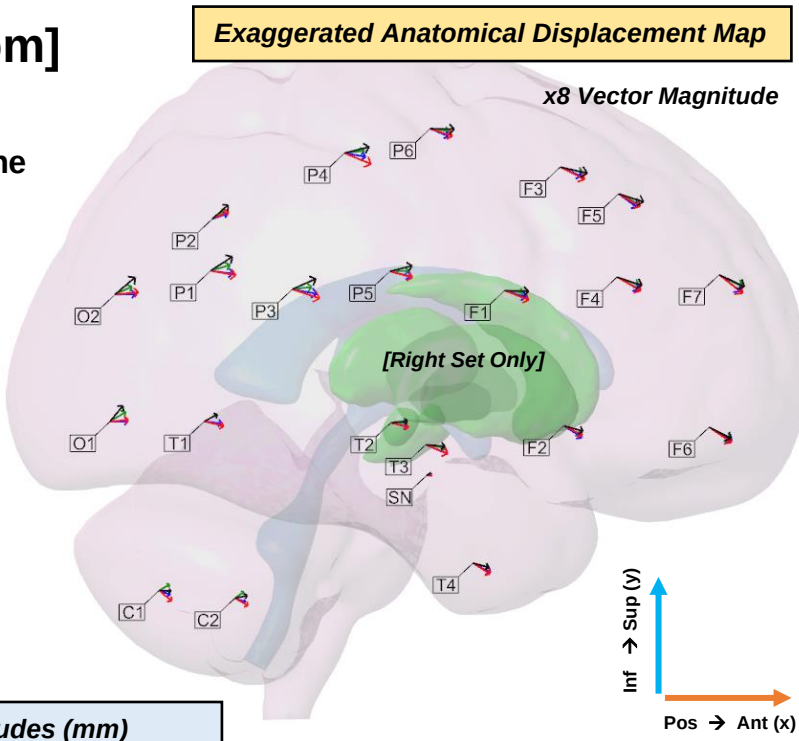

True Component Magnitudes (mm)

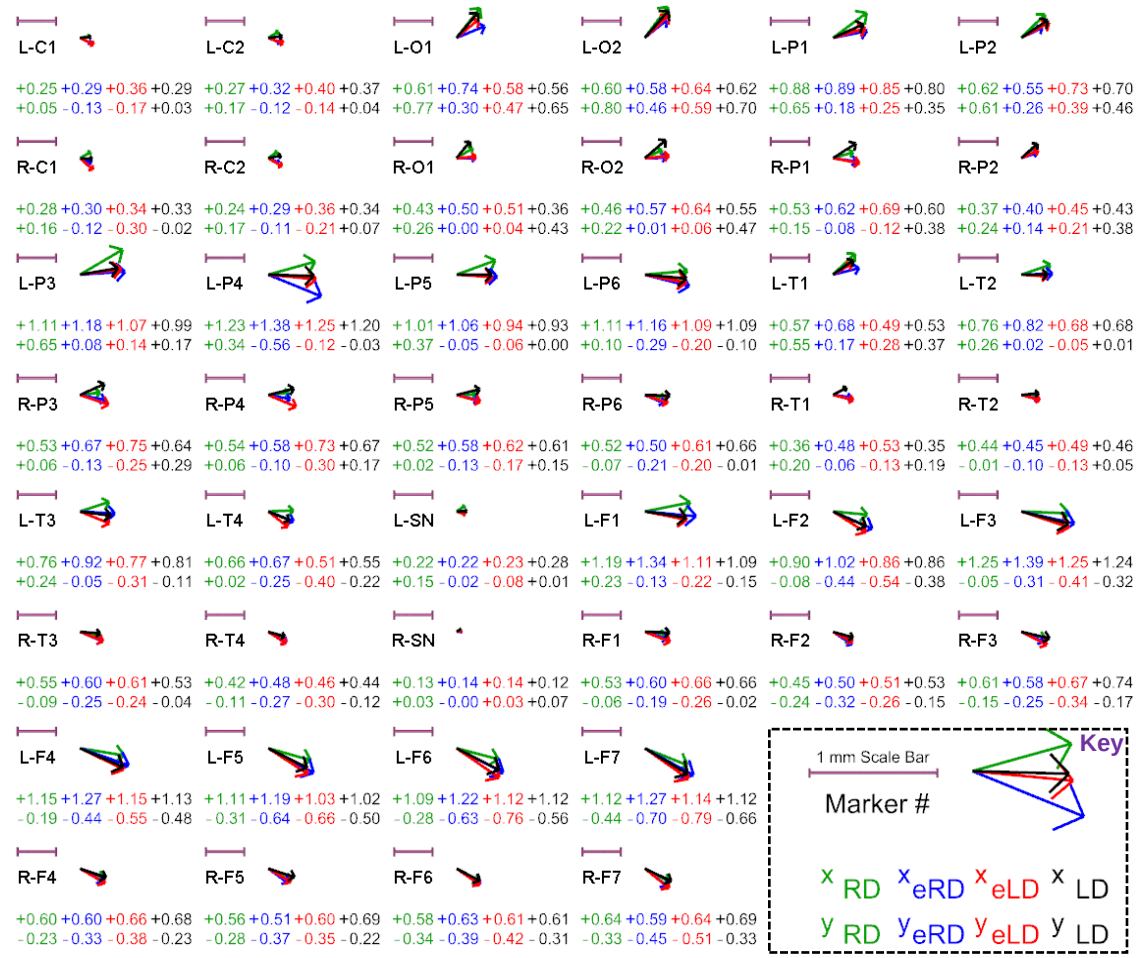

Figure 9.15: Average (n=3) sagittal plane marker displacement in the study phantom upon transition from the supine position to right decubitus (green), elevated right decubitus (blue), elevated left decubitus (red) and left decubitus (black). Please refer back to Figure 8.19 (p156) for a greater description of the figure's general format and its key. [x_{RD} x_{eRD} x_{eLD} x_{LD}] and [y_{RD} y_{eRD} y_{eLD} y_{LD}] represent the x and y displacement, respectively, in the right decubitus (RD), elevated right decubitus (eRD), elevated left decubitus (eLD) and left decubitus (LD) positions.

[Study Phantom]

Exaggerated Anatomical Displacement Map

Average Axial Plane Displacement upon Transition from the Supine Position to:

Right Decubitus (RD)

Elevated Right Decubitus (eRD)

Elevated Left Decubitus (eLD)

Left Decubitus (LD)

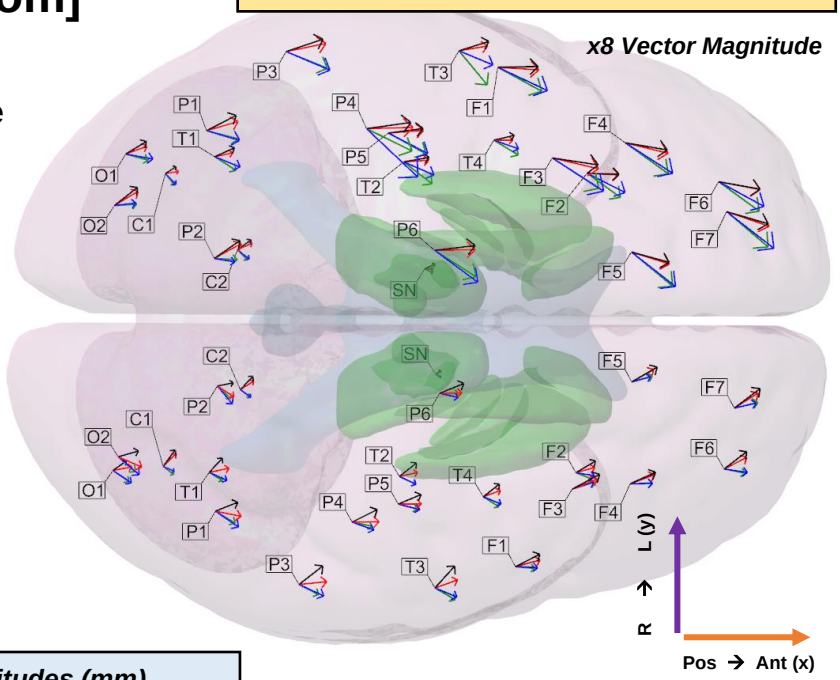

True Component Magnitudes (mm)

L-C1	L-C2	L-O1	L-O2	L-P1	L-P2
+0.25 +0.29 +0.36 +0.29 -0.31 -0.29 +0.06 +0.19	+0.27 +0.32 +0.40 +0.37 -0.27 -0.25 +0.18 +0.27	+0.61 +0.74 +0.58 +0.56 -0.17 -0.13 +0.21 +0.34	+0.60 +0.58 +0.64 +0.62 +0.03 +0.07 +0.39 +0.49	+0.88 +0.89 +0.85 +0.80 -0.22 -0.26 +0.25 +0.41	+0.62 +0.55 +0.73 +0.70 -0.03 -0.09 +0.40 +0.48
R-C1	**R-C2**	**R-O1**	**R-O2**	**R-P1**	**R-P2**
+0.28 +0.30 +0.34 +0.33 -0.22 -0.14 +0.34 +0.44	+0.24 +0.29 +0.36 +0.34 -0.18 -0.20 +0.23 +0.36	+0.43 +0.50 +0.51 +0.36 -0.30 -0.33 +0.10 +0.26	+0.46 +0.57 +0.64 +0.55 -0.40 -0.48 -0.28 +0.16	+0.53 +0.62 +0.69 +0.60 -0.32 -0.43 -0.14 +0.24	+0.37 +0.40 +0.45 +0.43 -0.34 -0.48 -0.29 +0.09
L-P3	**L-P4**	**L-P5**	**L-P6**	**L-T1**	**L-T2**
+1.11 +1.18 +1.07 +0.99 -0.45 -0.50 +0.22 +0.33	+1.23 +1.38 +1.25 +1.20 -0.60 -1.30 +0.03 +0.17	+1.01 +1.06 +0.94 +0.93 -0.56 -0.55 +0.07 +0.12	+1.11 +1.16 +1.09 +1.09 -0.71 -0.86 +0.02 +0.13	+0.57 +0.68 +0.49 +0.53 -0.37 -0.28 +0.11 +0.24	+0.76 +0.82 +0.68 +0.68 -0.59 -0.35 +0.05 +0.12
R-P3	**R-P4**	**R-P5**	**R-P6**	**R-T1**	**R-T2**
+0.53 +0.67 +0.75 +0.64 -0.27 -0.31 +0.08 +0.50	+0.54 +0.58 +0.73 +0.67 -0.11 -0.21 +0.01 +0.34	+0.52 +0.58 +0.62 +0.61 -0.13 -0.15 +0.01 +0.26	+0.52 +0.50 +0.61 +0.66 -0.02 -0.11 +0.01 +0.27	+0.36 +0.48 +0.53 +0.35 -0.22 -0.21 +0.11 +0.38	+0.44 +0.45 +0.49 +0.46 -0.21 -0.21 +0.11 +0.36
L-T3	**L-T4**	**L-SN**	**L-F1**	**L-F2**	**L-F3**
+0.76 +0.92 +0.77 +0.81 -0.92 -0.38 +0.13 +0.25	+0.66 +0.67 +0.51 +0.55 -0.40 -0.23 -0.00 +0.13	+0.22 +0.22 +0.23 +0.28 -0.11 -0.01 +0.02 +0.13	+1.19 +1.34 +1.11 +1.09 -0.65 -0.62 -0.07 +0.02	+0.90 +1.02 +0.86 +0.86 -0.65 -0.52 -0.05 -0.03	+1.25 +1.39 +1.25 +1.24 -0.82 -0.89 -0.29 -0.19
R-T3	**R-T4**	**R-SN**	**R-F1**	**R-F2**	**R-F3**
+0.55 +0.60 +0.61 +0.53 -0.32 -0.24 +0.22 +0.59	+0.42 +0.48 +0.46 +0.44 -0.27 -0.20 +0.17 +0.34	+0.13 +0.14 +0.14 +0.12 -0.08 -0.06 +0.09 +0.12	+0.53 +0.60 +0.66 +0.66 -0.04 -0.02 +0.18 +0.34	+0.45 +0.50 +0.51 +0.53 -0.17 -0.08 +0.14 +0.32	+0.61 +0.58 +0.67 +0.74 +0.19 +0.19 +0.27 +0.40
L-F4	**L-F5**	**L-F6**	**L-F7**		
+1.15 +1.27 +1.15 +1.13 -0.83 -0.82 -0.28 -0.19	+1.11 +1.19 +1.03 +1.02 -0.92 -0.93 -0.32 -0.28	+1.09 +1.22 +1.12 +1.12 -0.79 -0.66 -0.21 -0.20	+1.12 +1.27 +1.14 +1.12 -0.95 -0.99 -0.39 -0.33		
R-F4	**R-F5**	**R-F6**	**R-F7**		
+0.60 +0.60 +0.66 +0.68 +0.01 +0.02 +0.24 +0.31	+0.56 +0.51 +0.60 +0.69 +0.16 +0.14 +0.34 +0.40	+0.58 +0.63 +0.61 +0.61 -0.11 -0.09 +0.31 +0.47	+0.64 +0.59 +0.64 +0.69 +0.15 +0.13 +0.40 +0.52		

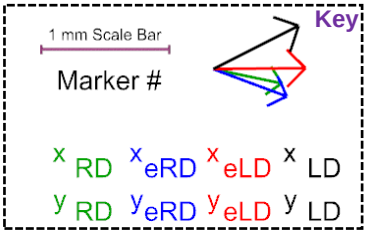

Figure 9.16: Average (n=3) axial plane marker displacement in the study phantom upon transition from the supine position to right decubitus (green), elevated right decubitus (blue), elevated left decubitus (red) and left decubitus (black). Please refer back to Figure 8.19 (p156) for a greater description of the figure's general format and its key. [x_{RD} x_{eRD} x_{eLD} x_{LD}] and [y_{RD} y_{eRD} y_{eLD} y_{LD}] represent the x and y displacement, respectively, in the right decubitus (RD), elevated right decubitus (eRD), elevated left decubitus (eLD) and left decubitus (LD) positions.

Displayed in Figure 9.17 (p189) is the sagittal plane displacement for the three repeat measurements of the elevated supine, upright, elevated prone and prone positions. Here it can be seen that there was a large intra-position variation in the magnitude and direction of the phantom's brain shift. The variability also appears to be comparatively larger on the left side of the brain.

This variability is further demonstrated in the total displacement graphs and the component displacement graphs for the elevated supine (Figure 9.18, p190), upright (Figure 9.19, p191), elevated prone (Figure 9.20, p192), prone (Figure 9.21, p193), right decubitus (Figure 9.22, p194), elevated right decubitus (Figure 9.23, p195), elevated left decubitus (Figure 9.24, p196) and left decubitus (Figure 9.25, p197) positions. Notably, these graphs show that the pattern of brain shift can change quite dramatically between repeat measurements. In some repeats, the shift can appear to be taking place almost rigidly (indicated by a circular interconnection of data points), while for others, the shift can appear to be taking place more non-rigidly (indicated by a jagged interconnection of data points). Furthermore, some repeats can be seen to have large differences in magnitude of displacement. The right-hand markers of the decubitus positions, for example, all exhibit large intra-position variability in shift magnitude.

Displayed in Figure 9.26 (p198) are average shift graphs for the eight non-supine positions. Within each graph there is an average for the individual measurements and an average across the measurements. An average is provided for the shift across all the markers, across the right-hand markers and across the left-hand markers. Here, the aforementioned evolution of brain shift upon progressive rotation in the sagittal plane can be best seen, with mean displacements of 0.39 ± 0.14, 0.53 ± 0.12, 0.75 ± 0.21 and 0.94 ± 0.31 mm measured for the elevated supine, upright, elevated prone and prone positions, respectively. Conversely, the average brain shift across the coronal positions remained reasonably static, with mean displacements of 0.84 ± 0.38, 0.87 ± 0.44, 0.81 ± 0.29 and 0.83 ± 0.26 mm measured for the right decubitus, elevated right decubitus, elevated left decubitus and left decubitus positions, respectively.

The aforementioned right-left asymmetry in shift magnitude is also quite evident in the average shift graphs. Asymmetry among the decubitus positions is not surprising, as the gravitational direction in these positions runs with the left-right axis, however, one might expect the asymmetry to be mirrored to some degree when changing from the right the left decubitus positions. Yet, this was not observed in the phantom.

Asymmetry was absent in the SF phantom, however, only one measurement was performed. Nonetheless, in Figure 9.21 (p193) and Figure 9.26 (p198) it can be seen that the supine to prone brain shift was similar between the SF phantom and the study phantom, in both magnitude, direction and non-rigid pattern of shift.

[Study Phantom]

Sagittal Plane Displacements upon Transition from the Supine Position to:

Elevated Supine (eS) x3

Upright (U) x3

Elevated Prone (eP) x3

Prone (P) x3

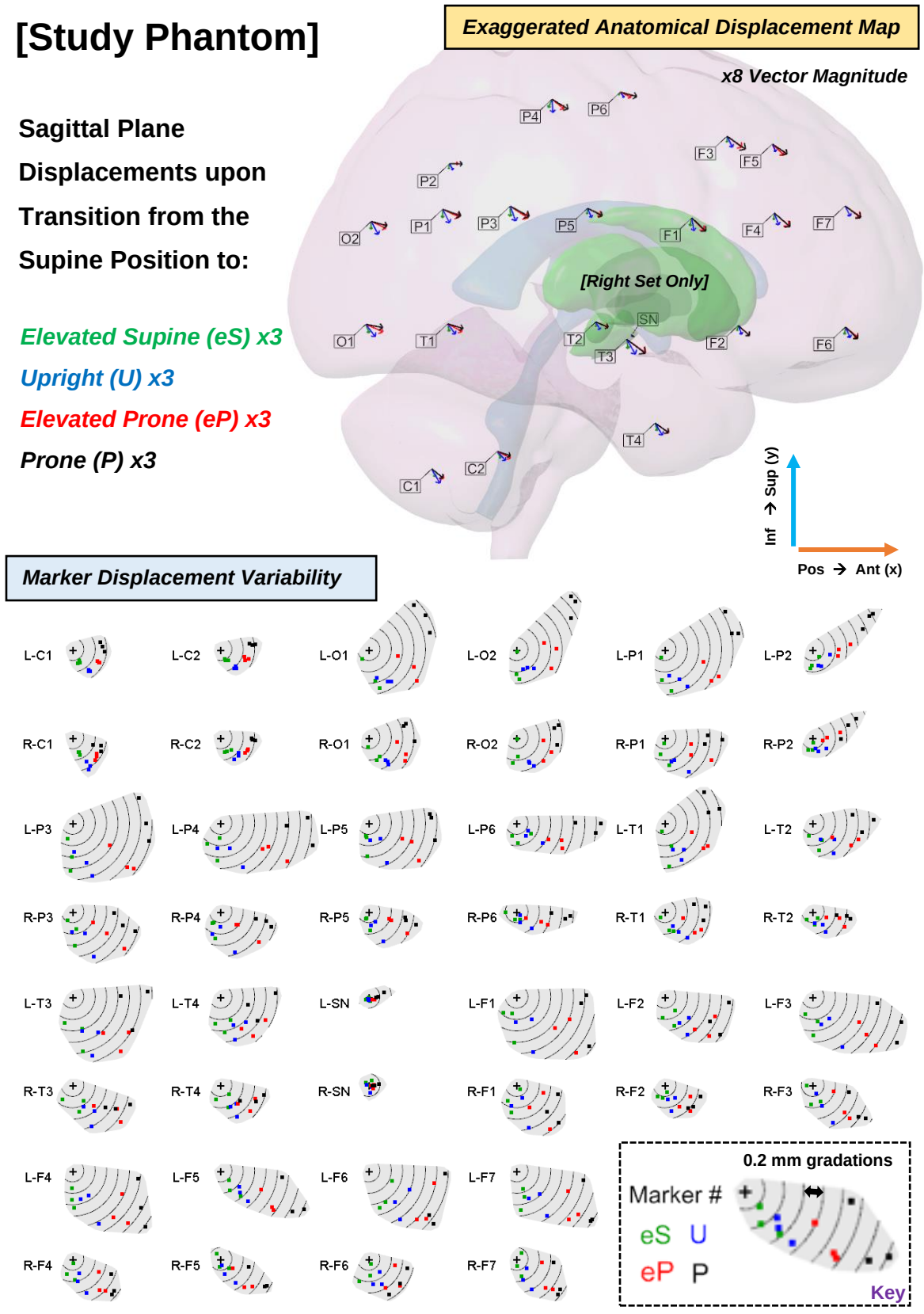

Figure 9.17: Sagittal plane marker displacement in the study phantom upon transition from the supine position to elevated supine (green), upright (blue), elevated prone (red) and prone (black), showing displacement for each repeat. Shown in the Exaggerated Anatomical Displacement Map graphic are the averaged displacement vectors with length exaggerated by a factor of eight but with real anatomical start position. Shown in the Marker Displacement Variability graphic are the displacements for each individual repositioning (marked by the coloured squares) from the supine position (represented by the central cross). The concentric rings are spaced 0.2 mm apart.

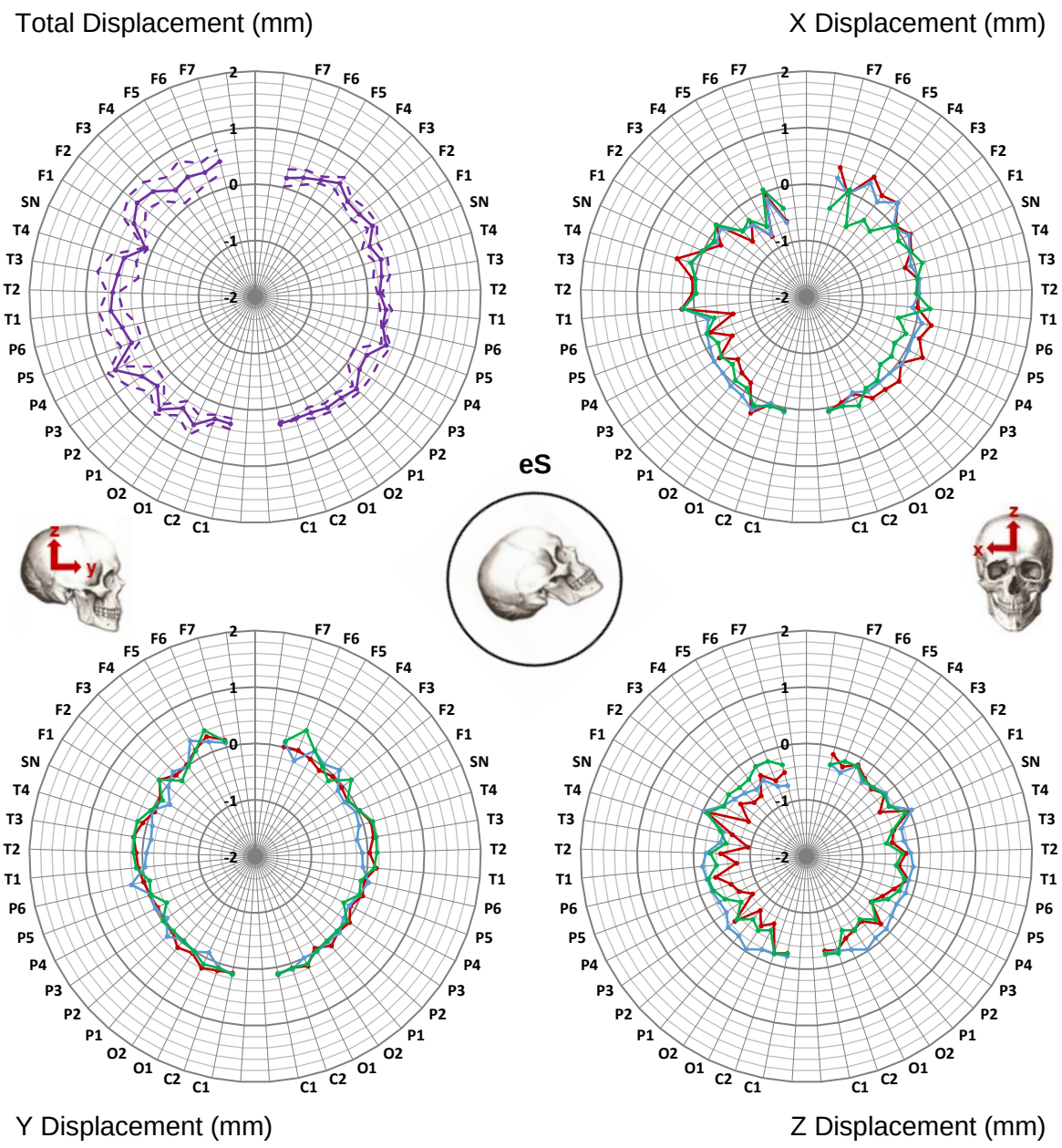

Figure 9.18: Displacement of markers upon transitions S1 -> eS1, S2 -> eS2 and S3 -> eS3. Top-left radar graph shows total displacement, top-right shows displacement along the x axis, bottom-left shows displacement along the y axis and bottom-right shows displacement along the z axis. In the coordinate system employed, the x axis points towards the right side of the head, the y axis points anteriorly and the z axis points superiorly. For the total displacement graph, the solid line corresponds to the mean total displacement across the three measurements for the studied transition, whilst the dotted lines correspond to the standard deviation from the mean. The x, y and z displacement graphs, on the other hand, show the displacement profile for each measurement as a separate line.

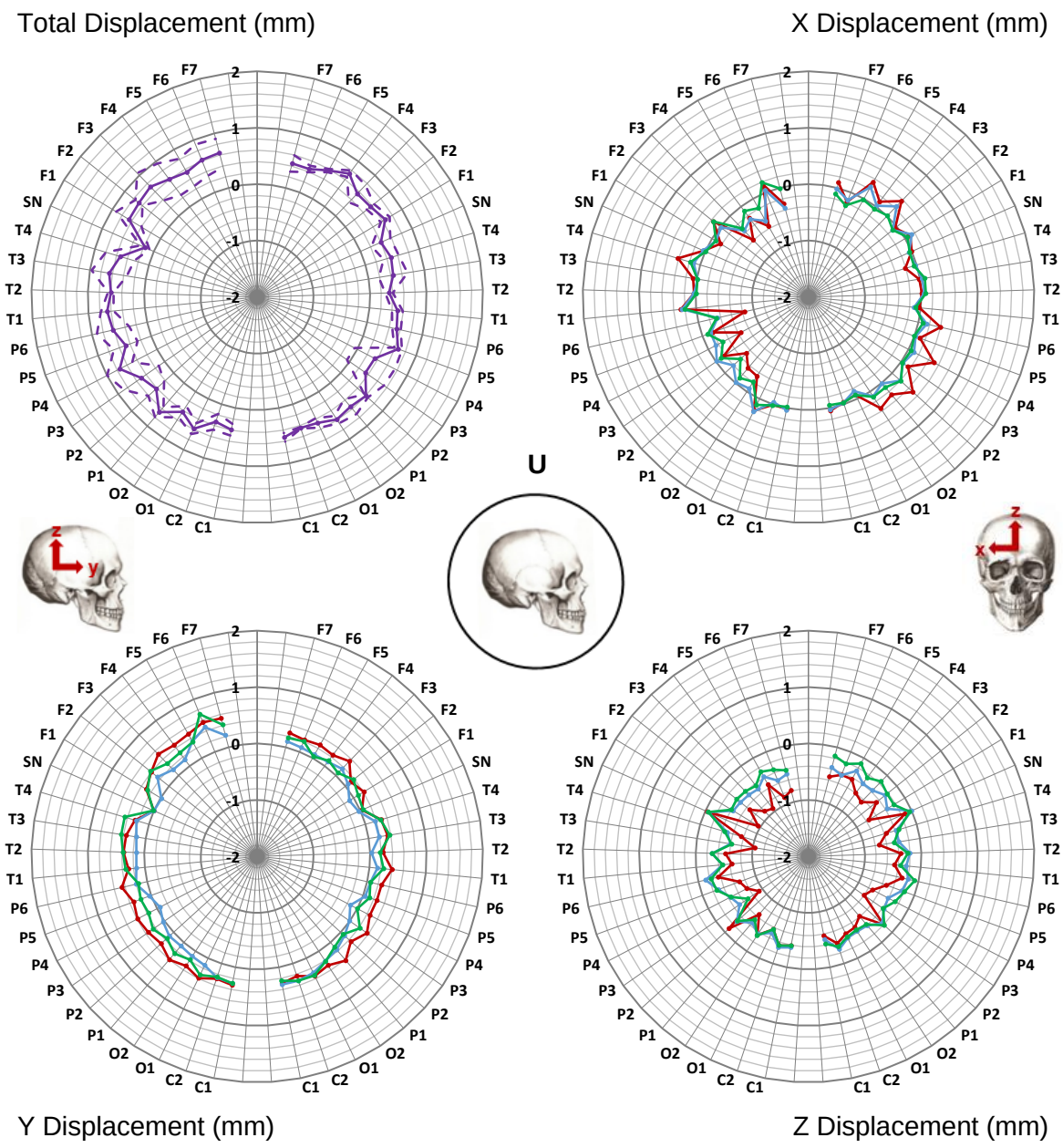

Figure 9.19: Displacement of markers upon transitions S1 -> U1, S2 -> U2 and S3 -> U3. Top-left radar graph shows total displacement, top-right shows displacement along the x axis, bottom-left shows displacement along the y axis and bottom-right shows displacement along the z axis. In the coordinate system employed, the x axis points towards the right side of the head, the y axis points anteriorly and the z axis points superiorly. For the total displacement graph, the solid line corresponds to the mean total displacement across the three measurements for the studied transition, whilst the dotted lines correspond to the standard deviation from the mean. The x, y and z displacement graphs, on the other hand, show the displacement profile for each measurement as a separate line.

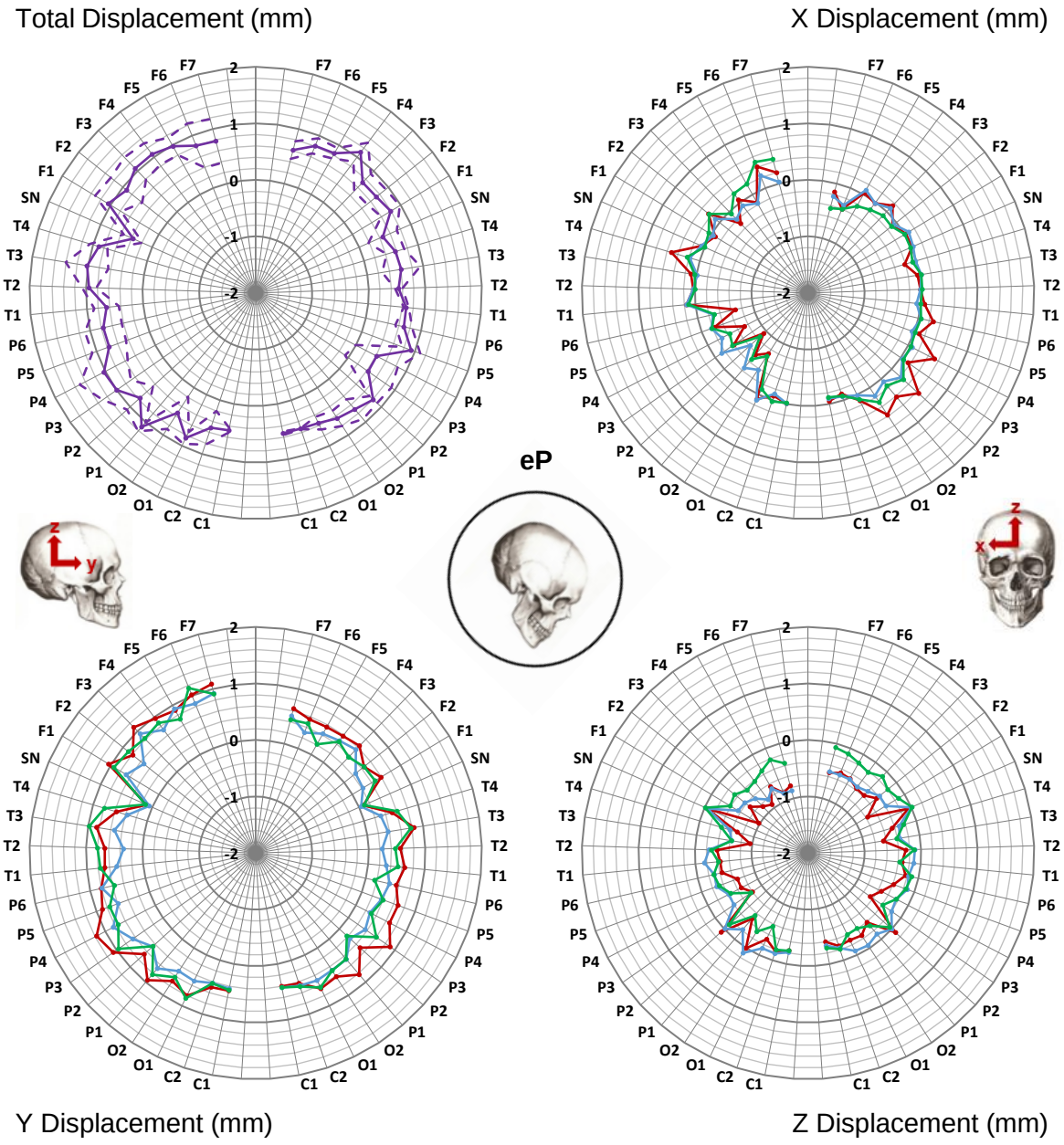

Figure 9.20: Displacement of markers upon transitions S1 -> eP1, S2 -> eP2 and S3 -> eP3. Top-left radar graph shows total displacement, top-right shows displacement along the x axis, bottom-left shows displacement along the y axis and bottom-right shows displacement along the z axis. In the coordinate system employed, the x axis points towards the right side of the head, the y axis points anteriorly and the z axis points superiorly. For the total displacement graph, the solid line corresponds to the mean total displacement across the three measurements for the studied transition, whilst the dotted lines correspond to the standard deviation from the mean. The x, y and z displacement graphs, on the other hand, show the displacement profile for each measurement as a separate line.

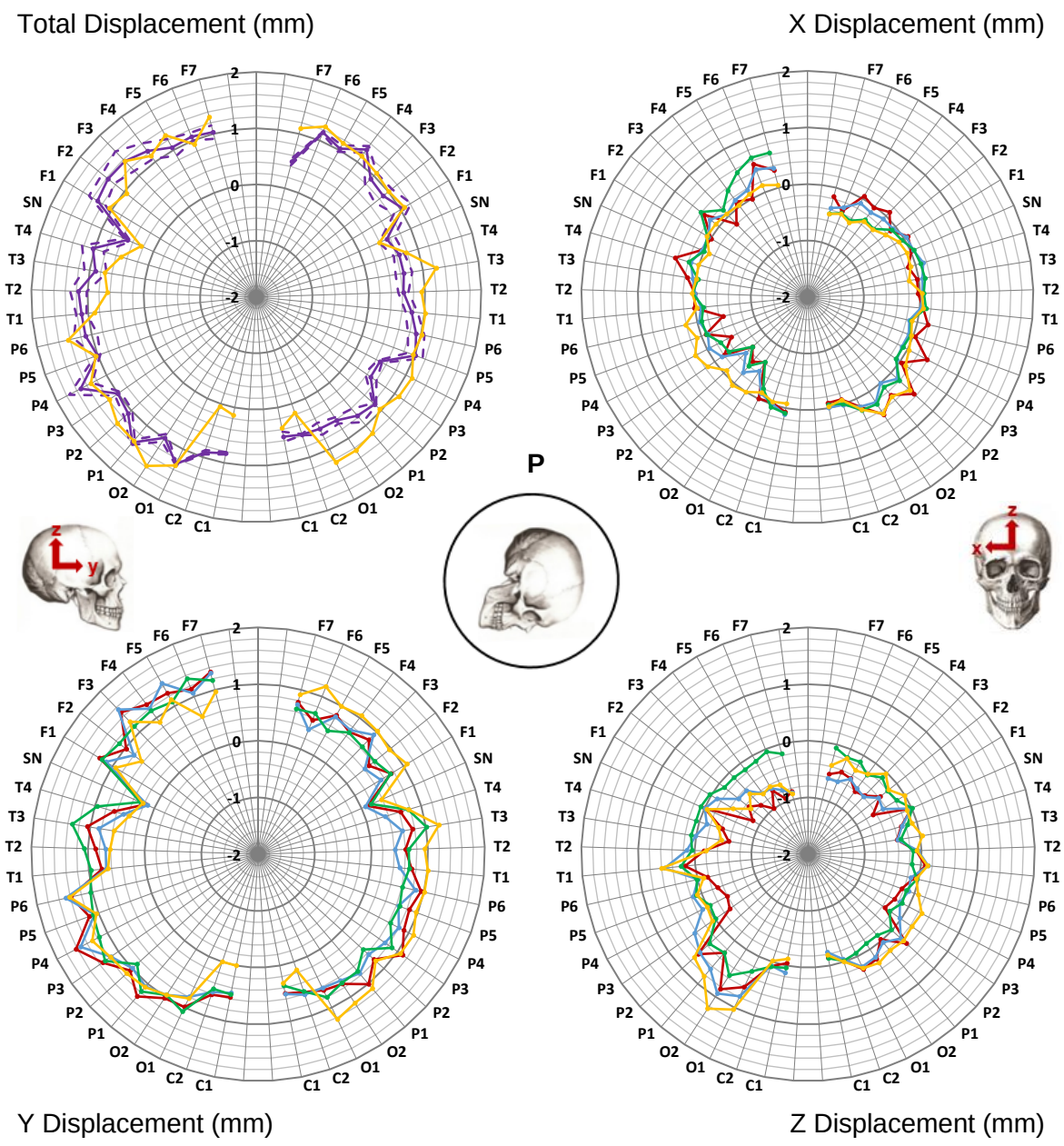

Figure 9.21: Displacement of markers upon transitions S1 -> P1, S2 -> P2 and S3 -> P3. For comparison, the displacement measured in the SF phantom is displayed as a yellow line. Top-left radar graph shows total displacement, top-right shows displacement along the x axis, bottom-left shows displacement along the y axis and bottom-right shows displacement along the z axis. In the coordinate system employed, the x axis points towards the right side of the head, the y axis points anteriorly and the z axis points superiorly. For the total displacement graph, the solid line corresponds to the mean total displacement across the three measurements for the studied transition, whilst the dotted lines correspond to the standard deviation from the mean. The x, y and z displacement graphs, on the other hand, show the displacement profile for each measurement as a separate line.

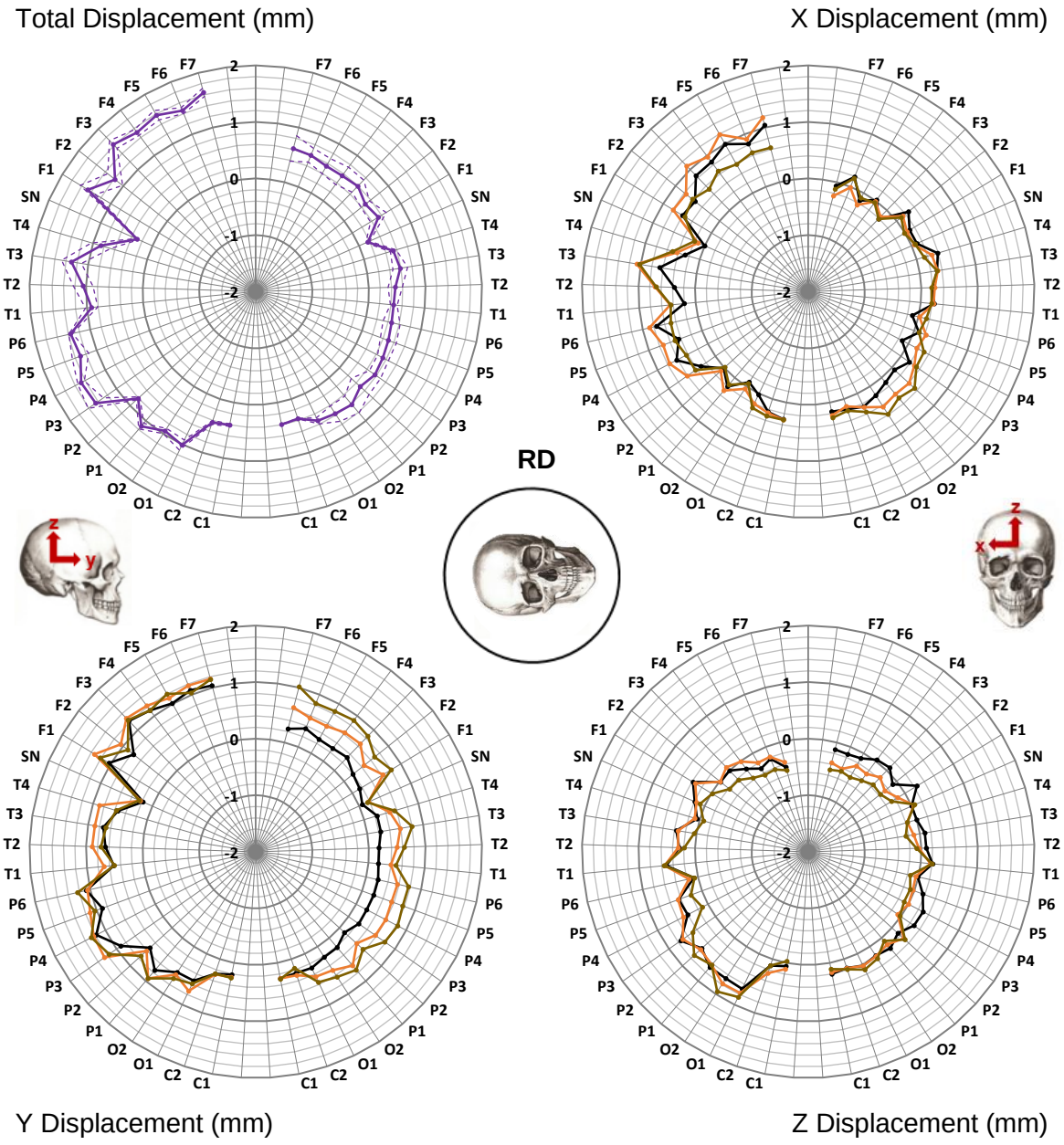

Figure 9.22: Displacement of markers upon transitions S4 -> RD4, S5 -> RD5 and S6 -> RD6. Top-left radar graph shows total displacement, top-right shows displacement along the x axis, bottom-left shows displacement along the y axis and bottom-right shows displacement along the z axis. In the coordinate system employed, the x axis points towards the right side of the head, the y axis points anteriorly and the z axis points superiorly. For the total displacement graph, the solid line corresponds to the mean total displacement across the three measurements for the studied transition, whilst the dotted lines correspond to the standard deviation from the mean. The x, y and z displacement graphs, on the other hand, show the displacement profile for each measurement as a separate line.

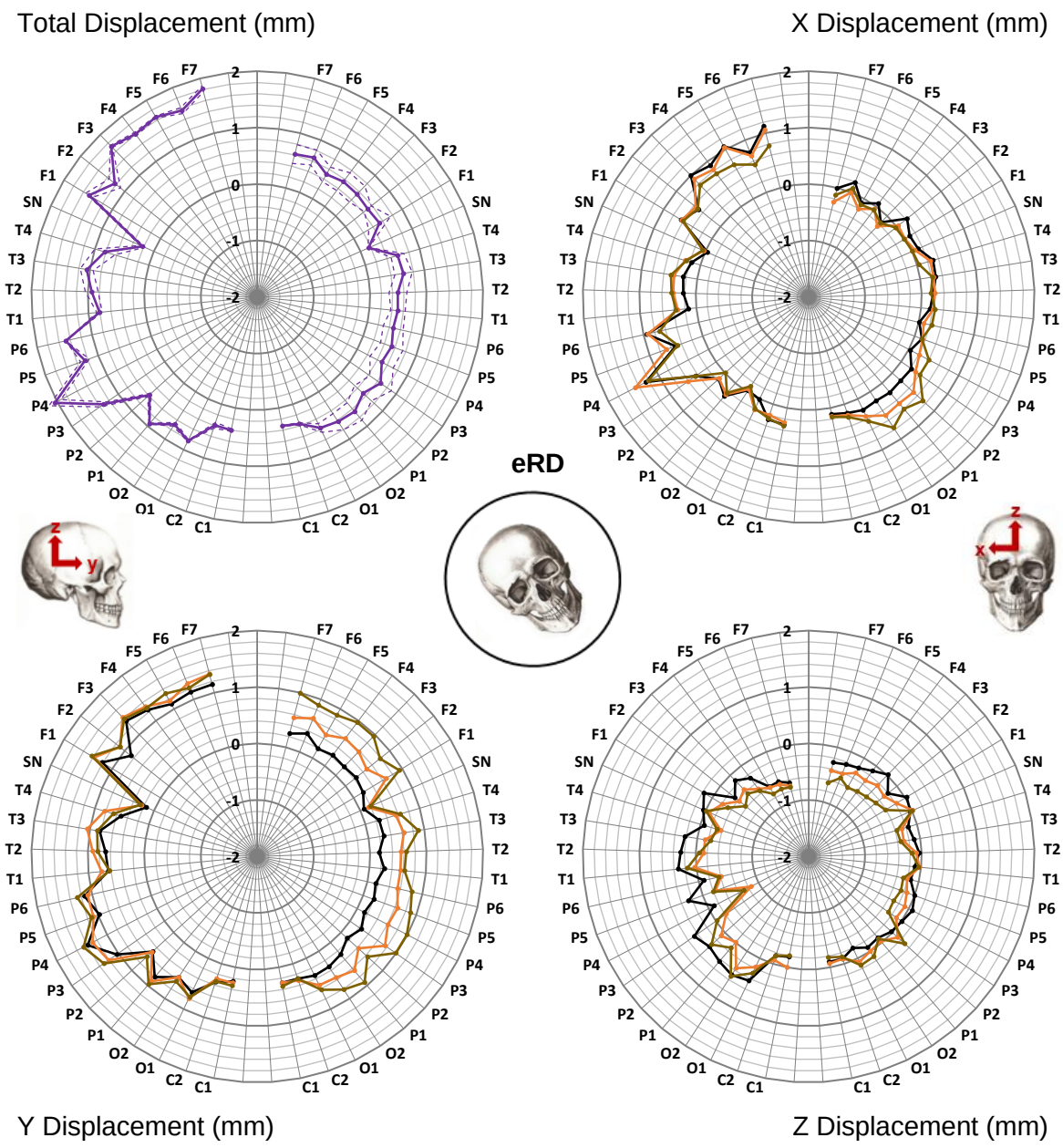

Figure 9.23: Displacement of markers upon transitions S4 -> eRD4, S5 -> eRD5 and S6 -> eRD6. Top-left radar graph shows total displacement, top-right shows displacement along the x axis, bottom-left shows displacement along the y axis and bottom-right shows displacement along the z axis. In the coordinate system employed, the x axis points towards the right side of the head, the y axis points anteriorly and the z axis points superiorly. For the total displacement graph, the solid line corresponds to the mean total displacement across the three measurements for the studied transition, whilst the dotted lines correspond to the standard deviation from the mean. The x, y and z displacement graphs, on the other hand, show the displacement profile for each measurement as a separate line.

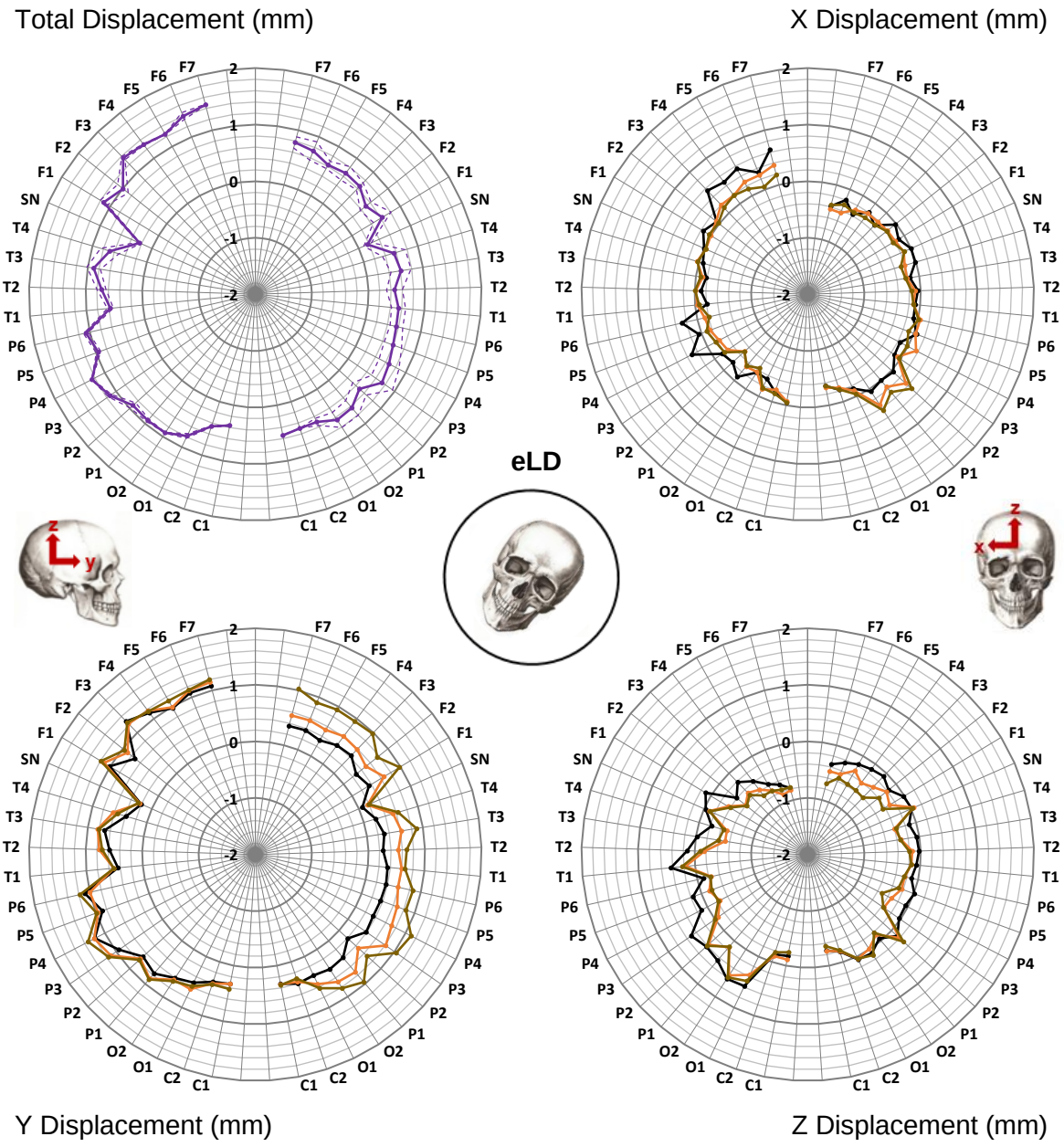

Figure 9.24: Displacement of markers upon transitions S4 -> eLD4, S5 -> eLD5 and S6 -> eLD6. Top-left radar graph shows total displacement, top-right shows displacement along the x axis, bottom-left shows displacement along the y axis and bottom-right shows displacement along the z axis. In the coordinate system employed, the x axis points towards the right side of the head, the y axis points anteriorly and the z axis points superiorly. For the total displacement graph, the solid line corresponds to the mean total displacement across the three measurements for the studied transition, whilst the dotted lines correspond to the standard deviation from the mean. The x, y and z displacement graphs, on the other hand, show the displacement profile for each measurement as a separate line.

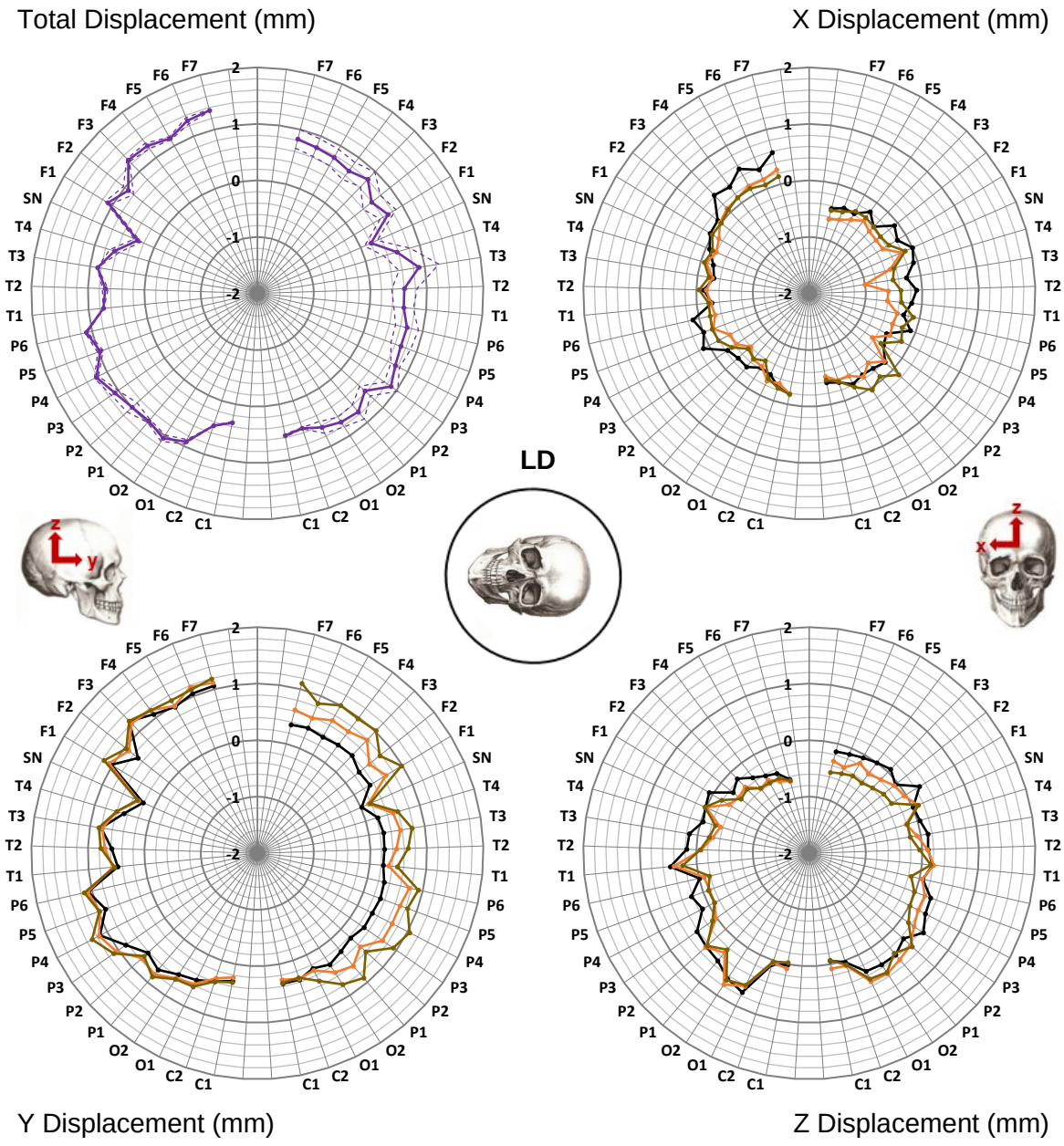

Figure 9.25: Displacement of markers upon transitions S4 -> LD4, S5 -> LD5 and S6 -> LD6. Top-left radar graph shows total displacement, top-right shows displacement along the x axis, bottom-left shows displacement along the y axis and bottom-right shows displacement along the z axis. In the coordinate system employed, the x axis points towards the right side of the head, the y axis points anteriorly and the z axis points superiorly. For the total displacement graph, the solid line corresponds to the mean total displacement across the three measurements for the studied transition, whilst the dotted lines correspond to the standard deviation from the mean. The x, y and z displacement graphs, on the other hand, show the displacement profile for each measurement as a separate line.

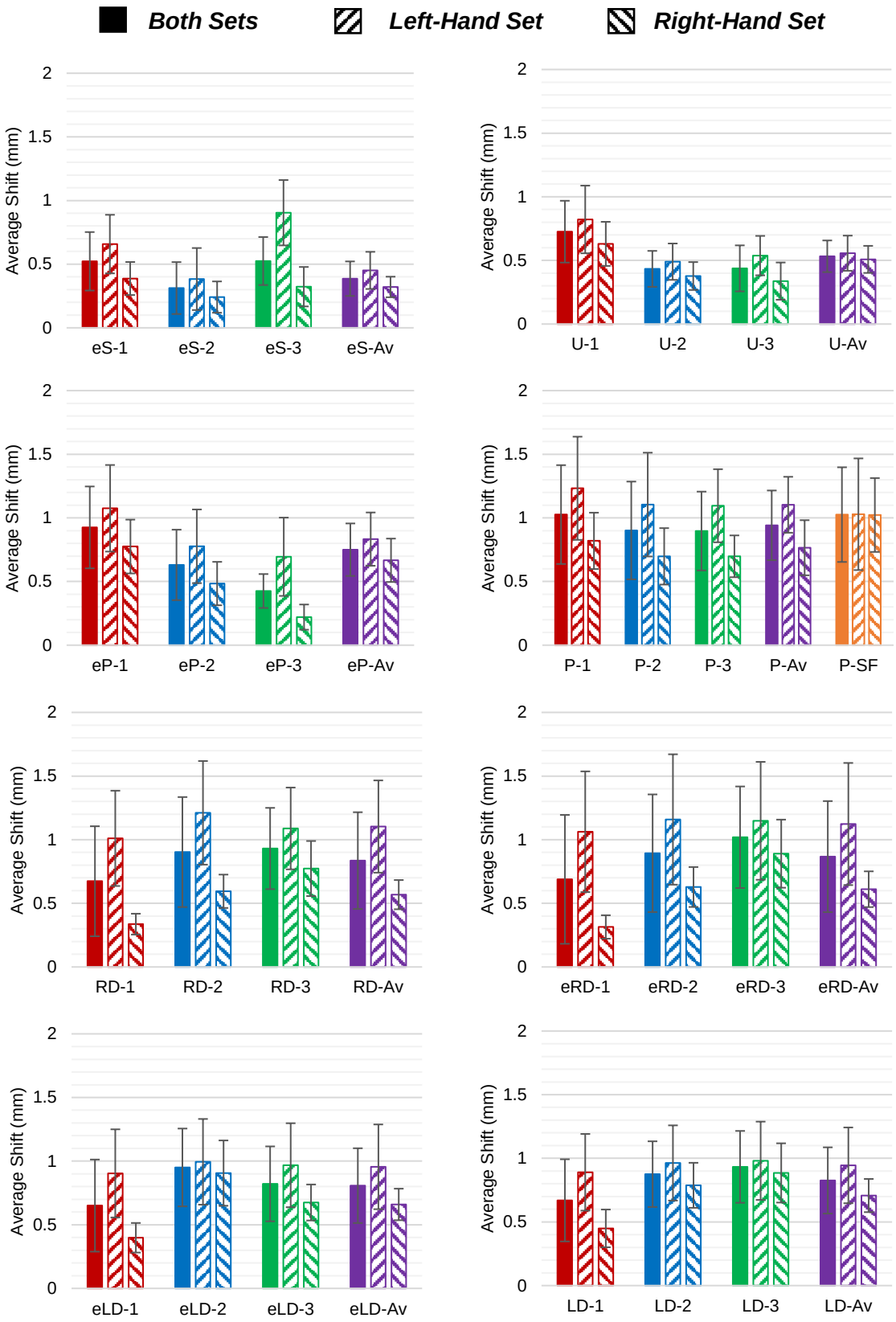

Figure 9.26: Average shift of markers upon transition from supine to elevated supine (eS), upright (U), elevated prone (eP), prone (P), right decubitus (RD), elevated right decubitus (eRD) elevated left decubitus (eLD) and left decubitus (LD). The numerical suffixes indicate the repeat number, the Av suffix indicates the mean of the repeats, and the SF suffix indicates the shift measured in the SF phantom.

9.3.7 Inter-Project Brain Shift

Displayed in Figure 9.27 (p200) are sagittal and axial plane displacement maps for the average brain shift measured in the study phantom, the average brain shift measured across the three human subjects in the *in vivo* project and the brain shift simulated with the computational model from the *in silico* project (a single mathematically derived dataset). Total and component displacement graphs for these datasets is shown in Figure 9.28 (p201). The displacement data for the study phantom and *in vivo* measurements correspond to the per-marker averages across the three repeats and three subjects, respectively.

Collectively, these graphics show a consistent level of brain shift being measured across the three investigatory routes. The *in vivo* measurement can be seen to produce the lowest levels of brain shift with a mean of 0.37 ± 0.22 mm and a range of 0.12 - 1.07 mm, while the phantom measurement can be seen to produce the highest levels of brain shift with a mean of 0.94 ± 0.34 mm and a range of 0.13 - 1.52 mm. The *in silico* measurement, on the other hand, can be seen to produce intermediate levels of brain shift with a mean of 0.71 ± 0.19 mm and a range of 0.24 - 0.96 mm. For the phantom and *in vivo* data, the means and ranges pertain to the per-marker averaged shifts across the three repeats / three subjects.

The phantom and *in silico* brain shift appear to have the closest match across magnitude, direction and non-rigid pattern, with the right-side marker sites especially exhibiting high similarity. The magnitude of shift on the left side is considerably higher in the phantom (likely due to the larger phantom air volume being on the left), however, the direction seems to be relatively consistent, with the shift taking place predominantly in the direction of gravity.

The *in vivo* measurement of brain shift appears to have the greatest dissimilarity in magnitude and direction. The dissimilarity in direction is most evident in Figure 9.27 (p200), where it can be seen that some of the *in vivo* vectors (e.g. O1 or F5 in sagittal plane) are even at obtuse angles from the phantom and *in silico* vectors. The per-marker difference in displacement magnitude can also be seen to be generally very large, making the *in vivo* vector set somewhat dissimilar from the phantom and *in silico* vector sets.

One caveat, however, is that the right T2 and P5 markers are in very close agreement across all datasets. Furthermore, while there is some discrepancy in magnitude and direction, the SN markers can be seen to exhibit little displacement across all datasets. The SN markers lie beneath the left and right subtantia nigra nuclei, which are a common target in stereotactic electrode implantation surgery.

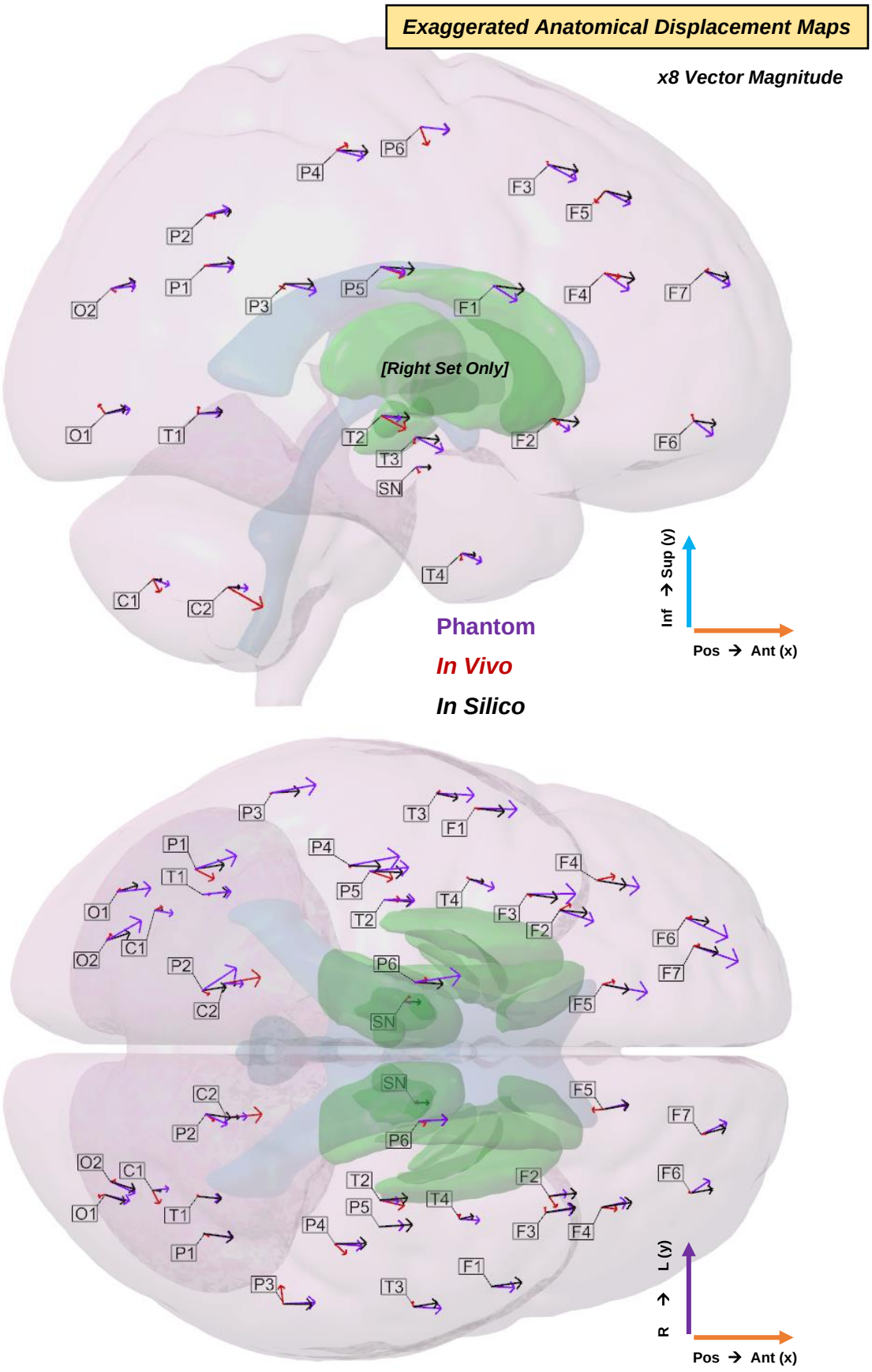

Figure 9.27: Exaggerated (x8 vector magnitude) sagittal and axial plane supine to prone displacement measured in the phantom project (average across the three repeats), the in vivo project (average across three subjects) and in silico project (single simulation). Phantom vectors are in purple, in vivo vectors are in red and in silico vectors are in black.

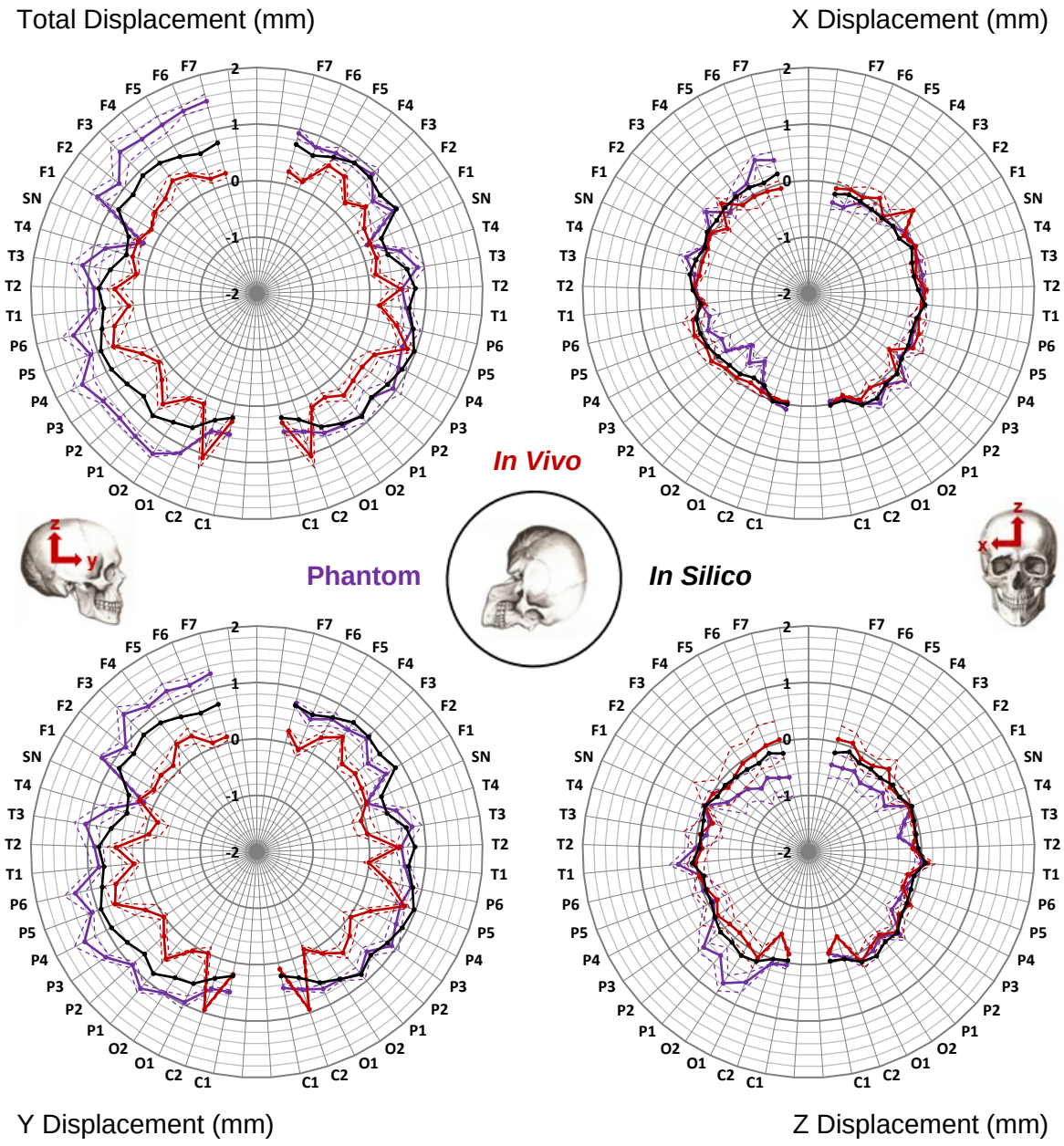

Figure 9.28: Displacement of markers upon transition from the supine to prone position in the study phantom, in vivo and in silico datasets. Top-left radar graph shows total displacement, top-right shows displacement along the x axis, bottom-left shows displacement along the y axis and bottom-right shows displacement along the z axis. In the coordinate system employed, the x axis points towards the right side of the head, the y axis points anteriorly and the z axis points superiorly. Solid lines correspond to the mean total displacement across the three measurements for the dataset, whilst the dotted lines correspond to the standard deviation from the mean. The in silico dataset stems from a mathematical simulation and so no repeats were made.

9.4 Discussion

9.4.1 Global Brain Shift

The global brain shift captured by the study phantom upon repositioning from the supine position to the eight imaged non-supine positions is in line with that reported in the literature and with the emerging measurements from the *in vivo* and *in silico* projects, as presented in Table 9.3. Primarily, this data shows a consensus in the general global magnitude of brain shift that is taking place in PBS. The only outlier is perhaps the emerging data from the *in vivo* project, which reports lower levels of PBS for the S→P transition. It is important to note, however, that this data is unpublished and from a preliminary study which is part of a much larger body of developing work.

Table 9.3: Global brain shift measured in the phantom, in vivo and in silico projects and global brain shift reported in PBS studies. Mean and standard deviation is presented primarily; where these metrics are not available, other available measures are used instead (e.g. range).

Data Source	Brain Shift Measurements
Phantom Project	S→eS: 0.39 ± 0.14 mm S→U: 0.53 ± 0.12 mm S→eP: 0.75 ± 0.21 mm S→P: 0.94 ± 0.31 mm S→RD: 0.84 ± 0.38 mm S→eRD: 0.87 ± 0.44 mm S→eLD: 0.81 ± 0.29 mm S→LD: 0.83 ± 0.26 mm
In Vivo Project	P→S: 0.37 ± 0.22 mm
In Silico Project	P→S: 0.71 ± 0.19 mm
Thulin et al. [121]	S→U: 0.55 to 0.90 mm range
Hill et al. [122]	S→P: “up to 1 mm”
Rice et al. [39]	S→P: “approximately 1 mm”
Schnaudigel et al. [123]	S→P: 0.6 to 1.3 mm range LD→RD: “up to 1.8 mm”
Monea et al. [124]	< 20 years age S→P cortical shift: -0.25 ± 1.62 mm S→P ventricular shift: 0.12 ± 0.87 mm LD→RD cortical shift: -0.66 ± 2.33 mm LD→RD ventricular shift: 0.18 ± 1.08 mm 25-40 years age S→P cortical shift: -0.47 ± 1.90 mm S→P ventricular shift: 0.06 ± 0.63 mm LD→RD cortical shift: -0.23 ± 1.35 mm LD→RD ventricular shift: 0.18 ± 1.09 mm >60 years age S→P cortical shift: -0.16 ± 1.19 mm S→P ventricular shift: 0.23 ± 0.81 mm LD→RD cortical shift: -0.05 ± 1.52 mm LD→RD ventricular shift: 0.04 ± 1.18 mm
Mikkonen and Laakso [125]	S→P right hemisphere: 0.8 ± 1.1 mm S→P left hemisphere: 0.7 ± 1.0 mm S→LD right hemisphere: 0.4 ± 0.8 mm S→LD left hemisphere: 0.9 ± 0.9 mm

For the S→P transition, the study phantom manifested similar brain shift to the *in silico* measurement and the accounts by Rice et al. [39], Hill et al. [122], Schnaudigel et al. [123], and Mikkonen and Laakso [125], with shift lying close to 1 mm. Contrastingly, the levels of shift found in the *in vivo* project measurements and Monea et al. [124] are somewhat lesser. The comparisons to Monea et al., however, are difficult due to the shift quantification methods used in the study.

For the S→U transition, the study phantom manifested a comparable shift range of 0.17 to 0.75 mm to the range of 0.55 to 0.90 mm reported in Thulin et al. [121].

For the LD→RD transition, the study phantom manifested a comparable shift range of 0.20 to 1.22 mm (calculable from the LD and RD scans) to the “up to 1.8mm” reported in Schnaudigel et al. [123]. Shifts in Monea et al. [124] are again difficult to compare due to the contrasting shift quantification method.

For the S→LD transition, the study phantom manifested a comparable shift of 0.77 ± 0.19 mm in the right side of the brain and 1.10 ± 0.22 mm in the left to Mikkonen and Laakso [125], which measured 0.40 ± 0.80 mm in the right hemisphere and 0.90 ± 0.22 mm in the left.

But while the study phantom manifested comparable levels of average shift across the entire brain volume, a sizeable left-right discrepancy in brain shift was measured across all positions, with a consistently greater displacement occurring on the left side of the brain, as measured by the average and standard deviation. Substantial asymmetry is not reported in the literature accounts of S→P brain shift and cannot be seen in the *in silico*, *in vivo* or SF phantom datasets and could be in-part a result of the intracranial air which was unintentionally incorporated into the phantom during assembly. Air contamination was found in the IF and SF phantoms, but at smaller volumes of 0.9 and 1.7 ml, respectively.

The 4 ml asymmetrically distributed volume of intracranial air incorporated into the phantom is far smaller than the cm^3 scale volumes of air which are typically referred to in PMBS (see Figure 3.15, p45), however, the mechanism by which the shift occurs is somewhat different. PMBS is conjectured to be a consequence of the delamination of the dura at the junction between the dural border cells and the arachnoid barrier cells (see Section 2.2.1, p14), which arises due to altered buoyancy forces within the SAS as a consequence of CSF loss and the concurrent influx of air. Delamination of the dura then creates the pathological subdural space and the loss of the material continuum between the pia mater and the skull, removing the tethering of the brain to the skull and allowing the brain to sag further towards the bottom of the orientation. The effect of air inclusion in the phantom, however, is purely a change in the buoyancy force acting on the hydrogel brain and presents as a unique phantom-specific event that requires further investigation to understand.

Second to the differing mechanism is that the PMBS event is a brain shift event between an air-free supine position and an air-containing non-supine position. In the phantom's case, however, the brain shift event takes place between two air-containing positions and, therefore, the air will likely be having an increased effect as enhanced sag of the brain will take place in both images but in different directions.

The SF phantom contained a much smaller 1.7 ml air volume and produced symmetrical levels of brain shift, however, with only a single measurement taken and with the observation of quite variable intra-supine brain resting position in the study phantom (Figure 9.12 - p182), it is wrong to conclude that the asymmetrical shift would not have occurred if repeat measurements were taken. The small left-dominant volume of air does appear to correlate with the equally small level of left-dominance in the brain shift, however, it could equally be due to other factors such as subtle differences in brain geometry arising from the manufacturing process or trapping of the brain against the tight fitting skull on assembly.

Although the left side of the study phantom featured enhanced shift magnitude, the direction of shift appears to be consistent with that of the right side, as demonstrated in Figure 9.29, which shows axial plane displacement with left side vectors reduced in magnitude by 40%. Here it can be seen that the adjusted left side vectors are largely symmetrical with their corresponding right side vectors.

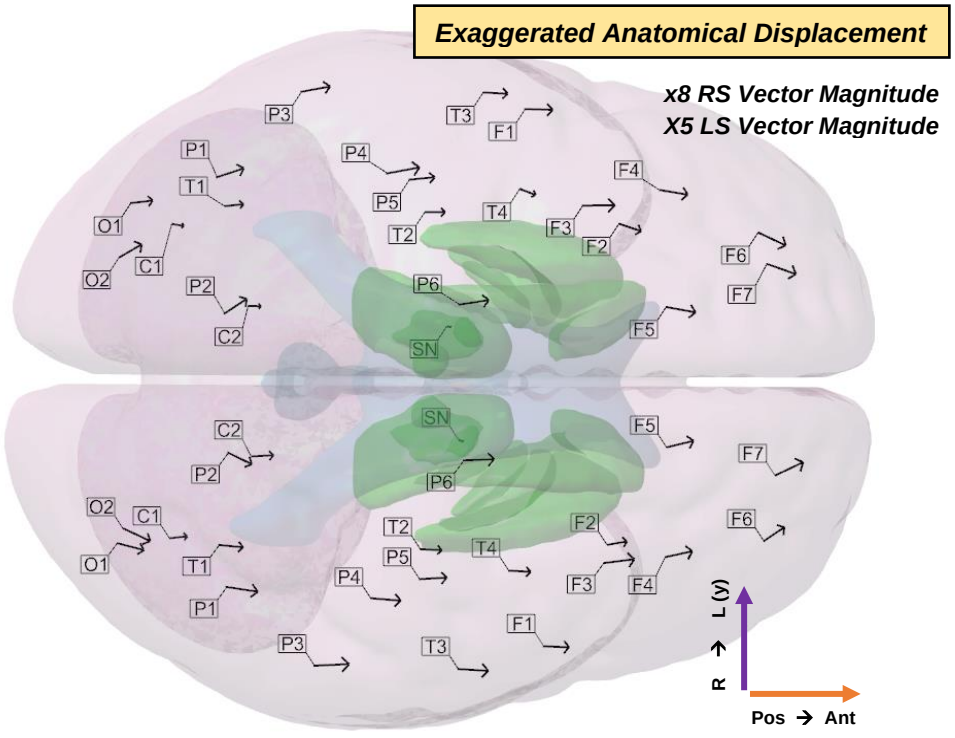

Figure 9.29: Axial plane exaggerated anatomical displacement map of supine to prone brain shift with magnitude of left side vectors reduced by 40% to match right side vectors.

Yet, if it is indeed the inclusion of air that is causing the asymmetry, it may also be the case that the larger collection of air on the left side acts to reduce brain shift on the right, as identified in [163]. In this study, Miyagi et al. observed lateral shift of the brain towards the contralateral side of the cranial cavity upon unilateral invasion of air (see Figure 9.30). A possible explanation for this is that the lateral motion is in fact part of a more global rotation event which occurs when the buoyancy force is lowered on only one side of the cranial cavity.

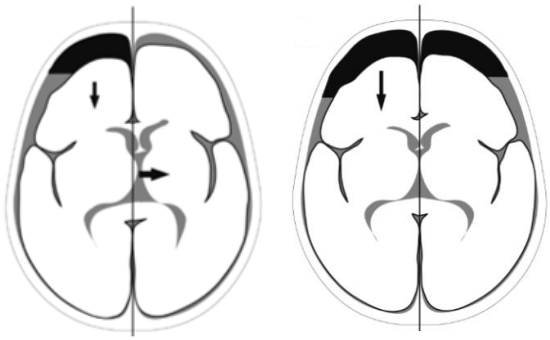

Figure 9.30: The effect of unilateral and bilateral air on brain shift. Adapted from [163].

It is possible that this lateral motion, causes the contralateral side of the brain to become pinned to some degree against the skull, reducing the extent at which it can shift upon repositioning. It could, therefore, be the case that the left side vectors are in fact 20% greater than they would be without the air and the right side vectors are 20% smaller due to contralateral pinning.

One avenue that can be taken towards determining the level of contribution of the air is the cross-comparison of the RD5 and LD5 shift measurements, as unlike the other sets of measurements, these positions can be seen to have a largely mirrored air distribution (see Figure 9.31) and therefore the effect of the air should be the same.

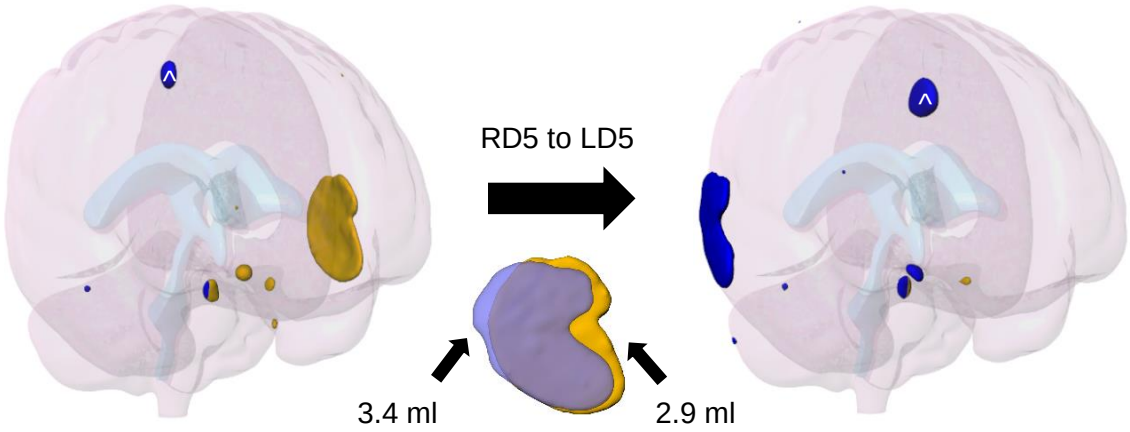

Figure 9.31: Air distribution in the 2nd repeat of the right and left decubitus positions, showing pseudo-mirrored air distribution between the two positions. Right to left view of overlaid air volumes shows similar location, size and shape between the two significant volumes.

If the air is solely responsible for the asymmetry which manifests in the brain shift one would expect the shift to be simply mirrored between these positions. However, as illustrated in Figure 9.32, this cannot be seen to be the case, especially in the right-left (x) and inferior-superior (z) components. These differences appear to be of similar magnitude to the right-left side differences in the sagittal positions and could suggest that the air is not entirely responsible for the asymmetrical shift in the sagittal positions.

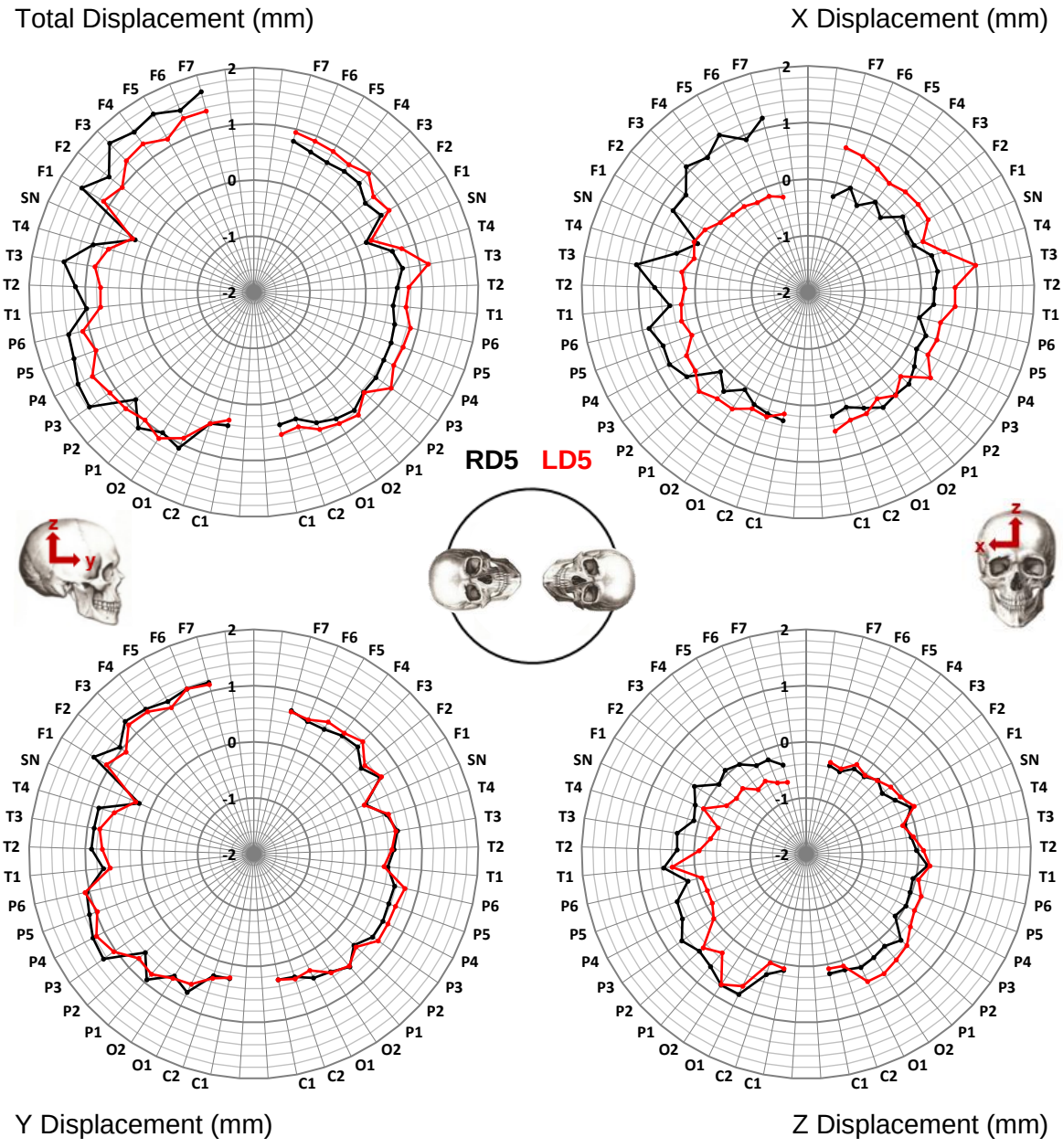

Figure 9.32: Displacement of markers upon transitions S5 -> RD5 and S5 -> LD5. Top-left radar graph shows total displacement, top-right shows displacement along the x axis, bottom-left shows displacement along the y axis and bottom-right shows displacement along the z axis. In the coordinate system employed, the x axis points towards the right side of the head, the y axis points anteriorly and the z axis points superiorly.

With such a complex mechanical system, however, it is inappropriate to use the observation of non-mirrored right/left decubitus shift with minimized air effects positions to conclude that the air is not responsible for at least a large part of the right-left asymmetrical shift in the sagittal positions, especially considering all the evidence of the effect of air collections in the literature. Yet, it is possible that some of the asymmetry is due to other factors specific to the phantom, such as the absence of brain-skull tethering.

With a symmetrical geometry, the absence of tethering would not induce asymmetry, however, the human brain features an anatomical right-left asymmetry that arises from an anti-clockwise twisting of the brain known as Yakovlevian Torque (Figure 9.33), that results in a wider left occipital lobe and wider frontal lobe, with respect to the central sagittal plane [164]. These brain asymmetries are paired with corresponding asymmetries of the cranial cavity and no statistical difference has been found in the SAS width between the right and left occipital and frontal lobes [23].

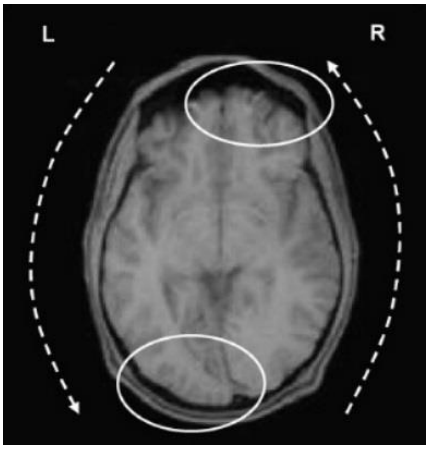

Figure 9.33: Yakovlevian torque. Adapted from [165].

As illustrated in Figure 9.34, the same right-left discrepancy can be seen in both the original brain model segmented from the MNI ICBM152 dataset and an MRI segmentation of the phantom itself. The asymmetry measured in the phantom segmentation is likely an over-exaggeration due to the high ambiguity at the brain-SAS boundary of the MR images, however, it can generally be seen that the anatomical feature of wider left occipital and right frontal lobes is present in the phantom.

Since the MNI ICBM152 segmented brain model was used to build the computer model, the same asymmetry is present in the *in silico* model, however no significant asymmetry can be seen in the measurements of S→P shift made with the *in silico* model. It is possible, however, that the effect of the geometrical asymmetry does result in a natural asymmetry in brain motion and that the brain skull tethering acts to minimize it.

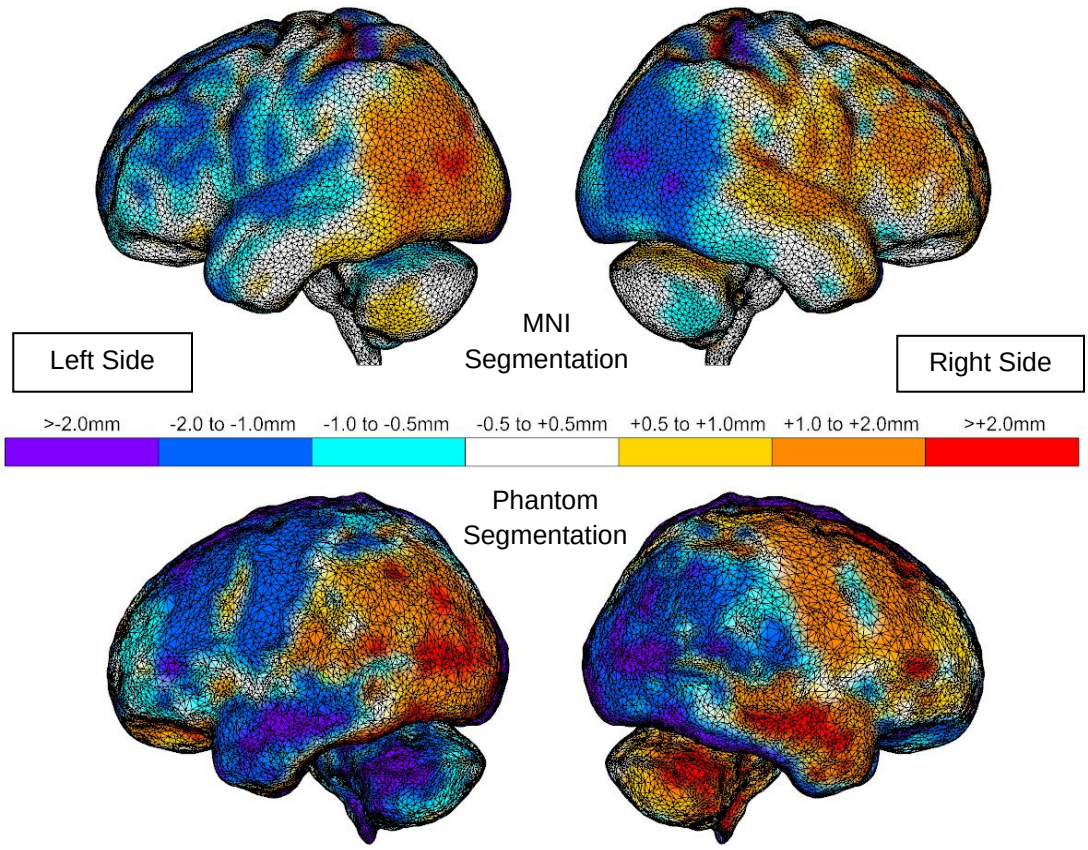

Figure 9.34: Brain asymmetry within the original CAD model segmented from the MNI dataset and an MR image segmented model of the phantoms brain, showing wider left occipital and right frontal lobes. Colours display the distance between the model and a mirrored version of itself down the central sagittal line.

Ultimately, with the data available, it is not possible to determine whether or not the air is responsible for the asymmetry in right-left shift levels. Unfortunately, the variable incorporation of air presents as a limitation of the phantom's current assembly workflow and repeats of the study were not possible within the scope of this project, due to practical constraints following a lengthy and problematic development profile for the phantom (see later in Section 9.5 - p211 for greater discussion of study limitations).

9.4.2 Regional Brain Shift

The phantom captured a variable pattern of non-rigid brain shift on repositioning from the supine position to the eight non-supine positions. Within all transitions, the variability of shift magnitude and direction between locations was found to be large, further bringing into question the utility of average brain shift metrics in the context of targeting error mitigation.

Direction of shift is equally as important as the magnitude (since correction of error in the wrong direction can act to worsen it) and local shift in the phantom can be seen in all positions to take place along directions different from the gravitational direction and in some cases the difference can be quite large. This was also observed in the S→P brain shift measurements of the *in vivo* and *in silico* projects, and has been reported in the three

regional PBS measuring studies [123,124,125], suggesting that the reconstruction of the PBS event in the phantom is somewhat realistic in this regard.

Closer comparison of the phantom's brain shift to the shift reported in the literature studies is difficult due to the largely incomparable methods utilised, with [123] reporting regional shift by means of select sagittal/coronal slices with overlaid vector displacement fields, [124] by means of cortical and ventricular normal-to-surface displacement, and [125] by means of surface displacement only. However, comparison to the *in silico* and *in vivo* datasets was made possible due to the ability to obtain and reduce the displacement fields to locally averaged vectors at the marker sites of the phantom.

Displayed in Figure 9.35 (p210) are the total and component displacement graphs of the S→P shift from the study phantom, *in vivo* and *in silico* datasets, but unlike as displayed in Figure 9.28 (p201), these graphs feature the study phantom's dataset with left side vectors with 40% reduced magnitude. In doing this it can be seen that the pattern of non-rigid shift was reasonably symmetrical in the study phantom, regardless of any artificial exaggerated motion on the left side. Furthermore, it can also be seen that this action creates high agreement with the *in silico* dataset, especially in the frontal and occipital regions.

Agreement upon reduction of the left side phantom vectors perhaps indicates that the air is indeed having a substantial effect, however, one would expect that without the same brain-skull tethering the shift in the phantom would be higher in magnitude than the computer model. Yet, if unilateral air does cause contralateral pinning and reduction of brain shift on the contralateral side, and the more accurate action is indeed to reduce the left side vectors by 20% and increase the right side by 20%, then a globally higher level of brain shift would be achieved.

While the phantom and *in silico* datasets seem to be in close agreement, the *in vivo* dataset does not share the same degree of agreement in non-rigid pattern or magnitude. Shift at sites such as R-P5 and L-C1 can be seen to be in close agreement, with averages within 0.2 mm of each other, but on the whole, lesser similarity (>0.2 mm) can be seen. Furthermore, a small degree of rotation can be seen in the *x* and *z* components of the phantom and *in silico* datasets which is absent from the *in vivo* dataset.

However, it is important to note that the observed dissimilarities are of the same general magnitude as the imaging resolution of the systems used to a) obtain the MR images of which the phantom and computer models were based off and, b) measure the brain shift taking place within the phantom and human subjects. One could therefore consider the dissimilarities to be just a part of the inherent noise of the projects and that the three datasets generally say the same thing: that S→P brain shift takes place non-rigidly and with a majority of the magnitude approximately ranging from 0 to 1 mm.

There are also, of course, many elements missing from the phantom and computer models which may account for some of the disparity. For example, in both models the brain was made homogeneous, which may or may not be incorrect in the context of PBS. Further experimentation is needed to determine what omissions, if any, account for the dissimilarity.

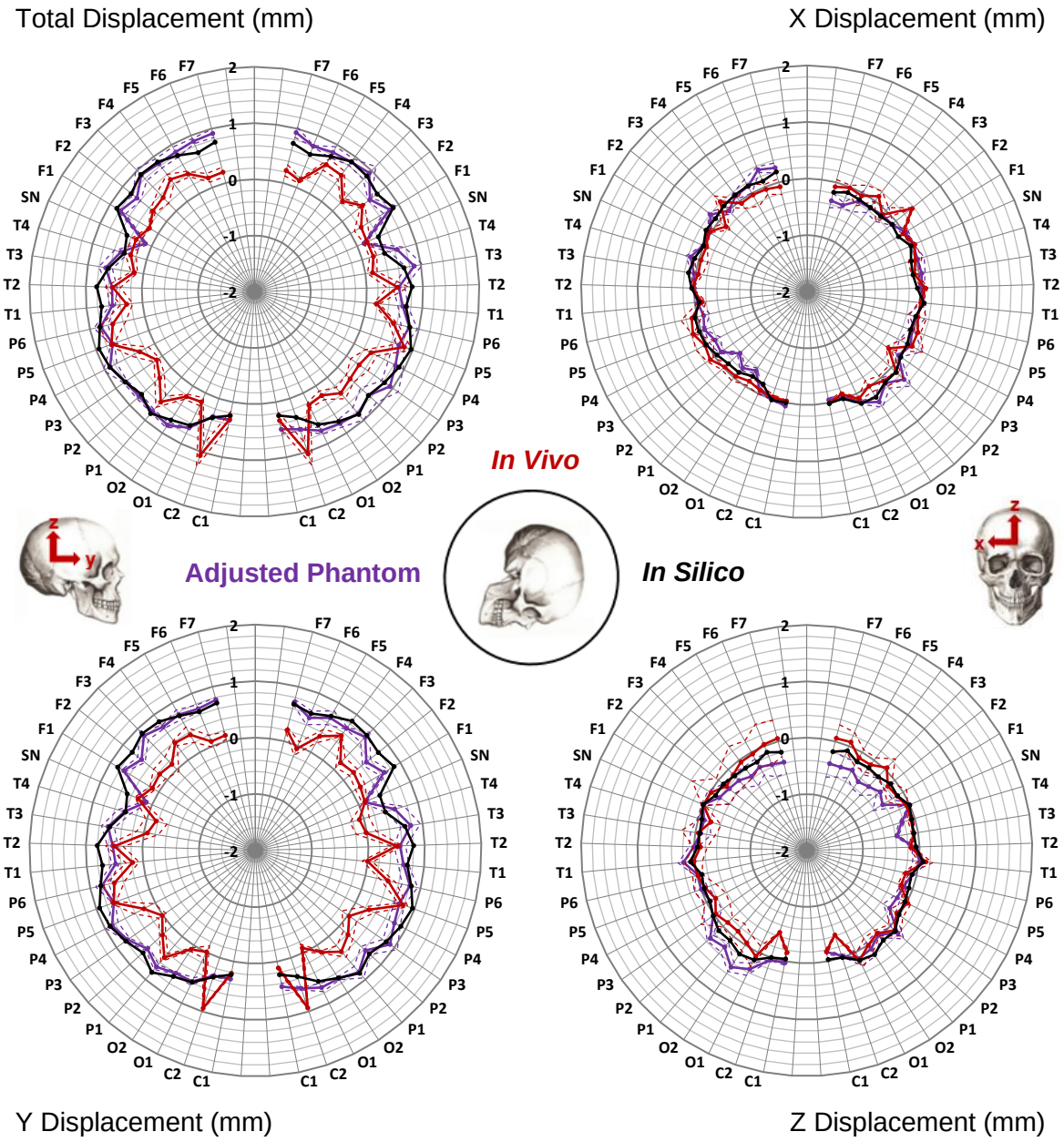

Figure 9.35: Displacement of markers upon transition from the supine to prone position in the adjusted study phantom, in vivo and in silico datasets. In the adjusted study phantom dataset the left side displacement is reduced by 40%. Top-left radar graph shows total displacement, top-right shows displacement along the x axis, bottom-left shows displacement along the y axis and bottom-right shows displacement along the z axis. In the coordinate system employed, the x axis points towards the right side of the head, the y axis points anteriorly and the z axis points superiorly. Solid lines correspond to the mean total displacement across the three measurements for the dataset, whilst the dotted lines correspond to the standard deviation from the mean. The in silico dataset stems from a simulation and so no repeats were made.

The high similarity between the phantom and *in silico* brain shift suggests that the reproduction of the brain-skull tethering element is not overly critical in a PBS simulating phantom. This could be because the tethering is not overly influential in PBS, but it also could be because its absence was unintentionally accounted for elsewhere in the phantom's design. One such area could be the phantom's SAS geometry which was not found to be measurable due to MR distortion at the boundary of the cranial cavity and insufficient resolution. It may be, for example, that the phantom's SAS is smaller than it should be in regions, setting up a frictional effect that limits the rigid shift of the brain in a similar way to the tethering. However, one effect that can be seen to possibly arise from the absence of tethering is the variability in settling position in the supine position. Without elastic forces in the tethers returning the brain's boundary to a particular position at rest, it is possible that the brain is free to settle in a number of positions, depending on its history of motion.

Regardless, given the general agreement of the S→P datasets, a degree of confidence can be placed in the datasets produced by the phantom for the other seven positional transitions. However, ideally these should be remeasured without air contamination and each supported with matching computer simulations, as the absence of tethering may lead to abnormal displacement in some positions.

Of the limited comparisons that can be made between the phantom and the literature accounts of brain shift, major discrepancies can only be seen in the accounts by Mikkonen and Laakso. In their measurements, the predominant displacement direction for the S→P transition was found to be in the inferior direction (Figure 3.18, p48), perpendicular to the gravitational direction, whilst for the phantom, the displacement direction was seen to align predominantly with the gravitational direction. The measurements by Schnaudigel et al. and Monea et al., do not share the findings by Mikkonen and Laakso and it seems unlikely for the brain to shift in this manner for this transition. Secondly, a large anterior displacement was measured in the phantom for the S→LD transition which cannot be found in the measurements by Mikkonen and Laakso. For this transition, however, there are no other measurements to compare and so it is difficult to say which one is more correct.

9.5 Limitations

The foremost limitation of this study was the 4 ml collection of air that was incorporated into the phantom during assembly. As discussed, the air volume was only discovered upon scanning for data collection and the full extent of the volume was only comprehendible upon post-processing of the scans and conversion of the air volumes to 3D models. Air removal systems were trialled with the phantom during its development, but they were found to be ineffective and increased the risk of leakage.

As can be seen in Figure 9.9 (p179) and Figure 9.10 (p180), the air which makes its way into the phantom becomes trapped in the various folds of the brain and the ventricles. Removal of these volumes through Luer Lock syringe ports fabricated into iterations of the phantom (Figure 9.36) was found to be challenging due to what appeared to be blockage by the brains surface on application of suction. For this reason, an “include no air in the first place” policy was adopted. However, despite assembling the phantoms completely underwater in a large bucket, and taking great care not to include any air, it was still found that a sizeable collection of air could still be accidentally incorporated. It is possible that the collections of air which present on the scans sometimes originate as smaller bubbles dispersed throughout the cranial cavity which only collect on the handling and rotation of the assembled phantom. An accompanying difficulty is that it is not easy to identify without MRI/CT imaging how much air is in the phantom prior to conducting costly studies with it.

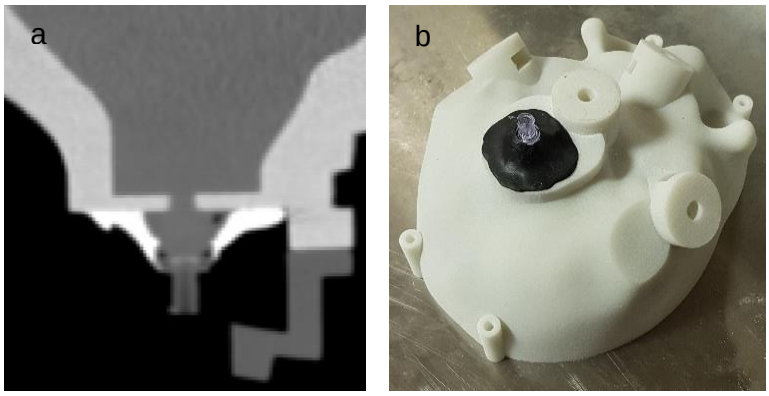

Figure 9.36: Example of trialled Luer Lock air removal port. a) cross-sectional CT image of port; b) image of a port attached to the base of the lower skull half (black material is butyl rubber sealant).

The second principal limitation of the study is that further measurements without air and with separate phantoms could not be taken due to practical limitations. Primarily, this was due to a long and problematic development profile for the phantom, made so by a) the week long cycle time for the fabrication, MR/CT imaging and mechanical testing of each iteration of the phantom, b) the loss of time due to fabrication failures and, c) the accruement of cost at each scanning stage.

The third principal limitation pertains to the phantom itself and the absence of brain-skull tethering and pia layer boundary. These were not implementable, however, due to the limitations of the available fabrication technologies. Yet, from the data, it is not clear these omissions were particularly impactful in the PBS simulating capacity of the phantom.

The fourth principal limitation pertains to the resolution of the CT scanner, which at 0.625 mm^3, could be considered ill-suited to measure displacements ranging 0-2 mm. However, the Discovery PET/CT 690 VCT system was found to be very reliable, with displacements less than 0.1 mm being measured between repeat supine scans of the phantom.

9.6 Study Conclusions

This study has shown the developed phantom to be a useful tool in the research of PBS. Despite its limitations, the phantom was shown to accurately recreate supine to prone brain shift, as demonstrated through per-marker comparisons to measurements made *in silico* and *in vivo*. The air that was accidentally included in the phantom can be seen to exaggerate the shift on the left side, however, this was shown to enhance the shift rigidly and its removal leads to well matching of both the left and right sides with the *in silico* brain shift. The *in vivo* brain shift was found to be lesser, but this could be in-part due to the noise across the imaging systems instrumental to the three projects and the simplifications made with the phantom and computational model.

The brain shift magnitude measured in the phantom was also shown to fall well in line with that reported in the literature. A similar per-marker comparison was not available with the literature data, however, aside from a few discrepancies, the general direction of motion could be seen to be in agreement for the few transitions studied in humans.

In addition to the creation of further PBS data for the S→U, S→P and S→LD transitions, the phantom was used to create comprehensive PBS datasets for five previously unstudied transitions, which together cover a discrete representation of the continuous spectrum of possible positional transitions in neurosurgery (from the supine scanning position).

Overall, the data gathered in this study suggests that, a) clinically significant brain shift takes place across all transitions and, b) there is clinically significant variability between the brain shift patterns of individual transitions at the local level. These findings further highlight the need for the consideration of PBS in surgical planning and strongly suggest that versatile parametric software are likely needed to account for the variable shifting of neurosurgical targets.

9.7 Chapter Summary

This chapter began with the definition of a multi-positional phantom study of PBS. The purpose of this study was to generate a novel comprehensive dataset which would allow clinicians to better plan surgeries and minimize the targeting error which arises from PBS.

A study wherein PBS would be measured upon transition from the supine position to eight non-supine positions was, therefore, defined. These positions were chosen to cover a discrete representation of the continuous spectrum of possible positional transitions in neurosurgery. The study was next performed and reported in traditional format, with the methods used, the results obtained, the discussion of the results and the conclusions of the study all presented.

As intended, the study produced an entirely new dataset for PBS which covers a much broader range of positional transitions (8) than that provided by the literature *in vivo* studies (1-2 in each study). Except for a small right-left asymmetry due to accidental air inclusion in the phantom, the PBS measured was found to be largely in agreement with the literature studies and the emerging measurements from the concurrent *in vivo* and *in silico* projects being conducted at Cardiff University. For the novel transitions, an expected pattern and magnitude of brain shift was observed, further suggesting that the recreation of the system was sufficiently achieved in the phantom, and suggesting that perhaps the brain-skull tethering does not need to be recreated in a phantom to simulate PBS.

Ultimately, the study showed the phantom to be a useful research tool in the research of PBS. A large collection of data was collected with it which would have been otherwise difficult to achieve through *in vivo* measurement and it allowed for two novel suggestions to be made. These are that:

1. Clinically significant brain shift takes place across all transitions.
2. There is clinically significant variability between the brain shift patterns of individual transitions at the local level.

These have important implications for the planning of high precision neurosurgery and reinforce the value of the phantom and PBS dataset produced here.

With the aims of the project met (see next sections), the next and final chapter provides a conclusion to thesis.

10 CONCLUSIONS

10.1 Project Conclusions

This project was concerned with, a) the development of a phantom for the simulation of positional brain shift and, b) the generation of novel data to aid targeting error mitigation in neurosurgery. As stated at the start of the thesis, the aims of this project were to:

1) *Develop a geometrically and mechanically realistic (biofidelic), imageable phantom of the brain-skull system that is capable of simulating the positional brain shift event.*

2) *Develop an apparatus for the orientation of the phantom in MRI/CT environments.*

3) *Generate brain shift data for a representative range of the spectrum of possible positional transitions in neurosurgery.*

4) *Compare and contrast brain shift data captured by the phantom to that produced in the literature and the emerging data being produced by the in vivo and in silico routes.*

10.1.1 Meeting the First and Second Project Aims

The first aim was by far the most difficult to achieve since there was no real blueprint in the literature for the building of a geometrically and mechanically realistic (biofidelic) model of the entire brain-skull system. There were established techniques for the recreation of some parts of the system, but not for all parts, and certainly not for the assembly of all elements together into the larger mechanical system. Therefore, the development of a PBS phantom presented as a novel, but challenging, endeavour.

An assessment of the anatomical features necessary to produce a PBS simulating phantom resulted in a feature set much more extensive than that found for previous phantoms. This importantly included the geometrically complex brain-skull tethering and, consequently, a novel fabrication workflow was sought for the construction of a tethered model. This was identified as being necessary due to the recognized impossibility of separately producing the model parts and assembling them together.

A potential fabrication route was identified which consisted of a combination of multi-material 3D printing and *in situ* brain casting. Here, it was identified that a majority of the model's parts could be 3D printed in a single build (skull, dural septa and PAC), followed by the subsequent casting of the brain part into the printed part. In fleshing out the design, however, two problems were encountered. The first was that the brain would have to be made out of an unideal silicone material (due to casting requirements), while the second was that the pia would have to be made unrealistically thick (due to printing limitations).

It was theorized that these design limitations might result in too little non-rigid brain shift occuring in the model, due to the thick pia creating an over stiff brain boundary and the silicone brain not having the correct low strain rate loading response. However, it was not clear that omitting the tethering would be overall beneficial since the brain then becomes completely free to move in and out of the SAS. It was identified, that in this situation, there would be a counter risk of too much rigid displacement occurring instead.

With this uncertainty in mind, it was decided that a secondary non-tethered model would be designed, with the aim to build both and compare their PBS simulating capacity. Without the PAC to act as the mould for the brain in this model, it was identified that a novel elaborate workflow needed to be designed for the separate production and subsequent assembly of individual parts.

A novel workflow was designed for the casting of a geometrically and mechanically realistic brain in the biofidelic CH material, and its subsequent assembly into a larger model comprising hydrogel brain, elastomer dural septa, deionised water CSF and rigid plastic skull. This model contained no pia-like brain boundary or brain skull tethering.

Unfortunately, when it came to fabricating the tethered model, it was discovered that there were significant fragility issues with the Skull-DS-PAC when fabricated with Polyjet printing. Given that no other way of fabricating the model than the *in situ* casting method could be identified and that the Polyjet technology presented as the only multi-material technology capable of printing the Skull-DS-PAC part, it was decided that the development of the tethered model would be discontinued. It was identified, however, that the design would likely be buildable in the future, with even the entire model perhaps being printable if sufficiently versatile multi-material printers were to be developed.

Unlike the tethered model design, the non-tethered model design was found to be entirely fabricable, albeit with a few changes required in the part and workflow designs. This model (hereafter “the phantom” again) included:

1. The entire brain (cerebrum, cerebellum and brain stem), complete with medial longitudinal fissure, transverse cerebral fissure and fluid filled ventricles.
2. The falx cerebri and tentorium cerebelli (dural septa).
3. The entire fluid filled SAS.
4. The entire neurocranium.

Although not particularly surprising given the identified effect of thaw rate on freeze-thaw hydrogel stiffness and the unique thawing profile employed in the phantom’s brain fabrication workflow, the starting CH formulation identified from the literature was found to

be overly stiff. A new hydrogel formulation was consequently developed, which brought the loading response of the hydrogel in line with reports for brain tissue. However, the density of this formulation was found to be much lower than that of the anatomical brain and, when paired with the deionised water CSF, created a density differential much lower than that found in the anatomy. It was identified that this would probably result in lower levels of brain shift in PBS simulation, yet, it was decided that this would be confirmed first before implementing further changes.

Before the PBS simulation capability of the phantom could be assessed, however, a brain shift measurement system needed to be developed and a phantom orientating cradle needed to be built for accurate positioning of the phantom with respect to gravity (second aim). An MR and CT compatible cradle which allowed for the positioning of the phantom around the sagittal and coronal axes at 15 degree intervals was built and a glass bead delivery method was developed and integrated into the brain's fabrication workflow for the positioning of 44 glass beads, pseudo-symmetrically into the brain with decent regional coverage. This marker set was found to function well when paired with CT imaging as the brain shift imaging modality, as both the segmentation of the markers and the registration of differently orientated phantom scans was found to be highly accurate and reliable.

Ready for brain shift measurement, the simulation capability of the phantom was next assessed by simulating the supine to prone brain shift event and comparing the measured brain shift (imaged with CT) to that reported in the literature. As predicted, the brain shift that manifested was unrealistically small. To bring the brain shift in line with literature accounts, a new formulation was developed which was approximately half as stiff and created a brain with a higher density that approximately doubled the submerged weight produced by the initial formulation. Use of this formulation was found to produce realistic levels of brain shift and, at this stage, the phantom was considered to be validated enough to produce novel PBS data for previously unstudied positional transitions.

This achievement marked the fulfilment of the first and second aims of the project.

10.1.2 Meeting the Third and Fourth Project Aims

To meet the third and fourth aims, a study was next performed with the phantom, wherein brain shift was measured upon repositioning from the supine position to eight non-supine positions. This study was designed to produce a novel comprehensive dataset for a discrete representation of the continuous spectrum of possible positional transitions in neurosurgery.

The study covered a much broader range of positional transitions (8) than those featured in the literature *in vivo* studies (1-2 in each study), producing 8 unique PBS displacement maps. Except for a small right-left asymmetry due to accidental air inclusion in the study phantom, the PBS measured for shared transitions was found to be largely in agreement

with the literature studies and the emerging measurements from the concurrent *in vivo* and *in silico* projects. For the novel transitions, an expected pattern and magnitude of brain shift was observed, indicating validity in the measurements. Overall, this suggested that a good approximation of the mechanical system had been achieved in the phantom and that perhaps the brain-skull tethering was not as critical as originally theorized.

The air present in the study phantom was only 4 ml in volume, but was still seen to have a sizeable effect on the brain shift. Comparisons to the *in silico* and *in vivo* project data, however, showed the effect of the air to be a largely subtractable element of additional rigid shift. The shift measured from the phantom, *in silico* and *in vivo* projects was otherwise found to be in agreement and so the data collected was not considered to be particularly tarnished by the presence of the air. It was recognized, however, that it would be beneficial to repeat the measurements of the study with a number of separate air-free phantoms. Yet, to do this, the air contamination problem would need to be solved first and it is not obvious how such small air volumes could be prevented given the level of manipulation required to assemble the phantom.

With only a small asymmetric rigid enhancement of shift, the presence of air also did not change the key suggestions by the data, which are that:

1. Clinically significant brain shift takes place across all transitions.
2. There is clinically significant variability between the brain shift patterns of individual transitions at the local level.

These novel findings further highlight the need for the consideration of PBS in surgical planning and strongly suggest that versatile parametric software are likely needed to account for the variable shifting of neurosurgical targets.

In conclusion, this work has allowed for novel insights into a problematic event otherwise difficult to study in humans. The biofidelic phantom developed is unique, with no parallel to be found in the literature at the time of writing, and presents as a significant advancement in the field of phantom technology.

10.2 Future Work

The immediate work that should be taken with the phantom is to address the air contamination problem. However, it is unclear how this problem could be easily solved as the traditional vacuum systems do not provide the access needed to manipulate the parts together in assembly. Yet, one possible solution might be to apply vibration to the water filled bucket containing the unassembled brain, dural septa and skull parts in order to free small hidden air volumes held on the surface or in crevices. This avoids the problems of trying to remove the air once assembled, which seems to be inherently problematic. With the air problem solved, it would then be useful to repeat the set of simulations made in the study a number of times with different phantoms to gain a greater sense of both the repeatability and to better understand the effect of air in the phantom.

Beyond this, there is scope for further development of the phantom for PBS. The marker system, for example could be refined to obtain an even greater coverage of brain shift and additional features such as the tumour/cyst volumes could be incorporated into the brain to study how such masses affect the PBS pattern. Ultimately, many avenues could be taken.

Given that the CH material has been shown to be capable of simulating the mechanical response of brain tissue to cutting [57] and penetration [166], the phantom could potentially also be used to assess the deformation of the brain due to surgical implement insertion forces and the anchoring by previously inserted implements (e.g. catheters). This is particularly of interest in bilateral electrode implantation surgeries wherein electrodes are implanted sequentially. Yet, before the phantom could be used in this way, the appropriate properties would need to be confirmed in the sugar formulation (SF) developed here.

Application of the phantom to function as a stereotactic surgical practice tool is also a possible avenue. Addition of extra features to optimally recreate the feel of the procedure, such as an external skin/fat layer or more realistic drilling properties for the skull, may need to be developed, but again this should not present as substantial work for a majority of cases.

There is also great opportunity for further research with the phantom in areas such as traumatic brain injury (TBI), for which ethical *in vivo* measurements cannot be obtained. The phantom is currently lacking the brain tethering and bridging vessels which are believed to play a significant role in the mechanics of TBI, however, the phantom could still be used to produce an assessment of the influence of the feature, by virtue of not having it. Tailoring of the phantom (e.g. brain mechanical properties) may be necessary to apply it outside of PBS, but with the general system developed, this should not present as substantial work for a majority of cases.

Yet, finding a way to better control the density of the hydrogel so that the stiffness can be varied independently is critical to the adaption of the phantom beyond PBS. A number of additives were tried, however, most seemed to adversely affect the gelation of the hydrogel, while even small amounts of compatible additives, such as sugar, significantly softened the gel with only a miniscule increase in density. A possible method of increasing the density would be to develop and incorporate a heavy atom tagged PVA polymer, which would increase the mass of the hydrogel and not diffuse out like some additives. However, the chemical dynamics of hydrogels are complex and it is unclear how easy this would be to achieve.

11 REFERENCES

1. Peerlings J, Compter C, Janssen F, Wiggins CJ, Postma AA, Mottaghy FM, Lambin P, Hoffmann AL. Characterizing geometrical accuracy in clinically optimised 7T and 3T magnetic resonance images for high-precision radiation treatment of brain tumours. Phys Imaging Radiat Oncol. 2019;9:35-42.

2. Lee PS, Weiner GM, Corson D, Kappel J, Chang YF, Suski VR, Berman SB, Homayoun H, Van Laar AD, Crammond DJ, Richardson RM. Outcomes of Interventional-MRI Versus Microelectrode Recording-Guided Subthalamic Deep Brain Stimulation. Front Neurol. 2018;9:241.

3. Herculano-Houzel S. The glia/neuron ratio: how it varies uniformly across brain structures and species and what that means for brain physiology and evolution. Glia. 2014;62(9):1377-1391.

4. Sing V. Textbook of Clinical Neuroanatomy. 2nd ed. New Delhi: Elsevier; 2010.

5. Areas of the Brain and their Functions [Internet]. btbuddies.co.uk. [updated 2011; cited 10/06/2016]. Available from: http://www.btbuddies.org.uk/about-high-grade-brain-tumours/areas-of-the-brain-and-their-functions.htmll

6. Brain Facts and Figures [Internet]. Washington.edu. [date of last update unknown; cited 13/06/2016]. Available from: https://faculty.washington.edu/chudler/facts.html

7. Gur RC, Turetsky BI, Matsui M, Yan M, Bilker W, Hughett P, Gur RE. Sex differences in brain gray and white matter in healthy young adults: correlations with cognitive performance. J Neurosci. 1999;19(10):4065-4072.

8. Kopell BH, Greenberg BD. Anatomy and physiology of the basal ganglia: implications for DBS in psychiatry. Neurosci Biobehav Rev. 2008;32(3):408-422.

9. Education. Whats an MRI [Internet]. Barts MS. [updated 2015; cited 02/06/2016]. Available from: http://multiple-sclerosis-research.blogspot.com/2015/01/education-whats-mri.html

10. Ribas GC. The cerebral sulci and gyri. Neurosurg Focus. 2010;28(2):E2.

11. Axer H, Leunert M, Mürköster M, Grässel D, Larsen L, Griffin LD, Graf v Keyserlingk D. A 3D fiber model of the human brainstem. Comput Med Imaging Graph. 2002;26(6):439-444.

12. Voogd J, Glickstein G. The anatomy of the cerebellum. Trends in Cognitive Sciences.1998;2(9):307-313.

13. Brain Diagrams [Internet]. Brain Diagrams. [updated 2016; cited 08/06/2016]. Available from: http://braindiagram.blogspot.co.uk/

14. The Brain: Lower-Level Brain Structures [Internet]. Cognitive Consonance. [updated 2015; cited 08/06/2016]. Available from: http://cognitiveconsonance.info/2012/08/22/the-brain-lower-level-brain-structures/

15. Nervous System [Internet]. Biology4ISC. [date of last update unknown; cited 08/06/2016]. Available from: http://biology4isc.weebly.com/nervous-system.html

16. Central Nervous System [Internet]. Highlands.edu. [date of last update unknown; cited 23/03/2016]. Available from: http://www.highlands.edu/academics/divisions/scipe/biology/faculty/harnden/2121/notes/cns.html

17. Chapter 14: Cerebrospinal Fluid. Neuropathology. [updated 2013; cited 13/06/2016]. Available from: http://neuropathology-web.org/chapter14/chapter14CSF.html

18. Sakka G, Coll J. Chazal. Anatomy and physiology of cerebrospinal fluid. European Annals of Otorhinolaryngology: Head and Neck Diseases. 2011;128(6):309-316.

19. Engelhardt E. Magendie and Luschka: Holes in the 4th ventricle. Dement Neuropsychol. 2016;10(3):254-258.

20. Why is neuromyelitis optica (NMO) endlessly surprising neurology? [Internet]. The Neurology Lounge. [date of last update unknown; cited 12/06/2016]. Available from: https://theneurologylounge.com/category/not-to-miss-differentials/

21. Scahill RI, Frost C, Jenkins R, Whitwell JL, Rossor MN, Fox NC. A longitudinal study of brain volume changes in normal aging using serial registered magnetic resonance imaging. Arch Neurol. 2003;60(7):989-994.

22. Chilamkurthy S, Rao P, Maragkos G, Thomas A. Morphology of the Brain: Changes in Ventricular and Cranial Vault Volumes in 15000 subjects with Aging and Hydrocephalus [Internet]. Qure.ai Blog. [updated 2019; cited 26/09/2019]. Available from: http://blog.qure.ai/notes/brain-morphology-changes-in-ventricular-cranial-vault-volumes-with-aging

23. Frydrychowski AF, Szarmach A, Czaplewski B, Winklewski PJ. Subarachnoid Space: New Tricks by an Old Dog. PLoS ONE. 2012;7(5):e37529.

24. Saboori P, Sadegh A. Histology and Morphology of the Brain Subarachnoid Trabeculae. Anat Res Int. 2015; 279814.

25. Neurohistology ATLAS [Internet]. Veterinary Anatomy. [date of last update unknown; cited 10/06/2016]. Available from: http://vanat.cvm.umn.edu/neurHistAtls/pages/men1.html

26. Haines DE, Harkey HL, al-Mefty O. The "subdural" space: a new look at an outdated concept. Neurosurgery. 1993;32(1):111-120.

27. Zwirner J, Scholze M, Waddell JN, Ondruschka B, Hammer N. Mechanical Properties of Human Dura Mater in Tension - An Analysis at an Age Range of 2 to 94 Years. Sci Rep. 2019;9(1):16655.

28. Aydin HE, Kizmazoglu C, Kaya I, Husemoglu B, Sozer G, Havitcioglu H, Arslantas A. Biomechanical Properties of the Cranial Dura Mater with Puncture Defects : An In Vitro Study. J Korean Neurosurg Soc. 2019;62(4):382-388.

29. Reina MA, Prats-Galino A, Sola RG, Puigdellívol-Sánchez A, Arriazu Navarro R, De Andrés JA. [Structure of the arachnoid layer of the human spinal meninges: a barrier that regulates dural sac permeability]. Rev Esp Anestesiol Reanim. 2010;57(8):486-492. Spanish.

30. Weller RO. Microscopic morphology and histology of the human meninges. Morphologie. 2005;89(284):22-34.

31. Killer HE, Laeng HR, Flammer J, Groscurth P. Architecture of arachnoid trabeculae, pillars, and septa in the subarachnoid space of the human optic nerve: anatomy and clinical considerations. Br J Ophthalmol. 2003;87(6):777-781.

32. Saboori P, Sadegh A. Histology and Morphology of the Brain Subarachnoid Trabeculae. Anat Res Int. 2015;1-9.

33. Scott G, Coats B. Microstructural Characterization of the Pia-Arachnoid Complex Using Optical Coherence Tomography. IEEE Trans Med Imaging. 2015;34(7):1452-1459.

34. Hartmann K, Stein K, Neyazi B, Sandalcioglu I. First in vivo visualization of the human subarachnoid space and brain cortex via optical coherence tomography. Therapeutic Advances in Neurological Disorders. 2019;12:175628641984304.

35. Talbert D. Brain Motion under Sub-Traumatic Impact. Anat Physiol. 2016;6:1.

36. Neuroanatomy Video Lab: Brain Dissections [Internet]. University of Utah. [updated 2019; cited 24/04/2019]. Available from: https://neurologicexam.med.utah.edu/adult/html/brain-dissections.html

37. Julio Pereira – Neurocirurgião [YouTube Channel]. Microsurgery for Brain Aneurysm (sylvian fissure dissection) [Video Title]. Accessed on [24/04/2019] through: https://www.youtube.com/watch?v=GVe0p64VjTM

38. Kayalioglu G. The vertebral column and spinal meninges. In: Watson C, Paxinos G, Kayalioglu G. The spinal cord. Cambridge (MA): Elsevier; 2009.17-36.

39. Rice JK, Rorden C, Little JS, Parra LC. Subject position affects EEG magnitudes. Neuroimage. 2013;64:476-484.

40. Bechmann I, Galea G, Perry VH. What is the blood–brain barrier (not)? Trends Immunol. 2007;28(1):5-11.

41. Demes B. Mechanical Functions of the Dura Mater. In: Demes B. Biomechanics of the Primate Skull Base. 1st ed. Springer Berlin Heidelberg; 1985.14-15.

42. Wood H. Physiology, Pharmacology, and Dynamics of Cerebrospinal Fluid. In: Wood H. Neurobiology of Cerebrospinal Fluid 1. 1st ed. New York: Plenum Press; 1980.1-16.

43. Brain Ventricular System [Internet]. ABC Radiology. [date of last update unknown; cited 04/06/2016]. Available from: http://abcradiology.blogspot.co.uk/2011_12_28_archive.html

44. Chapter 15 - The Brain [Internet]. droualb.edu. [date of last update unknown; cited 05/06/2016]. Available from: https://droualb.faculty.mjc.edu/Lecture%20Notes/Unit%205/chapter_15_the_brain%20Spring%2007with%20figures.htm

45. “Craniosacral Therapy in Health and Disease [Internet]. Positive Health. [updated 2015; cited 01/06/2016]. Available from: http://www.positivehealth.com/article/craniosacral-therapy/craniosacral-therapy-in-health-and-disease

46. Ventricular system of the brain [Internet]. Human Physiology Academy. [date of last update unknown; cited 17/11/2019]. Available from: http://humanphysiology.academy/Neurosciences%202015/Chapter%203/A.3.2p%20Ventricles%20and%20Vessels.html

47. Interior of Cranium [Internet]. Duke Medicine. [updated 2014; cited 07/06/2016]. Available from: https://web.duke.edu/anatomy/lab19/lab19.html

48. Wolthuis R, van Aken M, Fountas K, Robinson JS Jr, Bruining HA, Puppels GJ. Determination of water concentration in brain tissue by Raman spectroscopy. Anal Chem. 2001;73(16):3915-3920.

49. Kovacs G, Berghold A, Scheidl S, Olschewski H. Pulmonary arterial pressure during rest and exercise in healthy subjects: a systematic review. Eur Respir J. 2009;34(4):888-894.

50. Chatelin S, Constantinesco A, Willinger R. Fifty years of brain tissue mechanical testing: from in vitro to in vivo investigations. Biorheology. 2010;47(5-6):255-276.

51. Bilston LE. Brain Tissue Mechanical Properties. In: Miller K. (eds) Biomechanics of the Brain. Biological and Medical Physics, Biomedical Engineering. New York: Springer; 2011.69-89.

52. Budday S, Ovaert TC, Holzapfel GA, Steinmann P, Kuhl E. Fifty Shades of Brain: A Review on the Mechanical Testing and Modelling of Brain Tissue. Arch Computat Methods Eng. 2019:1-44.

53. Budday S, Nay R, de Rooij R, Steinmann P, Wyrobek T; Ovaert TC; Kuhl E. Mechanical properties of gray and white matter brain tissue by indentation. J Mech Behav Biomed Mater. 2015;46:318-330.

54. Christ AF, Franze K, Gautier H, Moshayedi P, Fawcett J, Franklin RJ, Karadottir RT, Guck J. Mechanical difference between white and gray matter in the rat cerebellum measured by scanning force microscopy. J Biomech. 2010;43(15):2986-2992.

55. van Dommelen JA, van der Sande TP, Hrapko M, Peters GW. Mechanical properties of brain tissue by indentation: interregional variation. J Mech Behav Biomed Mater. 2010;3(2):158-66.

56. Kaster T, Sack I, Samani A. Measurement of the hyperelastic properties of ex vivo brain tissue slices. J Biomech. 2011;44(6):1158-1163.

57. Forte AE, Galvan S, Manieri F, Rodriguez y Baena F, Dini D. A composite hydrogel for brain tissue phantoms. Materials and Design. 2016;112:227-238.

58. Singh D, Boakye-Yiadom S, Cronin DS. Comparison of porcine brain mechanical properties to potential tissue simulant materials in quasi-static and sinusoidal compression. J Biomech. 2019;92:84-91.

59. Jin X, Zhu F, Mao H, Shen M, Yang KH. A comprehensive experimental study on material properties of human brain tissue. J Biomech. 2013;46(16):2795-2801.

60. Murphy MC, Jones DT, Jack CR Jr, Glaser KJ, Senjem ML, Manduca A, Felmlee JP, Carter RE, Ehman RL, Huston J. Regional brain stiffness changes across the Alzheimer's disease spectrum. Neuroimage Clin. 2015;10:283-290.

61. ElSheikh M, Arani A, Perry A, Boeve BF, Meyer FB, Savica R, Ehman RL, Huston J. MR Elastography Demonstrates Unique Regional Brain Stiffness Patterns in Dementias. AJR Am J Roentgenol. 2017;209(2):403-408.

62. Takamura T, Motosugi U, Sasaki Y, Kakegawa T, Sato K, Glaser KJ, Ehman RL, Onishi H. Influence of Age on Global and Regional Brain Stiffness in Young and Middle-Aged Adults. J Magn Reson Imaging. 2019. [Epub ahead of print] doi: 10.1002/jmri.26881

63. MacManus DB, Pierrat B, Murphy JG, Gilchrist MD. Region and species dependent mechanical properties of adolescent and young adult brain tissue. Sci Rep. 2017;7(1):13729.

64. Barber TW, Brockway JA, Higgins LS. The density of tissues in and about the head. Acta Neurol Scandinav. 1970;46:86-92.

65. Faas FH, Ommaya AK. Brain tissue electrolytes and water content in experimental concussion in the monkey. J Neurosurg. 1968;28(2):137-144.

66. Rouessle R, Roulet F. Mass und Zahl in der Pathologie. Pathologie und Klinik in Einzeldarstellungen. Berlin und Wien. Verlag yon Julius Springer.1932: 87.

67. Sankey. On the specific gravity of the brain. Brit Med Chir Review. 1853:240-257.

68. DiResta GR, Lee J, Lau N, Ali F, Galicich JH, Arbit E. Measurement of brain tissue density using pycnometry. Acta Neurochir Suppl (Wien). 1990;51:34-36.

69. Degos V, Lescot T, Zouaoui A, Hermann H, Préteux F, Coriat P, Puybasset L. Computed tomography-estimated specific gravity of noncontused brain areas as a marker of severity in human traumatic brain injury. Anesth Analg. 2006;103(5):1229-1236.

70. Ebrahimi AP. Mechanical properties of normal and diseased cerebrovascular system. J Vasc Interv Neurol. 2009;2(2):155-162.

71. Trudnowski RJ, Rico RC. Specific gravity of blood and plasma at 4 and 37 degrees C. Clin Chem. 1974;20(5):615-616.

72. Harteveld AA, Denswil NP, Van Hecke W, Kuijf HJ, Vink A, Spliet WG, Daemen MJ, Luijten PR, Zwanenburg JJ, Hendrikse J, van der Kolk AG. Data on vessel wall thickness measurements of intracranial arteries derived from human circle of Willis specimens. Data Brief. 2018;19:6-12.

73. Reinstrup P, Ryding E, Ohlsson T, Dahm PL, Uski T. Cerebral Blood Volume (CBV) in Humans during Normo- and Hypocapnia: Influence of Nitrous Oxide (N2O). Anesthesiology. 2001;95(5):1079-1082.

74. Duvernoy HM, Delon S, Vannson JL. Cortical blood vessels of the human brain. Brain Res Bull. 1981;7(5):519-579.

75. Levin E, Muravchick S, Gold MI. Density of normal human cerebrospinal fluid and tetracaine solutions. Anesth Analg. 1981;60(11):814-817.

76. Lui AC, Polis TZ, Cicutti NJ. Densities of cerebrospinal fluid and spinal anaesthetic solutions in surgical patients at body temperature. Can J Anaesth. 1998;45(4):297-303.

77. Schiffer E, Van Gessel E, Gamulin Z. Influence of sex on cerebrospinal fluid density in adults. Br J Anaesth. 1999;83(6):943-944.

78. Jin X, Lee JB, Leung LY, Zhang L, Yang KH, King AI. Biomechanical response of the bovine pia-arachnoid complex to tensile loading at varying strain-rates. Stapp Car Crash J. 2006;50:637-649.

79. Jin X, Ma C, Zhang L, Yang KH, King AI, Dong G, Zhang J. Biomechanical response of the bovine pia-arachnoid complex to normal traction loading at varying strain rates. Stapp Car Crash J. 2007;51:115-126.

80. Jin X, Yang KH, King AI. Mechanical properties of bovine pia-arachnoid complex in shear. J Biomech. 2011;44(3):467-74.

81. Jin X, Mao H, Yang KH, King AI. Constitutive modelling of pia-arachnoid complex. Ann Biomed Eng. 2014;42(4):812-821.

82. Natividad GC, Theodossiou S, Schiele NR, Murdoch G, Burla G, Potirniche G, Martin BA. Biomechanical characterization of ovine pia arachnoid complex. Summer Biomechanics, Bioengineering and Biotransport Conference. 25-28/06/2019.

83. Fabris G, M Suar Z, Kurt M. Micromechanical heterogeneity of the rat pia-arachnoid complex. Acta Biomater. 2019: pii: S1742-7061(19)30665-8.

84. Aimedieu P, Grebe R. Tensile strength of cranial pia mater: preliminary results. J Neurosurg. 2004;100(1):111-114.

85. Aydin HE, Kizmazoglu C, Kaya I, Husemoglu B, Sozer G, Havitcioglu H, Arslantas A. Biomechanical Properties of the Cranial Dura Mater with Puncture Defects : An In Vitro Study. J Korean Neurosurg Soc. 2019;62(4):382-388.

86. Wolfinbarger L Jr, Zhang YX, Adam BLT, Homsi D, Gates K, Sutherland V. Biomechanical aspects on rehydrated freeze-dried human allograft dura-mater tissues. J Appl Biomater. 1994;5:265-270.

87. McGarvey KA, Lee JM, Boughner DR. Mechanical suitability of glycerol preserved human dura mater for construvction of prosthetic cardiac valves. Biomaterials 1984;5:109-117.

88. van Noort R, Black MM, Martin TR, Meanley S. A study of the uniaxial mechanical properties of human dura mater preserved in glycerol. Biomaterials 1981;2:41-45.

89. Peterson J, Dechow PC. Material properties of the human cranial vault and zygoma. Anat Rec A Discov Mol Cell Evol Biol. 2003;274(1):785-97.

90. Grover VPB, Tognarelli JM, Crossey ME, Cox IJ, Taylor-Robinson SD, McPhail MJW. Magnetic Resonance Imaging: Principles and Techniques: Lessons for Clinicians. J Clin Exp Hepatol. 2015;5(3):246-255.

91. Goldman L. Principles of CT and CT Technology. Journal of Nuclear Medicine Technology. 2007;35(3):115-128.

92. Kim du S, Kong MH, Jang SY, Kim JH, Kang DS, Song KY. The usefulness of brain magnetic resonance imaging with mild head injury and the negative findings of brain computed tomography. J Korean Neurosurg Soc. 2013;54(2):100-106.

93. Neumann JO, Giese H, Biller A, Nagel AM, Kiening K. Spatial Distortion in MRI-Guided Stereotactic Procedures: Evaluation in 1.5-, 3- and 7-Tesla MRI Scanners. Stereotact Funct Neurosurg. 2015;93:380-386.

94. Fitzpatrick JM. The role of registration in accurate surgical guidance. Proc Inst Mech Eng H. 2010;224(5):607-622.

95. Blanchet L, Krooshof PW, Postma GJ, Idema AJ, Goraj B, Heerschap A, Buydens LM. Discrimination between metastasis and glioblastoma multiforme based on morphometric analysis of MR images. AJNR Am J Neuroradiol. 2011;32(1):67-73.

96. Cauley KA, Ratkovits B, Braff SP, Linnell G. Communicating hydrocephalus after gamma knife radiosurgery for vestibular schwannoma: an MR imaging study. AJNR Am J Neuroradiol. 2009;30(5):992-994.

97. Maugeri R, Anderson DG, Graziano F, Meccio F, Visocchi M, Iacopino DG. Conservative vs. Surgical Management of Post-Traumatic Epidural Hematoma: A Case and Review of Literature. Am J Case Rep. 2015;16:811-817.

98. Arachnoid cyst [Internet]. Radiopaedia. [date of last update unknown; cited 28/10/2019]. Available from: https://radiopaedia.org/cases/arachnoid-cyst-27

99. Surgery to remove your brain tumour [Internet]. Cancer Research UK. [updated 2015; cited 29/10/2019]. Available from: https://www.cancerresearchuk.org/about-cancer/brain-tumours/treatment/surgery/remove-brain-tumour

100. NCI Dictionary of Cancer Terms [Internet]. Cancer.gov. [date of last update unknown; cited 29/10/2019]. Available from: https://www.cancer.gov/publications/dictionaries/cancer-terms/def/craniotomy

101. Li Z, Zhang J G, Ye Y, Li X. Review on Factors Affecting Targeting Accuracy of Deep Brain Stimulation Electrode Implantation between 2001 and 2015. Stereotact Funct Neurosurg. 2016;94:351-362.

102. Dormont D, Cornu P, Pidoux B, Bonnet AM, Biondi A, Oppenheim C, Hasboun D, Damier P, Cuchet E, Philippon J, Agid Y, Marsault C. Chronic thalamic stimulation with three-dimensional MR stereotactic guidance. AJNR Am J Neuroradiol. 1997;18(6):1093-1107.

103. Gomez H, Barnett G, Estes M, Palmer J, Magdinec M. Stereotactic and computer-assisted neurosurgery at the Cleveland Clinic: review of 501 consecutive cases. Cleveland Clinic Journal of Medicine. 1993;60(5):399-410.

104. Guo Z, Leong MC, Su H, Kwok KW, Chan DT, Poon WS. Techniques for Stereotactic Neurosurgery: Beyond the Frame, Toward the Intraoperative Magnetic Resonance Imaging-Guided and Robot-Assisted Approaches. World Neurosurg. 2018;116:77-87.

105. Neudorfer C, Hunsche S, Hellmich M, El Majdoub F, Maarouf M. Comparative study of robot-assisted versus conventional frame-based deep brain stimulation stereotactic neurosurgery. Stereotact Funct Neurosurg. 2018;96(5):327-334.

106. “Leksell® Vantage™ Stereotactic System” [Internet]. Elekta.com. [date of last update unknown; cited 17/11/2019]. Available from: https://www.elekta.com/neurosurgery/leksell-vantage-stereotactic-system/

107. Zanotto V, Boscariol P, Gasparetto A, Lanzutti A, Vidoni R, Di Lorenzo N et al. A Master-Slave Haptic System for Neurosurgery. Appl Bionics Biomech. 2011;8(2):209-220.

108. Pappas EP, Alshanqity M, Moutsatsos A, Lababidi H, Alsafi K, Georgiou K, Karaiskos P, Georgiou E. MRI-Related Geometric Distortions in Stereotactic Radiotherapy Treatment Planning: Evaluation and Dosimetric Impact. Technol Cancer Res Treat. 2017;16(6):1120-1129.

109. Risholm P, Golby AJ, Wells W 3rd. Multimodal image registration for preoperative planning and image-guided neurosurgical procedures. Neurosurg Clin N Am. 2011;22(2):197–viii.

110. Batista PD, Machado IP, Roios P, Lavrador J, Cattoni M, Martins J, Carvalho H. Position and Orientation Errors in a Neuronavigation Procedure: A Stepwise Protocol Using a Cranial Phantom. World Neurosurgery.2019;126:e342-e350.

111. Miyagi Y, Samura K, Kishimoto and Chen X. Supine Position for the Prevention of Brain Shift in DBS Surgery: Technical Note and Novel Hypothesis “Water in the Inverted Cup” Mechanism. Austin Neurosurg Open Access. 2015;2(1):1027.

112. Matias CM, Frizon LA, Asfahan F, Uribe JD, Machado AG. Brain shift and pneumocephalus assessment during frame-based deep brain stimulation implantation with intraoperative magnetic resonance imaging. Oper Neurosurg (Hagerstown). 2018;14(6):668-674.

113. Giller CA, Jenkins P. Some technical nuances for deep brain stimulator implantation. Interdisciplinary Neurosurgery. 2015;2(1):29-39.

114. Sasaki T, Agari T, Kuwahara K, et al. Efficacy of Dural Sealant System for Preventing Brain Shift and Improving Accuracy in Deep Brain Stimulation Surgery. Neurol Med Chir (Tokyo). 2018;58(5):199-205.

115. Bilger A, Bardinet E, Fernández-Vidal S, Duriez C, Jannin P, Cotin S, "Intra-operative registration for deep brain stimulation procedures based on a full physics head model", MICCAI 2014 Workshop on Deep Brain Stimulation Methodological Challenges-2nd edition, 2014.

116. Leibinger A, Burrows C, Oldfield MJ, Rodriguez Y Baena F. Tissue motion due to needle deflection. Conf Proc IEEE Eng Med Biol Soc. 2015:1873-1876.

117. Abolhassani N, Patel RV, "Deflection of a flexible needle during insertion into soft tissue", Annual International Conference of the IEEE Engineering in Medicine and Biology – Proceedings. 2006;1:3858-3861.

118. Sillay KA, Kumbier LM, Ross C, Brady M, Alexander A, Gupta A, Adluru N, Miranpuri GS, Williams JC. Perioperative brain shift and deep brain stimulating electrode deformation analysis: implications for rigid and non-rigid devices. Ann Biomed Eng. 2013;41(2):293-304.

119. Morishita T, Hilliard JD, Okun MS, Neal D, Nestor KA, Peace D, Hozouri AA, Davidson MR, Bova FJ, Sporrer JM, Oyama G, Foote KD. Postoperative lead migration in deep brain stimulation surgery: Incidence, risk factors, and clinical impact. PLoS One. 2017;12(9):e0183711.

120. van den Munckhof P, Contarino MF, Bour LJ, Speelman JD, de Bie RM, Schuurman PR. Postoperative curving and upward displacement of deep brain stimulation electrodes caused by brain shift. Neurosurgery. 2010;67(1):49-53.

121. Thulin CA, von Essen C, Zeuchner E. Displacements of brain due to positional changes during stereotactic operations. Confin Neurol. 1972;34(5):348-54.

122. Hill DLG, Maurer CR, Maciunas RJ, Barwise JA, Fitzpatrick JM, Wang MY. Measurement of intraoperative brain surface deformation under a craniotomy. Neurosurgery. 1998;43(3):514-26.

123. Schnaudigel S, Preul C, Ugur T, Mentzel HJ, Witte OW, Tittgemeyer M, Hagemann G. Positional brain deformation visualized with magnetic resonance morphometry. Neurosurgery. 2010;66(2):376-384.

124. Monea AG, Verpoest I, Vander Sloten J, Van der Perre G, Goffin J, Depreitere B. Assessment of relative brain-skull motion in quasistatic circumstances by magnetic resonance imaging. J Neurotrauma. 2012;29(13):2305-2317.

125. Mikkonen M, Laakso I. Effects of posture on electric fields of non-invasive brain stimulation. Phys Med Biol. 2019;64(6):065019.

126. Ji S, Zhu Q, Dougherty L, Margulies SS. In vivo measurements of human brain displacement. Stapp Car Crash J. 2004;48:227-37.

127. Ji S, Margulies SS. In vivo pons motion within the skull. J Biomech. 2007;40(1):92-9.

128. Rozet I, Vavilala MS. Risks and benefits of patient positioning during neurosurgical care. Anesthesiol Clin. 2007;25(3):631-53.

129. Lam AM. Management of positioning of the neurosurgical patient. European Journal of Anaesthesiology. 1998;15:27-28.

130. Clatterbuck R, Tamargo R. Surgical Positioning and Exposures for Cranial Procedures. In: Winn H, editor. Youmans Neurological Surgery. 5 ed. Philadelphia, Pennsylvania: Sounders Elsevier Inc. 2004:623-645.

131. Forte AE, Galvan S, Dini D. Models and tissue mimics for brain shift simulations. Biomech Model Mechanobiol. 2018;17(1):249-261.

132. Reinertsen I, Collins DL. A realistic phantom for brain-shift simulations. Med Phys. 2006 33(9):3234-40.

133. Puzrin A, Skrinjarb O, Ozanc C, Kimc S, Mukund S. Image guided constitutive modelling of the silicone brain phantom. SPIE. 2005;5744:157-164.

134. Mohammadi A, Ahmadian A, Azar AD, Sheykh AD, Amiri F, Alirezaie J. Estimation of intraoperative brain shift by combination of stereovision and Doppler ultrasound: phantom and animal model study. Int J Comput Assist Radiol Surg. 2015; 10(11): 1753-64.

135. Chen SJ, Hellier P, Gauvrit JY, Marchal M, Morandi X, Collins DL. An anthropomorphic polyvinyl alcohol triple-modality brain phantom based on Colin27. Med Image Comput Comput Assist Interv. 2010;13(2):92-100.

136. Navarro-Lozoya M, Kennedy M, Dean D, Rodriguez-Devora J. Development of phantom material that resembles compression properties of human brain tissue for training models. Materialia. 2019;8 100438.

137. Chen I, Ong RE, Simpson AL, Sun K, Thompson RC, Miga MI. Integrating Retraction Modelling Into an Atlas-Based Framework for Brain Shift Prediction. IEEE Trans Biomed Eng. 2013; 60(12):3494-3504.

138. Ma J, Wittek A, Singh S, Joldes G, Washio T, Chinzei K, Miller K. Evaluation of accuracy of non-linear finite element computations for surgical simulation: study using brain phantom. Comput Methods Biomech Biomed Engin. 2010;13(6):783-94.

139. DeLorenzo C, Papademetris X, Vives KP, Spencer DD, Duncan JS. A comprehensive system for intraoperative 3D brain deformation recovery. Med Image Comput Comput Assist Interv. 2007;10(2):553-561.

140. Bayer S, Wydra A, Zhong X, Ravikumar N, Strumia M, Schaffert R, Ostermeier M, Fahrig R, Maier A. An anthropomorphic deformable phantom for brain shift simulation. In: 2018 IEEE NSS/MIC Conference Record (2018).

141. Hassan C, Peppas N. Structure and Morphology of Freeze/Thawed PVA Hydrogels. Macromolecules. 2000;33(7):2472-2479.

142. Leibinger A, Forte AE, Tan Z, Oldfield MJ, Beyrau F, Dini D, Rodriguez Y Baena F. Soft Tissue Phantoms for Realistic Needle Insertion: A Comparative Study. Ann Biomed Eng. 2016;44(8):2442-52.

143. Zachary Reinstein [YouTube Channel]. “Brain Autopsy at Banner Sun Health Research Institute” [Video Title]. Accessed on [17/11/2019] through: https://www.youtube.com/watch?v=IFiyZalv2_E&t=390s

144. Tan Z, Parisi C, Di Silvio L, Dini D, Forte A. Cryogenic 3D Printing of Super Soft Hydrogels. Scientific Reports. 2017;7(1).

145. Digital Materials Data Sheet [PDF]. Stratasys. [date of last update unknown; cited 18/11/2019] Available from: https://www.axisproto.com/app/uploads/2018/03/Objet-Digital-Materials-Data-Sheets-.pdf

146. Meththananda IM, Parker S, Patel MP, Braden M. The relationship between Shore hardness of elastomeric dental materials and Young's modulus. Dent Mater. 2009;25(8):956-959.

147. Merck safety data sheet for “Pure Water Density Standard” [PDF]. [updated 2019; cited 18/11/2019]. Available from: https://www.sigmaaldrich.com/catalog/product/sial/denwat?lang=en&region=GB. [Accessed 18/11/2019].

148. ICBM 152 Nonlinear atlases version 2009 [Internet]. The McConnell Brain Imaging Centre. [updated 2014; cited 17/06/2018]. Available from: http://www.bic.mni.mcgill.ca/ServicesAtlases/ICBM152NLin2009

149. Cutini S, Scatturin P, Zorzi M. A new method based on ICBM152 head surface for probe placement in multichannel fNIRS. NeuroImage. 2011;54(2):919-927.

150. Huang Y, Parra L, Haufe S. The New York Head—A precise standardized volume conductor model for EEG source localization and tES targeting. NeuroImage. 2016;140:150-162.

151. Valdés-Hernández P, von Ellenrieder N, Ojeda-Gonzalez A, Kochen S, Alemán-Gómez Y, Muravchik C et al. Approximate average head models for EEG source imaging. J Neurosci Methods. 2009;185(1):125-132.

152. SOMSO Ventricular Cavities Of The Brain [Internet]. GT Simulators. [date of last update unknown; cited 29/04/2019]. Available from: https://www.gtsimulators.com/SOMSO-Ventricular-Cavities-of-the-Brain-p/bs24.htm

153. Pietroni N, Tarini M, Cignoni P. Almost Isometric Mesh Parameterization through Abstract Domains. IEEE Trans Vis Comput Graph. 2010;16:621-635.

154. Moore J, Williams C. Fatigue properties of parts printed by PolyJet material jetting. Rapid Prototyping Journal. 2015;21(6):675-685.

155. Multi-material 3D printing with silicones in Facial Prosthetics [Internet]. ACEO. [updated 07/11/2019; cited 20/01/2020]. Available from: https://www.aceo3d.com/aceo-multi-material-3d-printing-with-silicones-in-facial-prosthetics/

156. DuraForm® Flex Data Sheet [PDF]. 3D Systems [updated 2017; cited [19/11/2019]. Available from https://uk.3dsystems.com/materials/duraform-flex/tech-specs.

157. DuraForm® GF Data Sheet [PDF]. 3D Systems [updated 2017; cited [19/11/2019]. Available from https://uk.3dsystems.com/materials/duraform-gf/tech-specs.

158. Czerner M, Fellay L, Suárez M, Frontini P, Fasce L. Determination of Elastic Modulus of Gelatin Gels by Indentation Experiments. Procedia Materials Science. 2015;8:287-296.

159. Iravani A, Mueller J, Yousefi AM. Producing homogeneous cryogel phantoms for medical imaging: a finite-element approach. J Biomater Sci Polym Ed. 2014;25(2):181-202.

160. Ridgway JP. Gradient Echo Versus Spin Echo. In: Plein S, Greenwood J, Ridgway J. Cardiovascular MR Manual. Springer, Cham; 2015. 91-95.

161. Jafar M, Jafar YM, Dean C, Miquel ME. Assessment of Geometric Distortion in Six Clinical Scanners Using a 3D-Printed Grid Phantom. Journal of Imaging. 2017;3(3):28.

162. Sucrose compound summary [Internet]. Pubchem. [date of last update unknown; cited 20/11/2019]. Available from: https://pubchem.ncbi.nlm.nih.gov/compound/Sucrose.

163. Miyagi Y, Shima F, Sasaki T. Brain shift: an error factor during implantation of deep brain stimulation electrodes. J Neurosurg. 2007;107(5):989-997.

164. Toga T, Narr KL, Thompson PM, Luders E. Brain Asymmetry: Evolution. Encyclopedia of Neuroscience, Academic Press; 2009.303-311.

165. Yakovlevian brain torque: The Snelson tension twist [Internet]. cerebrovortex.com. [updated 2012; cited 21/11/2019]. Available from: https://cerebrovortex.com/2012/10/19/brain-torque/

166. Tan Z, Dini D, Rodriguez y Baena F, Forte A. Composite hydrogel: A high fidelity soft tissue mimic for surgery. Materials & Design. 2018;160:886-894.

12 APPENDIX A

Displayed in Figure A.1 is the Grasshopper path used for the generation of the CAD geometries involved in the fabrication of the brain moulds and inserts. It is presented here for completeness and to show the complexity of the workflow involved.

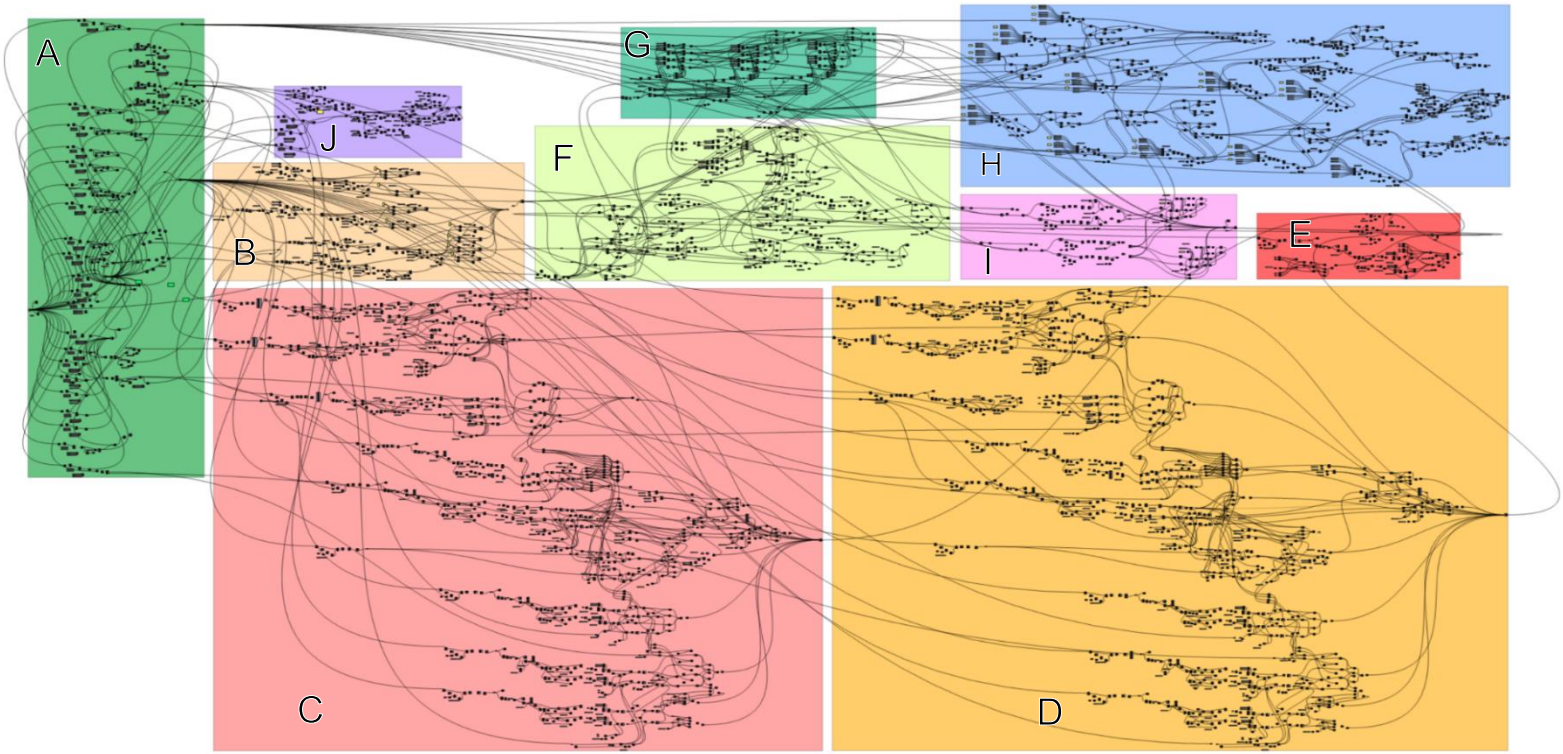

Figure A.1: Grasshopper path for the production of brain moulds and inserts. Block A builds the box construct and intersects it with the dilated brain mesh to generate the insert geometry; Block B builds the studs of the insert geometry; Block C builds the left hand components of the continuous ridge; Block D builds the right hand components of the continuous ridge; Block E builds components of the continuous ridge which connect the right and left components; Blocks F and G build the positive moulds using elements from blocks A to E; Blocks H and I build the mould inserts and the positive mould for the ventricle mould; Block J builds the thawing cap geometry. Entire path contains 4797 components.

13 **APPENDIX B**

Displayed in Figure B.1 is the Grasshopper path used for the generation of the CAD geometries involved in the fabrication of the skull, dural septa and phantom cradle parts. It is presented here for completeness and to show the complexity of the workflow involved.

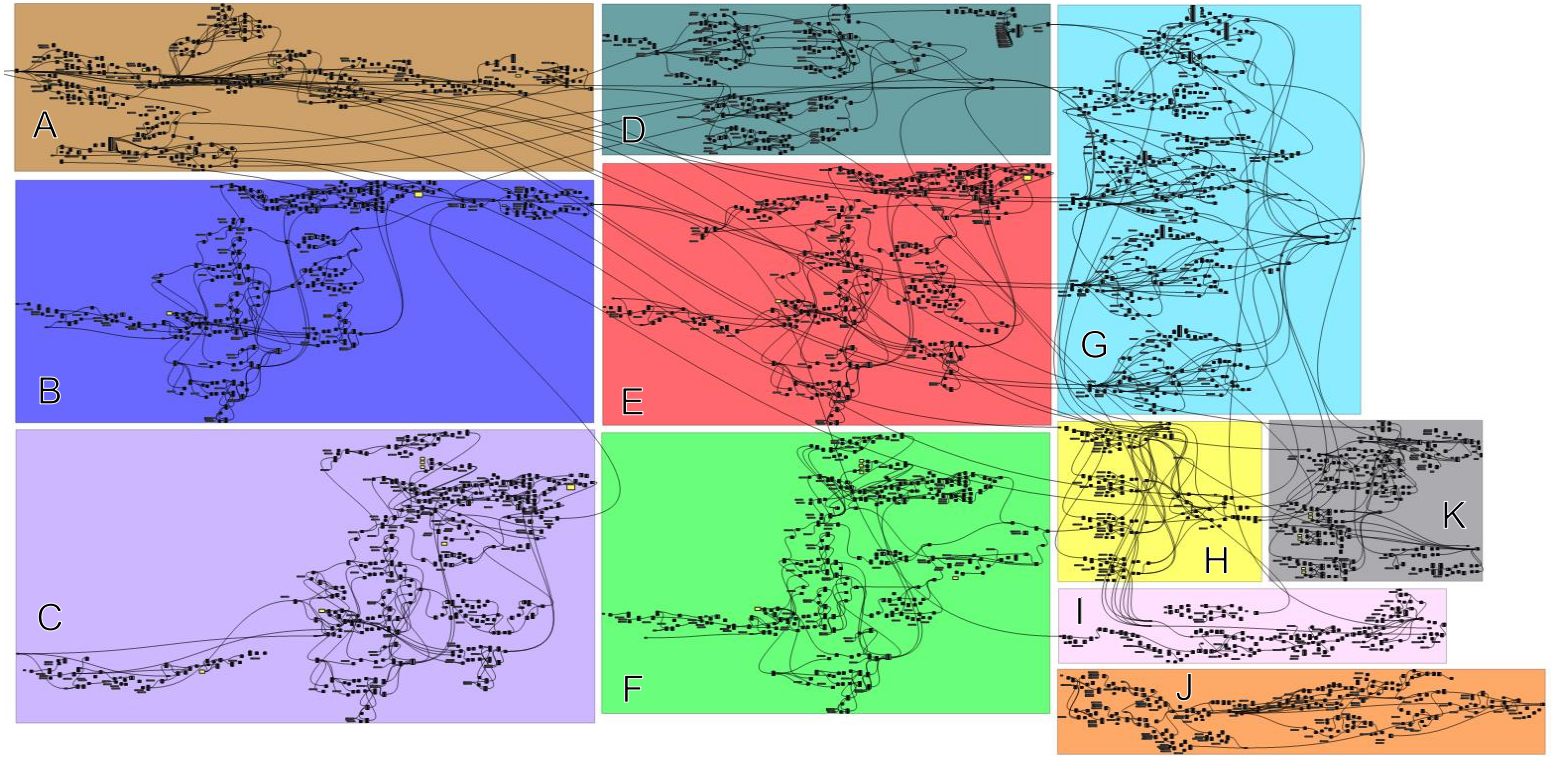

Figure B.1: Grasshopper path for the production of the skull, dural septa and phantom cradle. Block A processes the skull and splits it into its two halves and builds the general geometry for the cradle; Blocks B-F build the tabs of the dural septa and the corresponding grooves of the skull. Block G builds the fixation ring. Block H builds onto the skull the tubes which accept the threaded nylon rods. Block I builds the mould for the gasket. Block J attaches the tabs to the dural septa part and builds in the elements required to flex the part. Block K builds the fixer part and finishes the cradle geometry of Block A. Entire path contains 3908 components.